UNIVERSIDAD POLITÉCNICA DE MADRID
Escuela Técnica Superior de Ingenieros de Telecomunicación

Photonic integrated circuits for dual-comb interferometry

DOCTORAL THESIS

Submitted for the degree of Doctor by:

Pablo López Querol
MSc in Photonics Engineering

Madrid, 2025

UNIVERSIDAD POLITÉCNICA DE MADRID
Escuela Técnica Superior de Ingenieros de Telecomunicación

Doctoral Degree in Communication Technologies and Systems

Photonic integrated circuits for dual-comb interferometry

DOCTORAL THESIS

Submitted for the degree of Doctor by:

Pablo López Querol
MSc in Photonics Engineering

Under the supervision of:
Dr. Antonio Pérez Serrano

Madrid, 2025

Title: Photonic integrated circuits for dual-comb interferometry

Author: Pablo López Querol

Doctoral Programme: Communication Technologies and Systems

Thesis Supervision:

Dr. Antonio Pérez Serrano, Profesor Titular de Universidad, Universidad Politécnica de Madrid (Supervisor)

External Reviewers:

Thesis Defense Committee:

Thesis Defense Date:

This thesis has been supported by the Ministerio de Economía y Competitividad of Spain through grants TED2021-131957B-100 and PID2021-1234590B-C21, which have been funded by MCIN/AEI/10.13039/501100011033 and by the European Union through the NextGenerationEU/PRTR and ERDF programs ("A way of making Europe"). The international research stay was supported by the Programa Propio UPM of the Universidad Politécnica de Madrid.

I have seized the light. I have arrested its flight
– Louis Daguerre

Acknowledgement

La cita anterior la pronunció Louis Daguerre en algún momento incierto después de conseguir demostrar el procedimiento que lleva su nombre, el daguerrotipo, antecedente directo de la fotografía. Aunque la cita que he escogido pueda resultar hoy pretenciosa e incluso ingenua, en su época debemos entenderla desde la perspectiva del siglo XIX. La posibilidad de manipular la luz hasta fijarla en una imagen estática rozaba lo mágico. Y hasta cierto punto lo es. Podría haber elegido cualquier cita de alguno de los científicos que contribuyeron a comprender la naturaleza de la luz (materia base de esta tesis), pero como aficionado a la fotografía, y porque la frase me divierte, he decidido quedarme con esta.

Tras realizar esta tesis, sin embargo, no puedo sino estar en profundo desacuerdo con Daguerre y su cita. Atrapar la luz y detener su vuelo sigue siendo extraordinariamente difícil. La luz continúa siendo tan caprichosa en el siglo XXI como lo ha sido siempre, y quizá este mismo campo de investigación lo demuestra. Hemos avanzado enormemente en su estudio, generación y manipulación, pero ¿llegaremos algún día a dominarla o comprenderla plenamente y a poder afirmarlo sin sonar ingenuos o pretenciosos? Quién sabe. Por ahora, esta tesis representa tan solo un pequeñísimo esfuerzo más en ese camino.

Así funciona el mundo, supongo. Es caprichoso y complejo, pero nuestra tarea consiste en intentar comprenderlo y, sobre esa comprensión, esforzarnos por mejorarlo. Aun sin haber logrado atrapar la luz ni detener su vuelo, sí he conseguido otras cosas igual de valiosas en el plano personal. He tenido la fortuna de trabajar en un grupo cuyo ambiente me ha permitido desarrollarme como investigador y alimentar mi curiosidad. Mis compañeros han sido un apoyo constante durante la realización de esta tesis. Al final, creo que la tarea de hacer una tesis doctoral es un proceso de preparación, aprendizaje y maduración. Y al final de todo, como dijo B. B. King, “lo hermoso de aprender es que nadie puede quitártelo”.

Quiero agradecer sinceramente a quienes me han guiado en este proceso. En primer lugar, a Toni, mi director, por orientarme, motivarme y enseñarme que, incluso en las situaciones en las que uno exclama *cuánto de sufrir* acaban dando frutos. A Ignacio, por transmitir su sabiduría y encender en mí, en más de una ocasión, la chispa de querer saber y comprender más. A José Manuel, por mostrarme que el rigor y la metodología son casi tan importantes como el resultado, o incluso más. A Clara, por su acompañamiento durante todos estos años y su amistad. Y a las incorporaciones más recientes del grupo, una advertencia: dejaos guiar, disfrutad del proceso y conservad vuestra curiosidad por aprender.

Si hablamos de hacer el mundo mejor, quiero agradecer a la gente que me acompaña en ello y que son mis amigos. Gracias a todas y todos. Intentar mejorar el mundo a vuestro lado es una de las tareas más hermosas que existen. Y una mención especial para ti, Clara: gracias por construirlo conmigo cada día. Por supuesto, mi familia ha sido un pilar fundamental. A mis padres y a mi hermana, gracias por vuestro apoyo, vuestro cariño y por sostenerme siempre. Extiendo este agradecimiento también a mis abuelos. Aunque algunos ya no estén, su recuerdo permanece en mí con profundo cariño.

Quiero agradecer también a Xavi, que me acogió durante mi estancia en Glasgow, una experiencia fenomenal para mí. Y por supuesto, a todas las personas que allí me acompañaron. Finalmente, gracias a quienes lean esta tesis. Principalmente, a la gente que ha revisado y mejorado este documento, y a la gente que lo evalúa. Y si por casualidad alguien está leyendo esto y no entra en ninguna de las anteriores categorías, gracias simplemente por dedicarle algo de tiempo.

No quiero extender más los agradecimientos, y sé que dejo a gente atrás; soy consciente de ello. Pero tranquilidad, prefiero agradeceros en persona o esperar a que vengáis a reprocharme (espero que cariñosamente) no aparecer aquí y poder compensarlo.

Para terminar, quiero romper una lanza a favor de Daguerre y su cita, porque en algo sí tenía razón. La luz es bella y cualquier intento de atraparla permite atrapar la belleza del mundo.

Abstract

Dual comb interferometry is an optical measurement technique that enables a broad range of applications, including distance measurement, spectroscopy, and imaging, with high spectral resolution and accuracy. It relies on multiheterodyne interference between two optical frequency combs with slightly different repetition rates, which allows optical information to be converted into the radio-frequency domain. This approach eliminates the need for moving parts, enabling fast, single-shot measurements to be taken using low-bandwidth electronics. Since its initial demonstrations, dual-comb interferometry has demonstrated significant potential in spectroscopy, distance metrology, imaging, and distributed sensing applications.

In order to deploy dual-comb systems in practical applications, sources that are compact, stable, and cost-effective are required. Thanks to their efficiency, small footprint, and compatibility with integrated photonic technologies, semiconductor lasers are ideal candidates. Monolithically integrating such sources on indium phosphide photonic integrated circuits using open-access, generic fabrication processes is a key step towards miniaturising and scaling up dual-comb interferometry systems.

This PhD thesis describes the design, implementation, and characterisation of a dual-comb interferometer integrated onto a generic indium phosphide photonic platform. The work investigates optical frequency comb generation using directly modulated and optically injected semiconductor lasers, exploring strategies to enhance coherence, stability, and spectral characteristics. Furthermore, the development and integration of the key subsystems required for a fully functional on-chip interferometer are also covered. All designs and experiments were realised within the framework of European open-access generic integration processes, providing a benchmark for assessing the maturity of these technologies in advanced photonic systems.

The results demonstrate the feasibility and potential of indium phosphide based integrated photonics for compact and scalable dual-comb interferometry, thereby enabling future high-performance, chip-scale spectroscopic and interferometric sensing applications.

Resumen

La interferometría de peines duales es una técnica de medición óptica que ofrece un amplio abanico de aplicaciones, entre las que se incluyen la medida de distancias, la espectroscopía y la formación de imágenes, con elevada resolución espectral y gran exactitud. Se basa en la interferencia multiheterodina entre dos peines de frecuencias ópticas con tasas de repetición ligeramente diferentes, lo que permite convertir la información del dominio óptico al dominio de radiofrecuencia a través de un proceso de compresión espectral. De este modo, se eliminan los componentes móviles y el tiempo de adquisición se reduce a una sola medida. Gracias a ello, los sistemas interferometría de peine dual ofrecen medidas rápidas, precisas y compatibles con electrónica de bajo ancho de banda. Desde sus primeras demostraciones, esta técnica ha mostrado un enorme potencial en espectroscopía, metrología de distancias, imagen y sensado distribuido.

El despliegue de sistemas de peine dual en entornos prácticos requiere fuentes compactas, estables y de bajo coste. En este contexto, los láseres de semiconductor son candidatos idóneos debido a su eficiencia, reducido tamaño y compatibilidad con tecnologías fotónicas integradas. La integración monolítica de estos generadores en circuitos fotónicos integrados de fosfuro de indio mediante procesos de fabricación genéricos es un paso fundamental para conseguir la miniaturización y escalabilidad de los sistemas de interferometría de peine dual.

En esta tesis doctoral se aborda el desarrollo y la caracterización de un interferómetro de peine dual completamente integrado en una plataforma fotónica de fosfuro de indio de acceso abierto. Se estudian en detalle los mecanismos de generación de peines ópticos mediante técnicas de modulación directa e inyección óptica, así como estrategias para mejorar su coherencia, estabilidad y características espectrales. Además, se desarrollan e integran subsistemas clave para implementar un interferómetro de peine dual funcional sobre chip. Todo el trabajo se lleva a cabo en el marco de los procesos de integración genérica europeos, lo que además permite evaluar el grado de madurez tecnológica de estas plataformas para el desarrollo de sistemas fotónicos avanzados.

Los resultados obtenidos demuestran el potencial de la fotónica integrada basada en fosfuro de indio para la implementación de sistemas de interferometría de peine dual compactos y escalables, allanando el camino hacia futuras aplicaciones de sensado espectroscópico e interferométrico de altas prestaciones completamente integradas en chip.

Table of Contents

List of Figures

List of Tables

Abbreviations and acronyms

AOM	Acousto-optic modulator
AWG	Arrayed waveguide grating; arbitrary waveform generator
BB	Building block
BPD	Balanced photodiode
CBB	Composite building block
CC-W	Counter-clockwise
CF	Compression factor
CMOS	Complementary metal–oxide–semiconductor
CNR	Carrier-to-noise ratio
CPW	Coplanar waveguide
CW	Continuous wave
C-W	Clockwise
DCI	Dual-comb interferometry
DCS	Dual-comb spectroscopy
DDS	Direct digital synthesiser
DFB	Distributed feedback
DRC	Design rule check
EAM	Electro-absorption modulator
ECL	External cavity laser
EDFA	Erbium-doped fibre amplifier
EO	Electro-optic
EOM	Electro-optic modulator
EOPM	Electro-optic phase modulator
ESA	Electrical spectrum analyser

FMCW	Frequency-modulated continuous wave
FTIR	Fourier-transform infrared
FS	Frequency shifter
FSR	Free spectral range
FWM	Four-wave mixing
HR-OSA	High-resolution optical spectrum analyser
I/O	Input/output
IC	Integrated circuit
ISO	Isolator
ITU	International Telecommunication Union
JePPIX	Joint European Platform for Photonic Integration of Components and Circuits
LFSR	Linear feedback shift register
LiDAR	Light detection and ranging
LN	Lithium niobate
LNOI	Lithium niobate on insulator
LSI	Large-scale integration
ML	Master laser
MLL	Mode-locked laser
MMI	Multi-mode interference
MPW	Multi-project wafer
MQW	Multi-quantum well
MSI	Medium-scale integration
MZM	Mach–Zehnder modulator
NDA	Non-disclosure agreement
PCB	Printed circuit board
PD	Photodiode
PDK	Process design kit

PIC	Photonic integrated circuit
PI	Power-current
PM	Power meter
PPG	Pulse-pattern generator
PRBS	Pseudo-random binary sequence
QCS	Quantum-confined Stark effect
QW	Quantum well
QS	Q-switching
RF	Radio-frequency
RIN	Relative intensity noise
RMCW	Random-modulated continuous wave
SA	Saturable absorber
SBSR	Sideband suppression ratio
SDR	Software-defined radio
SEM	Scanning electron microscope
SESAM	Semiconductor saturable absorber mirror
SG-DBR	Sampled-grating distributed Bragg reflector
SHG	Second-harmonic generation
SiN	Silicon nitride
SiPh	Silicon photonics
SOI	Silicon-on-insulator
SL	Slave laser
SNR	Signal-to-noise ratio
SOA	Semiconductor optical amplifier
SOI	Silicon-on-insulator
SSC	Spot-size converter
SRH	Shockley–Read–Hall

SRL	Semiconductor ring laser
SSI	Small-scale integration
TEC	Thermoelectric cooler
TE	Transverse electric
TFLN	Thin-film lithium niobate
TM	Transverse magnetic
ToF	Time of flight
TWE	Travelling-wave electrode
UPM	Universidad Politécnica de Madrid
VLSI	Very-large-scale integration
WDM	Wavelength-division multiplexing

Chapter 1

Introduction

1.1 Motivation

Photonics is the branch of science and technology devoted to the generation, control and detection of light, encompassing its transmission, modulation, amplification and guidance. Its foundations were established through centuries of exploration, from early studies on refraction and diffraction to Maxwell's unification of electromagnetism and the rise of quantum optics. The laser, the first coherent light source, was demonstrated in 1960. Of particular relevance to this work, stimulated emission in semiconductors was shown in 1962 [1], leading to the diode laser which became one of the most significant achievements in applied photonics. As fabrication techniques advanced, semiconductor heterostructures enabled efficient and compact laser sources and miniaturised waveguides, preparing the ground for what later became integrated photonics. The concept of integrated optics was articulated in 1969 [2]. Integrated photonics brings together optical functions such as light generation, modulation, detection, and routing on a single chip, in much the same way that microelectronics integrates transistors and circuits. Photonic integrated circuits (PICs) now provide a wide range of applications, including high-speed communications [3], [4], precision sensing [5], [6], quantum technologies[7], and biomedical diagnostics [8], [9].

The growing demand for PICs has given rise to a specialised manufacturing ecosystem, with several foundries now offering services comparable to those in the microelectronics industry. A key aspect of this work is the use of generic integration platforms through multi-project wafer (MPW) runs. In such runs, the available area of a semiconductor wafer is shared among multiple designs from different users, including research groups and companies. Compared with exclusive manufacturing, sharing a wafer reduces fabrication costs, greatly accelerates prototyping and provides access to advanced processes without the need for large-scale investment in in-house facilities.

Generic integration relies on a standardised set of processes through which basic functional components, known as building blocks (BBs), are realised without modifying the fabrication process itself. Designers can access these platforms via commercially available Process Design Kits (PDKs), which offer validated BB libraries, BB simulation models, design-rule checks, and the ability to generate PIC layouts. This approach streamlines the design process, enabling engineers to concentrate on system architecture and interconnection rather than device-level specifics.

An optical frequency comb (OFC) is a coherent light source whose spectrum comprises a discrete set of equally spaced lines within a certain optical bandwidth. Comb generation was first demonstrated in bulk mode-locked lasers, and the importance of the concept was recognised with the 2005 Nobel Prize in Physics awarded to John L. Hall and Theodor Hänsch [10], [11]. Optical frequency combs support a wide range of applications, including precision metrology, high-resolution spectroscopy, microwave photonics, coherent communications, and ranging. Many mechanisms can generate combs and produce multiple discrete frequencies from a single source. Integrated photonics has enabled on-chip OFC sources. Alongside monolithic approaches, there are hybrid and heterogeneous schemes that combine PICs from different material platforms. Semiconductor lasers are especially attractive because they offer simplicity, compactness, and low cost, and they enable a full monolithic implementation of comb sources. Although integrated combs can now deliver characteristics comparable to bulk implementations, combining them with other on-chip components to realise complete systems remains challenging.

One of the most important applications of OFCs is dual-comb interferometry (DCI). This technique involves multi-heterodyne beating between two combs with slightly different repetition rates or line spacings. When these spectral lines are mixed in a photodetector, a new comb is produced in the radio frequency (RF) domain, whose spacing equals the difference between the optical repetition frequencies. This process effectively maps the optical spectrum, including amplitude and phase, into the RF domain, enabling rapid, high-resolution measurements to be made in a single acquisition without moving parts and with low electronic bandwidth requirements.

The potential of DCI systems integrated on PICs goes far beyond laboratory demonstrations. In the context of an intensifying climate crisis and increasingly frequent and intense extreme weather events such as floods, droughts, and wildfires, the ability to monitor greenhouse gases and atmospheric pollutants with high sensitivity is of great importance. Dual-comb spectroscopy (DCS) is a powerful tool for this purpose, enabling the precise, real-time detection of multiple gas species over wide spectral ranges using compact, cost-effective instruments. In addition to environmental sensing, integrated DCI systems offer significant opportunities in areas such as high-precision ranging, coherent imaging, and optical metrology. Their abilities make them ideal for use in portable, reconfigurable instruments. Monolithic integration of such systems on a photonic platform enhances their robustness and scalability further, paving the way for practical devices to be deployed to the market.

This thesis explores the monolithic integration of DCI within PICs fabricated on generic indium phosphide (InP) platforms available through open-access foundries. The primary objective is to realise a flexible, reconfigurable DCI architecture that can be fully integrated onto a single photonic platform. To this end, the first part of this work focuses on on-chip OFC generation via direct modulation of optically injected semiconductor lasers, encompassing gain switching (GS) and Q-switching (QS) techniques. The latter is explored as an alternative to GS to generate broader OFCs which can be beneficial for the DCI applications targeted here.

Both techniques offer flexible control of comb line spacing and are compatible with low-cost electronic drivers. Leveraging this implementation with generic integration and standard PDKs aims to reduce system costs and simplify the implementation process through rapid prototyping.

This work addresses a key technical challenge arising from the absence of optical isolators in generic integration platforms, which makes stable operation under optical injection (OI) particularly difficult. Since on-chip isolators are not typically included in standard PDKs, alternative approaches are required in OI schemes to prevent perturbations in the system. This thesis therefore proposes and validates strategies to mitigate feedback effects, enabling dual-comb implementation based on optically injected gain-switched semiconductor ring lasers (SRLs) with stable operation.

In addition to the implementation of OFC generation mechanisms and the DCI architecture in monolithic InP PICs, this work includes the design and experimental realisation of key DCI subsystems aimed at enhancing overall system performance. In particular, an integrated frequency shifter has been developed on the same platform. This element plays a crucial role in achieving the full functionality of the DCI system in the detection of the down-converted comb, representing an important step towards complete DCI integration. The successful demonstration of such subsystems paves the way for future work on the realisation of more complex and advanced monolithic DCI systems on a single PIC.

1.2 Antecedents and context

This thesis was conducted within the Applied Photonics Group at CEMDATIC (Advanced Materials and Devices for Information and Communication Technologies Centre, from its Spanish acronym) at the Universidad Politécnica de Madrid (UPM). The group has a well-established and extensive expertise in both the theoretical and experimental study of semiconductor lasers. When this work began, the group had extensive experience in generating OFCs using the GS technique and applying them to the spectroscopy of greenhouse gases and distance measurement. Furthermore, when this thesis commenced, the group had begun work on designing and characterising PICs fabricated in open-access foundries based on the generic integration approach. This thesis is framed within this context and aims to contribute to the development of integrated solutions to replace the bulky systems in which the group already specialised.

A direct antecedent of this thesis is the PhD thesis of Clara Quevedo, which focused on generating OFCs with low repetition rates in laboratory setups to enhance the spectral resolution of dual-comb interferometers for spectroscopy and ranging applications. Her research built upon earlier work within the group by Alejandro Rosado, who investigated OFC generation in optically injected GS lasers. Building on these foundations, Quevedo implemented and experimentally demonstrated high-resolution dual-comb interferometers based on GS and discrete component architectures. Subsequently, efforts were made to reduce system costs by replacing a high-end detection scheme with a low-cost software-defined radio (SDR) and an RF signal generator with a direct digital synthesiser (DDS) to drive the gain-switched lasers. In parallel, high-resolution ranging with DCI was developed, and comb-densification schemes were proposed to enhance spectral resolution while reducing the repetition rate to a few kHz. Alongside Quevedo's PhD thesis, the group demonstrated tunable DCS across the C and L bands for multi-gas spectroscopy. This enabled the measurement of pollutants such as ammonia (NH_3), carbon monoxide (CO), hydrogen cyanide (HCN) and carbon dioxide (CO_2). Finally, we demonstrated that a single optically injected laser could be used for dual-comb generation, albeit at the cost of careful optical path design.

With these antecedents, I initially contributed to the study of GS OFC generation in discrete semiconductor lasers at low repetition rates, focussing on the generation and analysis of the resulting combs. Building on this experience, the doctoral research was initiated, first supported by the SINFOTON2-CM consortium and later by the national project PICSAR (Photonic Integrated Circuits for Sensing And Ranging). This project extended the previous work towards the integration of GS OFC sources on InP PICs fabricated through open-access foundries using generic integration processes, and towards their application in remote gas sensing. In parallel, research within the project also explored random-number generation on PICs in collaboration with the Instituto de Física de Cantabria (IFCA).

This thesis was inspired by the availability of open-access platforms for integrated photonics and their potential to incorporate the comb systems that we had been studying. The aim was to translate our expertise from bulky laboratory implementations to PICs. This approach offered a way to reduce system costs and explore higher levels of integration for GS combs in system-level applications. To the best of the author's knowledge, demonstrations of fully monolithic dual-comb implementations based on GS OFCs were unavailable at the time of writing.

1.3 Objectives

The main objective of this thesis is to develop a monolithically integrated dual-comb interferometer. To this end, generic InP platforms have been adopted for integrating such systems, as this allows lasers to be co-integrated with passive and active photonic components while accelerating prototyping and reducing costs via MPW runs. The system is designed to be flexible and reconfigurable while achieving enhanced spectral resolution. The specific objectives are:

- Review and analyse the state of the art in OFC generation in PICs, with particular emphasis on GS OFC sources.
- Investigate OFC generation on PICs via the direct modulation of optically injected semiconductor lasers, employing GS and QS techniques to enable reconfigurability and high spectral resolution.
- Develop integration strategies for comb sources that require optical injection to overcome the practical limitations of current platforms regarding the absence of optical isolators.
- Design and demonstrate an integrated dual-comb generator suitable for DCI.
- Design and demonstrate an integrated frequency shifter subsystem compatible with the dual-comb generator, contributing to the further integration of a complete DCI system.

- Assess the viability and constraints of open-access foundries for implementing the above.

1.4 Structure of this thesis

The structure of this thesis dissertation is as follows:

- Chapter 2: This chapter introduces the fundamentals of integrated photonics. It begins with an overview of PICs and their key historical milestones. It then provides an overview of integration technologies across the main platforms and materials, before concluding with an overview of the generic InP platforms employed.

- Chapter 3: Optical frequency combs. This chapter introduces the fundamentals of OFCs and their generation techniques, alongside the fundamentals of DCI. The current state of integrated OFC sources is reviewed and concludes with an overview of integrated dual-comb interferometers.

- Chapter 4: Experimental methods for characterising photonic integrated circuits. This chapter covers the experimental methods developed and employed for the characterisation of PICs throughout this thesis. Concerning the measurement of the chips, two complementary approaches were implemented: a probe station for characterising PICs at the die level, and an electrical packaging solution. In addition, a general description of the measurement procedures and the automation strategies used in this work is provided.

- Chapter 5: Integrated optical frequency comb generation. This chapter presents the results obtained regarding OFC generation in PICs. First, QS is introduced as an alternative to GS for generating broader combs. The results are presented based on a theoretical rate-equation model, and the implementation of this technique on a PIC is also described. Next, a system based on integrated GS OFCs is presented. Finally, a design is proposed to overcome the absence of optical isolators by employing SRLs. All the devices and systems discussed in this chapter were implemented on InP technology through open-access foundry platforms within MPW runs.

- Chapter 6: Integrated dual-comb interferometry. This chapter presents the results obtained for the integrated dual comb interferometer and the frequency shifter subsystem, which were designed, simulated, and experimentally characterised. Both systems were implemented through open-access InP platforms within MPW runs, encompassing all stages from design to experimental validation.

- Chapter 7: Conclusions and outlook. This final chapter outlines the main conclusions drawn from the dissertation. Proposed future lines are also suggested.

Furthermore, an annex provides details of additional PIC designs developed during this research but ultimately falling outside the scope of the thesis. These include designs for ranging and gas sensing that do not rely on frequency combs, as well as comb-generation concepts extending beyond direct modulation of semiconductor lasers.

Chapter 2

Photonic integrated circuits

This chapter introduces integrated photonics, outlining its key historical milestones, current technological status, and the main integration platforms, with particular emphasis on generic InP technologies. Since the concept of PICs was first proposed in 1969, the field has developed to reduce the size, weight, power, and cost (SWaP-C) of optical communication systems. This evolution has been marked by a series of technological milestones, each of which has enabled the realisation of new on-chip functionalities. A key milestone has been the emergence of open-access foundries in the mid-2000s, which have transformed the PIC ecosystem by making fabrication accessible to a broader research and industrial community.

Integrated photonics is supported by materials that exhibit optical and optoelectronic properties. The set of technologies based on a specific material offering functional devices is known as an integration platform. The main integration platforms and technologies are summarised in Section 2.2, including silicon-on-insulator (SOI), silicon nitride (SiN), lithium niobate (LN), and indium phosphide (InP), each offering different characteristics. This can be combined in heterogeneous and hybrid integration, and co-packaging with electronics is a key milestone in the integrated photonics roadmap.

Finally, Section 2.3 focuses on the generic InP integration platform. This platform enables the monolithic integration of passive and active devices, such as lasers, modulators, and photodetectors, on the same chip. This makes it especially suitable for developing compact, fully integrated OFC sources and dual-comb systems.

2.1 Introduction and historical perspective

PICs are devices in which multiple optical components are miniaturised and interconnected at the chip scale on a single substrate. They can generate, manipulate, guide, and detect light using elements such as lasers, modulators, waveguides, and photodetectors (PDs). PICs are the optical equivalent to electronic integrated circuits (ICs) and have followed a broadly similar trajectory, albeit at a slower pace. Table 2.1 illustrates this, summarising the most significant milestones in integrated electronics and photonics.

Following the demonstration of the semiconductor laser by Robert Hall in 1962 and earlier proposals of ICs, the concept of integrated photonics was first proposed by Bell Laboratories scientist Stewart E. Miller in 1969. In his work, Miller proposed the integration of multiple optical components on a planar substrate using lithographic fabrication, with passive and active elements interconnected by miniaturised waveguides. The idea of integrating multiple functions on a single chip attracted a great deal of attention, and efforts were made to demonstrate the first functional devices.

Table 2.1: Most relevant milestones in the development of electronic and photonic integration adapted from [12]. CMOS: Complementary Metal-Oxide Semiconductor; MPW: Multi-project wafer run; SSI: Small Scale Integration; MSI: Medium Scale Integration; LSI: Large Scale Integration; VLSI: Very Large Scale Integration.

	Electronics	Photonics
Integration concept proposed	1952	1969
First integrated circuit	1958 (Hybrid) 1960 (Monolithic)	1976
Generic integration technology (CMOS / MPWs)	1979	circa 2008
SSI (1-10 components)	1960–mid-1960s	mid-1990s
MSI (100-1,000 components)	mid-1960s–early 1970s	2000s
LSI (1,000 to 10,000 components)	early 1970s–mid-1980s	2010s
VLSI (millions of components)	mid-1980s onward	Not achieved yet
Materials	Silicon, Germanium	Silicon, InP, GaAs, $LiNbO_3$, polymers

Initial research on integrated optics focused primarily on glass materials due to their full optical compatibility with optical fibers. However, during the 1970s, early devices were fabricated employing different materials with optical and optoelectronic properties. Notable examples include low-loss channel waveguides fabricated in LN [13], [14], and compound III-V semiconductors such as Gallium Arsenide (GaAs) [15], [16], Zinc Telluride (ZnTe) [17] and Gallium Phosphide (GaP) [18] for the visible range, and Aluminium Gallium Arsenide (AlGaAs) for active and passive components [19], [20], [21]. In his excellent state-of-the-art review from 1977, Ping King Tien [22] framed the goal of integrated photonics as “the integration of a large number of optical devices on a small substrate, so forming an optical circuit reminiscent of the integrated circuit in microelectronics”, and "to apply thin-film technology to the formation of optical devices and circuits". By that time, one of the first examples of an advanced monolithic integrated circuit with full functionality was demonstrated, comprising six distributed feedback (DFB) lasers connected to six channel waveguides, forming an integrated wavelength multiplexing light source [23].

By the 1980s, the telecommunications industry was leaning towards fiber optics, and the fabrication of devices had matured. The early development of integrated photonics was primarily driven by optical communications. A key milestone came in 1985 with the introduction of silicon-based PICs, proposed by R. Soref and seeding the field of silicon photonics (SiPh) [24]. SiPh emerged primarily because silicon is transparent within the 1.3 μm to 1.6 μm range, a region that is highly advantageous for optical communications as it coincides with the low-loss transmission bands of standard silica optical fibers. Its compatibility with well-established complementary metal-oxide-semiconductor (CMOS) fabrication processes within the electronics industry further accelerated its development. Shortly afterwards, low-loss waveguides were demonstrated in silicon-on-insulator (SOI) technology, offering propagation losses of less than 0.5 dB/cm [25] within the aforementioned wavelength range. SiPh evolved rapidly from small-scale integration (SSI) to medium-scale integration (MSI) at the turn of the century.

Another key milestone was achieved by the late 1980s with the proposal of the arrayed-waveguide grating (AWG) by M. Smit [26], which was demonstrated shortly thereafter [27], [28]. AWGs enabled dense WDM (DWDM) achieving channel spacings below 100 GHz [29]. Combined with the maturing integration of lasers, modulators, and photodiodes, this capability propelled the field beyond SSI to MSI, particularly on the InP platform. AWG-based architectures often achieved the highest on-chip complexities in terms of component density until now.

Following the emergence of AWGs, the next significant milestone was the scaling of fabrication and design through generic photonic integration. In this approach, open-access foundries coordinate MPW runs in which multiple independent designs are fabricated on the same wafer. The key idea is that these designs use a fixed, standardised set of device structures from which a wide variety of functional components known as BBs can be realised. By reusing the same process and BBs, designers assemble circuits without application-specific process changes, while the wafer cost is shared among participants. This standardisation reduces production costs, shortens time to prototype, and improves design portability across process updates, thereby broadening access to complex PICs to research institutes, universities, and companies.

Generic integration platforms are supported through PDKs, which enable this model by providing a comprehensive design framework that includes libraries of validated BBs such as lasers, modulators, detectors, filters, and passive routing elements, together with simulation models, layout abstractions, and design rule checks (DRC). The PDK encapsulates proprietary process details, including layer stacks and materials, providing the necessary interfaces for design, simulation, and layout. Consequently, system design becomes independent of device fabrication. Circuit design focuses on functionality and architecture, combining basic BBs into higher-level composite building blocks (CBBs) and complete circuits, while process optimisation, characterisation, and fabrication learning remain within the foundry. Portability across process updates is ensured through the continuous update of models within the PDK, which is typically made available to designers under a non-disclosure agreement (NDA).

These developments have driven an increase in integration density and functional complexity. Early demonstrations with tens of elements have given way to large-scale integration (LSI) in which thousands of components can be integrated within the same chip [30]. Fig. 2.1 illustrates this trajectory for integration platforms based on InP and silicon substrates, which currently exhibit the most mature levels of integration, together with heterogeneous InP/Si and GaAs/Si, highlighting the progression from early prototypes with a few components to application-specific PICs (ASPICs) with increased complexity.

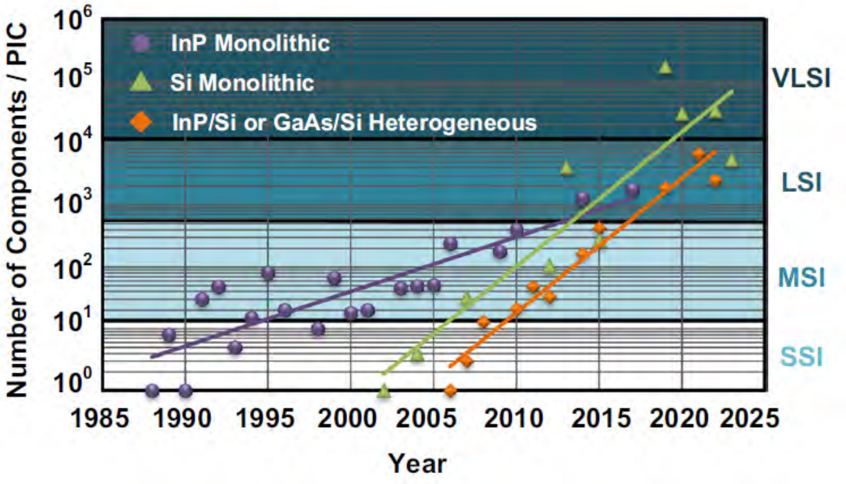

Figure 2.1: Evolution of number of components per PIC over the years for three different platforms: monolithic InP, monolithic Si, and hetergeneous InP/Si or GaAs/Si. SSI: small-scale integration; MSI: medium-scale integration; LSI: large-scale integration; VLSI: very large-scale integration. Source: [31]

Concurrently, the field is evolving beyond single-platform solutions towards hybrid and heterogeneous integration, aiming to combine the strengths of different material platforms within a single package or integrated system. In heterogeneous schemes, multiple materials are integrated at the wafer or die level through techniques such as wafer bonding, die-to-wafer bonding, or micro-transfer printing [32], [33]. This approach, for instance, enables the combination of III–V optical gain with low-loss silicon or silicon nitride (SiN) waveguides. In hybrid approaches, by contrast, separately fabricated chips are co-packaged using high-density interconnects to form multi-chip assemblies.

Looking ahead, electronic-photonic co-integration, or co-packaged optics (CPO), constitutes a key direction in the roadmap of integrated photonics. The tight co-packaging of core communication application-specific integrated circuits (ASICs) with optical components reduces interconnect parasitics and energy per bit, increases bandwidth density, and enables enhanced monitoring and control capabilities in data centres [34]. Further integration, ranging from 2.5D/3D stacking to CMOS-compatible photonics, extends these benefits towards system-on-package solutions [31], [34].

Despite these advances, both hybrid and heterogeneous integration and, more broadly, electronic–photonic co-integration still lack standardised and widely adopted manufacturing processes. This absence of standardisation limits scalability, increases development and packaging costs, and hinders interoperability across foundries and design ecosystems. Establishing robust process standards therefore remains a key challenge for the widespread industrial adoption of integrated photonic technologies, although recent initiatives such as multi-project packaging runs coordinated by Tyndall and Europractice represent important steps towards standardisation [35].

Applications for PICs are vast and continually expanding. Telecommunications utilise PICs in order to implement high-capacity optical transceivers [3]. Energy-efficient interconnects for use in data centres are supported by PICs, which alleviate bandwidth bottlenecks in electronics [4]. PICs are used in sensing [5], for compact and precise systems in optical phased array beam scanners for LiDAR systems [36], biomedical diagnostics [8][9], as well as in environmental monitoring [6]. Photonic integration is equally essential in next-generation quantum technologies, in which stable and scalable platforms for entangling as well as manipulating photons are provided [7]. In addition, it plays an important role in subwavelength optics and metamaterials [37], [38], [39]. PICs are further at the foundation for developments in microwave photonics [40] for microwave generation and THz communications [41], [42], [43], spectroscopy [44], as well as metrology and optical frequency comb generation [45], [46], whereby functionalities not possible with conventional electronics or bulk optical assemblies are made available. Lastly, a new paradigm for integrated photonics has emerged, known as programmable photonics, where the aim is to develop PICs whose functionality can be reconfigured at runtime rather than being hard-wired for a single application [47].

2.2 Integration technologies

Fundamental material characteristics

Photonic integration platforms comprise the materials and fabrication technologies that enable the design and large-scale manufacturing of PICs, from the development of fundamental BBs to their implementation. Table 2.2 summarises the principal characteristics of the main photonic integration platforms, comparing their material properties, available BBs, and overall capabilities. The table lists the main advantages and disadvantages of each technology, providing an overview of their respective strengths and limitations.

A key distinction between integration platforms lies in whether they are active or passive. Active platforms, such as III–V materials (InP and GaAs), possess a direct bandgap that enables native light generation, amplification, and detection, supporting the realisation of integrated lasers, semiconductor optical amplifiers (SOAs), and photodetectors (PDs) alongside standard passive components. In contrast, passive platforms, including SOI, SiN, and LN on insulator (LNOI), lack native optical gain and need heterogeneous and hybrid integration to incorporate detectors and other active devices. For example, germanium can be integrated on silicon (GeSi) to enable photodetection, while additional functionalities such as III-V-on-Si lasers or LN modulators on Si/SiN can be implemented to extend the capabilities of the platform.

The transparency window of a photonic integration platform defines the spectral range over which light can propagate with low loss. This range is set by the bandgap of the material at short wavelengths and by infrared (IR) absorption at long wavelengths, and it determines the suitability of a platform for operation in specific International Telecommunication Union (ITU) bands in the near-IR (O, C, and L bands), as well as in the visible or mid-IR regions. Within this transparency window, the total propagation loss in integrated waveguides arises from several mechanisms that depend on both the material and the device geometry. Intrinsic absorption, free-carrier absorption, and nonlinear processes such as two-photon absorption can contribute significantly to losses in semiconductor platforms, particularly in high-index materials like silicon or InP under strong optical confinement. In contrast, in dielectric platforms such as SiN or LNOI, propagation losses are typically dominated by scattering from sidewall roughness and radiation at bends or tapers. The relative contribution of these mechanisms and their wavelength dependence determine the attainable propagation losses and, ultimately, the performance of the PIC. Typically, InP exhibits higher propagation losses than passive platforms such as SiN or Si, mainly due to stronger intrinsic absorption and surface recombination effects associated with its direct bandgap.

These loss mechanisms are strongly influenced by the degree of optical confinement. Light confinement in a given platform is determined by the refractive index contrast between the core and the surrounding materials, namely the upper cladding and the substrate. For illustration, and without loss of generality, this can be described using a ridge-waveguide geometry, as shown in Fig. 2.2, where a high-index core is embedded between lower-index layers so that the optical mode is guided with an effective refractive index ($\mathrm{n_{eff}}$) that lies between the core and the surrounding media. A higher index contrast provides stronger confinement and allows tighter bend radii, enabling more compact circuits and a reduced footprint. However, while stronger confinement mitigates radiation losses at bends, it also increases the overlap of the optical mode with the waveguide sidewalls, enhancing its sensitivity to surface roughness and fabrication imperfections, which can lead to higher scattering losses.

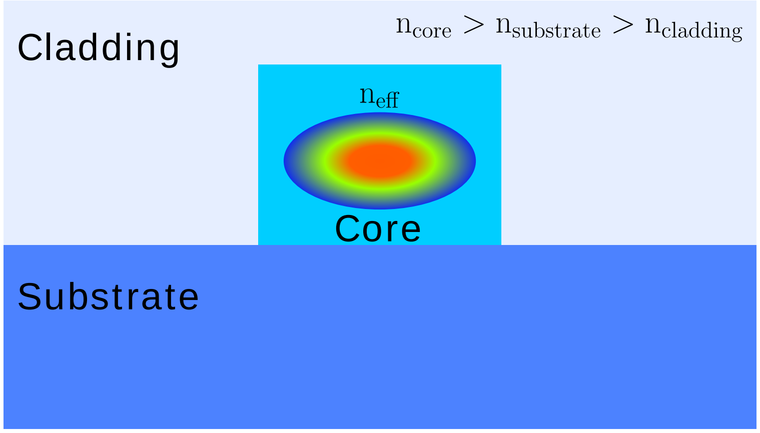

Figure 2.2: Basic schematic of a ridge waveguide. The high refractive index of the core provides lateral and vertical optical confinement, enabling the mode to propagate with an effective refractive index $\mathrm{n_{eff}}$. For guidance to occur, this effective index must remain higher than that of the substrate and the cladding. The waveguide geometry, together with the material indices, determines the value of $\mathrm{n_{eff}}$ and the resulting modal confinement.

Electro-optic (EO) effects are fundamental mechanisms that determine the modulation performance and nonlinear functionality of each photonic integration platform. They originate from the response of a material to an applied electric or optical field, which modifies its optical properties, either absorption or refractive index. Electroabsorption, which is characteristic of direct-bandgap III-V semiconductors, relies on field-induced changes in absorption via mechanisms such as the Franz-Keldysh effect and the quantum-confined Stark effect (QCSE), enabling high-speed intensity modulation.

The linear EO effect (Pockels effect, $\chi^{(2)}$) occurs in non-centrosymmetric materials such as LNOI, InP, and aluminium nitride (AlN), allowing low-V_π linear phase modulation. The quadratic EO effect (Kerr effect, $\chi^{(3)}$) is present in all materials but dominates in centrosymmetric systems such as silicon and SiN, where $\chi^{(2)} = 0$. At sufficiently high optical intensities, the optical field itself can induce refractive index changes through the Kerr effect, giving rise to nonlinear optical phenomena such as self-phase modulation and four-wave mixing (FWM), which can be exploited for OFC generation [48].

Each integration platform provides a specific set of BBs that define its functionality and level of maturity. These include passive components such as splitters, couplers, and filters, as well as active devices such as modulators, PDs, lasers, and SOAs. The type and performance of these BBs determine not only the achievable circuit complexity but also the suitability of the platform for particular applications.

Table 2.2: Summary of the key characteristics of the main photonic integration platforms.

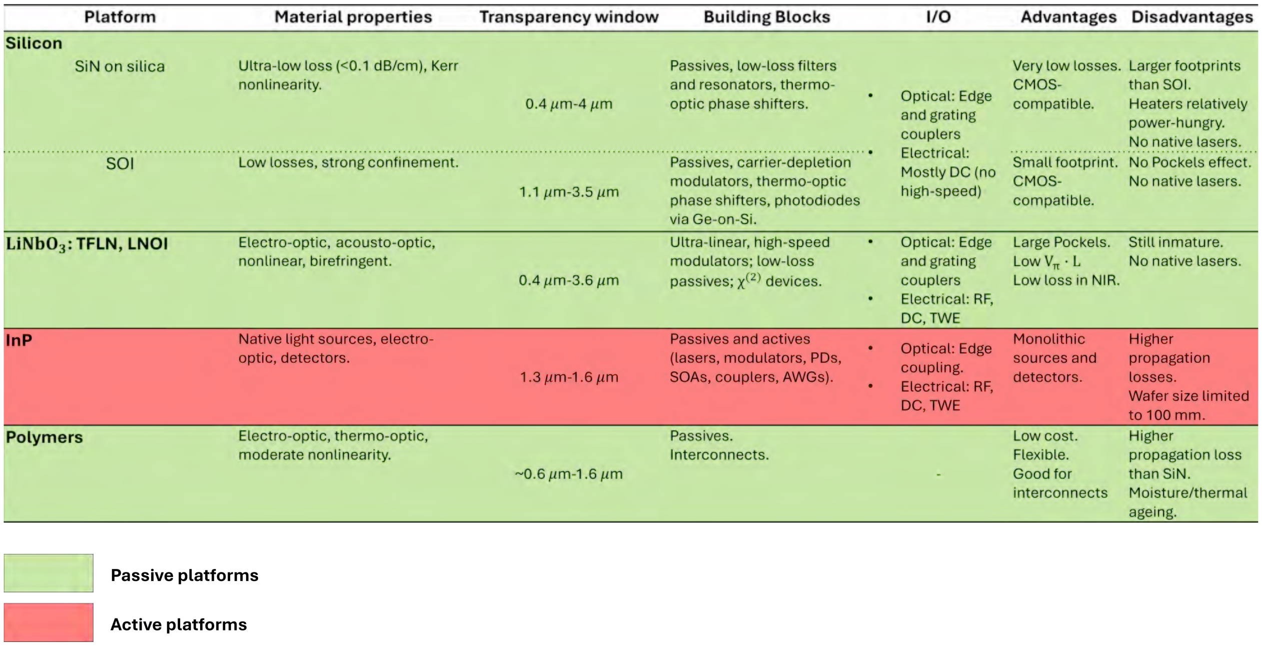

Platform	Material properties	Transparency window	Building Blocks	I/O	Advantages	Disadvantages
Silicon						
SiN on silica	Ultra-low loss (<0.1 dB/cm), Kerr nonlinearity.	0.4 μm-4 μm	Passives, low-loss filters and resonators, thermo-optic phase shifters.	• Optical: Edge and grating couplers • Electrical: Mostly DC (no high-speed)	Very low losses. CMOS-compatible.	Larger footprints than SOI. Heaters relatively power-hungry. No native lasers.
SOI	Low losses, strong confinement.	1.1 μm-3.5 μm	Passives, carrier-depletion modulators, thermo-optic phase shifters, photodiodes via Ge-on-Si.		Small footprint. CMOS-compatible.	No Pockels effect. No native lasers.
$LiNbO_3$: TFLN, LNOI	Electro-optic, acousto-optic, nonlinear, birefringent.	0.4 μm-3.6 μm	Ultra-linear, high-speed modulators; low-loss passives; $\chi^{(2)}$ devices.	• Optical: Edge and grating couplers • Electrical: RF, DC, TWE	Large Pockels. Low $V_\pi \cdot L$ Low loss in NIR.	Still inmature. No native lasers.
InP	Native light sources, electro-optic, detectors.	1.3 μm-1.6 μm	Passives and actives (lasers, modulators, PDs, SOAs, couplers, AWGs).	• Optical: Edge coupling. • Electrical: RF, DC, TWE	Monolithic sources and detectors.	Higher propagation losses. Wafer size limited to 100 mm.
Polymers	Electro-optic, thermo-optic, moderate nonlinearity.	~0.6 μm-1.6 μm	Passives. Interconnects.	-	Low cost. Flexible. Good for interconnects	Higher propagation loss than SiN. Moisture/thermal ageing.

🟩 **Passive platforms**

🟥 **Active platforms**

In addition to the availability of integrated BBs, optical and electrical interfaces are essential for enabling interaction between the PIC and external systems. Optical input and output (I/O) coupling is typically realised either through edge couplers or grating couplers. Edge couplers provide efficient, broadband, and polarisation-insensitive in-plane coupling but require precise alignment and die-level assembly, which can limit scalability. Grating couplers, in contrast, enable out-of-plane coupling that facilitates wafer-level testing and assembly, though at the expense of higher insertion losses, narrower bandwidth, and stronger polarisation dependence.

Electrical interfaces provide access to active devices such as modulators, lasers, and PDs. These connections can be optimised for high-speed operation using RF transmission lines matched to 50 Ω such coplanar waveguides (CPW). In high-speed modulators, travelling-wave electrodes (TWE) are commonly employed connected to these transmission lines. For DC biasing, metal interconnects are typically used. In packaged systems, electrical connections can be implemented through wire bonding, which is widely used for prototyping and device characterisation, or through advanced approaches such as flip-chip, 2.5D, or 3D integration, which allow high-density electrical interconnects and high bandwidth operation for complex photonic-electronic circuits.

Material platforms

The SOI platform comprises a thin, high-index monocrystalline silicon device layer separated from the bulk silicon substrate by an insulating film, typically a buried silicon dioxide (BOX) layer [49]. Early demonstrations of the concept were achieved with silicon-on-sapphire structures. The large refractive-index contrast between silicon and the insulator enables strong optical confinement and compact waveguide routing. Circuit layers commonly employ single-mode strip or rib waveguides. In addition to its optical benefits, SOI provides electrical isolation between circuit elements and enhanced resistance to latch-up, advantageous for co-integration with electronic components. The device-layer and BOX thicknesses can be tuned to realise both thin- and thick-film SOI variants, each offering distinct confinement-loss trade-offs and compatibility with different CMOS manufacturing processes [31], [50].

Thin-film SOI offers strong optical confinement and compact devices, with propagation losses lower than 1 dB/cm in the telecommunication band. In contrast, thick-film SOI can achieve lower propagation losses at the expense of increased footprint. The SOI platform supports several modulation mechanisms. Thermo-optic phase shifters and doped waveguides are simple and readily available in commercial foundries, although they are relatively slow (1–10 μs response time) and power-hungry [51], [52]. Carrier-dispersion modulators, realised through p/n doping in either depletion or injection configurations, enable high-speed operation but introduce additional optical loss. In commercially available platforms, EO bandwidths of up to 60 GHz have been demonstrated using travelling-wave Mach–Zehnder modulators (TWMZMs) [53], with trade-offs between insertion loss and bandwidth well documented [54], [55].

Silicon is an indirect-bandgap material with no native optical gain. Therefore, laser integration relies on hybrid or heterogeneous approaches [56]. Photodetection in the C and L bands is typically implemented using germanium-on-silicon (Ge-on-Si) integration, which is supported by most commercial foundries. This integration has also enabled demonstrations of electro-absorption modulators (EAMs) based either on the Franz–Keldysh effect in bulk Ge for the C/L bands, with limited optical bandwidth, or on the QCSE in Ge/SiGe quantum-well (QW) structures, which offer wider tunability at the cost of increased insertion loss [57]. For optical I/O, both grating and edge couplers with spot-size converters (SSCs) are commonly employed.

Electrical access to the PICs must account for travelling-wave electrodes (TWEs) in high-speed components. Thanks to its large transparent window and advanced CMOS-compatible ecosystem, the SOI platform is particularly well-suited to photonic integrated circuits in the telecommunications band.

The SiN platform consists of a SiN core clad by silica or air, typically supported on a silicon substrate. Compared with SOI, its lower refractive index contrast results in larger bend radii. However, the wide bandgap of SiN enables ultra-low propagation losses, down to about 0.1 $\mathrm{dB\,cm^{-1}}$ in optimised structures, together with high optical power handling and broad spectral transparency from the visible to the mid-infrared [58], [59], [60]. These references provide an excellent overview of the state of the art. Single-mode strip waveguides are commonly employed, although thicker and more strongly confined geometries support tighter routing and high-Q resonators at the expense of greater sensitivity to dimensional tolerances. Due to its lower thermo-optic coefficient relative to silicon, SiN offers improved passive thermal stability. Nevertheless, thermo-optic phase shifters generally require higher heater power for a given phase shift. In addition, the intrinsic tensile stress of SiN films, together with the thermal-expansion mismatch with the underlying oxide, requires careful stress management during the growth and fabrication of thicker layers.

Because SiN is centrosymmetric, it does not exhibit the Pockels effect. However, its Kerr nonlinearity, combined with low propagation losses and the possibility of dispersion engineering, makes the platform particularly suitable for FWM and microcomb generation [61]. The material provides no native optical gain or photodetection, so active functions are added through heterogeneous or hybrid integration [62]. Demonstrations include InP/SiN lasers with sub-kHz linewidths [63] and high-speed modulators based on LNOI/SiN integration [64]. In contrast, the passive BB library is mature [65] and enables high functionality, including low-loss waveguides and adiabatic tapers, directional and multimode interference couplers, high quality factor (Q) ring resonators, AWGs and Bragg gratings, among others. Optical I/O are typically realised through edge coupling with SSCs and through grating couplers. In terms of manufacturing, the platform is CMOS-compatible and fabricated using low-pressure chemical vapour deposition (LPCVD). Furthermore, commercial variants of SiN, such as amorphous SiN, silicon oxynitride (SiON) and silicon-rich nitride (SRN), offer different optical and mechanical characteristics. SRN provides higher refractive index and stronger optical nonlinearity at the cost of increased absorption. SiON enables flexible refractive index control and improved film stress management, while amorphous SiN offers smoother surfaces but a slightly narrower transparency window. The SiN integration platform is widely used in nonlinear optics, sensing and optical communications.

Thick-film LN platforms rely on bulk materials that support a wide variety of designs but involve complex fabrication processes and large device footprints. In contrast, thin-film LN platforms (TFLN) consist of a thin film of LN bonded to an insulator, typically silicon oxide (SiO_2), on a carrier substrate. LNOI refers to LN supported by an SiO_2 insulator, whereas TFLN highlights its use in integrated photonics [66]. TFLN platforms exhibit a lower refractive-index contrast than SOI, which results in weaker optical confinement and, therefore, larger device footprints, although they remain more compact than several other material platforms [67]. Because LN possesses a strong intrinsic Pockels EO effect, TFLN enables phase modulation with low $V_\pi \cdot L$ and high linearity [68]. It also shows low linear propagation losses, negligible two-photon and free-carrier absorption in the telecommunications bands, and a broad transparency window from the visible to the mid-infrared [69]. Additional beneficial properties include a strong acousto-optic effect, while a moderate thermo-optic coefficient improves passive thermal stability compared with SOI but makes thermo-optic phase shifters less power efficient. In contrast, the intrinsic birefringence of LN is typically regarded as a drawback, as it leads to polarisation-dependent behaviour that must be carefully managed in device design. As with other passive platforms, LNOI does not provide native optical gain or photodetection.

The most relevant BBs on TFLN platforms are high-speed TWMZMs and phase modulators, with reported operation beyond 100 Gb/s and $V_\pi = 1.25$ V [68]. The practical bandwidth is limited mainly by RF parasitic capacitances, so careful design of microwave electrodes with impedance and velocity matching through TWEs is required. Additional BBs include low-loss waveguides [70] and tapers, directional and multimode interference (MMI) couplers, high-Q resonators [71], edge and grating couplers, acousto-optic elements [72] and other passive components. Hybrid integration of LNOI-on-Si or LNOI-on-SiN has produced compact modulators [73]. Laser integration has been demonstrated through heterogeneous bonding with III-V materials [74][75]. The platform continues to mature, and recent work focuses on the development of standardised PDKs [76], [77]. For comprehensive reviews of LNOI PICs and their applications, see [66], [67], [69], [76].

III-V platforms for photonic integration are dominated by InP and its quaternary alloys, such as InGaAsP, which form direct-bandgap heterostructures on InP substrates. The refractive index contrast in III–V platforms is generally higher than that of silica or SiN but lower than that of SOI. However, the exact contrast in InP/InGaAsP waveguides depends strongly on the specific heterostructure and alloy composition employed, so the resulting device footprints can vary accordingly. The key advantage of the InP platform is its native optical gain and photodetection across the 1.3 to 1.6 μm bands, with variants extending operation towards approximately 2 μm. Ridge and deep-etched waveguides are standard. Passive propagation losses are generally the highest among the platforms considered (around 3 $\mathrm{dB\,cm^{-1}}$), although they remain acceptable for on-chip routing. InP offers high overall performance for active photonic integration. However, it is mechanically more delicate than the others and processed on smaller wafers of about 50 to 100 mm. Moreover, its processing differs from standard CMOS processes.

The III-V BB library on InP is highly developed and includes lasers such as DFB and distributed Bragg reflectors (DBR), widely tunable DBRs and sampled-grating DBRs (SG-DBRs), and external-cavity lasers [78], [79], [80], as well as SOAs and high-responsivity PDs. It also features compact and high-speed EAMs based on QCSE and MZMs that offer high linearity at the expense of large footprint and high drive voltage. Standard passive components include waveguides, SSCs, MMI couplers, AWGs, and Bragg gratings. Edge coupling with SSCs is the most common approach for optical I/O. Integration strategies range from monolithic InP PICs to heterogeneous bonding of III-V materials onto Si or SiN, which combines active gain with compact or ultra-low-loss passive platforms, and to membrane InP-on-Si technologies.

Platforms based on polymers include fluorinated polymers such as perfluorinated PFCB and CYTOP, acrylates and epoxies such as SU-8 and Ormocers, silicones such as PDMS, and hybrid organic–inorganic formulations. These materials typically form low to moderate index cores or claddings on glass or silicon carriers, with silica or air cladding, which leads to larger footprints than those in SOI. However, high-index multilayer stacks are used in certain biophotonic applications [81]. Their main advantages are low cost, large-area and low-temperature processing, mechanical flexibility, and broad transparency from the visible to the near-infrared. The device properties include low linear losses, large thermo-optic coefficients that enable low-power thermo-optic devices, electrical insulation, and mechanical flexibility. Due to their compatibility with other photonic platforms, polymers are widely used for CPO in data centres [82] and for hybrid integration in PICs. The main limitations are thermal stability, ageing, sensitivity to moisture and ultraviolet radiation, and stress-induced birefringence. Mature passive BBs include waveguides, tapers, splitters and couplers, MMIs, AWGs, Bragg gratings, microlenses, and fiber I/O optimised for ribbon arrays. UV-imprint and mould-transfer processes have enabled the fabrication of rings, AWGs and other devices with low insertion loss and wafer-scale replication [83]. For board-level links and CPO, flexible polymer waveguides achieve sub-dB cm^{-1} losses, support cm-scale bends, and allow relaxed alignment tolerances to fiber arrays [84]. Active functions are typically realised through hybrid or heterogeneous integration with III-V sources or GeSi photodetectors. When EO polymers are combined with SiPh, silicon-organic hybrid (SOH) and SiN-organic hybrid modulators can achieve sub-volt V_π with high GHz bandwidths, while plasmonic-organic hybrid devices can reach even higher speeds at the expense of increased optical loss [85].

Beyond the platforms discussed above, several emerging platforms merit brief mention. These include aluminium oxide (Al_2O_3), barium titanate ($BaTiO_3$), and silicon carbide (SiC). Al_2O_3 is broadly transparent from about 250 nm to beyond 5 μm [86]. Its wide bandgap enables low-loss UV operation, and its moderate refractive index contrast with SiO_2 allows compact devices. It can be deposited by atomic layer deposition (ALD), achieving losses as low as 1.8 dB cm^{-1} at 405 nm, or by reactive sputtering, with approximately 2 dB cm^{-1} [86]. When doped with rare-earth elements, Al_2O_3 supports on-chip amplifiers and lasers [87], making it attractive for integration in hybrid stacks with SiN or SOI.

$BaTiO_3$ exhibits a strong intrinsic Pockels effect. Thin films integrated through CMOS-compatible bonding enable efficient, high-speed and low-power phase modulation with high linearity, and there is a roadmap towards 200 mm wafer-scale hybrid and monolithic integration [88].

SiC combines a wide bandgap, high refractive index and transparency from about 0.4 to 6 μm with useful $\chi^{(2)}$ and $\chi^{(3)}$ nonlinearities that enable second-harmonic generation (SHG) and parametric down-conversion [89].

2.3 Overview of generic indium phosphide platforms

The origins of generic InP photonic integration platforms date back to the early 2000s, when the COBRA Research Institute at Eindhoven University of Technology pioneered a standardised fabrication process for PICs under the ePIXnet framework [12]. COBRA introduced a MPW model based on a shared epitaxial layer structure and a fixed process flow comprising almost 243 individual steps [90]. These can be grouped into four main stages. The first is epitaxy, typically involving butt-joint regrowth to define active and passive regions. This is followed by waveguide etching, then planarisation and passivation, in which benzocyclobutene (BCB) or polyimide smooths the surface topography, passivates sidewalls, and defines via heights for subsequent metallisation. The final stage involves metallisation and interconnection, generally implemented through lift-off contacts.

The generic InP epitaxial stack consisted of an n-InP lower cladding and a p-InP upper cladding surrounding a quaternary InGaAsP core, optimised for operation around 1.55 μm. This platform enabled the realisation of diverse BBs, including passive ridge waveguides, AWGs, SOAs, and PDs. The successful demonstration of the first MPW runs in the mid-2000s validated the concept of a unified PDK and laid the foundation for the subsequent development and the establishment of European open-access foundries. Early demonstrations included a pulse shaper [91], a multifunctional current-controlled delay interferometer [92], and microwave PICs for millimetre-wave wireless communication [42].

Building on this approach, the Joint European Platform for Photonic Integration of Components and Circuits (JePPIX) was established to coordinate access to shared InP fabrication processes across Europe. JePPIX provides a framework that connects researchers, design houses, and commercial users to open-access foundries through a single entry point offering the necessary tools for PIC development through standardised PDKs and regular MPW runs. Through this initiative, several European foundries adopted the generic InP model. JePPIX brings together InP foundries such as SMART Photonics in the Netherlands and Fraunhofer HHI in Germany, alongside SiN foundries such as LioniX International in the Netherlands and Ligentec in Switzerland. In addition, JePPIX promotes training, standardisation, and roadmap activities that define long-term targets for performance, scalability, and manufacturing maturity.

According to the JePPIX 2021–2025 roadmap, the next generation of the generic InP process focusses on achieving higher-speed active devices, targeting modulators and lasers operating at 56 GBaud and beyond, and transitioning towards 193 nm deep ultraviolet (DUV) lithography and larger diameter wafers. The roadmap also emphasises reducing on-chip propagation loss, and fibre-to-chip coupling loss to below 1 dB per interface, improving process reproducibility, and deploying pilot-line services that bridge MPW prototyping with low-volume industrial production [93]. In parallel, efforts are directed towards heterogeneous integration between InP, SiN, and electronic platforms, as well as the standardisation of packaging and test frameworks [94], [95].

Among the foundries participating in the JePPIX ecosystem, two have been employed for the PIC development in this thesis: SMART Photonics and Fraunhofer HHI. SMART Photonics operates as a pure-play foundry dedicated exclusively to InP manufacturing, providing wafer-scale production capabilities and placing a strong emphasis on reproducibility and industrial scalability [96]. In contrast, Fraunhofer HHI combines foundry services with extensive in-house research and development, focussing on high-speed and high-performance devices for advanced telecom and datacom applications [97].

Both the SMART and HHI InP generic platforms are based on semi-insulating substrates that enable the integration of active and passive components on a common wafer while minimising parasitic electrical effects and improving the performance of the components in terms of electrical bandwidth. In the HHI process, Fe-doped InP is used as the semi-insulating layer. In the SMART Photonics process, similar isolation is achieved through the use of semi-insulating buffer layers. However, the inclusion of semi-insulating substrates in SMART Photonics was introduced only recently, and in some of the PICs developed in this work (see Section 6.2) the platform was still based on a common backside n-contact shared by all components.

The SMART and HHI platforms employ a similar overall layer structure, consisting of two main stacks: a passive-stack for photonic routing elements and an active-stack for gain and modulation. The structures are shown in Fig. 2.3, together with a scanning electron microscope (SEM) image reproduced from [98]. Epitaxial layer growth is typically performed using metal–organic vapour phase epitaxy (MOVPE). The passive stack typically consists of a quaternary InGaAsP core layer (commonly denoted as Q1.25, indicating an alloy composition with a bandgap wavelength of approximately 1.25 μm) grown on an n-type InP lower cladding and the semi-insulating InP substrate, with either a p-InP upper cladding or air cladding depending on the waveguide geometry [98], [99].

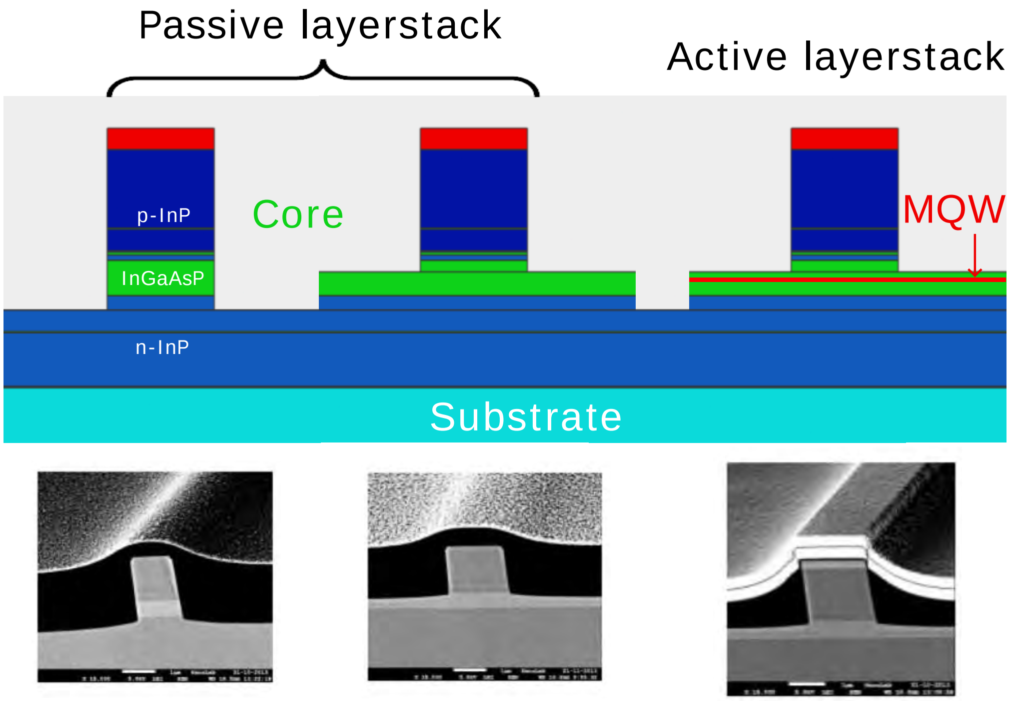

Figure 2.3: Illustration of the passive and active layer stacks employed in InP photonic integration platforms, together with a SEM image reproduced from [98].

The passive stack typically consists of a quaternary InGaAsP core layer (Q1.25, bandgap wavelength $\approx 1.25\,\mu$m) grown on an n-type InP lower cladding and the semi-insulating InP substrate, with either a p-InP upper cladding or an air cladding depending on the waveguide geometry [98], [99]. Waveguides are based on either shallow or deep ridge etching, as illustrated schematically in Fig. 2.3. Deeply etched waveguides provide stronger optical confinement and tighter bending radii, resulting in more compact routing, whereas shallowly etched waveguides exhibit lower propagation losses and larger mode sizes.

In the HHI process, Fe-doped InP is used to form the passive waveguide layers, minimising losses associated with free-carrier absorption [99]. In addition, the I/O waveguides are implemented as thick diluted waveguide structures terminated with vertically tapered SSCs, achieving coupling efficiencies to standard single-mode fibres below 2 dB [99].

For active devices, the layer stack is modified by incorporating an active region within the waveguide core, typically consisting of a multi-quantum-well (MQW) structure based on InGaAsP or InAlGaAs, designed to provide optical gain or controlled absorption in the C band to part of the L band ($\sim$ 1500 nm to 1580 nm). This configuration enables the fabrication of lasers, SOAs, EAMs, and PDs alongside passive components. Active and passive regions are integrated on the same wafer using butt-joint regrowth, a technique in which different epitaxial stacks are grown in separate steps and joined laterally after selective etching to form an abrupt, low-loss interface between them. Coupling-loss optimisation typically ensures interface losses below 1 dB [99].

With these layer structures, it is possible to realise a set of standard basic BBs which are summarised in Fig. 2.4(a). These BBs are proprietary to the foundry, and the detailed structural information is not made available to the designer. Instead, their performance specifications and the necessary information for layout and use are provided through a design manual, which is accessed in conjunction with the PDK. Representative BBs include passive elements such as distributed Bragg reflector (DBR) gratings, waveguides with various cross-sections, and MMI couplers, as well as active elements such as electro-optic phase modulators (EOPMs), EAMs, SOAs, PDs, and several laser types.

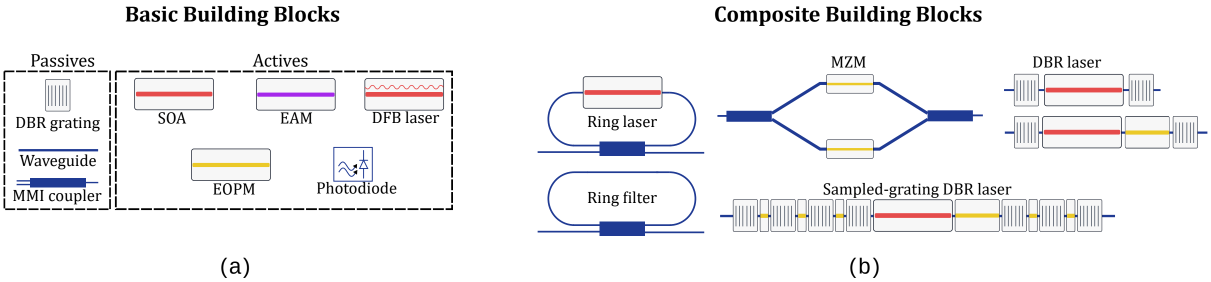

Figure 2.4: (a) Basic BBs include both passive and active elements such as waveguides, MMIs, SOAs, EOPMs, EAMs, DBR gratings and PDs, implemented within either the passive or active layer stacks.(b) Composite BBs are formed by combining these elements to realise higher functionality, including DBR and SG-DBR lasers, MZMs, ring filters and semiconductor ring lasers. Active and passive sections are integrated on a common substrate.

These BBs can be combined to form the CBBs illustrated in Fig. 2.4(b), enabling higher functional complexity. SOAs can be placed between two reflectors to form lasers, and the inclusion of tuning sections allows for the implementation of tunable configurations such as four-section DBR lasers or SG-DBR lasers [100]. EOPMs can be arranged to create MZMs, and passive components such as waveguides and couplers can be combined to realise ring filters or semiconductor ring lasers (SRLs). The figure also shows a three-dimensional simulation model of a ring filter performed using Tidy3D finite-domain time-difference (FDTD) software.

The performance of the BBs available in the standard PDK of SMART and HHI platforms is summarised in Table 2.3. The detailed performance data from the foundry design manuals is accessed through a non-disclosure agreement. The values presented here are based on data reported in the literature. For SMART Photonics, indicative figures are taken from the work of Smit et al. [98], while for HHI, data are taken from Grote et al. [99]. Although the results in [98] refer to an earlier version of the COBRA platform, the process developed by SMART Photonics builds directly upon it. The values provided here offer a representative overview of the typical performance that can be expected from both platforms.

Table 2.3: Comparison of representative BB performance in the SMART Photonics and Fraunhofer HHI generic InP platforms. Values are indicative and based on the available data in [98] for SMART Photonics and [99] for HHI.

Building Block	**Parameter**	**SMART Photonics**	**Fraunhofer HHI**
Straight waveguide	Propagation loss	2–3 dB/cm	0.5–2 dB/cm
SOA	Gain	20 dB @ 120 mA, 800 μm length	3–4 dB per 100 μm
EAM	3-dB bandwidth	$>$ 30 GHz	40 GHz
	Extinction ratio	$>$ 10 dB	–
EOPM	$V_\pi L$ product	15 V mm	–
	Bandwidth	20 GHz	–
Laser	Output power (CW)	Design dependent	DFB: $>$ 5 mW
	Modulation bandwidth	Design dependent	DFB: 20 GHz
Photodiode (PIN)	Responsivity	0.6–0.9 A/W	0.9–1.0 A/W
	3-dB bandwidth	–	$>$ 30 GHz

The SMART and HHI platforms offer waveguides with different degrees of optical confinement, defined by the etch depth of the ridge. In the SMART process, shallow-etched waveguides and deep-etched waveguides are available, where the latter is etched down to a depth of over 150 nm below the core layer. The HHI platform features three ridge geometries with different etch depths corresponding to weakly, moderately, and strongly guiding structures.

The propagation losses of the available waveguides are typically around 2 dB/cm for shallow-etched structures and dB/cm for deep-etched ones in the SMART platform [98]. In the

HHI platform, losses range from approximately 0.5 dB/cm for the shallowest to about 2 dB/cm for the deepest waveguides, with TE-polarised modes generally exhibiting lower losses than TM-polarised ones [99]. The dominant loss mechanisms are free-carrier absorption and sidewall scattering due to surface roughness.

The level of optical confinement also determines the minimum bend radius that can be achieved without significant radiation loss, typically ranging from about 50 μm for deep-etched to 500 μm for shallow-etched waveguides. Standard single-mode waveguide widths lie between 1.5 μm and 2 μm. Transitions between different waveguide geometries are provided as dedicated BBs with low insertion loss. In addition, the SMART Photonics PDK includes linear tapers that facilitate mode conversion between waveguides with different cross-sections.

Regarding optical couplers, HHI provides both MMI and directional couplers in 1×2 and 2×2 configurations, with typical 50:50 splitting ratios, low insertion losses, and negligible imbalance. SMART Photonics also offers 1×2 and 2×2 MMI couplers with comparable performance. Devices for polarisation management are available on both platforms.

Active devices in both SMART and HHI platforms are designed primarily for operation with TE polarisation, as the MQW active region provides stronger optical confinement for TE than for TM modes. Consequently, when coupling external light into the PIC or using on-chip booster amplifiers, TE-polarised input light is preferred. In the SMART process, the SOA structure is based on an MQW stack embedded within a 500 nm Q1.25 InGaAsP confinement layer. The ridge width is typically 2 μm, and the devices are defined using a shallow etch to prevent penetration into the active region and to minimise surface recombination. A SOA section of 800 μm length provides a gain of around 20 dB at a driving current of approximately 120 mA [98]. The HHI platform employs an eight-quantum-well active region, and the amplifier length can be specified by the designer, typically ranging from 100 μm up to several mm. These devices exhibit a modal gain of roughly 3-4 dB per 100 μm and a 3 dB optical bandwidth of about 40 nm centred near 1550 nm [99].

EAMs in both SMART and HHI platforms exploit the QCSE to modulate the optical absorption near the material band edge. In the SMART process, the EAM section is derived from the same MQW stack used in the gain blocks. The bandgap of this region is engineered to be slightly detuned from the operating wavelength. The structure is implemented within the standard active layer stack using a PIN configuration. Recent process refinements in the SMART platform have demonstrated significant performance improvements, with static extinction ratios around 18 dB at bias voltages below 1 V and optimised bandwidths higher than 30 GHz [101]. In the HHI platform, the EAMs are also based on InGaAsP MQW layers designed for operation around 1.55 μm and an operating bandwidth of up to 40 GHz [99].

Phase modulators in InP platforms operate by varying the refractive index of the waveguide through the EO effect, thereby inducing a controlled phase shift in the propagating optical signal. Both SMART and HHI provide these devices in DC and high-frequency versions, the latter incorporating travelling-wave electrodes (TWEs) to support high speed operation. MZMs implemented on both platforms achieve electrical bandwidths higher than 25 GHz [102]. In the SMART process, MZMs typically exhibit a V_π below 7.5 V for a device length of 2 mm. HHI modulators integrate on-chip 50 Ω terminations for impedance matching, whereas SMART Photonics devices rely on external off-chip terminations. Dual-drive MZMs are available in both foundries (for SMART Photonics in the form of co-planar stripline modulators [102]), enabling push-pull operation. Thermo-optic phase shifters are available as well.

In the HHI platform, DFB lasers are available with a fixed cavity length of 200 μm, designed to deliver modulation bandwidths up to 20 GHz, supporting operation at data rates of around 25 Gb/s [99]. Transmission at 56 Gb/s using 4-level PAM at 28 Gbaud has also been demonstrated [103]. The emission wavelength can be selected across the C-band and part of the L-band. Typical threshold currents are 8-10 mA, and on-chip output powers reach about 5 mW at 100 mA. In the SMART platform, lasers are not predefined BBs but can be realised by combining standard active and passive elements. Widely tunable lasers based on multi-section DBR and SG-DBR [100] and narrow linewidth external cavity lasers (ECLs) [104] have been reported on the SMART Photonics platform.

For optical detection, both platforms employ waveguide-integrated PIN photodiodes optimised for DC and high-frequency operation. In the HHI platform, high-speed photodiodes achieve 3-dB bandwidths exceeding 30 GHz, with typical dark currents around 1 nA at -2 V bias, and balanced photodiodes (BPDs) are also available [99]. In the SMART platform, photodetectors are implemented using reverse-biassed, deep-etched SOA structures with a width of 10 µm, providing efficient coupling from adjacent waveguides. A 50 μm-long bulk detector absorbs more than 95% of the incident light, with operation speeds beyond 10 Gb/s and dark currents below 1 nA μm^{-1} of device length [98].

Additional BBs available in the PDKs include on-chip RF transmission lines, coplanar waveguide (CPW) structures for high-speed, and metal pads for electrical interfacing. Both foundries permit metal deposition over optical waveguides. SMART Photonics allows metal crossings anywhere on the chip, while HHI provides a dedicated BB to minimise associated optical losses. The SMART platform also includes electrical isolators, implemented as high-resistance sections created by removing the p-doped layer between adjacent active devices to prevent crosstalk and enable independent biasing [98]. Both foundries offer low-loss 90° optical crossings and shallow-etched waveguides for optical I/O, whose mode profiles match standard single-mode fibers. The output facets can be angled and anti-reflection (AR)-coated to reduce back reflections, and HHI further provides SSCs for efficient fiber coupling. Typical chip sizes are below 10 × 10 mm, depending on design complexity and price.

Design and simulation tools for photonic integrated circuits

Following the general overview of the two InP foundries, this section presents the design and simulation tools employed throughout the work for the development of the PICs within these foundries. The selection of software environments was guided by the need to accurately model the optical behaviour of the foundry material platforms and to ensure consistency between simulation and fabrication, both of which were supported by the PDKs provided by the foundries.

For the design of several passive components (see Chapter A) and for simulations at the device level, commercial Finite-Difference Time-Domain (FDTD) solvers were employed, namely Ansys Lumerical FDTD and Flexcompute Tidy3D. Both tools numerically solve Maxwell's equations in the time domain, providing a rigorous description of light propagation, interference, and confinement within complex photonic geometries. Lumerical FDTD provides a mature and comprehensive environment for the design and optimisation of integrated photonic devices, with advanced capabilities for mesh refinement, mode expansion, and broadband material modelling. Tidy3D offers comparable functionality through a modern cloud-based platform, which allows large and complex simulations to be performed without the need for local computational resources, significantly reducing simulation time and improving workflow scalability.

All FDTD simulations were carried out using the layer stack definitions and material parameters provided by the foundries in their respective PDKs. This ensured that the numerical analyses reflected the actual optical behaviour of the fabricated devices, taking into account realistic refractive indices, layer thicknesses, and material losses. Where appropriate, tolerance analysis can also be employed to account for differences between MPW runs.

To simulate and evaluate the performance of complete PIC systems, the VPIphotonics Design Suite (VPI) was employed. This comprehensive system-level simulation environment supports both time- and frequency-domain analysis, enabling the study of transient and steady-state circuit responses under realistic operating conditions. It allows the construction of complete circuit schematics from interconnected components and includes extensive libraries of optical and optoelectronic models such as modulators, photodetectors, and passive devices.

A key advantage of VPI lies in its capability to incorporate realistic component models derived directly from the PDK data provided by the foundries. These models include experimentally validated characteristics such as wavelength-dependent transmission, gain, group index, insertion loss, and phase response. This approach ensures that simulations accurately reproduce the behaviour of fabricated devices, enabling reliable prediction of overall circuit performance prior to fabrication and facilitating optimisation.

Finally, all circuit layouts were implemented using Nazca Design, an open-source, Python-based photonic layout environment. Nazca enables hierarchical and parameterised design through scripting, ensuring reproducibility and flexibility throughout the design process. The PDK library can be used in this environment, allowing seamless integration of standard and custom components. In addition, Nazca includes powerful tools for DRC, automated routing, and waveguide connectivity management, which greatly simplify the development of complex circuits. The software allows generating the final GDSII layout files required for fabrication, ensuring full compliance with the PDK specifications and an efficient transition from schematic design to tape-out.

Chapter 3

Optical Frequency Combs

Since their initial demonstrations in the 1980s, OFCs have become powerful tools in a variety of photonic applications, including optical communications, spectroscopy, and precision metrology. Extensive research has been conducted to develop OFC technology and explore novel applications that exploit their unique properties. Current efforts aim to reduce the cost, size, weight, and power consumption of comb sources while enhancing their scalability for mass production and portability for field deployment. These goals have driven the development of integrated comb sources, or OFCs implemented on PIC platforms, with the objective of realising compact, chip-scale comb systems as practical alternatives to bulky laboratory-based setups.

Section 3.1 introduces the fundamentals of OFCs and the main generation mechanisms in bulk lasers, including mode-locked, electro-optic, Kerr, and, most relevant to this thesis, gain-switched OFCs, the latter being detailed in Section 3.2. Section 3.3 outlines the principles of dual-comb interferometry (DCI), one of the key applications of OFCs widely used for spectroscopy, ranging, and imaging.

Section 3.4 reviews integration strategies for OFCs, highlighting how performance depends on the generation technique. While microcombs and integrated mode-locked lasers offer wide bandwidths, GS and electro-optic OFCs provide flexibility and reconfigurability. Monolithic integration offers simplicity and process maturity, whereas heterogeneous and hybrid approaches enhance performance at the cost of higher complexity and reduced scalability.

Finally, Section 3.5 presents applications of integrated OFCs with an emphasis on the state of the art in dual-comb interferometry.

3.1 Fundamentals and generation

Optical frequency combs (OFCs) are coherent light sources whose optical spectrum consists of a set of discrete, evenly spaced modes or teeth (Fig. 3.1). The spacing between these tones, namely the repetition rate f_r, is determined by the mechanism used to generate the comb. The tooth frequencies follow [105]

$$\nu_n = f_{\mathrm{CEO}} + n f_r \tag{3.1}$$

where f_{CEO} is known as the carrier-envelope offset (CEO) frequency and n is an integer. The origin of the term f_{CEO} comes from mode-locked lasers (MLLs) but it remains general for all types of OFCs. In the time domain, usually OFCs correspond to a periodic train of short optical pulses at f_r. In this thesis, it is more convenient to reference the comb lines to a reference optical mode ν_0 defined as the lowest frequency mode with sufficient power:

$$\nu_n = \nu_0 + n \cdot f_r \tag{3.2}$$

Therefore, considering an ideal comb with delta-like teeth, the complex amplitude of its optical field can be described by

$$E(t) = \sum_{n=0}^{N-1} A_n e^{-j(2\pi\nu_n t + \Phi_n)} \tag{3.3}$$

where A_n, ν_n and Φ_n are the amplitude, frequency, and phase of the n^{th} line, respectively. N represents the total number of lines.

There are three common figures of merit that are useful throughout this thesis to analyse the characteristics of the generated combs. First, the spectral width at 10 dB ($\Delta f_{10\mathrm{dB}}$) is defined as the frequency span of the comb within 10 dB. Second, the carrier-to-noise ratio (CNR), defined as the average ratio of the intensities of the tones within the 10 dB bandwidth to the noise level [106]. Last, the spectral flatness, defined using a definition from audio signals [107] and obtained by calculating the ratio between the geometric and arithmetic mean of the intensity of all the comb tones within 10 dB

$$SF = \frac{\sqrt[N]{\prod_{n=0}^{N-1} |A_n|^2}}{\frac{\sum_{n=0}^{N-1} |A_n|^2}{N}}. \tag{3.4}$$

This value ranges from 0 to 1, with 1 representing the greatest degree of flatness.

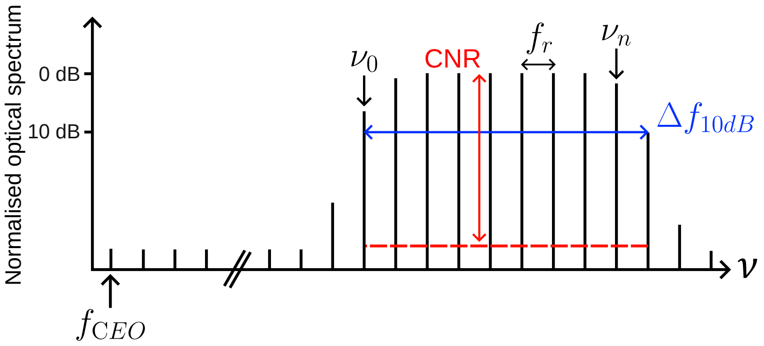

Figure 3.1: Representation of an OFC with selected figures of merit indicated. The comb spectrum consists of equally spaced lines at optical frequencies ν_n, separated by the repetition rate f_r. The spectral width at 10 dB, denoted as $\Delta f_{10\mathrm{dB}}$, defines the span of the comb within 10 dB of the maximum power level. The CNR represents the ratio between the average power of the comb lines and the noise power level within the 10 dB bandwidth.

An OFC is fully specified by two radio frequencies: f_r and f_{CEO}. Once these are known, every tooth frequency follows Eq. (3.2), thus each comb line is uniquely addressed. In practice, the integer mode index n is fixed by referencing one tooth to a known optical transition [105]. This one-to-one mapping between the optical frequencies and the RF pair (f_r and f_{CEO}) makes OFCs exceptionally precise optical frequency rulers. They provide state-of-the-art atomic clocks and feature prominently in roadmaps for a future redefinition of the SI second unit in 2030 [108].

The first laser sources exhibiting comb-like spectra were demonstrated in 1978, enabled by advances in laser stabilisation, ultrafast lasers, and nonlinear optics [109]. Theodor Hänsch's group at Stanford generated a comb from a picosecond mode-locked dye laser to probe the sodium 3s–4d transition [10], but the limited spectral span prevented the determination of the carrier–envelope offset f_{CEO} and thus absolute optical frequencies. Progress accelerated with the advent of commercial femtosecond Ti:sapphire lasers in the early 1990s and, later, with nonlinear spectral broadening in microstructured (photonic-crystal) fibers [110], which enabled shorter pulses and much broader spectra. Hänsch subsequently proposed f–$2f$ self-referencing, whereby an octave-spanning comb is employed to determine f_{CEO} by beating the frequency-doubled tooth at index m with the tooth at $2m$ ($2\nu_m - \nu_{2m} = f_{\mathrm{CEO}}$). Building on these ideas, the groups led by John L. Hall and Hänsch demonstrated octave-spanning, self-referenced OFCs using microstructured fibers [111], [112]. These advances transformed OFCs into practical tools for measuring absolute optical frequencies, substituting complex chains of frequency synthesizers with a single MLL [113]. In parallel, equal mode spacing was experimentally verified [114] and precision spectroscopy with femtosecond lasers was demonstrated [11].

Since their first demonstrations, OFCs have advanced rapidly and have become fundamental to a broad range of applications, including absolute optical-frequency metrology, broadband and dual-comb spectroscopy (DCS), astronomical spectrograph calibration, low-noise microwave generation, optical ranging and LiDAR, and coherent optical communications [113]. Commercial systems developed by Menlo Systems and TOPTICA Photonics have helped to expand the OFC technology.

The range of generation techniques has expanded to encompass MLLs, electro-optic (EO) modulation of a continuous-wave (CW) laser, Kerr combs, and techniques that generate combs directly from semiconductor lasers, such as gain-switching (GS). Each comb source exhibits distinct characteristics, and the specific application dictates which is most suitable. In many platforms, there exists a trade-off between the repetition rate, f_r, and the achievable optical span. For a given comb bandwidth, reducing the repetition frequency distributes the optical power among a larger number of comb lines, thereby lowering the power per line. Low repetition rates (< 1 GHz) yield densely spaced combs but with reduced power per tooth, whereas high repetition rates provide coarser spectral resolution yet higher power per line. Their broader spectra, however, demand careful dispersion management and the use of broadband optical components.

High-repetition-rate broadband combs are particularly attractive for wavelength-division multiplexing (WDM) transmitters, astronomical spectrograph calibration, and photonic microwave synthesis. Conversely, low-repetition-rate combs, typically exhibiting narrower spans, are advantageous for ultra-high-resolution molecular spectroscopy, dual-comb interferometry (DCI) at low digitiser rates, and precision ranging.

Mode-locked lasers

Mode-locking generates an OFC by enforcing a fixed phase relationship among the longitudinal modes of a laser cavity, resulting in an intracavity field that forms a periodic train of short pulses [115]. The pulse period equals the cavity round-trip time, T_r, leading to a repetition rate of $f_r = 1/T_r \approx c/(2n_gL)$, where L is the cavity length and n_g the group refractive index.

There are three principal mode-locking mechanisms: passive, active, and hybrid. Passive mode-locking relies on a saturable-absorption mechanism within the cavity, typically implemented using a saturable absorber (SA) or a semiconductor saturable absorber mirror (SESAM). When the SESAM saturates, the cavity losses briefly decrease, enabling the formation of short, high-peak-power pulses [116], [117]. As the pulse builds up, the SA bleaches for a short fraction of T_r, sustaining the pulse train without any external RF drive. Compared with active schemes, passive mode-locking generally produces shorter pulses and broader optical bandwidths for a given cavity length, albeit with some intrinsic timing jitter.

Active mode-locking, in contrast, modulates either the gain or the intracavity losses using an intracavity modulator driven by an external RF signal at the cavity repetition rate, f_r. Dispersion and nonlinearity determine the steady-state pulse regime (e.g., soliton, stretched-pulse, or dissipative-soliton operation), while the gain bandwidth determines the minimum achievable pulse duration through the Fourier-transform limit. Because the carrier phase does not propagate at the group velocity, successive pulses experience a carrier–envelope phase slip, $\Delta\Phi_{\mathrm{CEO}}$, giving rise to the carrier–envelope offset frequency, f_{CEO} [111]. This mechanism historically defines the physical origin of the carrier–envelope offset described in Eq. (3.1).

Hybrid mode-locking combines both approaches by modulating the SA of a passively MLL with an RF signal at the cavity repetition rate. This technique benefits from the short pulse durations achieved by passive mode-locking and the reduced timing jitter characteristic of active schemes.

OFCs generated from MLLs exhibit fixed, typically high repetition rates ranging from a few GHz to several hundred GHz, primarily determined by the cavity length. The optical bandwidth (comb span) is Fourier-limited by the pulse duration and constrained by the available gain bandwidth. In semiconductor devices, passive or hybrid MLLs commonly deliver pulses of approximately 300 fs duration, while active MLLs typically produce pulses in the 1–10 ps range, leading to relatively broad spectra. OFCs based on MLLs have been demonstrated across multiple spectral regions, from the visible to the mid-IR [46].

These combs are used in a wide range of applications. In precision metrology, their broad span allows for $f-2f$ self-referencing and optical frequency synthesis [118]. Their wide bandwidths also make them valuable for broadband molecular spectroscopy, enabling the simultaneous interrogation of numerous molecular absorption features. Moreover, their typical repetition rates align well with specified ITU grids for communications, making them attractive for high-capacity WDM systems [119], [120].

Electro-optic frequency combs

EO combs are generated by externally modulating a CW laser using one or several EO modulators driven by a RF signal [121]. When a phase modulator is driven at an RF frequency f_{RF}, the resulting optical field can be expressed as

$$E(t) = E_0 e^{j(\omega_0 t + \beta sin(2\pi f_{RF} t))} \tag{3.5}$$

where the modulation index $\beta = \pi V_m/\mathrm{V}_\pi$, with V_m the modulating amplitude and V_π is the switching voltage of the phase modulator. The output optical field expands into discrete lines at $\omega_0 + 2\pi f_r t$ with weights given by the Bessel functions $J_m(\beta)$. The corresponding optical frequencies follow $\nu_m = \nu_{\mathrm{CW}} + n f_r$, where n is an integer and $f_r = f_{RF}$ is the comb spacing. Since all comb teeth are phase-locked to the CW source, EO combs exhibit no independent CEO frequency.

Because the comb-line amplitudes follow the Bessel distribution, several modulation architectures have been proposed to improve spectral flatness. Examples include the use of dual-drive MZMs [122] or cascaded phase and intensity modulators [123], which can generate flat-topped combs [124]. In such schemes, the temporal pulse shape is mapped onto the spectral envelope [125], enabling user-defined comb-shape engineering.

EO combs are valued for their deterministic line spacing, high coherence inherited from the CW laser, and low timing jitter. Typical repetition rates range from a few to several tens of GHz, limited mainly by the bandwidth of the modulators. The achievable spectral span is usually narrower than that of mode-locked combs and depends approximately linearly on the modulation index β [121] and on the specific modulation scheme. Low-V_π modulators enable operation at larger β, thereby extending the comb span. Another approach involves cascading multiple phase modulators, at the cost of increased insertion losses and added complexity in the RF drive chain [121]. EO combs can also be spectrally broadened using nonlinear optical processes [126].

Due to their tunability of line spacing, EO combs have been proven useful for a wide range of applications, such as spectroscopy [127], sensing [128], ranging [129], optical communications, and microwave signal generation [130].

Kerr microcombs

Kerr microcombs, often simply referred to as microcombs, are generated in high-Q optical resonators fabricated from materials exhibiting Kerr nonlinearity [131]. When a CW laser pumps a high-Q microresonator, OFCs are produced through the process of parametric FWM, whereby pump photons are converted into equally spaced sidebands [48], [132]. The resonator length determines the free spectral range (FSR), so the comb spacing follows $f_r \approx \mathrm{FSR} = c/(n_g L)$, where L is the round-trip length and n_g the group refractive index [132]. Above a threshold set by the cavity Q-factor, the interplay between dispersion and nonlinearity causes the initial sidebands to seed a cascade that can evolve into phase-locked states under suitable detuning and dispersion conditions [133].

In the anomalous group-velocity dispersion regime, dissipative Kerr solitons (DKSs) can form [134], which are femtosecond pulses circulating within the resonator and described by the Lugiato–Lefever equation [135]. These states exhibit low phase noise but typically low conversion efficiencies from the pump to the comb output (below 10%) [136]. Under normal dispersion, dark-pulse solitons can emerge, achieving higher efficiencies (up to 40%) [137]. The tooth frequencies follow $\nu_m = \nu_{\mathrm{pump}} + m f_r$, with the CW pump defining the offset [132].

Microcombs feature very high repetition rates, typically between 100 and 1,000 GHz, determined by the resonator geometry. Common material platforms include CMOS-compatible SiN, silica, AlGaAs, and LNOI, each offering distinct trade-offs in spectral span, nonlinear threshold, and integrability [48], [61], [138], [139]. Octave-spanning spectra enable f–$2f$ and $2f$–$3f$ self-referencing [133]. Recent developments include the integration of thermal tuning elements for fine detuning control, on-chip or co-packaged pump lasers [140], and even battery-operated systems [141]. Typical per-tooth optical powers are sufficient for direct detection or use as multi-wavelength carriers, while phase noise closely follows that of the pump laser and can be further reduced with ultra-narrow-linewidth sources.

In coherent communications, microcombs provide wavelength carriers aligned with the ITU grids for dense WDM transmitters and transceivers [142], [143]. Direct photodetection of high-f_r soliton combs enables low-phase-noise microwave and millimetre-wave signal generation for microwave photonics [144]. In precision metrology, octave-spanning microcombs allow compact, self-referenced optical frequency synthesizers [145]. Their broad spectral coverage also supports DCS [44], [146]. Additional emerging applications include photonic hardware accelerators [147], coherent LiDAR and ranging systems [148], and photonic microwave generation [149].

3.2 Gain-switched semiconductor lasers

GS of semiconductor lasers is a well-established technique that was first demonstrated in the 1980s [150], [151] [151] for generating short optical pulses with typical widths in the picosecond range. Due to this capability, GS can be employed as a method for OFC generation [152], [153], [154]. This technique can be implemented using monolithically integrated semiconductor lasers. In GS, the gain of the laser is directly modulated by driving the injection current below and above the threshold at a chosen repetition rate (f_r). This repetition rate determines the comb line spacing, allowing for flexible configuration.

Optical pulse generation under GS modulation is illustrated in Fig. 3.2. The figure was obtained by numerically solving a set of rate equations described in [115], [155], following [156]. The rate-equation model describes the dynamic response of a semiconductor laser by relating the temporal evolution of carrier density, photon density, and optical phase within the cavity to the injected current and device parameters. A detailed description of the model and the laser parameters used is presented in Section 5.1.

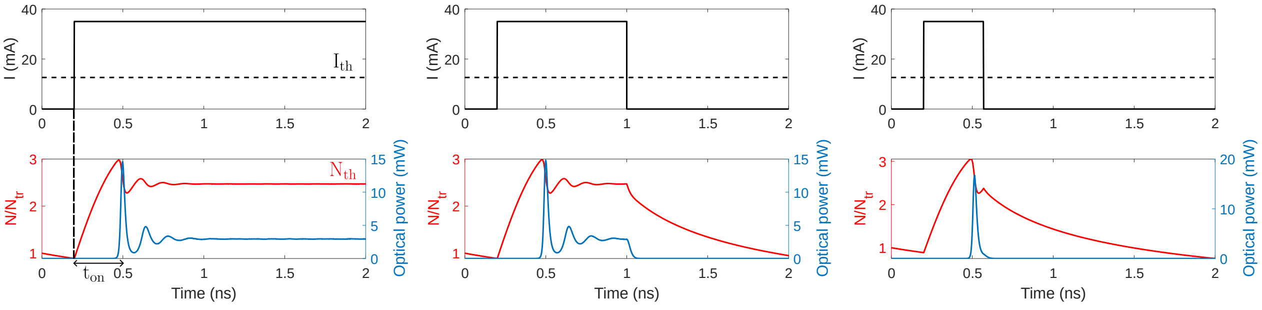

(a)

(b)

(c)

Figure 3.2: (a) Numerical simulation of the turn-on dynamics of a semiconductor laser driven by an ideal current step. The upper trace shows the injected current, while the lower trace plots the normalised carrier density (relative to N_{tr}, red) and the optical power (blue). (b) Numerical simulation of the carrier and photon density response to a rectangular current pulse. (c) Emission of a gain-switched optical pulse as the pulse duration is reduced. More details about the simulation model can be found in Section 5.1.

In the first case (Fig. 3.2(a)), an idealised current step with an infinitesimal rise time (black line) is applied to the laser diode. This causes the carrier density (red trace) to increase until it reaches the carrier concentration at which the gain of the material equals the losses of the cavity, i.e., the carrier threshold value (N$_{th}$). In this case, this occurs at two or three times the transparency carrier density (N_{tr}). At this point, lasing begins, and the photon density starts to increase. It can be noted that there is a turn-on delay ($\mathrm{t_{on}} \approx 300$ ps) due to the finite response of the carriers to electrical excitation. As the photon density increases, both the carrier and photon densities exhibit damped oscillations arising from the mismatch in their dynamic response: the increase in photon density depletes the carriers through stimulated recombination, reducing them below threshold and temporarily lowering photon density. Since the injected current is kept constant, the depleted carriers are recovered, causing the photon density to increase again. These oscillations, arising from the interaction between carrier and photon densities, are known as relaxation oscillations. Eventually, the steady state is reached where there is a balance between carrier depletion due to recombination and photon emission.

In Fig. 3.2 (b), the electrical excitation pulse is shortened but remains long enough for relaxation oscillations to occur. In Fig. 3.2(c), the pulse duration is sufficiently short (370 ps) to suppress the second relaxation oscillation, leading to the emission of a single optical pulse. GS consists of modulating the laser in such a way that only the first spike of the relaxation oscillations is emitted, using a periodic signal. If the laser is driven periodically, with the switch-on period being short enough to emit a single pulse, then a train of pulses with the repetition rate of the modulating signal is obtained.

An important feature of GS OFC generation is the frequency chirp that arises from changes in the refractive index induced by the carrier (see Section 5.1). The refractive index is altered by rapid modulation of the carrier density via the linewidth enhancement factor (α), producing an instantaneous frequency shift that broadens the optical spectrum. The magnitude of this chirp, and therefore the comb span, increases with the modulation depth and the rate at which the carrier varies. Therefore, the overall span of a GS OFC is primarily set by this chirp rather than by the Fourier-transform limit of the pulse duration. Consequently, the spectral bandwidth of GS OFCs is usually moderate compared to that of MLL or Kerr microcombs, in the range of several tens of GHz up to a few hundreds of GHz. Nevertheless, several techniques for expanding the spectral breadth of the GS OFCs have been demonstrated, based on different approaches [153], [157], [158], [159].

The repetition frequency of GS OFCs lies in the range of a few hundred MHz to below 10 GHz. A common criterion for classifying the repetition frequency as either high or low is to compare it with the relaxation oscillations of the laser. These oscillations are typically between 5 GHz and 10 GHz ($\sim$ 6.8 GHz in the example of Fig. 3.2). Therefore, if the repetition frequency is well below the relaxation oscillation frequency, typically below 1 GHz, it is considered low. Conversely, repetition frequencies around or above the relaxation oscillations frequency are generally regarded as high. Typical GS repetition frequencies range from a few MHz to 8 GHz, depending on the device and drive conditions. Moreover, by employing densification techniques, GS OFCs using discrete components have achieved repetition frequencies down to a few kHz [160].

At low repetition rates, pulses generated by GS typically lack a fixed phase relationship, since the laser is switched off between periods and each pulse originates from spontaneous emission. However, mutual coherence between pulses is essential for OFC formation. To achieve this, an additional mechanism is required to preserve coherence from pulse to pulse. One effective approach is to inject light from a secondary laser, often referred to as the master laser (ML), into the GS laser at a wavelength close enough to the emission wavelength of the slave laser (SL). This technique, known as OI locking, maintains coherence during long switch-off periods because the injected light seeds the GS laser, providing a coherent field from which the next pulse can build up through stimulated emission [161]. As a result, OI enables the generation of low-repetition-rate OFCs, which are highly desirable for ultra-high-resolution spectroscopy, where lower repetition frequencies translate into finer spectral resolution. While sinusoidal GS excitation tends to limit the comb bandwidth at low repetition rates, later studies demonstrated that combining OI locking with pulsed GS excitation allows repetition rates as low as 5 MHz without compromising the comb bandwidth [106], [162], [163]. This implementation is referred to as pulsed GS throughout this thesis.

Beyond ensuring coherence, OI locking offers several additional benefits. It reduces timing jitter, which refers to small temporal fluctuations that affect the periodicity arising from random fluctuations in the turn-on delays of subsequent pulses [164], [165]. Furthermore, it mitigates frequency chirp, improves the side mode suppression ratio (SMSR) [166], enhances the modulation response, and reduces the phase noise [167]. Importantly, the injecting laser transfers its optical properties, such as the linewidth [153]. This allows the use of a narrow linewidth laser to improve the linewidth of the optical lines of the comb.

OI also allows precise control over the emission wavelength, since the emission of the injected laser is pulled towards the injection frequency. This property is particularly valuable for applications that require or may benefit from tunability [159]. A tunability exceeding 40 nm in GS OFCs generation using discrete components has been demonstrated for multi-gas spectroscopy across different spectral regions by injecting at different longitudinal modes of a Fabry-Pérot (FP) laser [168]. GS OFCs have been employed for spectroscopy [169], ranging [170], coherent communications [171], [172] and microwave generation [173].

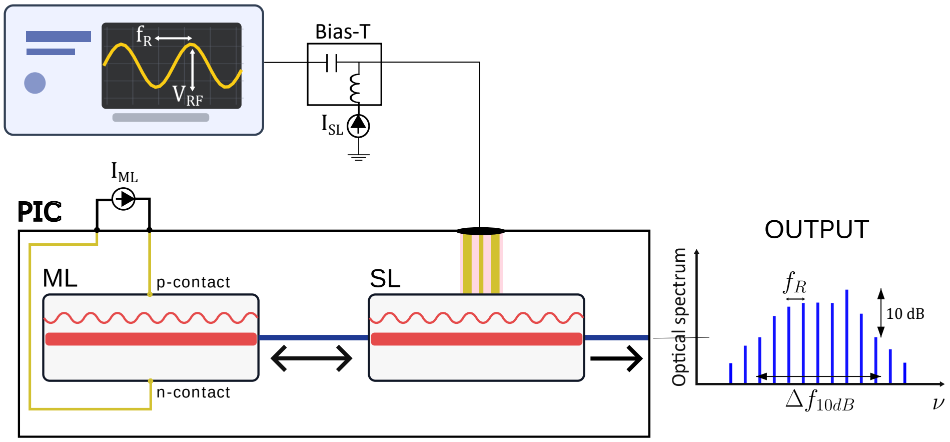

Figure 3.3: Typical implementation of a monolithic GS OFC in a PIC. The integrated lasers are represented as DFB lasers, similar to the system studied in Section 5.2. The ML is driven through the p-n junction with a DC current (I_{ML}) injecting light into the gain-switched laser SL. The latter is driven through a RF transmission line by combining in a Bias-Tee a DC bias current with an RF signal provided by an RF generator. The RF signal can be either a sinusoidal or pulsed signal. Consequently, and OFC is generated with a line spacing determined by the GS modulation frequency f_R. The arrow between the ML and the SL indicates that light propagates in both directions since there is no an isolation mechanism. DFB: Distributed Feedback; SOA: Semiconductor Optical Amplifier.

Integrated GS OFCs can be realised using a master–slave configuration, as illustrated in Fig. 3.3, where the ML injects light into the slave laser SL. In this scheme, both devices are represented as DFB lasers, consistent with the designs proposed later in Section 5.2. The ML and SL are forward-biased by currents supplied by a current source, denoted I_{ML} and I_{SL}, respectively. To implement GS, a Bias-Tee combines I_{SL} with an arbitrary RF signal from a generator operating at a repetition rate f_r and a peak-to-peak voltage V_{RF}. This signal is delivered to the PIC through an RF transmission line, typically a CPW, to enable high-speed modulation. In this configuration, I_{SL} defines the operating point of the SL, usually set just below threshold, around which the current is modulated by the RF waveform (pulsed for low repetition rates or sinusoidal for higher ones). The modulation repetition rate determines the comb-line spacing, while the modulation amplitude affects the comb span through the induced frequency chirp. Since the OI peak generally dominates the spectrum, the span, characterised in this thesis as $\Delta f_{10,\mathrm{dB}}$, is evaluated after filtering out the optical injection to isolate the comb lines generated by the GS process.

This scheme benefits from a configuration that can be monolithically implemented on a PIC using standard generic integration platforms, allowing the development of comb sources with a compact size, scalability, and reduced cost, albeit at the expense of requiring an external AC source. III–V semiconductor platforms are particularly suitable, as they enable the integration of lasers. To date, the InP platform has demonstrated strong potential for GS OFC integration (see Section 3.4.1).

The implementation of OI in generic integration platforms faces some challenges. Firstly, the ML must exhibit a narrow linewidth to ensure a high degree of coherence, as it is directly transferred to the comb tones. Furthermore, tunability of the ML is highly desirable, as it enables tuning of the OFC emission frequency. An additional complication arises from the absence of optical isolators in generic integration platforms, which leads to perturbations of the ML by the SL, as illustrated in Fig. 3.3 where the arrow indicates that light travels in both directions. To overcome these issues, several approaches have been investigated to realise integrated tunable narrow-linewidth single-mode lasers alongside strategies to mitigate the lack of isolators [174], [175]. In this thesis, this is addressed in Section 5.3.

3.3 Dual-comb interferometry

Dual-comb interferometry (DCI) [176] is an interferometric, multi-heterodyne technique that uses two OFCs with slightly different repetition rates, f_{r1} and $f_{r2} = f_{r1} + \delta f_r$, where δf_r is the repetition rate difference, thus being their optical tones given by

$$\nu_1 = \nu_{01} + n f_{r1}, \tag{3.6}$$

and

$$\nu_2 = \nu_{02} + m f_{r2} = \nu_{02} + m(f_{r1} + \delta f_r) \tag{3.7}$$

where n and m are integers.

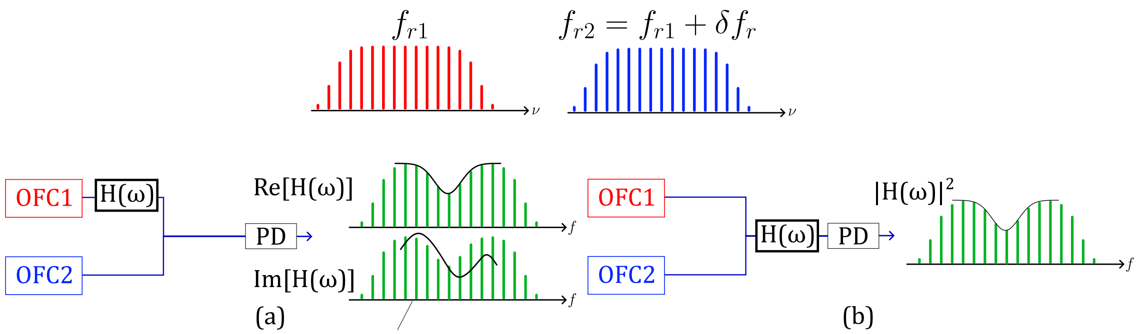

Figure 3.4: (a) Asymmetric configuration of DCI and (b) symmetric configuration.

In DCI, two common configurations are used to measure the response of a sample, as illustrated in Fig. 3.4. Since the multiheterodyne beating of the comb lines encodes the information of the optical domain, as will be shown later, a sample can be introduced into the system to characterise its response. The sample may correspond to a gas, a distance (for ranging), or, more generally, any element interacting with light, whose transfer function is denoted as H(ω). In the asymmetric configuration (Fig. 3.4(a)), the sample is placed in one arm only (the signal path), while the other arm serves as a local oscillator (LO). In contrast, in the symmetric configuration (Fig. 3.4(b)), both combs propagate through the sample.

Following Eq. (3.3), and assuming that the two combs are combined in a 50:50 coupler, the resulting optical field from the superposition of $E_1(t)$ (OFC1) and $E_2(t)$ (OFC2) can be expressed as

$$E_1(t) + E_2(t) \propto \sum_{n=0}^{N-1} A_{1n} e^{-j(2\pi\nu_{1n}t+\Phi_{1n})} t_{s1} e^{-j\Phi_{s1}} + \sum_{m=0}^{N-1} A_{2m} e^{-j(2\pi\nu_{2m}t+\Phi_{2m})} t_{s2} e^{-j\Phi_{s2}}, \tag{3.8}$$

where, for generality, each comb is assumed to acquire the sample's complex transmission $t_{s_i} e^{-j\Phi_{s_i}}$ ($i \in [1,2]$). In the asymmetric configuration, $t_{s_2} = 1$ and $\Phi_{s_2} = 0$, only the probe comb interacts with the sample. In the symmetric configuration, $t_{s_1} = t_{s_2} = t_s$ and $\Phi_{s_1} = \Phi_{s_2} = \Phi_s$, both combs traverse the sample.

When the two combs are mixed on a fast photodetector, the generated photocurrent is

$$I_{PD}(t) = \mathcal{R}\langle |E_1(t) + E_2(t)|^2 \rangle = \mathcal{R}\langle [E_1(t) + E_2(t)]\,[E_1(t) + E_2(t)]^* \rangle, \tag{3.9}$$

where $\langle \cdot \rangle$ denotes averaging over a time interval much longer than the optical cycle due to the limited bandwidth of the photodiode, $(\cdot)^*$ indicates the complex conjugate, and $\mathcal{R}$ is the responsivity of the photodiode. The signal comprises the beat of all the tones of the two combs, where the self-terms $\langle |E_k(t)|^2 \rangle$ contribute to a DC component, while the cross-terms $\langle E_1(t)E_2(t) \rangle$ and $\langle E_1(t)E_2(t)^* \rangle$ lead to the RF multiheterodyne signal that occupies successive spectral regions known as Nyquist zones (as discussed later).

If we consider only the beatnote of adjacent lines ($n = m$), Eq. (3.9) remains as

$$\begin{aligned}
I_{PD}(t)|_{n=m} = \mathcal{R} \sum_{n=0}^{N-1} &\Big(A_{1n} e^{-j(2\pi\nu_{1n}t+\Phi_{1n})} t_{s1} e^{-j\Phi_{s1}} + A_{2n} e^{-j(2\pi\nu_{2n}t+\Phi_{2n})} t_{s2} e^{-j\Phi_{s2}}\Big) \\
&\Big(A_{1n} e^{j(2\pi\nu_{1n}t+\Phi_{1n})} t_{s1} e^{j\Phi_{s1}} + A_{2n} e^{j(2\pi\nu_{2n}t+\Phi_{2n})} t_{s2} e^{j\Phi_{s2}}\Big) = \\
= \mathcal{R} \sum_{n=0}^{N-1} &\Big[A_{1n}^2 t_{s1}^2 + A_{2n}^2 t_{s2}^2 + 2A_{1n}A_{2n}t_{s1}t_{s2} \cos\Big(2\pi(\nu_{2n} - \nu_{1n})t + \Phi_{2n} - \Phi_{1n} + \Phi_{s2} - \Phi_{s1}\Big)\Big] = \\
= \mathcal{R} \sum_{n=0}^{N-1} &\Big[A_{1n}^2 t_{s1}^2 + A_{2n}^2 t_{s2}^2 + 2A_{1n}A_{2n}t_{s1}t_{s2} \cos\Big(2\pi(\nu_{02} - \nu_{01} + n\ \delta f_R)t + \Phi_{2n} - \Phi_{1n} + \Phi_{s2} - \Phi_{s1}\Big)\Big].
\end{aligned} \tag{3.10}$$

The first two terms in Eq. (3.10) are the direct-detection contributions $\langle |E_1|^2 \rangle$ and $\langle |E_2|^2 \rangle$. The third term corresponds to the heterodyne beating term and contains the information of interest, as it tracks changes in both the amplitude and the phase of the field at each down-converted component $n\delta f_r$. The Fourier transform of $I_{PD}(t)$ yields the dual-comb spectrum, which corresponds to a down-converted replica of the optical spectrum, given by

$$\begin{aligned}
I_{PD}(f)|_{n=m} \propto \sum_{n=0}^{N-1} \Big\{ &A_{1n}^2 t_{s1}^2 \delta(f) + A_{2n}^2 t_{s2}^2 \delta(f) + \\
&2A_{1n}A_{2n}t_{s1}t_{s2} \Big[e^{j(\Phi_{2n}-\Phi_{1n}+\Phi_{s2}-\Phi_{s1})} \delta\Big(2\pi(f - \delta f_0 - n\ \delta f_R)\Big) + \\
&e^{-j(\Phi_{2n}-\Phi_{1n}+\Phi_{s2}-\Phi_{s1})} \delta\Big(2\pi(f + \delta f_0 + n\ \delta f_R)\Big)\Big]\Big\},
\end{aligned} \tag{3.11}$$

$\delta f_0 = \nu_{02} - \nu_{01}$ denote the offset between the lowest frequency teeth of the two combs.

In the asymmetric configuration, the heterodyne term is proportional to the complex transfer function of the sample $t_s e^{-j\Phi_s}$, so both absorption (amplitude) and dispersion (phase) are retrieved directly. In the symmetric configuration, the heterodyne product carries the squared field factor t_s^2 and the sample-induced phase cancels ($\Phi_{s1} = \Phi_{s2}$), so only amplitude information remains. Although the symmetric configuration removes phase information, the interaction is effectively stronger because both arms pass through the sample, leading to an RF power that scales as t_s^4 (versus t_s^2 in the asymmetric case). This can increase contrast against the baseline but does not necessarily improve SNR, as both combs are attenuated and the result depends on the available optical power and detector sensitivity. In both schemes, measurements should be normalised with a reference RF comb acquired without the sample to remove the system response. In the asymmetric case, the retrieved optical power transmission is

$$T_{asym}(\omega) = PSD_{sample}/PSD_{ref} = t_s^2, \tag{3.12}$$

whereas in the symmetrical case the measured electrical transmission corresponds to the square of the optical transmission

$$T_{sym}(\omega) = PSD_{sample}/PSD_{ref} = t_s^4 = T_{asym}(\omega)^2 \tag{3.13}$$

therefore, $T_{asym}(\omega) = \sqrt{T_{sym}(\omega)}$. Consequently, in logarithmic units, the obtained transmission must be divided by two for the symmetric configuration.

The combination of the two combs in the frequency domain and the resulting down-converted spectrum from the interference of adjacent OFC lines are illustrated in Fig. 3.5 in the frequency domain panel. Pairs of optical teeth beat coherently to radio frequencies (Eq. (3.11)), producing an electrical comb with line spacing δf_r. In this way, the optical spectrum is mapped into the electrical domain. The mapping follows

$$f_{RF} = \delta f_0 + n f_{r1} - m f_{r2} = \delta f_0 + n f_{r1} - m\left(f_{r1} + \delta f_r\right) = \delta f_0 + l f_{r1} - m \delta f_r. \tag{3.14}$$

where $l = n - m$. This corresponds to a spectral compression of the optical spectrum down to the RF domain by the factor

$$\mathrm{CF} = \frac{f_{r1}}{\delta f_r}. \tag{3.15}$$

Thus, the compression factor can be controlled by adjusting the repetition rate f_{r1} and δf_r. For GS OFCs, this is achieved by changing the RF modulation frequency applied to one of the lasers in the dual-comb pair. Typical values of CF lie between 10^5 and 10^6, enabling single-shot, rapid measurements with high spectral resolution using standard RF electronics.

DCI can be understood in the time domain as a repeated cross-correlation of two pulse trains with slightly different repetition rates (Fig. 3.5, time domain panel). The periods of the two trains of pulses are $T_{r1} = 1/f_{r1}$ and $T_{r1} = 1/f_{r1} + \delta f_r$ with $\delta f_r \ll f_{r1}$. Because the periods differ slightly, successive pulse pairs slip past each other, and their relative delay for the n^{th} pair is $\Delta\tau_n = n(T_{r1} - T_{r2}) \approx n\delta f_r / f_{r1}^2$. Therefore, every point of the recorded interferogram is obtained at each delay step $\Delta\tau$, so the photodetector simply measures the cross-correlation as $\Delta\tau$ scans linearly. Maxima occur when $\Delta\tau = 0$, and after $N = f_{r1}/\delta f_r$ pulse pairs, the delay returns to zero, giving an interferogram burst period of $T_r = 1/\delta f_r$. In this way, a full delay range of one pulse period T_r is captured without moving parts, leading to equivalent-time sampling that provides spectral compression. The spectral resolution of the measurement is determined by the repetition rate of the comb since each tooth is a sampled frequency point [176]. The RF comb is obtained from the Fourier transform of the interferogram.

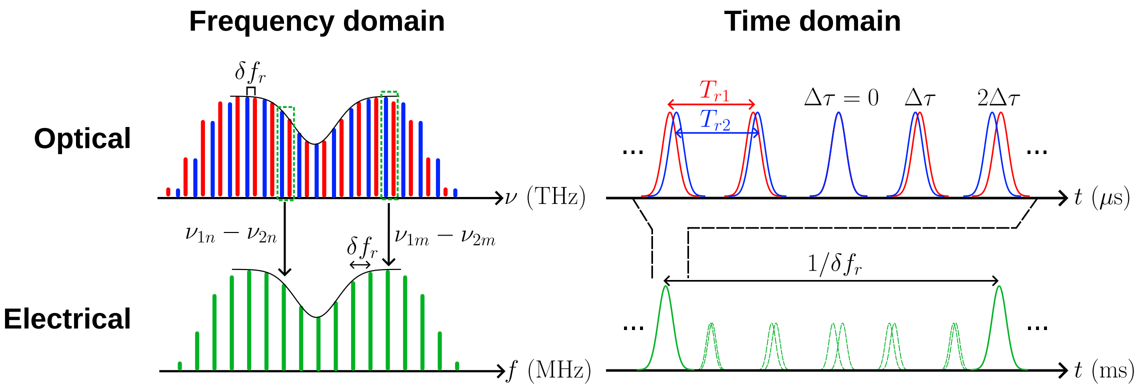

Figure 3.5: Illustration of the principle of DCI. In the frequency domain, the two OFCs differ slightly in their repetition rates. The beating between their corresponding optical lines generates RF tones separated by δf_r. In the time domain, the optical pulse trains gradually slip past each other because of the small difference in repetition rates. The time delay between consecutive pulses from the two OFCs is denoted $\Delta\tau$. When $\Delta\tau = 0$, the two pulse trains overlap, producing constructive interference that results in a maximum of the interferogram, often referred to as an interferogram burst. These bursts occur periodically every $1/\delta f_r$. Between consecutive bursts, the pulses slide through one another, and each time step of the interferogram corresponds to an incremental delay $\Delta\tau$.

In most dual-comb schemes $\delta f_0 = 0$. Thus, a common practice in DCI is to apply a frequency shift to one of the combs in order to move the interferogram away from DC and reduce low-frequency noise. When this shift is applied, the interferogram is modulated by a signal with frequency f_{shift}, and the beating terms appear at

$$f_{RF} = f_{shift} + l f_{r1} - m\delta f_r. \tag{3.16}$$

In a dual GS OFC system, the tones of each comb are defined relative to the same OI frequency. As this reference is shared by both combs, the effective offset difference satisfies $\delta f_0 = 0$. Consequently, the RF comb remains centred around f_{shift} upon detection. This frequency shift is typically introduced by inserting an acousto-optic modulator (AOM) in one branch of the interferometer, for example, in the branch associated with OFC1.

The beating of adjacent comb lines ($l = 0$) produces the dual-comb down-converted spectrum near DC (Eq. (3.14)), or f_{shift} in the presence of a frequency shifter (Eq. (3.16)). This spectrum is then comprised within the so-called first Nyquist zone spanning 0 Hz (f_{shift}) to $f_{r1}/2$ ($f_{shift} + f_{r1}/2$). However, the beat notes from other combinations result in spectral replicas centred around integer multiples of the repetition frequency comprised within higher Nyquist zones with a width of $f_{r1}/2$. These replicas arise from tooth pairs accomplishing $l \neq 0$. The even Nyquist zones (2nd, 4th, etc.) result from positive and negative odd l numbers. Consequently, the odd Nyquist zones (3rd, 5th, etc.) are those with even positive and negative l. This is illustrated in Fig. 3.6.

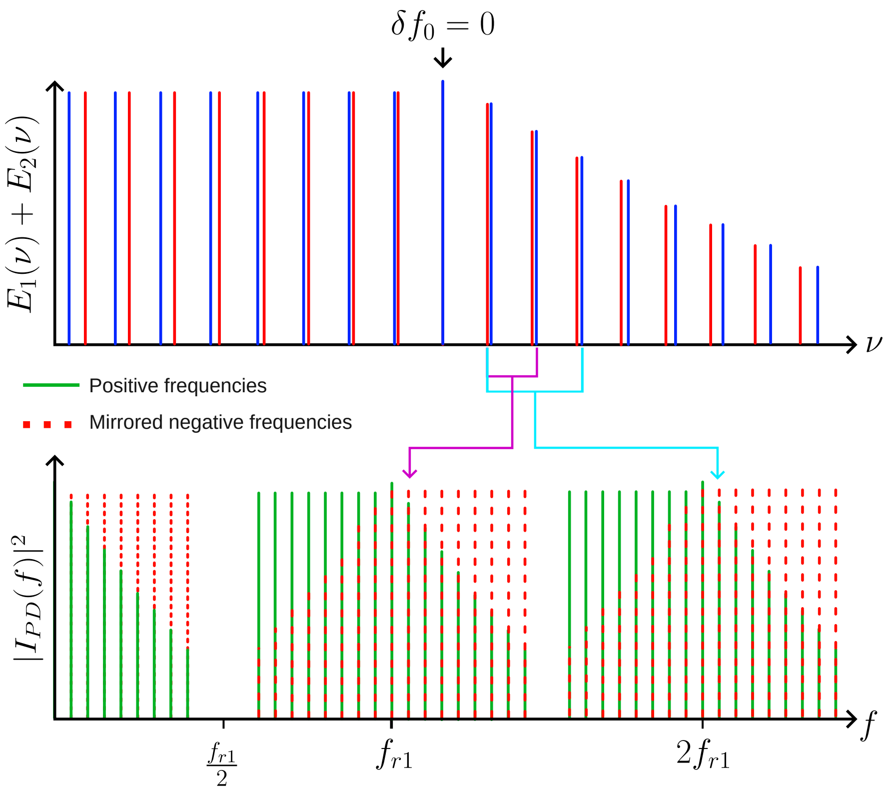

Figure 3.6: Illustration of the formation of different Nyquist zones. The two OFCs coincide at their central tone ($\delta f_0 = 0$) and exhibit an asymmetric spectral envelope, characterised by a flat spectrum on one side and a triangular profile on the other. When non-adjacent optical lines beat, they generate down-converted RF combs at higher frequencies occupying successive Nyquist zones, separated by integer multiples of $f_{r1}/2$. To prevent spectral overlap between zones, the CF must be sufficiently high, ensuring that there is no overlap between adjacent Nyquist zones. Because the detected signal is real, negative frequency components appear as mirrored replicas of the positive frequency spectrum due to the Fourier symmetry of real signals.

When the CF is sufficiently large, each spectral replica is entirely mapped within a single Nyquist zone, with no overlap between zones (see Fig. 3.6). However, since the detected signal is real, the negative frequency components resulting from the Fourier transform are superimposed on the positive frequency components within each Nyquist zone. In Fig. 3.6 Nyquist zones, the two OFCs are drawn asymmetrically, with one side flat and the other triangular, to illustrate this superposition.

The central tooth coincides for both combs ($\delta f_0 = 0$), and the subsequent tones on both sides increase in frequency proportionally to $n\delta f_r$. In the first Nyquist zone, the optical spectrum to the right of the common tooth (triangular) overlaps with the mirrored contribution of the optical spectrum to the left (flat). The same positive/mirrored-negative superposition is then repeated in all subsequent Nyquist zones. When interrogating a sample, this overlap can sometimes mask the spectral feature. Therefore, introducing a non-zero frequency shift provides an additional benefit as it shifts the first Nyquist zone away from the baseband. This mitigates overlap at DC and enables the full spectral information to be recovered without baseband superposition.

To perform a measurement, only the first Nyquist zone is needed since it contains all the information about the sample. However, to avoid spectral overlapping and aliasing between Nyquist zones, the CF must be high enough to compress the spectrum in an electrical bandwidth $\Delta f < f_{r1}/2$. This can be translated to a relation between the optical bandwidth $\Delta\nu$ and the CF as

$$\Delta\nu \leq \mathrm{CF} \cdot \Delta f = \frac{f_{r1}^2}{2\delta f_r} \tag{3.17}$$

Therefore, for a given $\Delta\nu$ if the repetition rate is lowered, the CF should be increased, which means to reduce δf_r. The optical bandwidth is then comprised within an electrical bandwidth of $\Delta f \leq \Delta\nu/\mathrm{CF}$. Therefore, for high-resolution spectroscopy, low repetition rates are preferred to increase the spectral resolution, together with high CFs to avoid overlapping and reduce the bandwidth detection requirements.

However, there is another consideration regarding the CF. Since each interferogram burst occurs at a period of $1/\delta f_r$, the minimum acquisition time to resolve the spectral information of the sample (RF comb envelope) and capture one interferogram burst should be

$$t_{\mathrm{acq}} \geq T_r = \frac{1}{\delta f_r}. \tag{3.18}$$

If the δf_r is low (high CF), the acquisition time increases. However, although a single burst enables the recovery of the RF comb, acquiring several periods of the interferogram (i.e. several bursts) enhances the SNR and allows the recovery of the individual RF comb teeth. An increased acquisition time leads to a finer frequency resolution in the frequency domain after the Fourier transform. It is common to interpret this as the resolution bandwidth of the measurement; thus, the greater the acquisition time, the smaller the resolution bandwidth and the greater the SNR and frequency resolution.

Taken together, these considerations reveal an inherent trade-off between acquisition time, sampled bandwidth, spectral resolution, and aliasing between Nyquist zones. For a given comb span, the spectral resolution improves as the repetition rate of the OFCs decreases. However, to avoid spectral overlap between zones, this requires a corresponding increase in CF, which in turn increases the acquisition time. For instance, if a spectral resolution of 100 MHz is required over an optical bandwidth of $\Delta\nu = 100$ GHz (corresponding to 1,000 optical lines), the CF must be, according to Eq. (3.17),

$$\mathrm{CF} \geq \frac{\Delta\nu}{\Delta \mathrm{f}} = \frac{2\Delta\nu}{\mathrm{f_{r1}}} = \frac{200\,\mathrm{GHz}}{100\,\mathrm{MHz}} = 2,000. \tag{3.19}$$

which requires $\delta f_r = 50$ kHz (Eq. (3.15)). Thus, the acquisition speed must be $t_{\mathrm{acq}} \geq 20\,\mu$s. The same derivation could be done for a spectral resolution of 1 GHz, leading to an acquisition time of $t_{\mathrm{acq}} \geq 200\,\mathrm{ns}$ (CF = 200, $\delta f_r = 5\,\mathrm{MHz}$).

As it can be noted, these considerations require careful design of the dual-comb parameters for the specific application. For high-resolution measurements, such as spectroscopy of narrow absorption lines (a few GHz), repetition rates of the order of MHz are required, increasing the acquisition time but relaxing the required electronics bandwidth. By contrast, when acquisition speed is prioritised over resolution, the CF can be reduced at the expense of higher bandwidth electronics. GS OFCs enable low repetition rate operation with a reconfigurable CF, and have been demonstrated for dual-comb spectroscopy using low-bandwidth electronics [169]. Their simple electronic control allows dynamic adjustment of the repetition rate, and therefore of the acquisition time and spectral resolution, enabling real-time optimisation of the trade-offs among these parameters.

A final consideration concerns the linewidth of the comb teeth. In free-running operation, with no common reference or mutual coherence, the two OFCs fluctuate independently according to the stability of each laser and phase noise. In this case, the RF spectrum arises from incoherent beating and exhibits unresolved tones [176]. By contrast, when the combs are phase-locked to a common reference (mutually coherent), they maintain a fixed relative phase and produce coherent beat notes with linewidths well below δf_r (typically Hz-level), set by the interline phase correlation. For stable measurements, this mutual coherence should persist over the full acquisition time. Consequently, the achievable coherence is ultimately limited by the noise and stability of the common reference used for the phase lock. In DCI based on GS OFCs, this reference can be provided by a single ML injecting two SLs through the OI locking mechanism.

DCI was first reported in 2001 to perform tomographic measurements [177] and its theoretical analysis and fundamentals were described in 2002 [178]. After that, DCI-based techniques have been widely used for different applications, such as spectroscopy [169], [179], interrogation of fiber Bragg gratings for strain and temperature sensing [180], imaging [181], [182], or ranging [170], [183], [184], to name a few.

DCI finds one of its most significant applications in DCS. In DCS, the interferogram generated by two OFCs is used to probe electronic, vibrational, and rotational molecular transitions, enabling high-resolution, high-accuracy single-shot measurements. DCS is closely related to conventional Fourier-transform infrared (FTIR) spectroscopy, as both are single-detector techniques. However, DCS provides higher nominal resolution set by the repetition rate of the OFCs and faster acquisition, since no moving mirror is required. In contrast, it demands that the two OFCs remain phase-locked and typically offers narrower spectral coverage. Owing to these characteristics, DCS is widely used in gas-phase spectroscopy.

Research in DCS has expanded rapidly, as reviewed in [176], [185]. One of the earliest demonstrations of the down-converted RF comb was reported in [186], which employed two mode-locked fiber lasers to generate OFCs broadened to 15.5 THz, enabling measurement of the rotational–vibrational band of the $^{13}C^{14}N$ isotopologue of hydrogen cyanide (HCN).

Of particular relevance to this thesis are demonstrations using optically injected GS semiconductor lasers. The first demonstration of these OFCs for DCS (2016) measured an HCN gas cell with high accuracy and resolution [187]. The OFCs featured a repetition rate of around 1 GHz with $\delta f_r = 100$ kHz, and an optical bandwidth of around 70 GHz. Later, the authors improved the resolution by a factor of two by lowering the repetition rate to 500 MHz, and employing an asymmetric configuration they retrieved both amplitude and dispersion from the same gas cell [188].

Further remarkable work on DCS with GS OFCs is reported in [189], where hydrogen sulphide measurements at different pressures were carried out using OFCs with repetition rates around 1.25 GHz, $\delta f_r = 125$ kHz and optical bandwidths of 60 GHz. The stability of these combs was later analysed in [190], observing maximum fluctuations of 2 pm in wavelength and 0.3 dB in power, and an interline phase correlation below 1 kHz.

Our research group has extensive experience in DCS employing GS OFCs, beginning with the work of Quevedo et al. in 2020 where DCS was demonstrated using two optically injected, pulsed gain-switched DFB lasers that generate flat, mutually coherent combs with 100 MHz spacing and 350 teeth (within 10 dB), $\delta f_r = 100$ kHz ($CF = 1,000$). One of the OFCs was shifted by an 80 MHz AOM to move the detection away from DC, and the large compression enabled low-bandwidth RF readout. Using a symmetric configuration and a HCN gas cell, they recovered transmission consistent with reference data and reported a figure of merit SNR×M (M being the number of comb lines), that scaled with acquisition time, showing that noise characteristics improved for long integration times. This significantly advanced the state of the art for GS-based DCS in terms of resolution. During my master's thesis within the same group, we further improved the resolution by reducing the repetition rate to 5 MHz without penalising the optical bandwidth ($\sim$ 100 GHz) [163].

Building on this approach, the low-bandwidth requirements of the detection electronics were exploited to propose a dual-comb spectrometer in which a low-cost software-defined radio (SDR) replaced a high-end oscilloscope as the RF receiver with minimal performance penalty [169]. Using a symmetric configuration, measurements of a HCN gas cell with 100 MHz resolution were again demonstrated. The SDR captured the down-converted spectrum near 80 MHz (AOM shift), yielding a down-converted RF comb with 1 s integration. After reference normalisation and baseline correction, the HCN absorption near 1550 nm was retrieved with good accuracy, consistent with reference data.

The group later showed that costs could be reduced further by replacing the high-end RF signal generator driving the GS lasers with a direct digital synthesiser (DDS) and step-recovery diodes (SRDs), while using the SDR as the receiver [191]. The generated OFCs were similar to those previously demonstrated, with repetition rates around 100 MHz, $\delta f_r = 7$ kHz and optical bandwidths around 35 GHz. Using a symmetric configuration, they measured a carbon dioxide (CO_2) absorption line at 1572 nm in agreement with the HITRAN database, with a total acquisition time below 20 s. In this way, the spectrometer cost was reduced.

Moreover, the group has demonstrated tunable DCS across the C- and L-bands for multi-gas spectroscopy by simply tuning the ML emission wavelength and injecting into different modes of a FP laser, enabling spectroscopic measurements of pollutant gases such as ammonia (NH_3), carbon monoxide (CO), HCN and CO_2 [168]. With a suitably tunable master laser, the DCS operating point can be swept to unlock its full potential for environmental monitoring. Finally, we have demonstrated that a single, optically injected laser can be employed for dual-comb generation at the expense of careful design of optical paths [179].

3.4 Integrated optical frequency comb sources

The development of technologies and systems based on OFCs has been limited to research laboratories due to the bulky equipment required, the high power consumption and the high cost. However, rapid advances in integrated photonics have made the miniaturisation of OFCs increasingly feasible. These advances could substantially reduce size, weight, power and cost (SWaP-C), paving the way for OFCs to transition from laboratory use to large-scale deployment.

The integration of OFCs within PICs has achieved numerous milestones and is one of the most active areas of current photonics research [45], [192]. Integrated OFCs have already demonstrated performance comparable to that of bulk implementations across several key metrics. Progress in combining them with other components and subsystems within the same package has resulted in the first demonstrations of chip-scale OFC systems. These achievements are an important step towards practical deployment. However, fully integrating the OFC source and all necessary optical subsystems within a single PIC remains a significant challenge. Consequently, ongoing research is focused on advancing integration strategies and optimising architectures to meet the specific requirements of each target application.

Regarding the integration of OFCs, various categories of integrated comb sources can be identified. These can be classified according to the generation technique employed, as follows:

- **Integrated MLLs OFCs:** Generated through mode-locking mechanisms in integrated semiconductor lasers, these combs provide a broad set of evenly spaced spectral lines. Depending on the design, they can offer repetition rates from the sub-GHz to tens-of-GHz range [193]. Integrated MLLs benefit from their compactness, direct on-chip generation, and relatively high efficiency. They are particularly attractive for applications requiring high optical power per line, such as optical communications and microwave photonics [46]. They can be integrated in monolithic III-V [194] platforms or following approaches of heterogeneous and hybrid integration [195].

- **Kerr combs:** Generated in high-Q microresonators or through supercontinuum generation in waveguides via the third-order Kerr nonlinearity [48], [131]. Within this family, two main on-chip implementations are commonly distinguished [192]: (i) supercontinuum OFCs, produced by pumping a dispersion-engineered straight waveguide with ultrashort pulses; and (ii) Kerr microresonator (soliton) OFCs [133], [136], generated by pumping a microresonator with a CW laser, where the line spacing corresponds to the FSR of the resonator [131]. These sources enable chip-scale realisations of OFCs with large line spacings, typically in the range of tens to hundreds of GHz [132]. Microcombs can span several optical octaves, making them highly relevant for applications in frequency metrology, spectroscopy, and optical clocks [131]. However, their operation requires an external pump laser and sophisticated stabilisation schemes [196], which remain challenging for fully integrated solutions. Because these OFCs rely on the nonlinear optical properties of the material and require an optical pump, their integration is generally pursued via heterogeneous or hybrid approaches that combine III–V light sources with platforms exhibiting strong Kerr nonlinearities, such as SiN or AlGaAs [140], [197].

- **Electro-optic modulator (EOM) combs:** Generated by applying phase and amplitude modulation to a CW laser, producing a comb spectrum whose repetition rate is determined by the RF driving frequency. In resonant EOM combs, a cavity or microresonator enhances the modulation efficiency and reduces the required RF power but limits achievable repetition frequencies and tunability. Conversely, non-resonant TWE modulators enable broadband operation and wide tunability at the cost of higher RF drive power and lower efficiency [198]. EOM combs are highly reconfigurable, as both the line spacing and central wavelength can be tuned [199]. Their integration involves combining lasers with high-speed modulators, which may be realised monolithically in III–V [200], LN [201], or hybrid platforms. These combs are particularly suitable for applications requiring precise frequency control, such as DCS and coherent optical communications [198].
- **Integrated GS OFCs:** Generated by directly modulating the injection current of a semiconductor laser, resulting in pulsed emission and a comb-like optical spectrum [152]. GS OFCs can be monolithically integrated, particularly on III–V platforms such as InP, and can be combined with other active components to achieve full system integration and high functionality [158], [202]. Their simplicity, efficiency, and tunability of both repetition rate and emission wavelength make them highly promising candidates for integrated dual-comb systems, LiDAR, and spectroscopy applications.

The underlying principles of these techniques, together with their implementation using discrete components, have already been discussed in Section 3.1, to which the reader is referred for further details. Here, the focus shifts to their realisation within PICs. In particular, the GS technique is of central importance to this thesis and is examined in greater detail in Section 3.2. Comprehensive reviews of integrated OFCs can be found in [45], [46], [192].

In addition to the categories mentioned above, two further approaches are currently gaining relevance, although they remain at a comparatively less mature stage of development. This is the case of integrated combs based on quantum cascade lasers (QCLs) and those referred to as quadratic combs. QCLs have emerged as an alternative technology for comb generation [203], [204], [205] in monolithic platforms, and several demonstrations on silicon have been reported [206]. Quadratic combs, by contrast, are at a somewhat more advanced stage. These are combs based on quadratic nonlinearity (first demonstrated in [207]), and may therefore be grouped together with microcombs under the umbrella of nonlinear integrated OFC technologies. They offer certain advantages, as second-order nonlinear interactions are generally stronger than the third-order processes underlying Kerr combs. Moreover, they may exploit both nonlinearities simultaneously to generate combs more efficiently than Kerr-based approaches [208], [209]. An additional benefit is their capability for limited tuning of the repetition frequency over a wide span.

The integration of such OFCs is becoming increasingly attractive, particularly with the emergence of LNOI platforms, since LN exhibits a strong second-order nonlinearity. Using this technology, octave-spanning integrated combs have been demonstrated that also enable $f - 2f$ self-referencing [210]. Nevertheless, this technology is not included in the detailed discussion that follows, as its development is still less advanced compared with the previously reviewed approaches, although it is more mature than QCL combs.

Table 3.1 summarises the key performance metrics of the integrated OFC sources discussed above. From an application perspective, two parameters are of particular relevance: the repetition frequency and the spectral breadth of the comb. High-resolution spectroscopy, for instance, benefits from low repetition frequencies. Moreover, in applications where down-conversion to the electrical domain is required, the line spacing must be sufficiently small to be measurable with conventional electronic instruments—typically on the order of tens of gigahertz or less. At the same time, a broad spectral span is advantageous in spectroscopy, as it enables the simultaneous measurement of a wider range of samples, and it is essential for metrology and frequency synthesis.

As discussed earlier, there exists an inherent trade-off between repetition rate and comb span. In spectroscopy, this trade-off can limit the achievable signal-to-noise ratio (SNR), while in communications it constrains the minimum attainable channel spacing, since each comb line must maintain a sufficient power level. A common strategy to mitigate this effect is to increase the conversion efficiency, defined as the ratio of the output comb power to the pump power involved in comb generation. In general, integrated OFCs based on MLLs or GS exhibit higher efficiencies than those relying on external nonlinear processes, as the comb is generated directly within the laser cavity. By contrast, microcombs and EO combs tend to exhibit lower efficiencies.

Integrated OFCs based on GS or EO modulation generally provide narrower bandwidths than other integrated OFC sources. Several techniques based on PICs have been proposed to address this issue. In EOM OFCs, cascading multiple modulators can extend the spectral span, though at the expense of increased optical losses and greater complexity in the RF driving network [200]. In GS combs, bandwidth expansion strategies implemented in PICs have achieved spans of up to 260 GHz [158]. OFCs based on MLLs can reach spectral spans of several tens of nm, particularly in hybrid configurations with sub-GHz repetition frequencies [193], [195]. Kerr combs, on the other hand, can cover extremely broad spans of up to several octaves, typically with repetition frequencies in the tens to hundreds of GHz range [61], [211]. In both cases, the repetition frequency is determined by the cavity length in MLLs or by the resonator size in Kerr combs and can therefore only be tuned marginally, if at all.

By contrast, OFCs based on EOM and GS allow direct tuning of the repetition frequency through the modulation signal, as well as straightforward adjustment of the central wavelength of the comb. This tunability in repetition rate and emission wavelength is highly advantageous for applications such as DCS, where it enables real-time balancing of the trade-off between spectral resolution and acquisition time, and for LiDAR systems. For instance, an InP monolithically integrated tunable EOM OFC based on cascaded modulators has been demonstrated in [199].

Reducing the repetition frequency in resonator-based techniques, such as MLLs and microcombs, typically requires cavities several mm or even cm long. This leads to lower resonant enhancement of intracavity power, complex dispersion engineering, and other design challenges. In MLLs, such cavity lengths are not practical in monolithic III–V platforms due to the high propagation losses of passive sections, and heterogeneous integration must therefore be

Table 3.1: Comparison of the main key metrics of integrated OFCs.

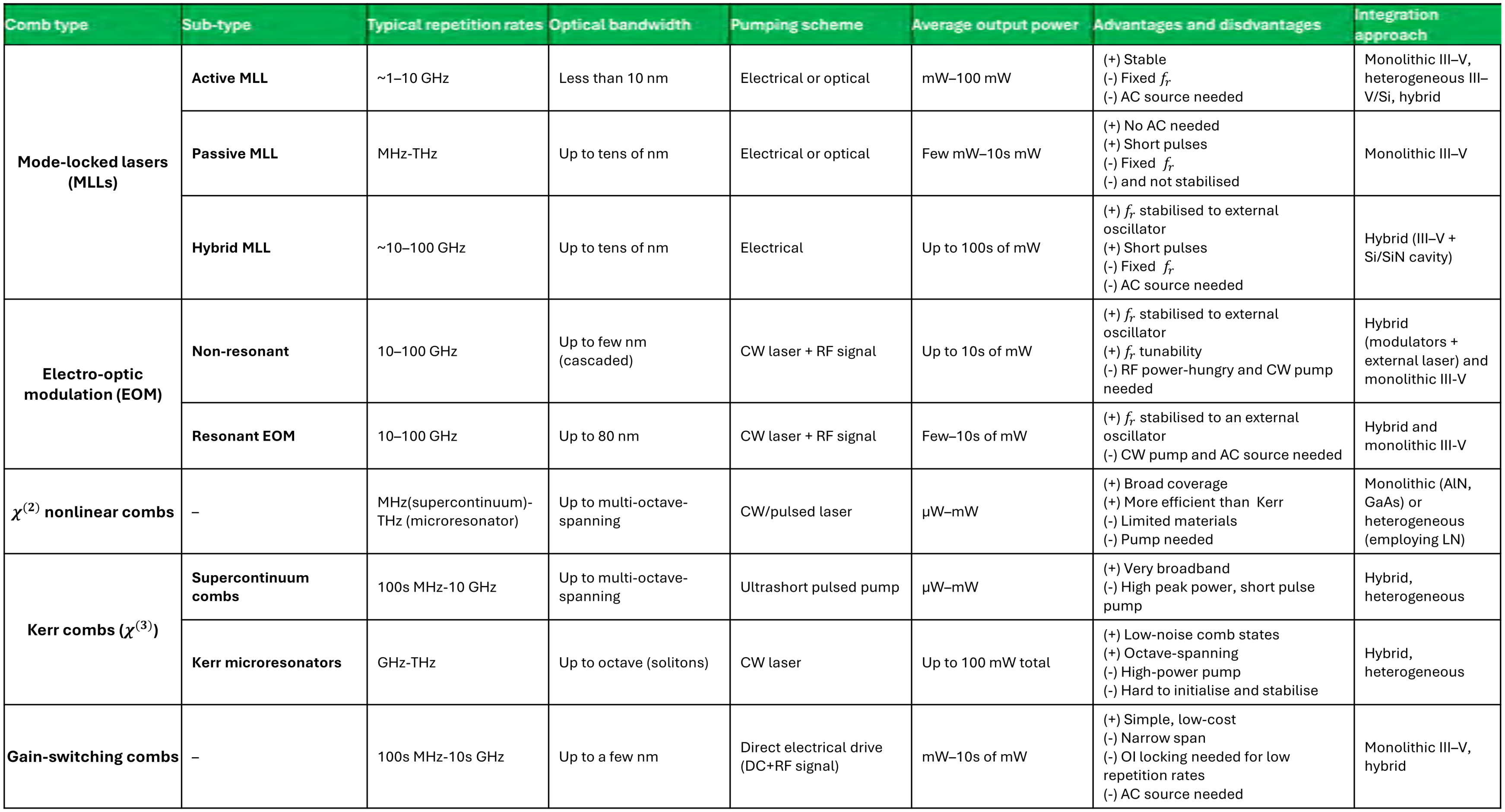

Comb type	Sub-type	Typical repetition rates	Optical bandwidth	Pumping scheme	Average output power	Advantages and disdvantages	Integration approach
Mode-locked lasers (MLLs)	**Active MLL**	~1–10 GHz	Less than 10 nm	Electrical or optical	mW–100 mW	(+) Stable (-) Fixed f_r (-) AC source needed	Monolithic III–V, heterogeneous III–V/Si, hybrid
	Passive MLL	MHz-THz	Up to tens of nm	Electrical or optical	Few mW–10s mW	(+) No AC needed (+) Short pulses (-) Fixed f_r (-) and not stabilised	Monolithic III–V
	Hybrid MLL	~10–100 GHz	Up to tens of nm	Electrical	Up to 100s of mW	(+) f_r stabilised to external oscillator (+) Short pulses (-) Fixed f_r (-) AC source needed	Hybrid (III–V + Si/SiN cavity)
Electro-optic modulation (EOM)	**Non-resonant**	10–100 GHz	Up to few nm (cascaded)	CW laser + RF signal	Up to 10s of mW	(+) f_r stabilised to external oscillator (+) f_r tunability (-) RF power-hungry and CW pump needed	Hybrid (modulators + external laser) and monolithic III-V
	Resonant EOM	10–100 GHz	Up to 80 nm	CW laser + RF signal	Few–10s of mW	(+) f_r stabilised to an external oscillator (-) CW pump and AC source needed	Hybrid and monolithic III-V
$\chi^{(2)}$ nonlinear combs	–	MHz(supercontinuum)-THz (microresonator)	Up to multi-octave-spanning	CW/pulsed laser	µW–mW	(+) Broad coverage (+) More efficient than Kerr (-) Limited materials (-) Pump needed	Monolithic (AlN, GaAs) or heterogeneous (employing LN)
Kerr combs ($\chi^{(3)}$)	**Supercontinuum combs**	100s MHz-10 GHz	Up to multi-octave-spanning	Ultrashort pulsed pump	µW–mW	(+) Very broadband (-) High peak power, short pulse pump	Hybrid, heterogeneous
	Kerr microresonators	GHz-THz	Up to octave (solitons)	CW laser	Up to 100 mW total	(+) Low-noise comb states (+) Octave-spanning (-) High-power pump (-) Hard to initialise and stabilise	Hybrid, heterogeneous
Gain-switching combs	–	100s MHz-10s GHz	Up to a few nm	Direct electrical drive (DC+RF signal)	mW–10s of mW	(+) Simple, low-cost (-) Narrow span (-) OI locking needed for low repetition rates (-) AC source needed	Monolithic III–V, hybrid

employed [212]. Repetition-rate tunability in MLLs can be achieved through carrier injection and thermal control, although it is typically limited to about 1 GHz [213]. In microcombs, limited repetition-rate tuning has been demonstrated through soliton-crystals [214], but this approach remains significantly more complex and indirect than in GS OFCs.

From an operational point of view, GS, EOM, and MLL OFCs can generally be initiated by appropriate electrical or optical driving of the laser, requiring no complex procedures. In contrast, microcomb operation is considerably more demanding, as it relies on exciting a coherent soliton state. Achieving and maintaining this state is highly sensitive to small temperature fluctuations and typically requires complex initialisation and stabilisation protocols [196]. This remains a major obstacle to the widespread integration of microcombs. Furthermore, the design of microcomb sources requires precise dispersion engineering and high-Q resonators, which demand mature fabrication processes.

Another important factor to consider is the optical noise associated with OFCs obtained through different integration strategies. In this context, noise refers to the noise floor far from the carrier frequency, or frequency noise, which can be represented by the fundamental Lorentzian linewidth [215]. In microcombs, it is mainly determined by the pump laser, although in some cases the nonlinear process also contributes. For MLL, GS, and EOM combs, the noise is governed by the Lorentzian linewidth of the laser itself. In GS OFCs, when OI is employed, the linewidth is defined by the ML through the OI locking process. Consequently, beyond the need for tunable integrated lasers, there is a strong motivation to develop sources with narrow linewidths to minimise overall noise.

The integration of OFC sources can be achieved monolithically, heterogeneously, or through hybrid schemes, depending on the specific generation technique. Monolithic integration offers compact functionality within mature industrial ecosystems supported by generic foundry platforms. Among them, III–V platforms based on InP or GaAs are particularly relevant, as they natively support integrated lasers and high-speed modulators, with InP representing the most advanced option. These properties enable the direct implementation of MLL, EOM, and GS OFCs, as well as their integration with other photonic components. Monolithic MLLs incorporating modulators and amplifiers have already been demonstrated through MPW runs in InP foundry processes [194], [216]. GS combs, which rely on direct laser diode modulation, are especially well suited to InP platforms, where fully monolithic demonstrations combining GS combs with other components have been reported [158], [217], [218].

Heterogeneous integration has proven essential for microcombs, as it combines III–V gain media with nonlinear materials such as SiN for Kerr processes, and LNOI or AlGaAsOI for quadratic ones. Within this framework, soliton microcombs have been demonstrated using III–V/Si/SiN integration [140], while octave-spanning combs have been achieved in LNOI [71], [138], [139], [219] and AlGaAsOI [197] platforms. MLLs have also benefited from heterogeneous InP/SiN integration, which allows for an increased cavity length [212], and EOM combs could gain from combining III–V lasers with LN modulators [220], leveraging their low-loss waveguides and strong EO response. Hybrid integration represents a promising route for microcombs, as it enables the combination of the best performance features from distinct technologies. However, these solutions currently face challenges related to scalability and cost, which limit their suitability for large-scale production.

3.4.1 Integrated gain-switched optical frequency combs

The first demonstration of an integrated GS OFC was reported in 2016 by J.K. Alexander et al. [217] in a monolithic InP platform. The device comprised a three-section laser with two single-facet slotted Fabry-Pérot (SFP) cavities acting as the master and slave, sharing a common slotted mirror, as shown in Fig. 3.7 (a). This slotted mirror provided electrical isolation between sections, allowing independent electrical biasing of all three. OI from the ML into the SL enhanced stable single-mode operation of the injected cavity. By tuning the drive currents of the master section and the shared mirror, injection locking to different longitudinal modes of the FP cavity was demonstrated, yielding discrete tuning of the emission frequency over a range of 10 nm across the L-band (1565 nm-1625 nm), with steps of 3.2 nm.

A high-power RF signal (> 20 dBm) at a 4 GHz repetition rate was applied to the slave section to generate OFCs, both with and without biasing the master section. Under OI, the optical bandwidth of the OFC increased by nearly a factor of two, attributed to the increased modulation bandwidth provided by the OI locking mechanism as the frequency of relaxation oscillations increased. The measured linewidth of the comb lines was as low as 600 kHz, and spectra measured at both device facets showed no asymmetry in the emitted comb. Even so, the overall span of the OFC remained modest, with approximately eight lines within 3.5 dB (32 GHz).

The device was fabricated using standard lithographic processes, but not through generic integration processes. The active regions comprised AlGaInAs quantum wells (QW) grown on an n-doped InP substrate. The overall device length was around 2 mm, partitioned into an 800 μm ML section, a 756 μm SL section, and a 756 μm slotted mirror.

These results provided foundations for a compact way of generating GS OFCs directly on-chip and marked a key milestone for integrated GS OFCs, demonstrating for the first time the feasibility of realising such sources in a fully integrated photonic platform.

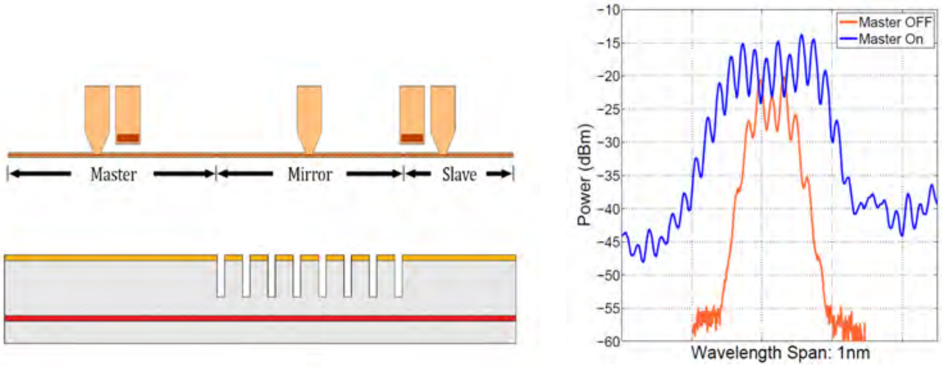

(a) (b)

Figure 3.7: GS OFC based on a monolithically integrated three-section laser proposed in [217]. (a) Scheme of the three-section laser with two FP cavities sharing a slotted mirror section. (b) Spectra of the generated OFC with and without biasing the master section.

Building on the scheme of Alexander et al. [217], M. Deseada et al. demonstrated an externally injected GS OFC on a monolithic InP PIC, adding a mirror to one facet of the master section to enhance the efficiency of the OI and enforce unidirectional emission. They observed that when the slave laser was GS and optically injected by appropriately tuning the currents of the master and the mirrors, the comb quality improved notably. The 20 dB optical bandwidth increased from 62.5 to 94 GHz, and the spectral flatness improved from two to nine lines within 3 dB at a 6.25 GHz comb line spacing. The comb line spacing could be tuned between 6 and 10 GHz by adjusting the RF modulation frequency. In addition, noise and coherence were comprehensively characterised, showing low relative intensity noise (RIN) (-127 to -130 dB/Hz), optical carrier-to-noise ratios (CNRs) greater than 40 dB, an intrinsic linewidth of 1.5 MHz, and strong interline phase correlation with a 10 Hz RF beat linewidth. These OFCs were also demonstrated for optical communication systems employing advanced modulation formats [221], constituting one of the first demonstrations of high-level integration of GS OFCs.

Another remarkable work in the field of integrated GS OFCs is that reported in [158]. This work presents a monolithic integration scheme in which two DFB lasers share the same ML, which consists of an active section sandwiched between two DBR mirrors. This device was manufactured through an MPW run on a generic InP integration platform. In this scheme, GS could be performed on the two DFB lasers using OI from the master DBR laser or an off-chip laser to generate two mutually coherent OFCs. In addition, the two SLs could be thermally tuned independently by a few nm using thermal heaters.

The DFBs exhibited good performance in both CW and GS operation. However, the on-chip master's emission wavelength did not overlap with that of the slaves, so the authors resorted to an external tunable master (via a circulator) to realise mutual OI locking of both DFB slaves.

Using off-chip ML, mutually injection-locked gain-switched lasers (MIL-GSL) with a repetition rate of 6.25 GHz were demonstrated. The spectral overlap of the generated OFCs yielded an expanded OFC with approximately 218 GHz and 256 GHz (36 and 42 lines) at 3 dB and 10 dB, respectively, consistent with prior GS OFC expansion using discrete components [222]. In terms of noise characteristics, the measured optical linewidth of the comb tones is approximately 50 kHz, and the RIN was also characterised at -145 dB/Hz. The interline phase correlation also demonstrated good performance as measured by the RF beat line width of about $12 - 15$ Hz. In addition, the repetition frequency demonstrated a tuning range showing OFCs at 10 GHz with a width of 100 GHz (11 lines) and at 12.5 GHz with a width of 75 GHz (7 lines), with reduced bandwidth at higher repetition rates. This MIL-GS-based work demonstrated a much higher bandwidth than previous GS OFCs integrated with a standard component-based implementation from a generic integration foundry, demonstrating a compact, low-complexity, energy-efficient implementation well suited to reconfigurable multicarrier sources for communications and mmW/THz generation.

As it has been mentioned earlier, the absence of on-chip optical isolators in generic integration platforms can constrain the implementation of integrated GS OFCs. To address this, contemporaneous work to this thesis reported a three-section master–slave configuration on an InP PIC comprising two mutually coupled lasers [174], [223]. The ML is a two-section slotted single-mode (SLM) device tunable across 1535 – 1560 nm and separated from the slave by a slotted mirror. The SL is FP that is gain-switched under OI from the SLM, producing an OFC with 6.8 GHz spacing. Two coupling schemes between the SLM and FP were compared: an asymmetric (primary–secondary) scheme, where light propagates only from the SLM to the FP (a conventional OI configuration), and a symmetric (mutual) scheme with bidirectional coupling. The mutual-coupling case enabled self-locked operation with enhanced phase stability, higher comb power and a broader comb bandwidth than the asymmetric case, showing that reciprocal coupling markedly improved GS OFC performance on a PIC.

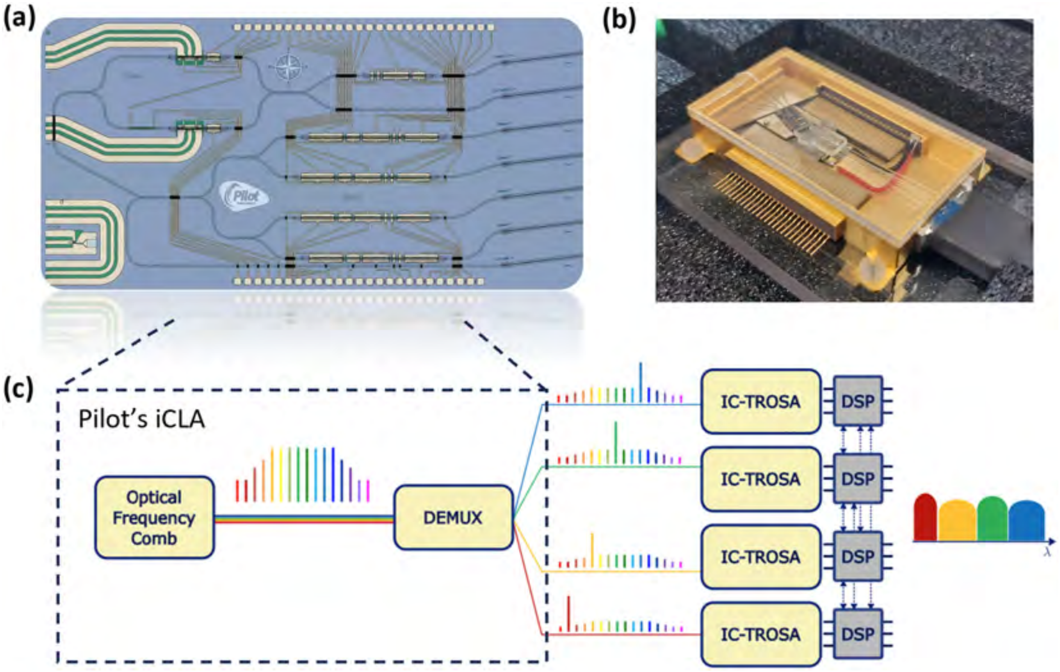

Figure 3.8: (a) Pilot Photonics monolithic PIC photograph for the iCLA; (b) packaged iCLA with thermal control and electrical and optical access; (c) proposed architecture for this iCLA to scale coherent transceivers. Source: [224]

Recently, integrated GS OFCs have achieved a high level of integration, reaching market applications. The work of H. Othman et al. [202] presents an integrated GS OFC engineered as a multi-tone local oscillator for a spectrally sliced coherent receiver. The comb is generated in what the authors term an integrated comb laser assembly (iCLA). The device combines two GS lasers, mutually injection-locked by a narrow-linewidth master. The spectral overlap of the two combs yields an expanded comb with four mutually coherent tones at 12.8 GHz spacing. Each tone exhibits an effective linewidth of approximately 30 kHz limited by the ML, and very high interline phase coherence (RF beat < 1 kHz at 12.8 GHz). To employ the OFC as the LO, the chip integrates a downstream active injection-locked 1×4 demultiplexer that selects, amplifies, and delivers about 0 dBm per tone with a comb line suppression ratio greater than 30 dB, overcoming the insertion loss of passive demultiplexers and easing receiver sensitivity. Using this OFC and the active demux, the authors demonstrate spectrally sliced coherent detection of a 100 Gb/s PDM-QPSK signal with good characteristics compared to conventional intradyne receivers.

This iCLA development has led to a commercial product marketed by Pilot Photonics that aims to serve in wavelength routing-based optical transport networks. Pilot Photonics was established in 2011, focusing on commercialising GS OFC sources and now monolithically integrated in InP. Fig. 3.8 shows the PIC together with its commercial package and a reference architecture for scaling coherent transceivers [225]. The device is delivered in a package comprising thermal control and both electrical and optical access or in die form for co-integration with other PICs. This device is currently the most advanced example of high-level integration of GS OFCs and offers numerous advantages in the commercial segment of optical communications in terms of SWaP-C, reconfigurability, and control.

It is important to note that, although GS OFCs are often realised monolithically, hybrid approaches have also been reported [226]. In that work, a hybrid-integrated GS OFC was demonstrated in which a commercial 1.55 μm DFB laser is butt-coupled to a high-Q Si$_3$N$_4$ microring reflector (MRR) that self-injection locks the laser by reflecting a single comb tooth, enhancing phase coherence, CNR, and spectral flatness. At $\tilde{6}$.5 GHz modulation (near the relaxation oscillation), the source produced eight comb lines within 3 dB of the envelope peak with 40 dB CNR, a 615 kHz per-line optical linewidth (vs 7.34 MHz for the solitary CW laser), and a 50 Hz RF beat tone indicating strong interline phase correlation. The MRR (measured FSR $\sim$ 50 GHz, FWHM $\sim$ 562 MHz, Q$\approx 3.45 \cdot 10^5$) ensured single-line feedback that suppressed mode competition, and the comb spacing was continuously tunable from 5.55 to 8.7 GHz via the RF drive.

3.5 Integrated optical frequency comb systems

Recent advances in integrated photonics have enabled advanced proof-of-concept demonstrations of OFC-based systems that extend beyond the comb generator itself, integrating multiple subsystems on a single chip. These demonstrations are a significant step towards practical, compact implementations and illustrate the potential of integrated OFCs in diverse application domains, such as sensing, communications, microwave generation, and metrology [45], [46], [192], [224].

One notable example is precision timing and frequency synthesis, where integrated combs can operate as chip-scale optical clocks or as optical-to-microwave links in coherent systems [145]. Soliton microcombs have already been employed in compact microwave synthesisers, achieving low phase-noise performance comparable to state-of-the-art electronic oscillators [149]. In optical communications and WDM, integrated combs can function as multi-wavelength sources, replacing arrays of individual lasers and providing a coherent grid of carriers [142], [143]. Integrated OFCs have also been applied in LiDAR [148] and ranging, where dual-comb techniques enable highly precise and fast distance measurements [227], [228]. DCI based on PICs is reviewed in more detail in Section 3.5.1.

Despite these achievements, most demonstrations to date represent advanced stages of integration that have not yet been consolidated into commercially deployable technologies. The adoption of OFC-based systems in PICs remains limited as integrating all the necessary subsystems, such as light sources, modulators, amplifiers and control electronics, into a fully functional, manufacturable platform continues to present significant challenges. However, substantial progress has been made in combining multiple integration strategies within a single device, as demonstrated by the highly integrated optical frequency synthesiser reported in [45] (Fig. 3.9), which is one of the most advanced demonstrations achieved so far together with the one presented in Fig. 3.8.

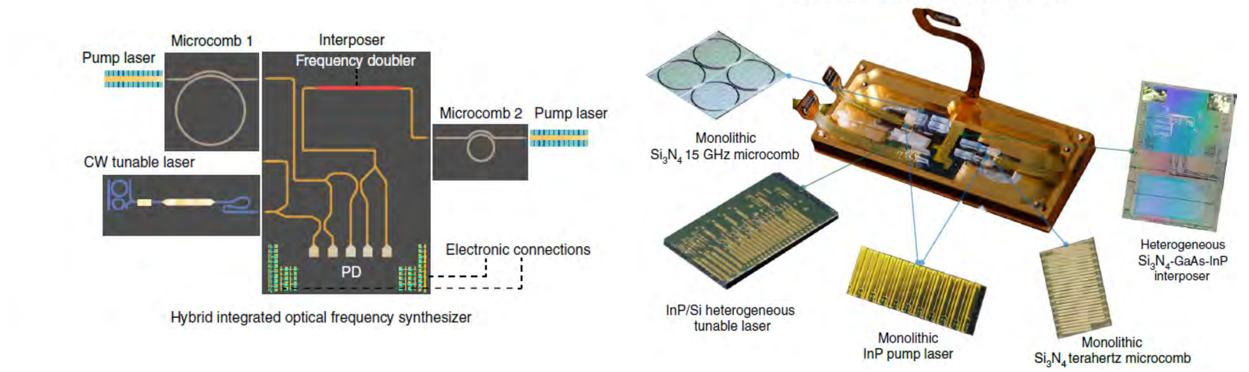

Figure 3.9: Integrated optical frequency synthesiser based on microcombs and three integration approaches: Monolithic, heterogeneous and hybrid. This representes one of the most advanced examples of integrated OFCs with full system functionality. Source: [45].

Nevertheless, the field has yet to converge on a universal approach that can meet the diverse requirements of different applications. As summarised in Table 3.1, each integration strategy and OFC generation technique offers distinct advantages and limitations. The deployment of these technologies will therefore be driven by the application, with OFC designs tailored to specific performance requirements. In communications, for instance, power efficiency and high power per line are paramount, favouring MLL OFCs. Conversely, applications demanding broad spectral coverage, such as metrology, typically favour microcombs and other nonlinear OFCs. In scenarios where only a limited spectral range is required, but operational flexibility, reconfigurability, and high spectral resolution are crucial, EOM and GS combs offer particularly attractive advantages.

3.5.1 Integrated dual-comb interferometry

The development of integrated OFC sources enables DCI to be realised at the chip scale. In DCS, in particular, various integrated comb technologies have been investigated as sources to perform gas measurements. Microcombs offer the advantage of very large optical bandwidths, which can cover extensive ranges of molecular responses. However, because their repetition frequencies are typically high, the spectral resolution attainable in the RF mapped domain is correspondingly limited [146].

One of the first demonstrations of dual-comb spectroscopy employing Kerr soliton OFCs can be found in [146]. In this article, two silica whispering-gallery resonators on a silicon chip are employed to generate two phase-locked femtosecond soliton pulse trains with approximately 22 GHz repetition rates. The corresponding OFCs exhibited spectral coverage of over 60 nm. The repetition rate difference is precisely matched to 2.6 MHz by precise control of the resonator diameter through advanced fabrication techniques. The multiheterodyne beat compresses more than 4 THz of optical bandwidth from 1535 nm to 1567 nm into approximately 500 MHz of RF spectrum, yielding narrow electrical comb lines with less than 50 kHz linewidth and a high SNR of around 30 dB, limited by the mutual coherence of the pump lasers. This dual-comb spectrometer is validated through the measurement of the absorption profile of the $2\nu^3$ band of $H^{13}CN$ showing good agreement with direct spectroscopy of the sample, although the resolution was limited by the high repetition rate of the OFCs compared to the profile of the sample.

Another demonstration of on-chip dual-comb spectroscopy employing Kerr combs was presented in [44]. The device consisted of two SiN microring resonators pumped by a single laser. The microrings could be thermally tuned via microheaters to reach the soliton regime deterministically. Two mutually coherent OFCs were obtained, covering a span of around 51 THz (400 nm) with a repetition rate of 450 GHz, and a repetition rate difference of 1.12 GHz. The dual-comb produced a compressed RF spectrum with 10 kHz beatnote linewidths. However, because the frequency offset is relatively large, the electrical bandwidth required resulted as high as 30 GHz, which hampers the use of low bandwidth electronics. The device also allowed observation of the comb formation in real time from the noisy states to the soliton formation, using one of the combs as a reference. The system is validated for spectroscopic measurements of dichloromethane (CH_2Cl_2), achieving measurements over a span of 170 nm with 20 μs acquisition time, with good agreement with OSA measurements.

In another study, dark solitons generated in photonic molecules were employed as more efficient OFC sources for dual-comb applications [229]. However, only the microresonators were integrated, and the dual-comb measurements relied on external laboratory setups. Furthermore, integrated dual-comb interferometers employing microcombs have been demonstrated for imaging [181] and ranging [227].

The search for greater flexibility and reconfigurability in integrated dual-comb systems has led to the development of such systems using resonant EO combs. In [201] the authors reported a high-Q microring EO comb generator with strong $\chi^{(2)}$ based on the TFLN platform. The strong phase modulation provided by the phase modulator enhanced the dynamic resonance condition, leading to a broad and flat OFC with more than 900 optical lines within a span higher than 80 nm over the L-band and a repetition rate of around 10.43 GHz, which is considerably lower than those typically obtained with Kerr combs. Furthermore, the authors demonstrate dual-comb generation in a single resonator with a controlled frequency offset ranging from 10 Hz to 100 MHz, indicating high configurability.

The same group used a similar approach to perform frequency-agile dual-comb spectroscopy on acetylene, achieving good agreement with the HITRAN database [230]. Furthermore, they discuss ways to lower the line spacing, increase the resolution of the measurements, and achieve broader spans with resonant EO combs in the TFLN platform.

Further reduction of the repetition rate to enhance the spectral resolution while maintaining a broad span using MLL OFCs with a 1 GHz repetition rate [231], [232]. The authors demonstrated an OFC based on MLL integrated in III-V-on-silicon featuring 300 GHz of optical bandwidth. In these works, however, the authors demonstrated dual-comb spectroscopy using two OFCs from different chips [232] and an external EO comb [231].

Dual-comb interferometry with integrated GS OFCs

Dual-comb interferometry based on GS combs offers several advantages over alternative approaches. It enables efficient, reconfigurable, fully monolithic implementations with a simple operating and initiation protocol. Crucially, the low repetition rates achievable with GS combs down to a few MHz are well suited to dual-comb spectroscopy, where very high spectral resolution is required, even though the optical span is typically more limited than in other comb-generation techniques.

The first demonstration of a dual-comb source based on GS OFCs was reported in 2020 by J.K. Alexander et al. [233]. The device was monolithically integrated in InP utilising a regrowth-free process, with deep-etched bends and slotted mirrors, as shown in Fig. 3.10. It integrated an SFP laser similar to that in [217], as the ML injected two FP SLs. The overall size of the PIC was 1.65 mm by 0.7 mm. The master output was split by a 1×2 MMI coupler to inject both SLs simultaneously, thereby providing mutual coherence. Single-mode OI locking of both SLs was obtained when the ML was driven well above threshold, the emitting wavelength being near 1584.5 nm. The GS operation of the two SLs generated OFCs with repetition rates of 5 GHz and 4.1 GHz, respectively. However, the acquisition of the RF down-converted comb was not reported but remained a good proof of concept for integrated dual-comb interferometers based on GS sources.

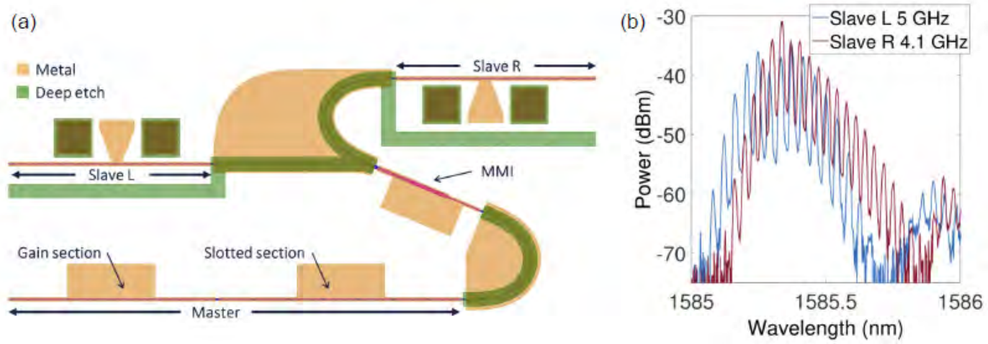

Figure 3.10: Proof-of-concept of a monolithically integrated InP dual-comb source based on GS OFCs presented in [233]. (a) Scheme of the device consisitng of two FP SLs which are optically injected by a SFP. (b) measured specturm of the two generated OFCs

This remained the only demonstration of an integrated GS dual-comb interferometer until the work presented in this thesis. The approach established in [233] provides a solid foundation for the development of reconfigurable dual-comb interferometers based on GS OFCs, which can be implemented using generic integration platforms. Such compatibility offers a practical and scalable path towards compact, low-SWaP dual-comb systems. Although the implementation reported here operated at relatively high repetition frequencies, the GS technique also allows operation at lower repetition rates to improve the spectral resolution of the dual-comb interferometers.

Chapter 4

Experimental methods for characterising photonic integrated circuits

This chapter presents the experimental methodologies employed to characterise the PICs developed in this thesis. The characterisation process involves defining the measurement objectives, designing appropriate experimental setups, and analysing the resulting data to assess device performance.

In general, PIC characterisation can be performed at three hierarchical levels: wafer, die, and package. Wafer-level characterisation enables rapid testing of multiple devices across a wafer before dicing, providing an overview of process uniformity and fabrication yield. Die-level characterisation focuses on individual chips that have been separated from the wafer but are not yet packaged, allowing detailed optical and electrical testing using temporary probing techniques. Finally, packaged-level characterisation evaluates fully assembled devices, integrating the PIC with electrical and optical interfaces suitable for system-level testing and long-term operation.

To address these stages, two complementary experimental platforms were developed in this work: a probe-station setup for die-level measurements, described in Section 4.1, and a custom electrical packaging scheme that enables laboratory testing of fully assembled PICs, detailed in Section 4.2. In both cases, the PIC must be mounted on a stable platform that permits reliable optical and electrical access while preventing direct manual contact with the chip surface.

4.1 Characterisation at die-level

PICs typically feature both electrical connections and optical interfaces. Therefore, effective characterisation requires a physical setup capable of interfacing laboratory instrumentation with the chip. Typical photonics laboratory instruments can broadly be classified into three categories:

1. Sources and signal generators, which provide drive currents, bias voltages, RF modulation signals, or optical sources.
2. Measurement instruments that monitor and quantify the PIC response. These include spectrum analysers, optical power meters, PDs, multimeters, or high-speed oscilloscopes, among others.
3. Actuators or controllers which provide different degrees of control over environmental or mechanical operating parameters, such as temperature, vibration, or vacuum.

Although carried out after fabrication, PIC characterisation must be anticipated at the design stage to guarantee that the device can be effectively tested. Factors such as the number of electrical contacts, the configuration of optical inputs and outputs, the device footprint, and the intended functionality should be defined together with the strategy for verifying that functionality. Once fabricated, the characterisation process typically follows a well-defined sequence of steps.

First, the experiment is planned, and the figures of merit or system parameters to be measured are identified. This is followed by the design of the experimental setup, which provides electrical and optical access to the PIC and includes the preparation and calibration of the required instrumentation. The PIC is then mounted in the setup, electrically connected, and aligned with the optical interfaces to enable the injection and collection of light. The optical and electrical responses of each individual device or component are then measured to verify that the components are operating correctly. Finally, system-level characterisation assesses the combined performance of all components to evaluate the overall behaviour of the circuit.

Throughout this thesis, extensive work has been carried out on both the design and characterisation of PICs. The following chapters focus on these aspects, while this section provides a general overview of the experimental setups and methodologies, together with the main practical considerations involved.

The measurement setup is based on a copper submount serving as the mechanical and thermal interface for the PIC. Temperature control is provided by a thermoelectric cooler (TEC) or Peltier cell, controlled by a TEC controller (ILX LDT-5412 or Newport 325), integrated into the probe station, that uses the reading from a thermistor placed close to the PIC (see Fig. 4.1). The copper submount provides heat sinking during electrical operation. The die is fixed by vacuum through an internal port in the copper base, which is connected to an external vacuum pump.

Electrical contact with the PIC is established using contact probes connected to the laboratory instruments. RF probing is performed with ground–signal–ground (GSG) probes, matched to an impedance of 50 Ω, and offering a bandwidth of up to 40 GHz, while DC needles are employed for low-frequency biasing. To avoid the need for aligning individual probes, probe arrays are used. These consist of multiple needles arranged at a fixed pitch, allowing simultaneous contact with several pads. This introduces a design constraint on the PIC layout, as the pad pitch and geometry must match the array specifications. The probe arrays are mounted on micropositioners providing fine X, Y, and Z control to enable precise alignment and contact. A goniometer is also included to allow controlled tilting of the probe array, if needed, facilitating accurate planarity adjustment between the probes and the chip surface.

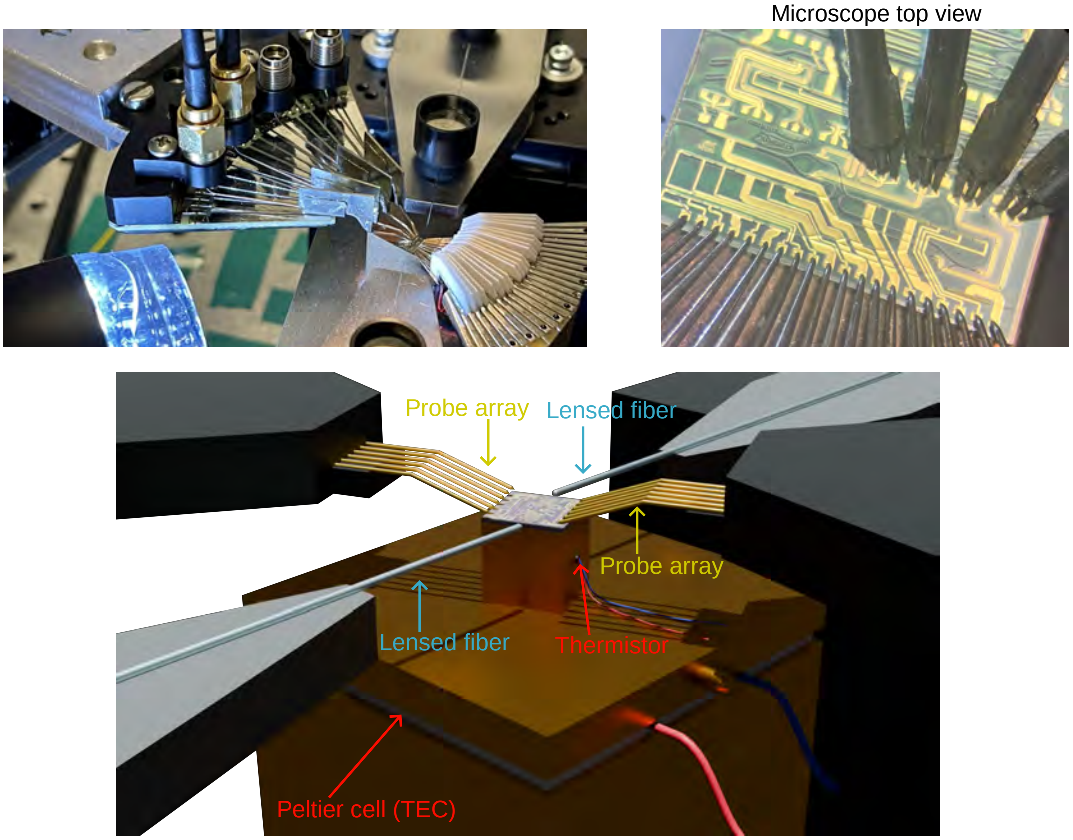

Figure 4.1: Description of the probe station experimental setup used for the characterisation of PICs at the die-level. The PIC is mounted on a copper submount that provides heat sinking and thermal control via a TEC controller which reads the temperature of the base by means of the thermistor. The chip is tilted by 23° to compensate for the tilt of the on-chip I/O waveguides. Electrical contact to the PIC is established using probe arrays mounted on linear micropositioners, offering both DC and RF measurement capabilities. Lensed fibers are positioned on V-grooves to inject and collect light from the PIC. The V-grooves are mounted on precision XYZ translation stages that enable fine optical alignment.

Optical coupling to and from the PIC is achieved using lensed fibers, either individually or arranged in arrays, to match the fiber mode to the on-chip waveguide mode and thereby minimise coupling losses. A lensed fiber is a standard single-mode optical fibre whose tip is processed to form a micro-lens that focuses or expands the guided mode, enabling efficient coupling between the fiber and the much smaller optical mode of the photonic chip.

By adjusting the separation between the fiber tip and the waveguide facet, and by selecting a fiber with an appropriate working distance and focal length, the beam waist can be positioned at the waveguide input to maximise mode overlap. Typical lensed fibers for operation around 1.55 μm exhibit a mode-field diameter (MFD) of 2–3 μm at focus and a working distance of a few μm (26 μm in this case). The achievable coupling loss primarily depends on the spatial mode overlap between the fiber and on-chip waveguide modes.

This thesis is based on InP PICs that employ edge couplers available in the foundry PDKs. In the setup illustrated in Fig. 4.1, the PIC is mounted with a 23º rotation relative to the optical table axis to compensate for the 7° tilt commonly incorporated into the input–output waveguides to suppress back-reflections. The estimated coupling loss per facet in this setup is approximately 6 dB.

For single lensed fibres, a V-groove holder is mounted on XYZ translation stages (Thorlabs MAX302 or M-562F-XYZ) to provide independent motion along the X, Y, and Z axes via manual differential micrometres. Fine alignment is achieved either with piezo actuators controlled by a piezo controller (Thorlabs MDT630B) or with a motorised actuator. Auxiliary rotational stages (Thorlabs PY003) provide pitch and yaw adjustment to optimise coupling, while alternative fixtures can accommodate fiber arrays when required. Prior to any long acquisition, thermal stability is verified. Once the chip has reached its temperature setpoint, the lensed fibers are coarsely aligned under a microscope and then finely optimised using the piezo stages while monitoring the coupled optical power.

Fig. 6.16 shows the standard characterisation setup used throughout this thesis. For input coupling, light from an external CW laser passes through a fiber-based polarisation controller (PC) to maximise the power coupled into the on-chip TE mode. On the output side, an optical isolator (ISO) is always inserted to prevent back reflections and unintentional re-injection into the PIC. When required, an optical circulator is used to inject and collect light simultaneously. In the subsequent measurements, the external laser is a low-linewidth tunable laser from PurePhotonics that can be tuned across the C-band (PPCL300) and L-band (PPCL301). This laser is based on an external cavity design and features a narrow linewidth of 10 kHz, which is useful for the experiments here, and a maximum emitting power of 13.5 dBm.

The output is then split into two branches by a fiber coupler. The first branch is used for monitoring and fundamental characterisation. This branch feeds an optical spectrum analyser (OSA, Ando AQ-6315A) and a low-frequency power monitor (PM), the latter implemented as a high-responsivity germanium DC photodiode (Graseby Optronics 261) connected to a precision digital multimeter (Keithley 2000). This branch is present in all experiments, as it simplifies alignment by maximising the DC photocurrent and enables quick checks of basic device behaviour, such as lasing modes, lasing threshold, and spontaneous emission level. The second branch is configured according to the experiment. It can be routed to a high-resolution OSA (HR-OSA, Aragon Photonics BOSA 400 C+L) for fine spectral measurements, offering a resolution of 10 MHz. For RF characterisation, fast photodetectors (DET08CFC/M, 5 GHz bandwidth; Finisar XPDV2120R-VF-FP, 50 GHz bandwidth) are used for measurements on an electrical spectrum analyser (ESA, Agilent E4446A) or for time-domain acquisition on a real-time oscilloscope (Keysight MSOS804A). All measurement instruments are located in a separate laboratory room and connected to the setup through a long optical fiber link.

The electrical instrumentation used to bias and drive the devices includes low-noise voltage sources (Aim TTi MX100TP) for heaters and phase shifters, precision low-noise current sources (Arroyo ARO-4205-DR) for lasers and SOAs, and RF drive equipment such as arbitrary waveform generators (AWG, Tektronix AWG70002B), pulse-pattern generators (PPG, Anritsu MU181020A), and RF signal generators (Rohde & Schwarz SMB-B112). Bias-tees are employed where necessary to superimpose RF waveforms onto DC bias, and all RF paths are matched to 50 Ω where the connections are provided by high-bandwidth coaxial cables. To connect the instruments to the probe arrays, a PCB acting as an interposer is employed, which adapts the output of the sources to the probe array connectors.

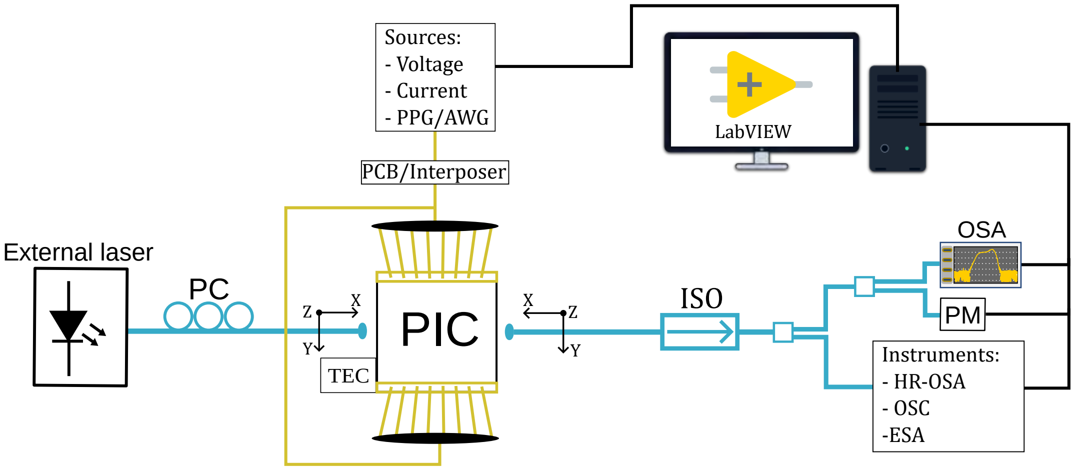

Figure 4.2: Experimental setup for PIC characterisation. Light is injected and collected using lensed fibers. When injecting light into the PIC, an external laser is employed with a polarisation controller to maximise the injected power in the TE mode. When required, an optical circulator can be placed at this input to inject and collect light simultanoeusly. The light is collected from the PIC and sent to the instrument branches via an optical isolator to prevent the light from being re-injected into the PIC. One of the branches consist of an OSA and a PM to align the fiber and to characterise the fundamental operation of the devices. The other branch can be sent to other instruments. The PIC is biased and driven with signals from different current, voltage and RF sources, that are connected to the probe arrays by means of a PCB interposer. Measurements are automated in LabVIEW, with all sources and instruments controlled from a laboratory computer. PC: Polarisation controller; TEC: Thermoelectric cooler; PPG: Pulse-pattern generator; AWG: Arbitrary waveform generator; PCB: Printed circuit board; ISO: Optical isolator; OSA: Optical spectrum analyser; OSC: Oscilloscope; ESA: Electrical spectrum analyser; HR-OSA: High-resolution OSA.

Both optical sources and measurement instruments are controlled from a laboratory to automate device characterisation. The automation is implemented in LabVIEW using NI-VISA and vendor-supplied drivers. The software has been developed as part of this thesis to meet the specific characterisation requirements. Typical routines include PI-curve acquisition (the program steps the drive current while reading the optical power from the power meter and/or OSA), current sweeps for controlling heaters, bias adjustment in GS operation or OI power, voltage sweeps for MZMs, and sequential acquisition of optical and electrical spectra.

The measurement data are stored in readable formats for subsequent post-processing in MATLAB or Python, where figures of merit such as the side-mode suppression ratio, comb flatness and 10 dB bandwidth, and linewidth are calculated and plotted for representation.

4.2 Electrical packaging for laboratory testing

As an alternative to the probe station described above, this section details the development of an electrical packaging approach for the laboratory characterisation of PICs. Packaging enhances reliability and repeatability, facilitates practical handling, and protects the die from environmental and mechanical stress. The approach implemented in this work reduces the overall footprint of the test bench, enables operation independently of a probe station, and ensures consistent device performance by providing a stable and reproducible electrical interface.

This work was initially developed as part of a bachelor's thesis entitled Development of a platform for the packaging and control of photonic integrated circuits (Desarrollo de una plataforma para el encapsulado y control de circuitos fotónicos integrados), carried out by Ismael Pintor Periáñez in 2023.

The proposed system employs a custom printed circuit board (PCB) that acts as a mechanical carrier, electrical interposer, and thermal management platform. The PIC is attached to the board using a thermally conductive adhesive and is connected through short wire bonds that deliver power and signals via the PCB tracks. Wire bonding, typically performed with thin gold or aluminium wires, ensures reliable electrical contact and low-resistance connections. Following the bonding process, the board is mounted on a rigid fixture to ensure stable handling and effective thermal control.

In terms of thermal management, the PCBs feature copper planes and thermal via arrays that conduct heat from the die towards the base of the assembly, which acts as a heat sink. Stable temperature is as important as heat removal for repeatable measurements. In this implementation, the final assembly uses a TEC together with a nearby thermistor, which are operated with the TEC controller to provide a stable operating temperature. This arrangement follows the approach outlined above and will be revisited later in the chapter.

The PCBs were designed to match the standard pad layout defined during the PIC design stage. Each PIC layout follows a convention in which the RF pads are placed along the northern edge of the die, while the DC pads are located along the southern edge. Consequently, the PCB pad pitch, pin assignment, and choice of external connectors were specified to ensure full compatibility with the packaged PICs.

Packaging is often among the most costly stages in commercial PIC production, partly because the limited standardisation of photonic layouts necessitates custom packaging for each die. Efforts have been made to standardise layouts and to automate testing processes that could mitigate this issue, for instance through open-access frameworks [95]. While wire bonding is a mature and widely adopted process in microelectronics, optical packaging remains a major bottleneck and still lacks a well-established set of best practices, although significant efforts are underway to expand and mature open-access packaging pilot lines [94]. The present system does not incorporate fiber attachment for optical packaging, as this would require additional specialised equipment. Instead, the PCBs are designed to be compatible with the V-grooves available in the laboratory.

The PCB layouts were designed using KiCad. Two variants were developed: one supporting both RF and DC connections, and another providing only DC interfaces for PICs without high-frequency pads. The PCBs providing both RF and DC connectivity employ a four-layer stack to ensure proper signal integrity and grounding, whereas the DC-only boards use a simpler two-layer structure. Separate designs were created for the SMART and HHI platforms to accommodate their different chip dimensions. Fig. 4.3 shows a three-dimensional rendering of the SMART boards featuring RF and DC connectivity, illustrating the top, bottom, and complete 3D views. The RF connectors are located on the northern side of the board, and the DC section is on the southern side. The RF area is isolated from the rest of the circuitry by a row of metallised vias forming a grounded fence.

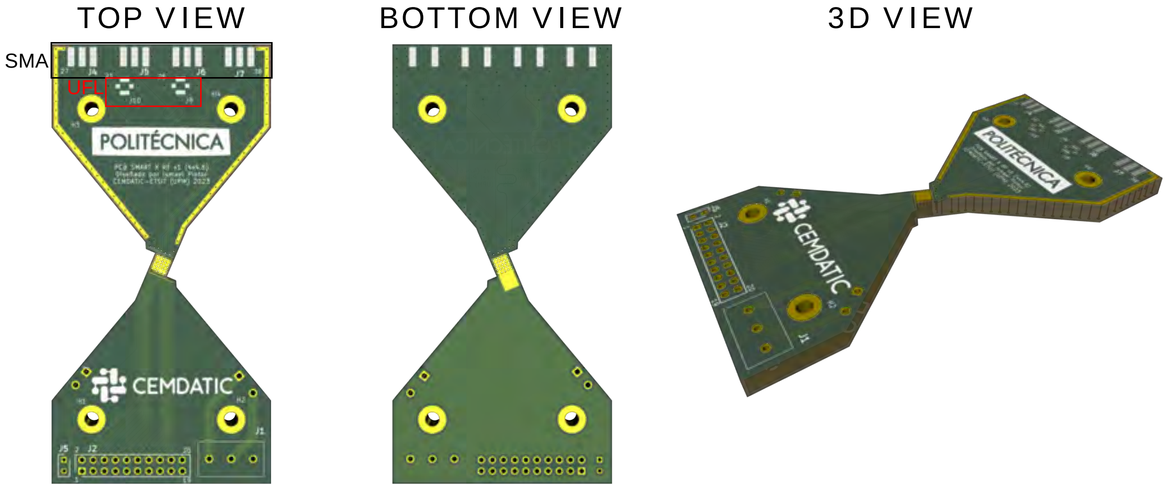

Figure 4.3: Three-dimensional renderings of the PCBs used for electrical packaging of the PIC, shown from different views and featuring RF connections on the north side and DC connections on the south side.

The PIC area is tilted by 23° to align with the angled input and output facets. RF input and output use two connector types: four SMA (Fig. 4.3 top view, J4-J7), which have a usable bandwidth of up to approximately 18 GHz, and two UFL (J9, J10), which have a bandwidth of up to approximately 6 GHz. The RF tracks are implemented as microstrip transmission lines matched to 50 Ω. All RF traces are designed to have equal electrical length in order to maintain consistent phase and impedance conditions across the different inputs. DC access is provided via soldered pin headers (J2), while additional connectors are included for the TEC and the thermistor (J1 and J5, respectively).

Fig. 4.4 shows the die-bonding area and pad distribution of the SMART Photonics PCBs. The HHI boards follow a similar layout, adapted to their different PIC dimensions. With a pad-to-pad spacing of 0.3 mm, the design accommodates twenty DC pads along the lower edge of the PIC area and six RF GSG connections. The central square indicates the bonding

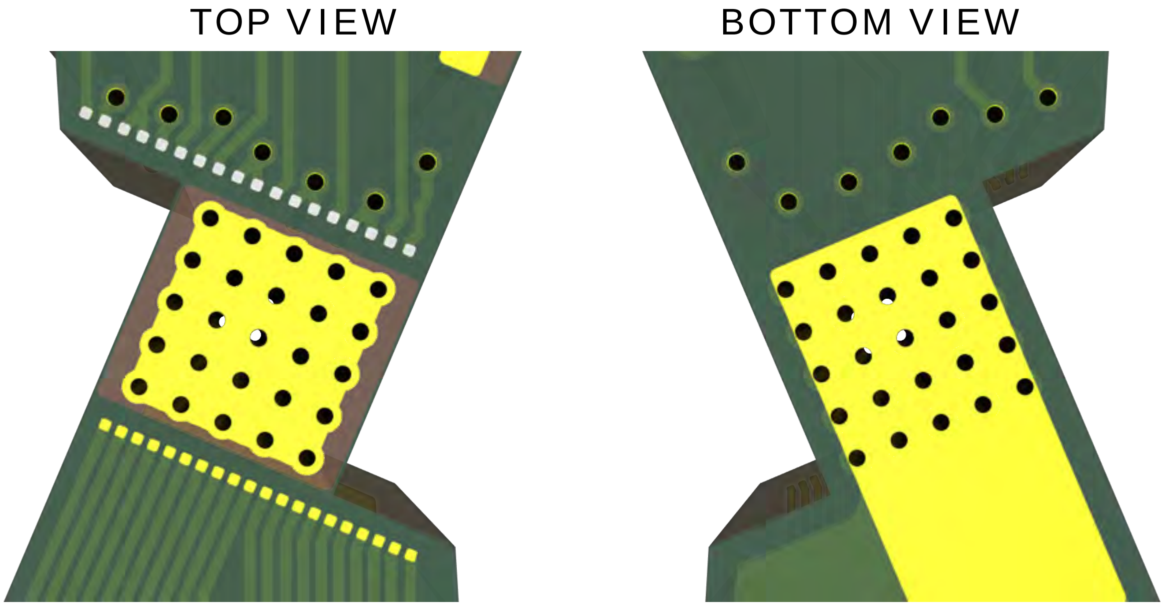

Figure 4.4: Top and bottom views of the PIC bonding area on the PCB, showing the die placement region and the surrounding contact pads.

region where the chip is secured during the die-bonding process. This central zone contains arrays of thermal vias that conduct heat between the front and back layers of the board, thereby enhancing thermal dissipation.

The PCBs were fabricated externally by PCBWay. Each PCB measures 100 × 50 × 1 mm and uses an FR4 substrate with a glass transition temperature T_g of 150 °C. The design employs two electrical layers with a 1 oz copper finish. The ENEPIG (Electroless Nickel Electroless Palladium Immersion Gold) surface finish consists of successive layers of approximately 200 microinches of nickel, 2 microinches of palladium, and 2 microinches of gold. The nickel layer provides a robust diffusion barrier and mechanical support; the palladium layer prevents nickel oxidation, and the thin gold layer ensures good bondability. This multilayer finish offers stable surface properties that enhance the consistency and reliability of wire bonding.

The assembly process comprises three main steps: die attach, wire bonding, and final packaging. Die bonding is performed using a custom setup in which the PIC is held by a vacuum pen, while the PCB is mounted on a manual XYZ stage equipped with linear micropositioners. Prior to placement, both the PCB landing area and the backside of the PIC are cleaned with isopropyl alcohol to remove particulates and light residues. A calibrated micropipette then dispenses a controlled volume of thermally conductive epoxy onto the die-bonding area on the PCB, forming a thin, uniform fillet once the PIC is positioned. The adhesive is selected for its high thermal conductivity, suitable viscosity at the dispensing temperature, and a cure profile compatible with the PIC. Using the micropositioners, the PCB, which is mounted on an XYZ translation stage, is levelled and aligned with the PIC in the lateral plane, that is, along the X and Y directions. Once the alignment is achieved, the stage is slowly raised in the vertical direction to bring the two surfaces into contact. The vias located beneath the PIC region allow any excess epoxy to escape, preventing it from spreading onto the bond pads and optical interfaces.

Curing of the epoxy is carried out according to the specifications of the manufacturer at room temperature for 48 hours, with the assembly being held in place to prevent movement. Electrostatic discharge control is maintained by grounding the work surface, tools, and operator, as well as minimising handling. Finally, the top surface is cleaned and the bond pads are inspected for contamination or oxidation to ensure suitable conditions for the subsequent wire bonding step.

Wire bonding is performed between the PIC and the PCB pads using a TPT HB100 wire bonder. The system operates by ultrasonic bonding and includes a heated stage to improve bond quality and adhesion. It supports both wedge and ball bonding techniques through interchangeable capillaries. Ball bonding is preferred, as it produces a uniform initial bond on the PIC pad and a reliable wedge stitch on the PCB pad. A 17 μm gold wire is employed, since gold promotes excellent adhesion between the ENEPIG surface finish of the PCB and the gold metallisation of the PIC. The small wire diameter also enables the formation of compact bond balls that remain confined within the on-chip pad area (100 $\times$ 100 μm). The free-air ball is generated by an electronic flame-off system at the tip of the capillary.

The optimisation of wire bonding comprises several parameters:

- **Temperature:** Higher substrate temperature tends to reduce the ultrasonic power required for bonding and can minimise pad damage. However, excessive heat may soften the epoxy resin or affect the devices. A typical operating temperature of 100 °C is used for this process.
- **Ultrasonic power:** This parameter controls the scrubbing energy at the bonding interface. Insufficient power results in weak bonds that often do not adhere to the pad. Excessive power, on the other hand, can produce craters in the pads or cause pad splash on thin metallisations. Optimisation involves gradually increasing the ultrasonic power until the ball deformation and imprint are uniform and non-destructive in pull tests. Dedicated dummy pads are included on the PIC and PCB to facilitate initial optimisation. Power is measured in mW, with typical operating values for this system ranging from 200 to 270 mW.
- **Force:** This parameter refers to the force applied to press the wire against the pad during bonding. Insufficient force can result in poor contact and potential bond lift-off, while excessive force may damage or create craters on the pad surface. The bonding force is optimised alongside ultrasonic power and bonding time, as these parameters are interdependent. It is specified in millinewtons (mN), with typical operating values of around 300 mN for this process.
- **Time:** This parameter refers to the duration for which ultrasonic energy and bonding force are applied. A longer bonding time can compensate for slightly lower power or cooler conditions, but it also increases the risk of pad damage. The first and second bonds may require different durations. In practice, bonding time is often kept constant while power and force are optimised first and then adjusted as necessary. Typical operating values are around 200 ms.

- **Loop profile:** This parameter defines the three-dimensional shape of the wire between the first and second bonds, determined by the programmed path of the capillary. Optimising the loop profile enhances the mechanical stability of the interconnect and improves long-term bond reliability. The loop shape is also adjusted to compensate for the height difference between the PCB and the PIC.

Additional settings recorded during optimisation include the tail length after the second bond, from which the ball for the next bonding is formed, the capillary approach speed, and the search height. Consistency in tail length is important for achieving a repeatable ball size.

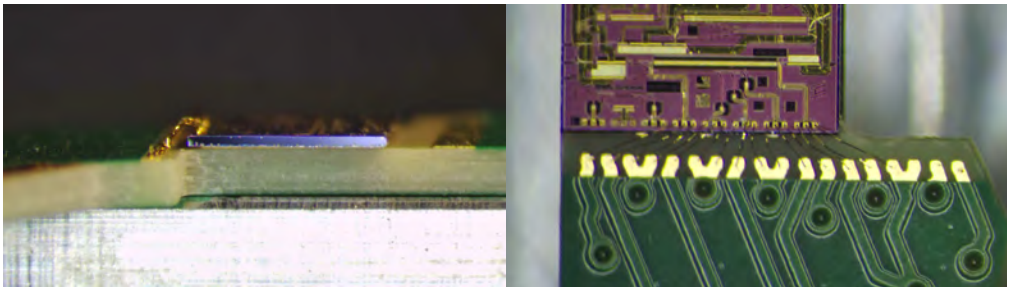
(a) (b)

Figure 4.5: (a) Lateral photograph showing the wire bonds connecting the PIC to the PCB, and (b) top view highlighting the wire bonds contacting the on-chip pads and the RF pads of the custom-designed PCB.

The choice of capillary is matched to the wire diameter and the pad pitch, enabling the tool to place bonds without scuffing adjacent pads. Parasitic inductance and crosstalk are further reduced by keeping the bonds short. The average length of the wirebonds is always kept below 1 mm. Each bonding session begins with tests on dummy or sacrificial pads at the end of the pad row to adjust the parameters. Visual criteria and electrical checks, including continuity and VNA measurements (if applicable for RF connections), are performed. As a result, the wirebonds are effectively providing connection between the PIC and the PCB, as shown in Fig. 4.5.

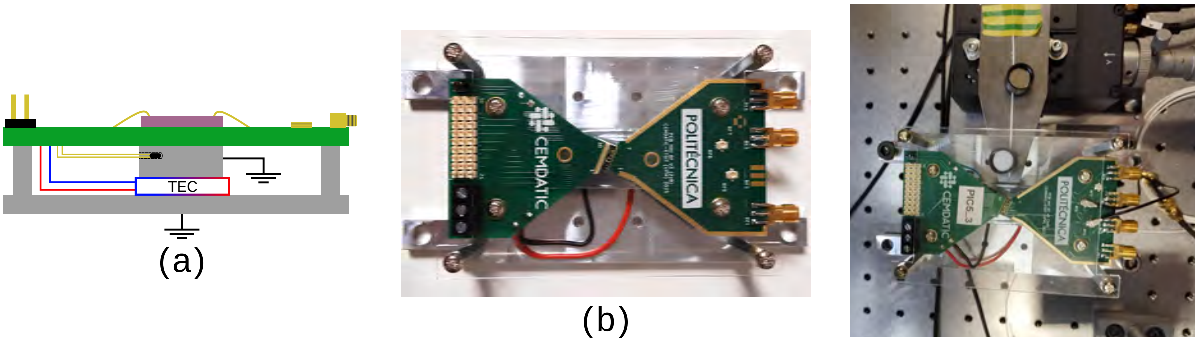

(a) (b) (c)

Figure 4.6: (a) Schematic of the final assembly. (b) Photograph of the final assembly from a top view. (c) Photograph of the experimental setup showing the PIC in the final assembly.

The final step involves mounting the PCB containing the PIC into its package for testing. The fully assembled device is schematically illustrated in Fig. 4.6(a) and shown in Fig. 4.6(b). The package comprises an aluminium 6082 (Al–Si1Mg) base plate and mounting block. This alloy exhibits a thermal conductivity between 170 and 220 $\mathrm{W\,m^{-1}\,K^{-1}}$ and a specific heat capacity of approximately 896 $\mathrm{J\,kg^{-1}\,K^{-1}}$. The PCB is secured to the metal base using PCB spacers. A TEC, positioned between the base plate and the mounting block, regulates the temperature of the assembly, while the upper surface of the mounting block contacts the underside of the PCB to provide efficient heat dissipation. The temperature is monitored using a thermistor embedded in the mounting block. Finally, a transparent methacrylate cover protects the assembly. Electrical connectors are soldered to provide access to the PIC contacts, the TEC, and the thermistor. The final assembly can be characterised as shown in Fig. 4.6(c).

Chapter 5

Integrated optical frequency comb generation

This chapter investigates the generation of OFCs on PICs using both Q-switching and GS, combining rate-equation modelling, numerical simulation and proof-of-concept experiments. In Section 5.1, a QS model is developed and applied to an optically injected four-section DBR laser incorporating an intracavity EAM. The analysis identifies design trade-offs in extinction ratio, insertion loss, length and detuning, and predicts broadband combs arising from the large dynamic chirp associated with rapid loss modulation. An initial InP implementation through an MPW, embedding the EAM within the cavity, was limited by excessive EAM absorption and insufficient net gain, preventing lasing and thus QS operation, but providing clear guidance for subsequent redesign. Part of these results were originally reported in López-Querol *et al.*, *Optics Express*, 31, 20, 33475–33485, (2023).

Section 5.2 then demonstrates GS OFCs in a monolithically integrated master–slave configuration employing DFB lasers, driven by a SRD generating short electrical pulses. This approach achieves reconfigurable combs with repetition rates from 5 GHz down to 500 MHz, offering good CNR and acceptable flatness. Practical limitations arise from strong mutual coupling in the absence of on-chip isolators, compound-cavity effects, detuning sensitivity and finite DFB linewidth, motivating an alternative approach based on optically injected SRLs described in Section 5.3. The SRL configuration enforces unidirectional emission and suppresses feedback to the ML. This provides a robust basis for achieving the stability required in integrated dual-comb interferometers.

5.1 Optically injected Q-switched lasers

This section presents a theoretical analysis, supported by simulations, of OFC generation by active QS of an optically injected multisection DBR laser via intracavity loss modulation. The DBR laser design is compatible with open-access foundries, and all simulation parameters are chosen to reflect realistic device behaviour. QS is implemented by inserting an EAM inside the cavity of the laser and driven with a pulsed electrical waveform to control the cavity losses, so that lasing occurs only during a brief time window and produces high-intensity short optical pulses. The EAM parameters and characteristics are taken from experimentally measured devices fabricated in the SMART Photonics foundry, as reported in [234]. The results show flat combs comprising 2,100 lines within a 10 dB envelope, equivalent to an optical bandwidth of 210 GHz, at a 100 MHz repetition rate. In contrast to typical GS OFCs, the enhanced pulse chirp broadens the optical spectrum, providing wider spectral coverage without the need for additional instrumentation and preserving high spectral resolution. This, in turn, would allow broader spectral sampling using integrated OFCs implemented in commercial foundries with standard BBs. Several Q-switched lasers based on this approach have been fabricated on a SMART Photonics MPW run to study experimental comb generation, and the corresponding results are reported in the following sections.

Theoretical model

QS is a well-established method for generating short, high-peak-power pulses, classically in solid-state and fiber lasers, by modulating the resonator losses (the cavity quality factor Q). During the high-loss time interval ('off'), energy accumulates in the gain medium. When the losses are rapidly reduced, that stored energy is released in a brief and intense pulse. The technique has been applied to semiconductor lasers since the earliest laser diode studies [235], and comprehensive reviews from the 1980s–1990s summarise the key theoretical and experimental advances [155]. Historically, the aims were either to obtain short pulses with large peak power or to realise high-speed intensity modulation for telecommunications.

The operating principle of QS is illustrated in Fig. 5.1. We consider a single-mode DBR laser that incorporates an intracavity EAM. Short pulses are applied to the EAM so that, within each repetition period T_r, the modulator is nearly transparent (low losses) for a time window of duration w_{pulse}, while it is strongly absorbing (high losses) for the remainder. Consequently, the photon lifetime, τ_{ph}, is large during the 'on' time intervals and small during the off intervals, as shown in Fig. 5.1 (a). The device operates at a constant bias current set between the lasing thresholds of the high- and low-loss states ($I_{\mathrm{th,OFF}}$ and $I_{\mathrm{th,ON}}$), enabling emission when the state is switched. During the off state, stimulated recombination is negligible and carriers accumulate, reaching a steady-state density that is much greater than the low-loss threshold density (see Fig. 5.1 (c)). When the EAM switches to the low-loss state (point A in Fig. 5.1), the net gain suddenly exceeds the losses, causing the intracavity photon number to rise with a time constant set by the photon lifetime (Fig. 5.1 (b)). The growing photon population depletes the carriers. If the on state were sufficiently long, further spikes of relaxation oscillations would appear. However, by reverting to the high-loss state before the second relaxation spike, the gain falls below the losses again, the photon number collapses and a short, high-power optical pulse is emitted. During the subsequent off state,

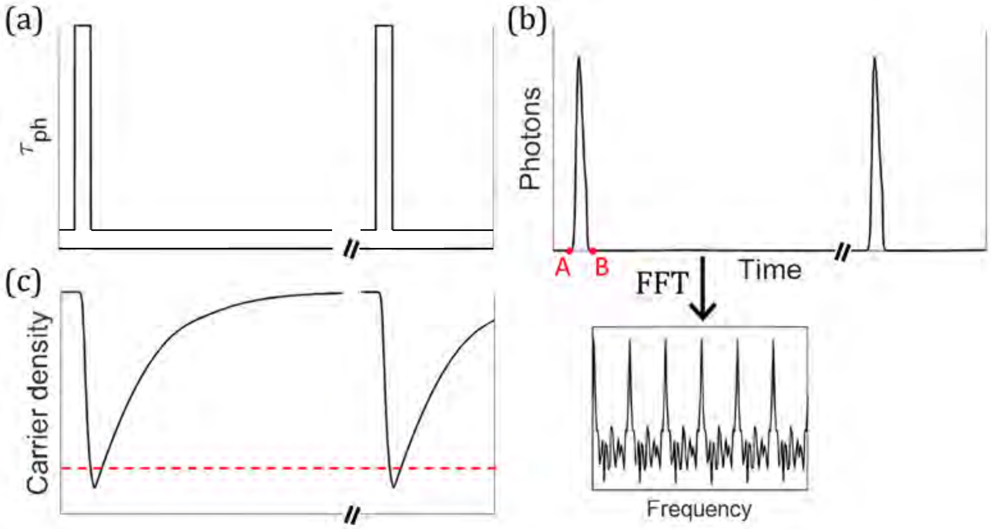

Figure 5.1: Principle of pulse generation in semiconductor lasers by QS. (a) Evolution of the photon lifetime, (b) photon density and (c) carrier density as a function of time. The losses of the cavity are modulated through an EAM between a low value during a short time and a high value for the rest of the repetition period. The laser is driven with a constant bias below the theshold current in the high losses condition. When the losses are switched to a low value, the accumulated carriers rapidly recombine by stimulated emission giving rise to a short optical pulse.

the carrier density recovers towards its high value, ready for the next cycle. If emission were fully extinguished between successive pulses, each pulse would originate from spontaneous emission, resulting in a noisy spectrum, an outcome familiar from GS lasers. However, with OI from a ML, phase coherence is maintained from pulse to pulse, producing an OFC, as illustrated in Fig. 5.1 (d).

Although the practical implementation of QS in a semiconductor laser is similar to GS, there are also key distinctions. In GS, pulse build-up begins once the gain just exceeds the losses. In QS, however, the transition drives the gain well above the instantaneous losses, resulting in faster growth and correspondingly shorter pulses. This rapid build-up also causes significant carrier depletion, resulting in an increased refractive index swing and pronounced dynamic chirp. As will be seen later, this broadens the resulting spectrum. This process depends on sufficient carrier recovery between pulses, which in turn requires a relatively long off time, the minimum of which is ultimately set by the carrier lifetime. Consequently, Q-switched OFC generation is better suited for relatively low repetition rates (up to a few hundred MHz), as the carriers cannot recover sufficiently between pulses at GHz rates. For the same reason, switching using electrical pulses is more appropriate than using sinusoidal signals, similar to what happens in GS at low repetition frequencies [236].

The principle of Q-switching can be best understood by analysing the dynamic response of a single-mode semiconductor laser. This response can be described by a standard set of single-mode rate equations governing the evolution of the carrier density in the active region ($N(t)$), the intracavity photon density ($S(t)$), and the optical phase ($\Phi(t)$) [115], [155], assuming spatial uniformity along the cavity. The model employed here is as follows:

$$\frac{dN(t)}{dt} = \frac{I(t)}{eV_{act}} - [R_{sp}(N) + R_{nr}(N)] - \frac{v_g g(N)S(t)}{1+\varepsilon S(t)} + F_N(t), \tag{5.1}$$

$$\frac{dS(t)}{dt} = \left[\frac{\Gamma v_g g(N)}{1+\varepsilon S(t)} - \frac{1}{\tau_{ph}(t)}\right] S(t) + \Gamma\beta_{sp}R_{sp}(N) + F_S(t), \tag{5.2}$$

$$\frac{d\phi(t)}{dt} = \frac{\alpha}{2}\left[\Gamma v_g g(N) - \frac{1}{\tau_{ph}}\right] + F_\Phi(t). \tag{5.3}$$

Here, $I(t)$ is the injected current; e the electron charge; V_{act} the active-region volume; $R_{sp}(N)$ and $R_{nr}(N)$ the spontaneous and non-radiative recombination rates; v_g the group velocity; $g(N)$ the material gain; ε the nonlinear gain-compression coefficient accounting for gain saturation at high photon densities; τ_{ph} the photon lifetime; β_{sp} the fraction of spontaneous emission coupled into the lasing mode; $\Gamma = \Gamma_y \cdot \Gamma_z$ the modal confinement factor in the active region, with Γ_y the vertical and Γ_z the longitudinal contribution, respectively; and α the linewidth-enhancement factor. The Langevin terms $F_N(t)$, $F_S(t)$, and $F_\Phi(t)$ represent additional stochastic noises from different sources. However, additional terms accounting for emission frequency variations induced by temperature changes have not been included. The reader is referred to [156] for further details on the model and on these additional terms.

Eq. (5.1) describes the carrier density dynamics. The first term generates carriers via the drive current ($I(t)$). The second term removes carriers through recombination processes, including both radiative (spontaneous emission) and non-radiative recombination. Finally, the third term accounts for stimulated recombination that is proportional to the intracavity photon density. Here $R_{sp}(N)$ denotes radiative band to band recombination (conduction band to valence band), which generates spontaneous photons. On the other hand, $R_{nr}(N)$ accounts for recombination processes that do not contribute to photon emission, such as recombination at defects, surfaces, and Auger processes. For compact analysis, these contributions are often linearised [79] with respect to the carrier density by means of the carrier lifetime τ_c, as $R_{sp} + R_{nr} = N/\tau_c$. The non-linear ABC model is used to provide a more detailed description, following

$$R_{sp} + R_{nr} = AN + BN^2 + CN^3, \tag{5.4}$$

where A represents the Shockley–Read–Hall (SRH) and surface recombination, B is the bimolecular radiative term, and C accounts for the Auger recombination. Thus, $R_{sp} \sim BN^2$ and $R_{nr} \sim (AN + CN^3)$.

Eq. (5.2) describes the evolution of the photon density in the active region. The first term in brackets represents the net change in photon density, including its growth by stimulated emission and its reduction due to cavity losses characterised by the photon lifetime $\tau_{ph}(t)$. The second term represents spontaneous emission coupled into the lasing mode. The decay rate of the photon density is expressed by τ_{ph}, which is given by

$$\tau_{ph}(t) = \frac{1}{v_g \alpha_T} = \frac{1}{\langle \alpha_i \rangle + \alpha_m + \alpha_{EAM}(t)} \tag{5.5}$$

with α_{T} represents the total cavity loss, v_g is the group velocity, $\langle \alpha_i \rangle$ the internal (distributed) loss, α_m the mirror loss and $\alpha_{\mathrm{EAM}}(t)$ the time-varying loss introduced by the intracavity EAM during Q-switching. It must be noted that this term introduces a time-dependency in the photon lifetime.

A linear dependence on the carrier density is considered for the material gain $g(N)$, given by

$$g(N) = \frac{dg}{dN}(N - N_{tr}), \tag{5.6}$$

with dg/dN and N_{tr} being the differential gain and the transparency carrier density.

Finally, Eq. (5.3) describes the evolution of the optical phase. Changes in carrier density affect both the material gain and the refractive index, the latter being responsible for the frequency chirp. This coupling between gain and phase is parameterised by the linewidth-enhancement factor α, which quantifies how index changes accompany gain changes expressed as $\alpha = -(4/\lambda)dn/dg$. In the single-mode rate equation model, this leads to an optical phase proportional to the net modal gain. This causes the frequency chirp $\Delta\nu$, which can be written proportionally to the emitted optical power as

$$\Delta\nu(t) = \frac{1}{2\pi}\frac{d\Phi(t)}{dt} = \frac{\alpha}{4\pi}\left(\frac{1}{P(t)}\frac{\mathrm{d}P(t)}{\mathrm{d}t} + \frac{2\,\Gamma\,\varepsilon}{V_{\mathrm{act}}\eta_d h\nu_0}\,P(t)\right) \tag{5.7}$$

where η_d is the differential quantum efficiency, h is the Planck constant, and the single-facet emitted optical power $P(t)$ is given by

$$P(t) = \eta_d \frac{h\nu_0 V_{act}}{2\Gamma \tau_{ph}(t)} S(t), \tag{5.8}$$

where ν_0 is the emission frequency.

The first term in Eq. (5.7) represents the dynamic (transient) chirp, which originates from rapid intensity variations caused by carrier fluctuations during transients. The second term, proportional to $P(t)$, corresponds to the adiabatic chirp that remains under steady-state operation. It arises from gain saturation (via ε) and reflects the steady-state component of the amplitude–phase coupling described by α. An additional adiabatic contribution due to thermal changes in the refractive index, not included in this formulation, is discussed in [156].

In both GS and QS operation, the optical pulses are dominated by dynamic chirp, as the laser does not reach a steady state between consecutive pulses. Since the chirp is intrinsically linked to direct modulation through the linewidth enhancement factor α, the emitted pulses deviate from the Fourier-transform-limited spectrum. Stronger dynamic chirp broadens the optical spectrum and increases the bandwidth of both GS and QS frequency combs [156], [237], [238]. In QS operation, the abrupt modulation of intracavity losses drives the gain well above the loss threshold, leading to a very large dynamic chirp. As a result, Q-switched pulses can exhibit spectral broadening comparable to, or even exceeding, that achieved through GS.

To include the OI terms that provide pulse-to-pulse coherence, the rate-equation model is extended to account for the injected field and for time-dependent cavity losses through the photon lifetime $\tau_{\text{ph}}(t)$. It should be noted that the bias current I is constant in this case, as in Q-switching, it remains within the range between $I_{\text{th}-\text{ON}}$ and $I_{\text{th}-\text{OFF}}$.

$$\frac{dN(t)}{dt} = \frac{I}{eV_{act}} - [R_{sp}(N) + R_{nr}(N)] - \frac{v_g g(N) S(t)}{1 + \varepsilon S(t)} + F_N(t) \tag{5.9}$$

$$\frac{dS(t)}{dt} = \left[\frac{\Gamma v_g g(N)}{1 + \varepsilon S(t)} - \frac{1}{\tau_{ph}(t)}\right] S(t) + \Gamma \beta_{sp} B N^2(t) + Y_S(t) + F_S(t), \tag{5.10}$$

$$\frac{d\phi(t)}{dt} = \frac{\alpha}{2}\left[\Gamma v_g g(N) - \frac{1}{\tau_{ph-ON}}\right] + Y_\Phi(t) + F_\Phi(t). \tag{5.11}$$

where $Y_S(t)$ and $Y_\Phi(t)$ are the terms describing the OI expressed as

$$Y_S(t) = 2k_c \sqrt{S(t) S_{inj}} \cos(\Phi(t) - \Phi_{inj}(t) - 2\pi\delta\nu t), \tag{5.12}$$

$$Y_S(t) = 2k_c \sqrt{\frac{S_{inj}(t)}{S(t)}} \sin(\Phi(t) - \Phi_{inj}(t) - 2\pi\delta\nu t), \tag{5.13}$$

where $S_{inj}(t)$ and $\Phi_{inj}(t)$ are the photon density and the phase of the injecting laser, k_c the master-slave coupling coefficient, and $\delta\nu$ is the detuning of the injected laser field with respect to the frequency of the SL at threshold. It must be noted that while $\tau_{ph}(t)$ in Eq. (5.10) has a time dependency as a result of the loss modulation, it is constant in Eq. (5.11) and corresponds to the on state. This is because the term in brackets on the right-hand side of the equation represents the difference between the instantaneous carrier density and the threshold carrier density in the on state [239]. It should be noted that the same set of equations can also describe GS operation under OI by setting the photon lifetime to a constant value (i.e. without loss modulation) and driving the bias current with a sinusoidal or pulsed waveform.

Theoretical results

The scheme of the multisection laser under consideration under QS operation with a scheme of its integration on a PIC, are shown in Fig. 5.2. External OI is performed using a circulator to enable simultaneous injection and measurement, while a PC is used to maximise coupling into the TE mode. The Q-switched laser consists of a four-section DBR laser similar to those fabricated in open-access foundries [240], [241] but with an additional intracavity EAM section. It consists of a rear DBR, a SOA, a EAM section, and a front DBR with lengths L_{RDBR}, L_{SOA}, L_{EAM}, and L_{FDBR}, respectively.

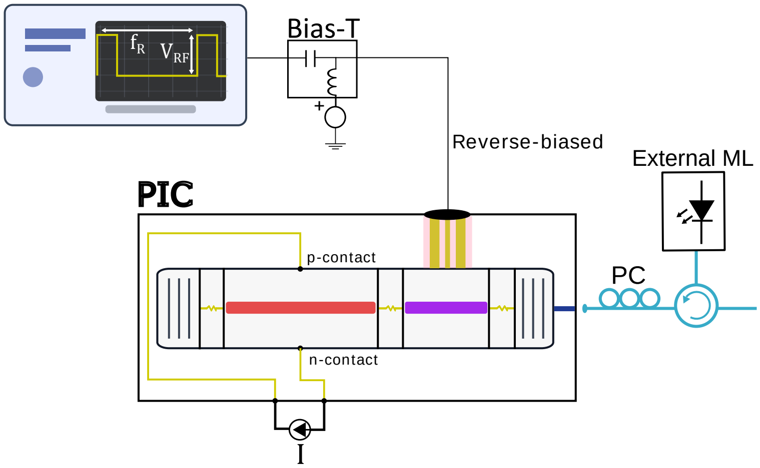

Figure 5.2: Implementation of a Q-switched three-section DBR laser on a PIC. The different sections are separated by electrical isolators, allowing independent biasing and electrical isolation of the individual elements. The EAM features a GSG RF track to enable high speed modulation. It is reverse-biased by a DC signal providing the bias point and a RF signal provided by an RF generator modulating the intracavity losses at f_r. The active section of the laser is an SOA biased at a current I. External optical injection is depicted for clarity and simplicity. PIC: Photonic integrated circuit; ML: Master laser; PC: Polarisation controller.

Making use of the effective length approximation [115] the laser can be analysed as a FP laser with two mirrors of effective reflectivities R'_{F} and R'_{R} placed at effective lengths $L_{eff\mathrm{R}}$ and $L_{eff\mathrm{F}}$, respectively. Then the total cavity length L_{T} is given by the addition of the SOA and EAM section lengths, the two DBR effective lengths, and three times the length of the electrical isolation region (L_{ISO}) between sections. These isolation sections are necessary in practical integrated laser implementations to isolate electrically each active section. A simple analysis of the round-trip condition shows that α_{T} in Eq. (5.5) can be expressed as

$$\alpha_{\mathrm{T}} = \langle \alpha_i \rangle + \frac{1}{L_{\mathrm{T}}} \ln\left(\frac{1}{R'_{\mathrm{F}} R'_{\mathrm{R}}}\right) + \frac{1}{L_{\mathrm{T}}} \ln\left(\frac{1}{T_{\mathrm{EAM}}(t)}\right) \tag{5.14}$$

where $T_{\mathrm{EAM}}(t)$ denotes the EAM, controlled by the reverse-bias RF signal. This transmittance is what is modulated between two values, the on and off state.

Therefore, the photon lifetime over one period T_r is

$$\tau_{ph}(t) = \frac{1}{v_g \alpha_{\mathrm{T}}(t)} = \begin{cases} \tau_{ph-\mathrm{ON}} & \text{for} \quad 0 < t < w_{pulse} \\ \tau_{ph-\mathrm{OFF}} & \text{for} \quad w_{pulse} < t < T_r \end{cases} \tag{5.15}$$

It is convenient to represent the photon lifetime in QS operation as a periodic modulation of τ_{ph} with a modulation factor given by

$$m = \frac{\tau_{ph-\mathrm{OFF}}}{\tau_{ph-\mathrm{ON}}} = \frac{\alpha_{\mathrm{ON}}}{\alpha_{\mathrm{ON}} + \frac{1}{L_{\mathrm{T}}} \ln\left(\frac{T_{\mathrm{ON}}}{T_{\mathrm{OFF}}}\right)} \tag{5.16}$$

where α_{ON} represents the total losses during the on state, and T_{ON} and T_{OFF} are the EAM transmittances in the on and off states, respectively. Thus, the extinction ratio (ER) is defined as ER $= T_{\mathrm{OFF}}/T_{\mathrm{ON}}$. Minimising m, (equivalently maximising ER) increases the gain–loss contrast between the on and off states, which translates directly into a stronger modulation of the photon lifetime and, consequently, a larger carrier excursion and enhanced dynamic chirp. Since the threshold current scales with total cavity loss, a small m leads to $I_{\mathrm{th-OFF}} \gg I_{\mathrm{th-ON}}$. If the laser bias current is set below $I_{\mathrm{th-OFF}}$, lasing does not occur and carriers accumulate. When the cavity switches to the on state, the threshold decreases and the carrier density undergoes a large excursion from its accumulated value down to the threshold carrier density in the on state, $N_{\mathrm{th,ON}}$, driving a rapid pulse build-up and a strong chirp. The larger this contrast, the greater the resulting chirp and, consequently, the broader the optical spectrum.

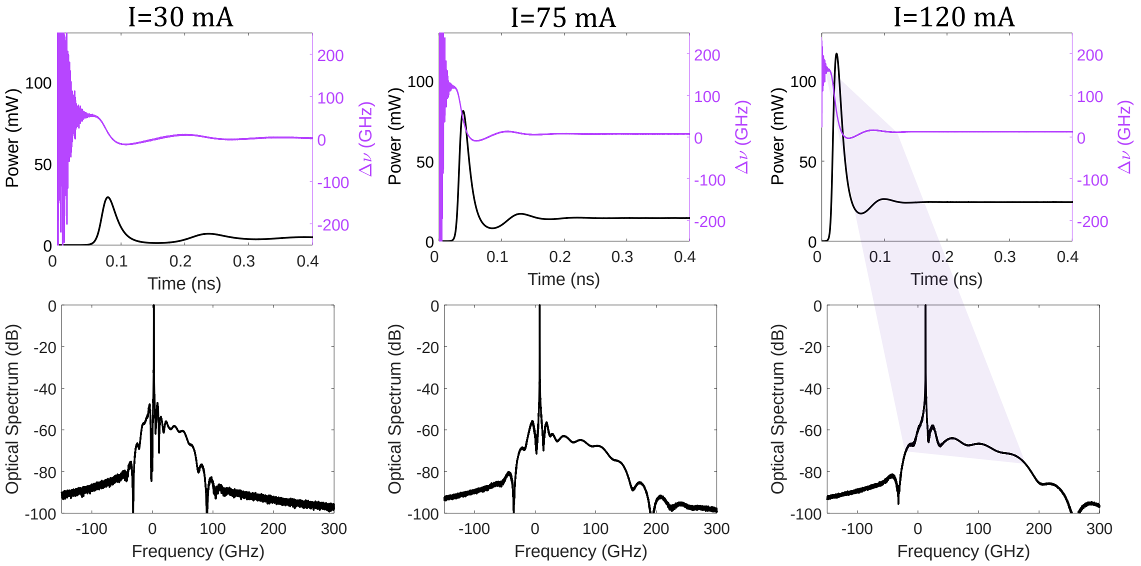

(a) (b) (c)

Figure 5.3: Spectral broadening and increased peak power of the optical signal emitted by the QS laser due to the increased dynamic chirp within the short optical pulse. The dynamic chirp increases with increasing currents for (a) $I = 30$ mA, (b) $I = 75$ mA and (c) $I = 120$ mA.

This is illustrated in Fig. 5.3, which shows the simulated laser turn-on response when the losses are switched from high to low with zero rise time for $m = 0.29$. Three different currents ((a) 30 mA, (b) 75 mA, and (c) 120 mA) are shown, chosen below $I_{\text{th}-\text{OFF}}$ (and above $I_{\text{th}-\text{ON}}$). As the bias increases, the carrier reservoir prior to switching is larger, leading to a larger carrier excursion at turn-on and consequently increased chirp, higher peak power, and wider spectra. The top panel shows the emitted power with the chirp calculated as in Eq. (5.7). Before the turn-on process begins, phase noise dominates and the chirp exhibits strong fluctuations. The bottom panel shows the emitted spectra, obtained by applying a Fast Fourier Transform (FFT) to the simulated complex optical field, with 0 Hz corresponding to the emission frequency of the laser at threshold, and normalised to the maximum power (0 dB).

To obtain these and the subsequent results, Eqs. (5.9) to (5.11) were integrated in MATLAB using a numerical Heun's algorithm for stochastic differential equations (SDEs). Material parameters follow the ones extracted for a high-speed 1.5 μm laser in [156], and are summarised in Table 5.1. For the other parameters, a standard DBR coupling coefficient $\kappa = 50\,cm^{-1}$ is assumed, and an SOA length $L_{\text{SOA}} = 500\,\mu$m similar to that of a previous experimental design in [242], giving $V_{act} = 7.65 \cdot 10^{-18}\,\text{m}^3$. We use a typical internal distributed loss for active and passive sections of $\langle \alpha_{\text{in}} \rangle = 25, \text{cm}^{-1}$ [243], on-state insertion losses of $T_{\text{ON}} = -2.3$ dB, and an extinction ratio of ER = 35 dB for an EAM length of 250, μm and a detuning of 55 nm from the SOA gain peak, consistent with the values reported in [234], where SMART Photonics EAMs are characterised.

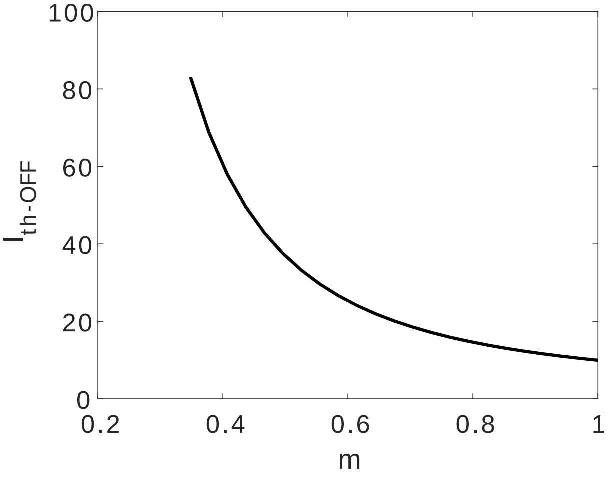

Figure 5.4: Threshold current in the off state as a function of the modulation index m.

Parameter	Value	Units
Γ_y	0.06	–
$\frac{dg}{dN}$	4.38×10^{-20}	m^2
α	3	–
ε	1.97×10^{-23}	m^3
N_{tr}	1.3×10^{24}	m^{-3}
A	2.8×10^{8}	s^{-1}
B	1.5×10^{-16}	m^3s^{-1}
C	9×10^{-41}	m^6s^{-1}
β	5.3×10^{-6}	–

Table 5.1: Material parameters of the simulated semiconductor laser, similar to those reported in [156].

A practical trade-off exists between maximising ER (minimising m) and keeping α_{ON} low, as higher extinction ratios generally entail increased insertion losses. Maintaining a low α_{ON} is desirable since it gives lower $I_{\text{th}-\text{ON}}$ and thus higher chirp. This balance is controlled through the wavelength detuning of the EAM relative to the lasing wavelength and the length of the device. Taking this into account, the DBR lengths were optimised to make $m = 0.29$ while keeping $I_{\text{th}-\text{ON}} = 9.2$ mA. The selected values were $L_{\text{RDBR}} = 250\,\mu$m and $L_{\text{FDBR}} = 100\,\mu$m, leading to a total cavity length of 971 μm (with $L_{\text{ISO}} = 30\,\mu$m), $\tau_{ph-\text{ON}} = 3.46$ ps.

Figure Fig. 5.4 shows the dependence of $I_{\text{th}-\text{OFF}}$ computed in steady state without optical injection by solving Eqs. (5.9) and (5.10) using the parameters of Table 5.1 and setting τ_{ph} to the value corresponding to each m. For $m = 0.29$, a drive current as high as 130 mA remains below $I_{\text{th}-\text{OFF}}$, thus maximising the carrier density in the off state.

These results provide the operating range within which the laser can be driven for QS. Employing these, we have simulated OFC generation under QS and OI. To do this, two systems of rate equations are solved: the first for the QS SL, as defined by Eqs. (5.9) to (5.11), and the second for the ML, as defined by Eqs. (5.1) to (5.3).

The OFCs generated by QS and OI with a repetition rate of 100 MHz while varying the bias current are shown in Fig. 5.5. The simulation time step was set to 34.6 fs. In each case, the OI frequency was adjusted to ensure injection locking and thus guarantee comb coherence. The injected power was fixed at 5 dBm with a coupling coefficient of $k_c = 3.5 \cdot 10^{10}\, s^{-1}$, corresponding to an effective injected power of $P_{inj} = 4.62$ dBm. Both the injection power and the detuning were optimised for each case to achieve stable locking of the SL. Fig. 5.5 shows the simulated OFCs for different bias currents with a pulse width of $w_{pulse} = 30$ ps. The choice of this value will be discussed later.

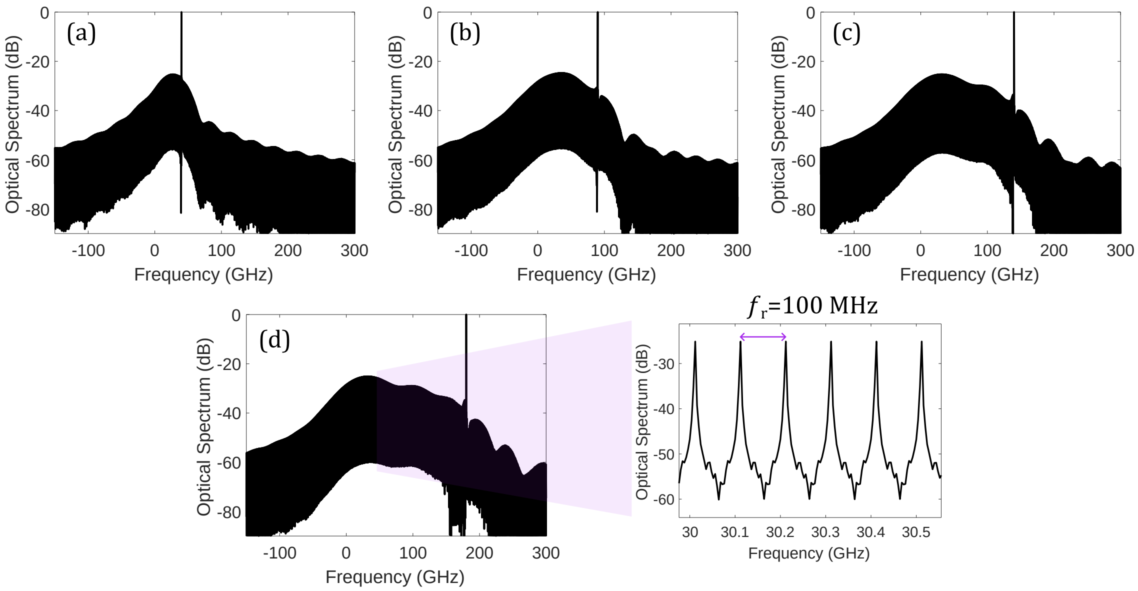

Figure 5.5: Simulated optical spectra for different bias and detuning for (a) $I = 20$ mA, $\delta\nu = 40$ GHz, (b) $I = 50$ mA, $\delta\nu = 90$ GHz, (c) $I = 80$ mA, $\delta\nu = 140$ GHz and (d) $I = 120$ mA, $\delta\nu = 180$ GHz. The pulse duration has been set to $w_{pulse} = 30$ ps. A zoomed region of the spectrum shown in (d) is also included, where the comb lines can be resolved.

At low bias current ($I = 20$ mA), the comb spans $\Delta f_{10\text{dB}} = 70$ GHz with CNR = 27 dB and a flatness of 0.8 (Fig. 5.5 (a)). The strongest peak corresponds to the optical injection, while the reference frequency (0 GHz) is set by the unmodulated laser emission at threshold ($I_{\text{th}-\text{ON}}$). As the bias current increases (Fig. 5.5 (b)-(d)), the comb bandwidth expands while both the CNR and flatness remain nearly constant. The widest comb is obtained at the highest bias tested, $I = 120$ mA (Fig. 5.5 (d)), with $\Delta f_{10\mathrm{dB}} = 202$ GHz, CNR = 27 dB, a flatness of 0.77, and an average optical power per line of -29.82 dBm. The inset in Fig. 5.5(d) shows a zoomed portion of the spectrum for this case, where the comb lines are clearly resolved with a spacing of 100 MHz, set by the repetition frequency.

The evolution of the comb width $\Delta f_{10\mathrm{dB}}$ as a function of the bias current is shown in Fig. 5.6, exhibiting an almost linear trend due to the linear dependence of chirp with α and the higher carrier excursion. This behaviour is explained by the carrier dynamics in Fig. 5.1(c): as I increases, the carrier density at the end of the off state rises. During the on state, sharper depletion of carriers takes place. The resulting larger carrier excursion within the pulse produces larger chirp, and therefore a broader optical spectrum. This high chirp is the origin of a broader optical spectrum compared to the case of GS, where the carrier variation during the pulse is not as abrupt.

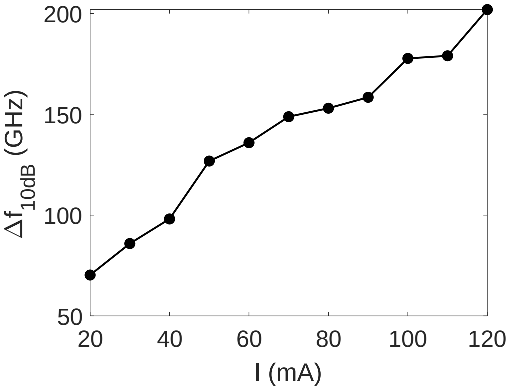

Figure 5.6: Spectral width at 10 dB of the OFCs $\Delta f_{10\mathrm{dB}}$ as a function of the bias current I.

To further contextualise the QS results, we compare pulses and combs against GS under similar driving conditions. We solved the same rate-equation model for GS with pulsed current drive (constant losses), using the same laser parameters and comparable settings, except that GS requires a wider electrical pulse (100 ps against 30 ps). These equations correspond to Eqs. (5.9) to (5.11), but with time varying current and fixed $\tau_{ph} = \tau_{ph-\mathrm{ON}}$. Fig. 5.7(a) contrasts the pulse intensity and chirp for the QS case of Fig. 5.5(d) with the GS case in Fig. 5.7(b).

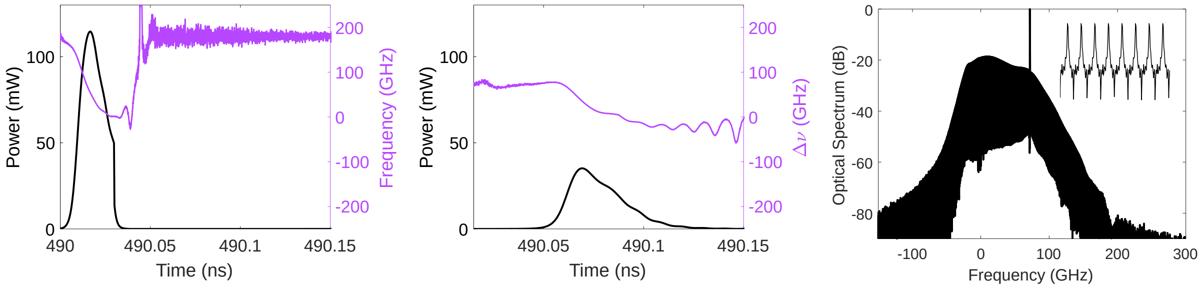

(a) (b) (c)

Figure 5.7: Comparison between the simulated optical pulses and chirp generated by (a) QS and (b) GS using similar driving conditions. (c) Simulated OFC corresponding to the GS case.

The Q-switched pulse builds up significantly faster and reaches a higher peak power, and the chirp excursion within the pulse is also larger. The GS spectrum (Fig. 5.7(c)) shows $\Delta f_{10\text{dB}} \approx 94$ GHz, CNR ≈ 27 dB, and flatness of 0.86. The detuning was $\delta\nu = 71$ GHz. Comparing with QS (Fig. 5.5(d)) the QS OFC is much wider at 10 dB, and even more at 20 dB (202 GHz vs 113 GHz), whereas the GS comb is flatter. The pronounced ripples on the high-frequency side of the QS envelope, absent in GS, are attributed to the fast decay of the optical pulse in the case of QS (see Fig. 5.7(a)), which resembles a rectangular pulse edge whose Fourier transform exhibits sidelobes with spacing inversely proportional to the pulse width.

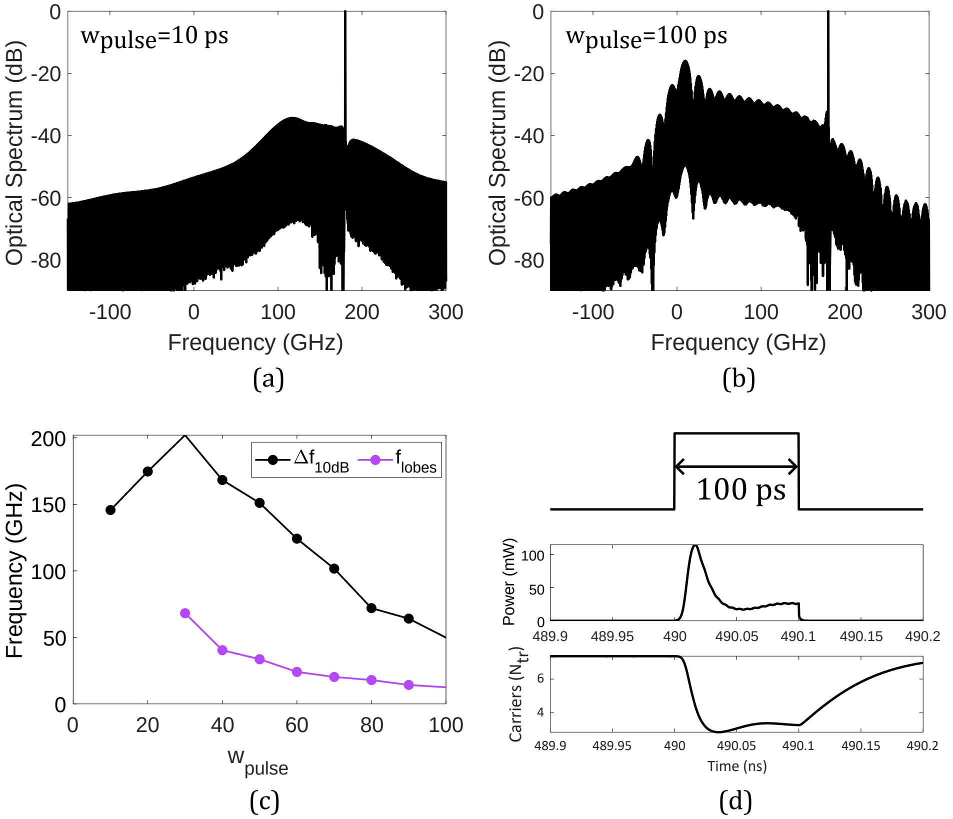

(a) (b)

(c) (d)

Figure 5.8: (a-b) Simulated optical spectra for $I = 120$ mA and different w_{pulse}: (a) 10 ps and (b) 100 ps. (c) Δf_{10dB} and average frequency distance between lobes f_{lobes} as a function of the pulse width for $I = 120$ mA. (d) Simulated optical pulse and carrier density when $w_{pulse} = 100$ ps.

The dependence of the OFCs on the excitation pulse width is illustrated in Fig. 5.8, which shows the optical spectra at the maximum bias of 120 mA for $w_{pulse} = 10$ and 100 ps, with detuning $\delta\nu = 180$ GHz. The corresponding evolution of $\Delta f_{10\text{dB}}$ for different durations is plotted in Fig. 5.8(b), where a clear maximum is observed at $w_{pulse} = 30$ ps, followed by an almost linear decrease of $\Delta f_{10\text{dB}}$ with increasing pulse width. In the same figure, it is also included the average spacing of the spectral lobes that appear on the high-frequency side of the envelope. This spacing decreases as the pulse width increases, consistent with their Fourier-transform origin.

These spectral changes are further clarified in Fig. 5.8(d), which depicts the temporal evolution of the optical power and carrier density for the case of $w_{pulse} = 100$ ps. When the drive pulse is very short (10 ps), the optical output cannot reach its maximum, limiting the comb span to about 150 GHz. At a pulse width of 30 ps, the spectral width is maximised (Fig. 5.5(a)), as this value coincides with the point of minimum carrier density during the first relaxation oscillation. For longer drive pulses, the comb width decreases and the spectral flatness worsens, owing to the more pronounced lobes in the spectral envelope. In general, short electrical drive pulses, or equivalently, low duty cycles, are required to maximise the comb bandwidth. For a repetition rate of 100 MHz and an optimal pulse duration of 30 ps, this corresponds to an electrical signal with a bandwidth on the order of tens of GHz.

PIC implementation and experimental results

To implement the proposed scheme in Fig. 5.2 and experimentally verify the generation of OFC with QS, the PIC was fabricated through SMART Photonics in a MPW run, using the available BBs from its PDK library. The integration followed the design considerations reported in [234] and the obtained simulation results. The operating point was set to achieve an effective balance between ER and insertion losses.

Increasing the modulation depth implies higher ER but this also raises the insertion losses and, consequently, the total cavity losses. Conversely, reducing the modulation depth lowers the insertion losses at the expense of ER. The chosen detuning therefore optimises these two trade-offs, ensuring that the device operates with a low α_{ON} while maintaining a sufficiently high ER to minimise the modulation factor m.

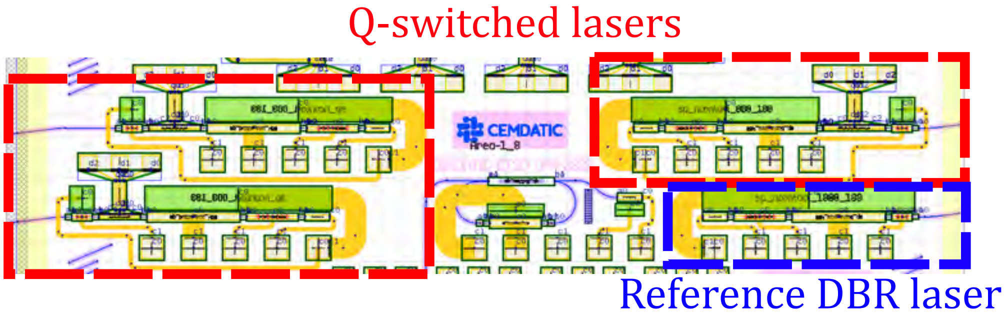

Figure 5.9: Layout of the integrated Q-switched multi-section DBR lasers fabricated in SMART Photonics via a MPW run. It consist of a monitor photodiode (Monitor PD), two front and rear DBR mirrors (FDBR and RDBR), a SOA and an EAM. The EAM features GSG metal tracks matched to 50 Ω for high speed modulation.

To experimentally study the impact of the EAM length on the device performance, three QS lasers with different EAM lengths were included on the same chip (200 μm, 250 μm, and 300 μm) together with a reference DBR laser without an EAM for comparison purposes. The layout is shown in Fig. 5.9 as shown in KLayout, a software for visualising GDS files.

The QS lasers are highlighted in red, and the reference DBR is in blue. Fig. 5.10 shows a photograph of one of the Q-switched lasers, indicating the different elements and the experimental characterisation setup. By integrating devices with different EAM lengths, it is possible to experimentally evaluate the trade-offs between ER enhancement and insertion loss increase. Longer modulators are expected to exhibit higher ER due to the extended absorption region, but at the expense of greater insertion losses. Comparing these three configurations enables a more comprehensive evaluation of the design and the impact of modulator length on the dynamics of QS OFC generation.

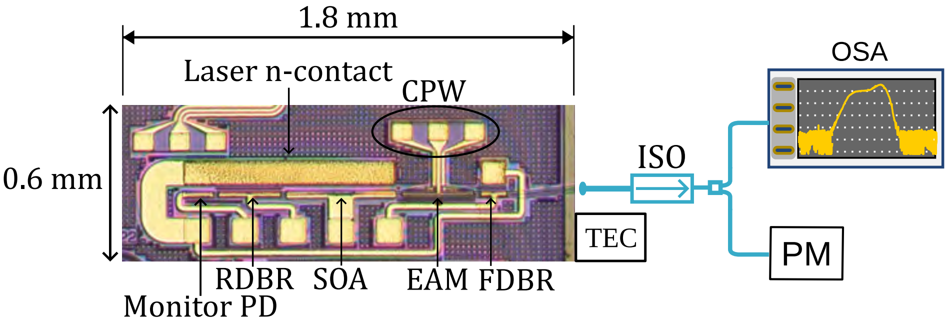

Figure 5.10: Photograph of one of the integrated Q-switched DBR.

The PIC was characterised with the temperature-controlled probe station described in Section 4.1. The temperature was stabilised to 25°C. Electrical access was provided via DC probe needles for the SOA and DBR sections, and RF GSG probes (40 GHz bandwidth) for the EAM, all contacting the on-chip pads. Optical injection and collection were performed using lensed fibers. The on-chip output facet is tilted 7° to minimise back-reflections into the laser, and the facets are anti-reflection (AR) coated. The experimental setup is illustrated in Fig. 5.10, where the SOA and DBRs are driven by the low-noise current sources, the EAM is reverse-biased with a DC voltage source and modulated by the PPG, and the on-chip monitor photodiode is read by a digital multimeter for power monitoring. The output of the PIC is recorded simultaneously in the OSA and the PM.

First, the power–current (PI) curve and the continuous-wave (CW) spectra as a function of the drive current were characterised. Fig. 5.11(a) shows the PI curve measured off-chip in the PM and on-chip with the internal monitor for the reference DBR laser. Both traces were normalised to their respective maxima, corresponding to measured photocurrents of 3.5 mA (off-chip) and 0.5 mA (on-chip). Measurements were taken in 1 mA steps from 0 to 100 mA. The lasing threshold was 25 mA. A mode hop was observed at 95 mA, as seen in the spectral map in Fig. 5.11(b), as expected in DBR lasers, due to the shift of the DBR mirror reflection peak and the gain peak at different rates with increasing drive current caused by thermal effects.

The same characterisation was carried out for the Q-switched lasers with the EAM biased at 0 V (low-loss state). It was observed that the cavity loss in the on state, α_{ON}, was sufficiently high that the lasing threshold could not be reached within the available drive range (up to 130 mA) for any of the three designed lasers. This behaviour is attributed to EAM insertion losses that were higher than expected and greater than the values reported in [234]. When the EAM was forward-biased, effectively operating as a short SOA, the additional gain compensated for these losses and lasing was achieved. Figure 5.12(a) shows the PI curve of the Q-switched laser with $L_{\mathrm{EAM}} = 250, \mu$m, when the EAM is forward-biased at 5 mA, measured off-chip by the PM. The corresponding spectrum for an SOA drive current of 90 mA, recorded with the OSA (Fig. 5.12(b)), shows single-mode emission near 1570 nm, coinciding with the emission wavelength of the DBR laser shown in Fig. 5.11(b).

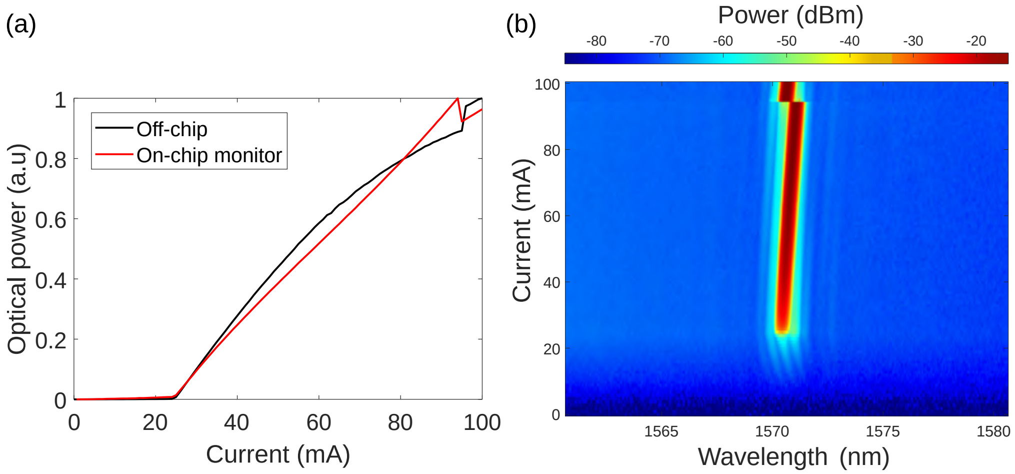

Figure 5.11: Characterisation of the reference DBR laser showing (a) the PI curve and (b) the optical spectra across the driving range.

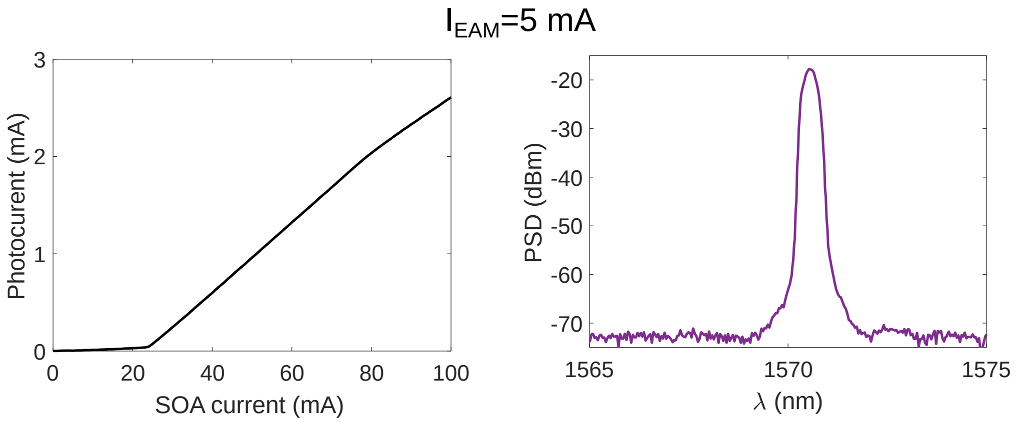

(a)
(b)

Figure 5.12: characterisation of the integrated Q-switched DBR laser showing (a) the PI curve and (b) the spectrum when the EAM is forward-biased to compensate the losses of the cavity.

Forward-biasing the EAM and comparing its behaviour with that of the isolated DBR laser proved useful for diagnosing excess α_{ON} and confirming single-mode operation. However, QS requires reverse-bias modulation of the EAM, which limits its practical implementation in this device, as maximising the comb span demands a low $I_{\mathrm{th-ON}}$. Further designs could increase the SOA length to enhance gain or extend the mirrors to reduce losses, although the latter would limit the minimum achievable modulation depth m. Although experimental validation was not possible within the thesis timeframe, the results provide valuable design guidelines for future iterations.

5.2 Gain-switched DFB lasers in master-slave configuration

This section reports a monolithically integrated, optically injected GS OFC source on a generic InP platform, consisting of two DFB lasers in a master–slave configuration, where the ML injects light into the SL through an MMI coupler. The PIC was fabricated through Fraunhofer HHI in an MPW run and characterised on a probe station (Section 4.1). The DFBs are characterised in CW, exhibiting unexpected mode hops and linewidths of 20-25 MHz. When operated simultaneously, the coupled lasers display complex mutual dynamical interactions. OFCs are generated at 5 GHz using sinusoidal drive and at 500 MHz using an SRD for pulsed GS, showing effective OI locking. OFC generation is investigated systematically to identify optimum operating conditions according to the RF signal excitation amplitude, the current of the ML, the current of the SL, and the fine detuning controlled by heaters on the DFBs. These OFCs are characterised by the figures of merit $\Delta f_{10\text{dB}}$, CNR, and flatness.

The generated OFCs indicate coupling between the two DFBs due to the absence of an on-chip isolator. The emission of the ML is perturbed by the SL, and CW characterisation indicates a weak compound cavity formed between the chip facets. Improving performance focuses on narrowing the DFB linewidth and mitigating the ML perturbation. Despite these challenges, the results demonstrate reconfigurable GS OFCs on PICs. Additionally, it has been demonstrated that the repetition rate of these GS OFCs can be reduced to the MHz range, thus indicating suitability for spectroscopic measurements. This system could be used as the OFC source for dual-comb spectrometers based on a single source, as described in [179].

PIC design and characterization of the laser sources

The schematic of the PIC design and the characterisation setup are shown in Fig. 5.13 (a), together with a photograph of the fabricated chip in Fig. 5.13 (b). The circuit was implemented using the standard BBs from the PDK of the Fraunhofer HHI InP foundry, and fabricated through an MPW run. It consists of two DFB lasers arranged in a master–slave configuration. Each DFB is designed to emit around 1550 nm. Both devices include an integrated photodiode (iPD) at one facet, used as a power monitor and read out via on-chip electrical connections and a multimeter, as well as integrated heaters for fine wavelength tuning of up to 1 nm.

OI is implemented by means of a 50:50 MMI coupler, as shown in Fig. 5.13(a), which routes the optical field from DFB2 to DFB1 while directing the emission of DFB1 towards the on-chip output. The output facet is tilted by 7° to minimise back-reflections and AR-coated to further suppress them. The waveguides are 2 μm wide, and an S-bend is used to connect the two DFBs, reducing the overall footprint.

Both DFBs are connected to the monitor PDs via deep-to-shallow etched waveguide transitions.

Electrical access is implemented through metal crossovers that contact the heaters and DFB2 monitor, while the DFBs use 50 Ω CPWs supporting modulation bandwidths up to 40 GHz with a minimum bend radius of 200 μm.

The PIC was mounted on the probe station described in Section 4.1, with the chip temperature stabilised at 25°C. Two probe arrays were employed: one for DC access (reading the iPDs and driving the heaters) and another for RF signals. The optical output was collected from the PIC using a lensed fibre and routed to the measurement instruments. After the optical isolator, the signal was split into two branches. One branch was amplified by an EDFA and analysed with the HR-OSA, while the other was sent to both the OSA and the PM. For comb generation, DFB1 was driven through a bias tee combining the DC bias current I_{SL} with an RF generator and an SRD to produce pulsed GS. DFB2 was biased by a low-noise current source at a current I_{ML}.

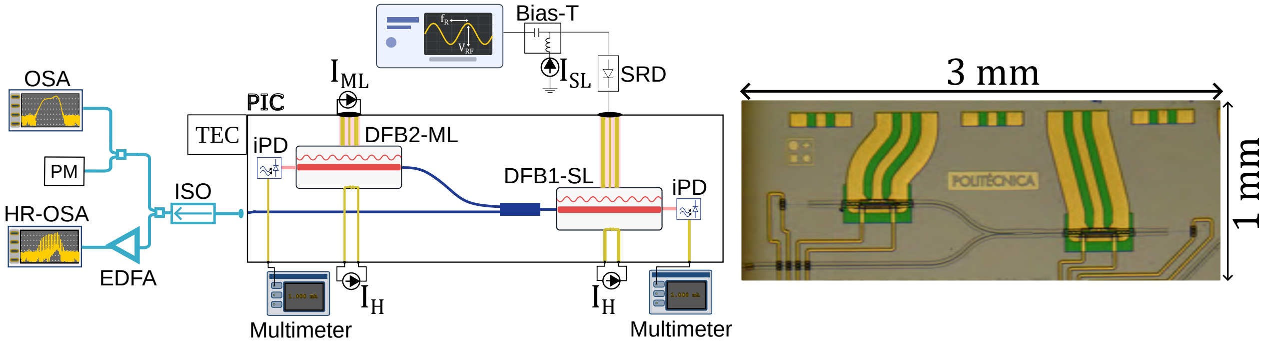

(a) (b)

Figure 5.13: (a) Scheme and (b) photograph of the fabricated device for GS OFC generation following a master-slave configuration based on DFB lasers. The PIC was fabricated in Fraunhofer HHI via a MPW run.

For CW characterisation of each laser, the drive currents I_{SL} and I_{ML} were swept while the DFB laser not under test was reverse-biased to induce absorption and minimise mutual coupling. Figure 5.14 shows the measured PI curve of DFB1, recorded simultaneously with iPD and the external PM (a), together with the corresponding optical spectra measured with the OSA (b). For clarity, the PI curves have been normalised. The peak readings correspond to optical powers proportional to 5 mA (iPD) and 0.4 mA (PM). The coupling loss between the PIC and the lensed fiber is estimated to be approximately 6 dB. Note that the optical path to the PM includes two 1×2 couplers, introducing an additional 6 dB of loss, and that the instruments are located in a separate room connected by a fiber link introducing further, unquantified losses.

Measurements were taken every 1 mA from 0 to 120 mA. The lasing threshold lies within the expected range according to foundry data (9 mA), and the spectra exhibit mode hops of ~ 0.14 nm (Fig. 5.14 (b)) at certain values of current occurring every 0.44 nm. Fig. 5.14 (b) shows an inset with two consecutive acquisitions where a mode hop occurs. Such hopping is not expected for a single-mode DFB and is attributed to the weak compound cavity and/or residual feedback. The mode hops occurring each 0.44 nm, which corresponds to an optical length of approximately 740 μm in FSR, could be related to the distance between the facets of DFB1 and DFB2. Furthermore, the PI curve shows saturation due to thermal roll-over beyond a certain current.

Fig. 5.14 (c) shows the measured spectra as a function of drive current. In addition to the mode hops, the emission wavelength is displaced by approximately 8 nm from the target 1550 nm. Current tuning spans up to 5.8 nm, and the integrated heater provides a further $\sim$ 1 nm red shift (not shown). The laser linewidth was characterised using the delayed self-heterodyne method [244], in which the laser is beaten with a delayed copy of itself after a sufficiently long fiber delay to eliminate mutual coherence. The RF beatnote, recorded for instance on an ESA, was fitted to a Voigt profile (the convolution of Lorentzian (intrinsic) and Gaussian (phase noise) contributions) to extract the optical linewidth. For currents above 30 mA, the measured linewidth lies between $20-25$ MHz, versus the $\sim$ 5 MHz expected. This corresponds to a coherence length on the order of 6 m.

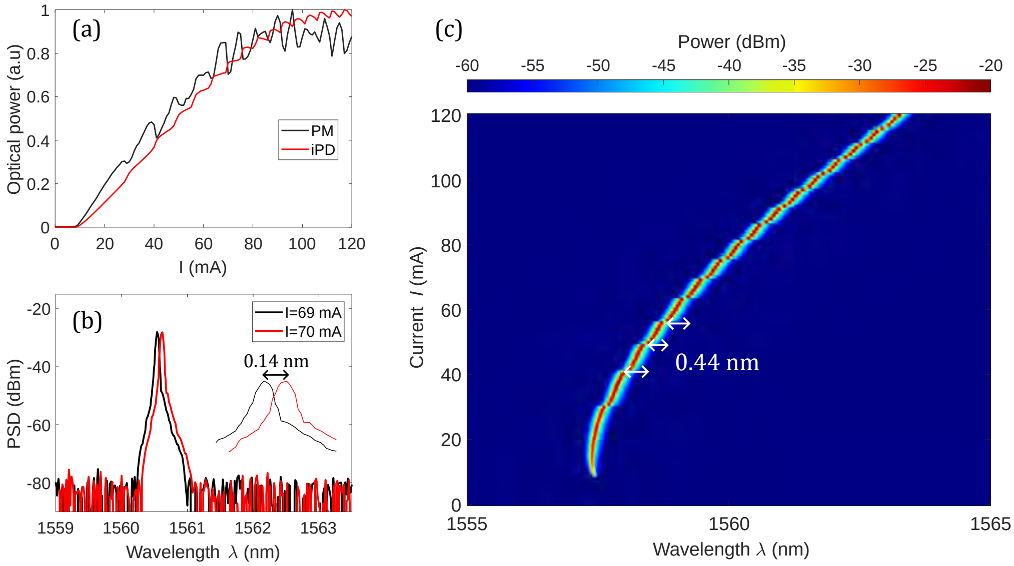

Figure 5.14: CW characterisation of DFB1: (a) PI curves measured with the PM and the on-chip iPD; (b) optical spectra recorded with the OSA showing two consecutive acquisitions where a mode hop is observed; (c) optical spectra measured with the OSA as a function of the drive current.

The same CW characterisation was performed for DFB2 (Fig. 5.15). Note that the light collected at the PIC output in this case does not come directly from DFB2. Rather, it corresponds to the light reflected at the output DFB1 facet and returned via the MMI. The PI curves in Fig. 5.15 (a) are shown both from iPD and PM, normalised to their respective maxima, which correspond to optical powers proportional to 5 mA (iPD) and 0.04 mA (PM). As expected, the PM reading at the PIC output is much lower because it stems from reflection rather than direct throughput. Mode hops are again evident in the PI curves.

In Fig. 5.15, clear minima are visible (marked in the figure) with a spacing of approximately 1.37 nm (FSR $\approx$ 169.2 GHz at 1560 nm). This spacing corresponds to an optical cavity length of about 240 μm, which matches the distance between the MMI output branch leading to the

PIC output and the output facet of DFB1. This indicates the presence of a parasitic cavity between the MMI output and the DFB1 output facet.

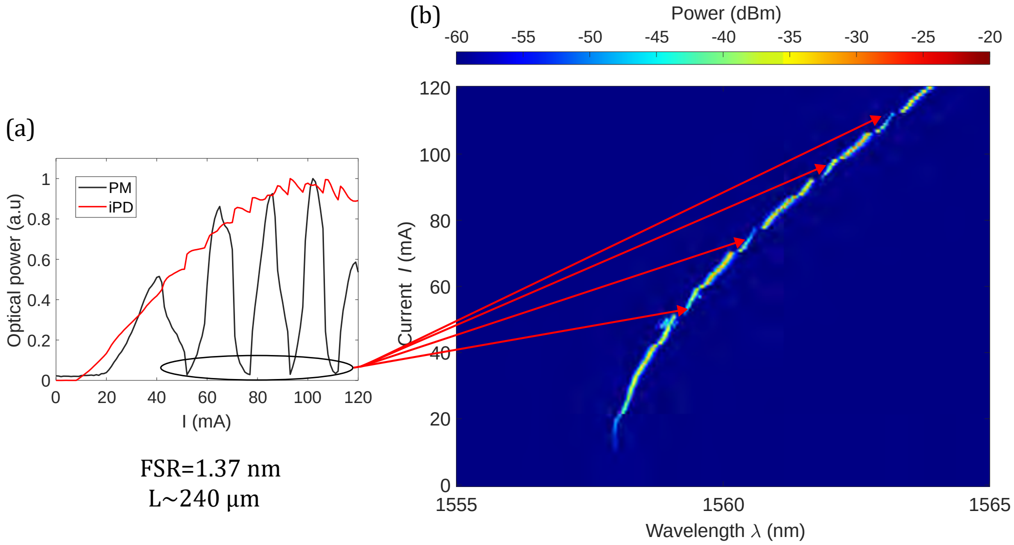

Figure 5.15: CW characterisation of DFB2: (a) PI curves measured with the PM and the on-chip iPD; (b) optical spectra recorded with the OSA as a function of the drive current. The PI curve measured at the PIC output exhibits minima associated with the compound cavity formed between the MMI and the output facet of DFB1.

Finally, the coupled behaviour of the two lasers was investigated under CW operation. To characterise the locking dynamics, optical spectra were recorded with the OSA, and the electrical beat signal between the two lasers was measured on a fast photodiode connected to the ESA. In the experimental layout shown in Fig. 5.13, the ESA replaces the HR-OSA. Figure 5.16 presents the spectra measured with the OSA (a, c) and the ESA (b, d) as the slave current I_{SL} was swept from 0 to 120 mA in 1 mA steps. The top row corresponds to $I_{\mathrm{ML}} = 65$ mA, i.e. a maximum in the PI curve of Fig. 5.15, while the bottom row corresponds to $I_{\mathrm{ML}} = 77$ mA, i.e. a minimum in the same curve. The RF spectra are normalised to the noise floor, such that 0 dB corresponds to the average noise-floor level.

Figure 5.16 illustrates the complex locking and coupling dynamics between the two lasers. In both cases, the ML exhibits a slight redshift with increasing I_{SL}, attributed to thermal effects, along with variations in ML power arising from the formation of a compound cavity between the two lasers. The SL PI curve closely follows its solitary-laser characteristic in regions where its emission does not overlap with that of DFB2, with mode hops still evident.

In Fig. 5.16(a, b), a region between 63 and 68 mA, where I_{SL} becomes comparable to I_{ML}, shows a broadened optical spectrum resulting from competition between the lasers. In the ESA, this appears as a broad RF spectrum extending up to approximately 30 GHz. Similar beat products occur at other bias points but collapse into a single narrow peak. Fig. 5.16(c, d) shows comparable behaviour when I_{ML} is tuned close to a resonance in Fig. 5.15. The beating is weaker here due to the lower ML optical power, as observed in Fig. 5.16(d).

In the absence of coupling, two CW lasers at optical frequencies ν_1 and $\nu_2 = \nu_1 + \Delta\nu$ produce an RF signal centred at $f_{\text{beat}} = |\Delta\nu|$ on the photodiode. When mutual optical coupling is present, frequency pulling reduces the effective detuning and the beatnote linewidth owing to increased phase coherence between the lasers. If $|\Delta\nu|$ lies within the locking range, full locking occurs and both lasers emit at a common optical frequency, eliminating any discrete beatnote. However, narrow beatnotes can still appear even when the optical spectra remain separated, reflecting partial or injection locking in which the optical frequencies are distinct but phase-correlated. Near the edge of the locking range, the interaction becomes dynamic, leading to broadened or multi-peaked RF spectra as power and phase fluctuate. This interpretation explains the observations in Fig. 5.16: the broad ESA features (up to ∼30 GHz) correspond to strong interaction without full locking, whereas the narrow beatnotes at other bias points indicate coherent coupling or partial locking between the two lasers.

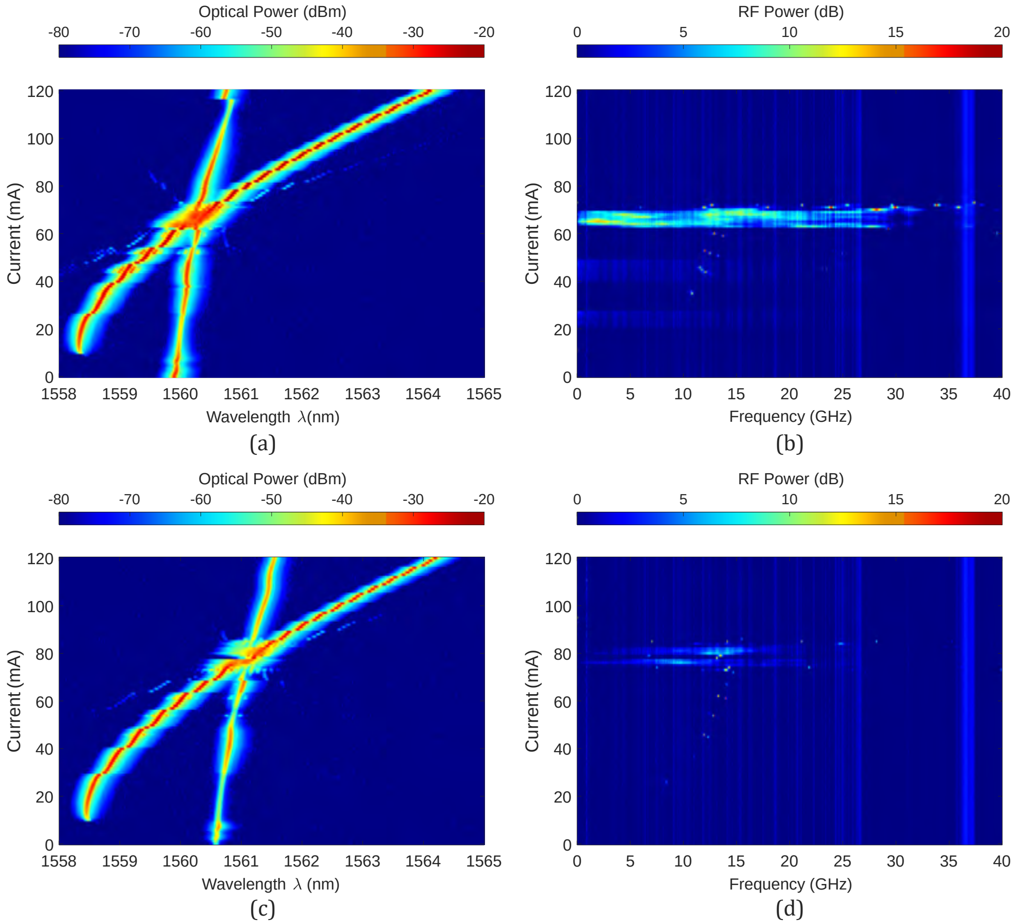

Figure 5.16: OI locking characterisation under CW operation. Optical (a, c) and RF (b, d) spectra measured with the OSA and the ESA, respectively, for I_{SL} swept from 0 to 120 mA in 1 mA steps. The top row corresponds to $I_{\text{ML}} = 65$ mA (PI-curve maximum in Fig. 5.15), and the bottom row to $I_{\text{ML}} = 77$ mA (PI-curve minimum). The RF spectra are normalised to the noise floor, with 0 dB indicating the average noise-floor level.

Adjustment of the SL heater current (I_{H}) in the region where the two lasers coincide in emission wavelength in Fig. 5.16(c) enables fine tuning of the detuning to observe locking.

Fig. 5.17(a, b) shows the OSA and ESA spectra as I_H is varied from 0 to 50 mA in 1 mA steps. For currents between 0 and 25 mA, several modes lase simultaneously, producing the beat terms observed in the ESA. This beating is coherent because, with the two lasers very close in frequency, mutual coherence arises from partial though not complete locking. Other regions display a more complex mutual coupling behaviour. A particularly relevant point occurs at $I_H = 33$ mA, where the optical spectrum narrows to a single line and no RF beat tones are observed in the ESA, indicating complete and stable locking between the two lasers. The individual spectra at this point recorded at OSA and ESA are shown in Fig. 5.17(c, d), respectively.

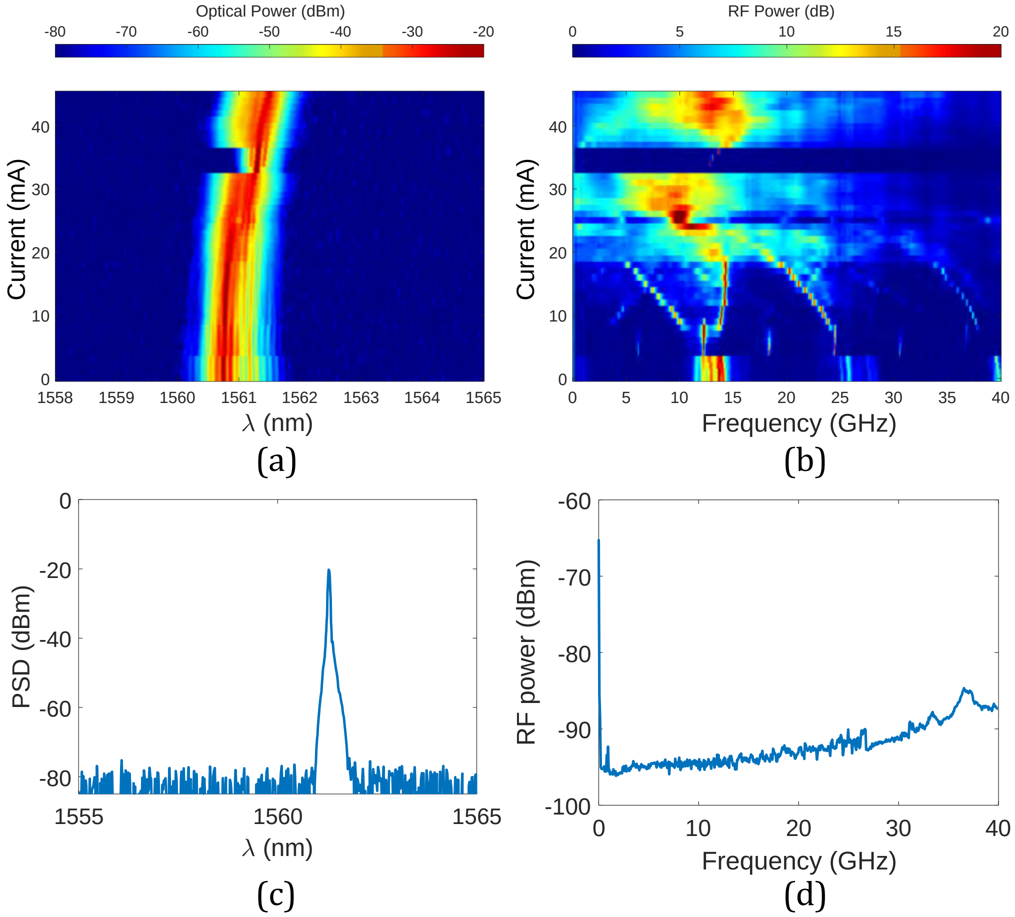

Figure 5.17: Fine tuning of the detuning between the two DFB lasers through I_H. (a) Optical spectra recorded with the OSA and (b) RF spectra measured with the ESA as the SL heater current I_H is varied from 0 to 50 mA in 1 mA steps. At $I_\mathrm{H} = 33$ mA, the optical spectrum collapses to a single line and no RF beatnote is observed, indicating complete and stable locking between the two lasers. (c, d) Optical and RF spectra corresponding to this locking condition.

OFC generation under GS and optical injection

OFCs were generated and characterised at several repetition rates using the setup shown in Fig. 5.13. We first examined the influence of OI on comb quality at high repetition rates. When the modulation frequency approaches the relaxation-oscillation frequency, OI is not strictly required for comb generation, since the limited carrier recovery allows each pulse to build upon the residual photon field from the previous one, maintaining partial coherence even without external stabilisation. Fig. 5.18 compares spectra at $f_r = 5$ GHz obtained without (black) and with (red) OI. In both cases, DFB1 was driven by a sinusoidal RF signal with $V_{RF} = 5.6$ V and $I_{\mathrm{SL}} = 10$ mA. The spectra were recorded with the HR-OSA. The 0 Hz component corresponds to the DFB1 emission wavelength at threshold. Without injection, the comb spans $\Delta f_{10\mathrm{dB}} \approx 30$ GHz with a CNR of 18 dB. Activating the master laser ($I_{\mathrm{ML}} = 85$ mA) leads to spectral broadening up to $\Delta f_{10\mathrm{dB}} \approx 70$ GHz and an improved CNR of 24 dB due to OI locking. This demonstrates that the proposed design can sustain OFC generation even at lower repetition rates when assisted by OI.

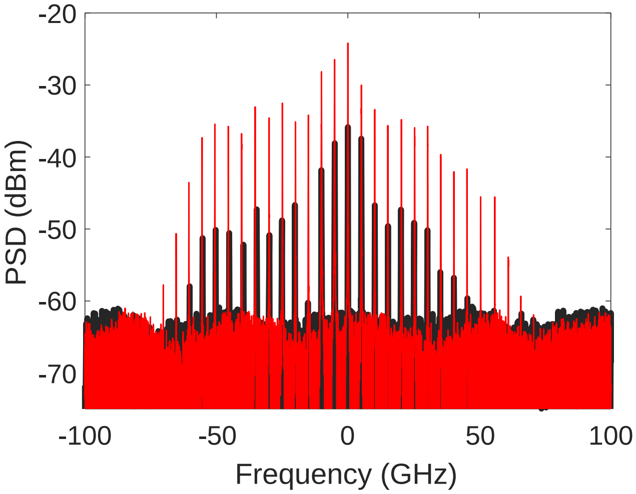

Figure 5.18: OFC generation at 5 GHz by GS the DFB1 without (black) and with (red) OI.

To investigate OFC generation at lower repetition rates, a SRD was inserted after the RF generator to produce pulsed gain switching at $f_r = 500$ MHz. A systematic study was conducted by varying four parameters: the RF amplitude at the generator output (V_{RF}), the slave-laser bias current (I_{SL}), the master-laser bias current (I_{ML}), which determines the injection power and detuning, and the DFB1 heater current (I_{H}) for fine wavelength tuning. The SRD generated electrical pulses of approximately 400 ps duration. However, at higher V_{RF}, parasitic oscillations appeared at the SRD output, ultimately degrading the comb quality.

Figure 5.19 shows representative comb spectra for several V_{RF} values chosen to avoid this distortion, while keeping the other parameters fixed ($I_{\mathrm{ML}} = 32.5$ mA, $I_{\mathrm{H}} = 0$ mA, and $I_{\mathrm{SL}} = 8$ mA). As V_{RF} increases, the comb bandwidth broadens due to enhanced dynamic chirp, consistent with previous observations in [163]. The inset in Fig. 5.19 confirms OI locking, with clearly resolved lines spaced by 500 MHz. The component at 0 Hz corresponds to the emission wavelength of DFB1 at threshold, while the dominant peak and adjacent lines spaced by 500

MHz originate from the OI, with the remaining weaker lines arising from the SL contribution.

As shown in Fig. 5.19, particularly in panel (a), a minimum is observed between the OI component and the comb generated by the GS SL. The corresponding measured values are: (a) $\Delta f_{10\mathrm{dB}} = 62$ GHz, CNR = 14 dB, and flatness = 0.68; (b) $\Delta f_{10\mathrm{dB}} = 87$ GHz, CNR = 18.8 dB, and flatness = 0.56; (c) $\Delta f_{10\mathrm{dB}} = 96$ GHz, $CNR = 17.4$ dB, and flatness = 0.69. In all cases, the average optical power per comb line is approximately −45 dBm.

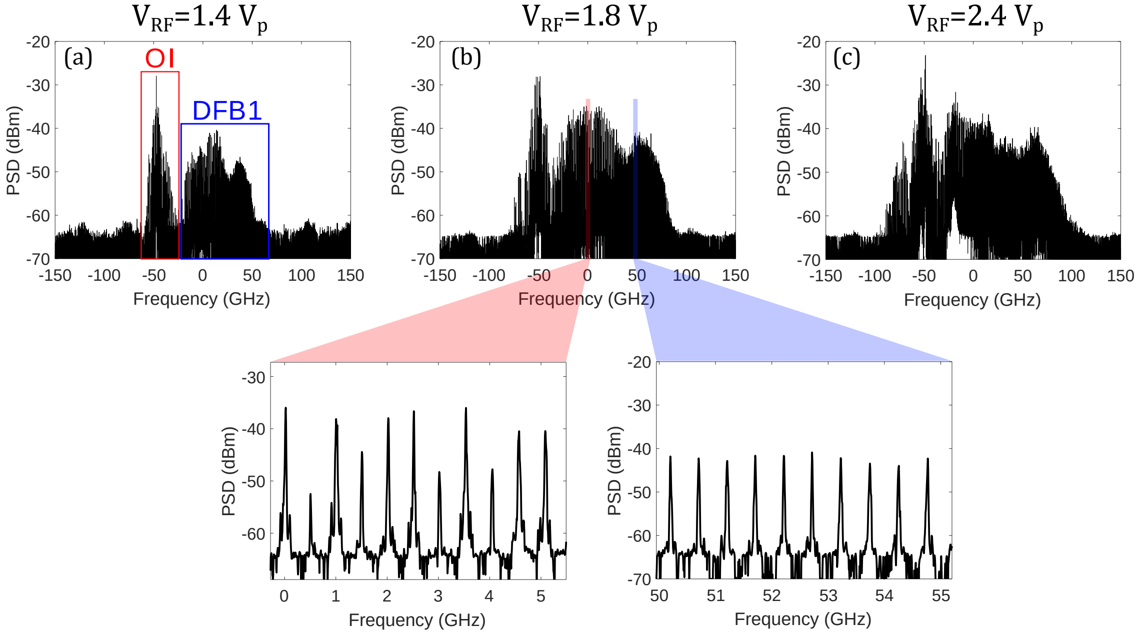

Figure 5.19: Optical frequency comb generation at 500 MHz using pulsed GS. (a–c) Optical spectra recorded with the HR-OSA for different RF amplitudes V_{RF} while keeping $I_{\mathrm{ML}} = 32.5$ mA, $I_{\mathrm{SL}} = 8$ mA, and $I_{\mathrm{H}} = 0$ mA constant. The comb bandwidth increases with V_{RF} due to the enhanced dynamic chirp. The inset shows clearly resolved 500 MHz-spaced lines, confirming OI locking. A spectral minimum appears between the OI component and the OFC.

Regarding flatness, the insets of Fig. 5.19 (b) reveal two regions. Close to the injection frequency, the power variation between lines is comparatively large, whereas farther from OI, the comb lines are more uniform. In both regions, the individual tones are clearly resolved, but the large differences in the tones close to the OI hinder the overall flatness of the OFC. Their measured 3 dB linewidth on the HR-OSA is approximately 25 MHz, equal to the ML linewidth, which is consistent with OI locking of the SL.

To assess the influence of OI on the OFC characteristics, the ML current I_{ML} was swept from 10 mA (threshold, no injection) to 60 mA (after the first resonance in Fig. 5.15) in 0.5 mA steps, while keeping the other parameters fixed ($V_{\mathrm{RF}} = 1.8$ V, $I_{\mathrm{H}} = 0$ mA, and $I_{\mathrm{SL}} = 6$ mA). Representative spectra are shown in Fig. 5.20 for (a) $I_{\mathrm{ML}} = 10$ mA, (b) $I_{\mathrm{ML}} = 31$ mA, (c) $I_{\mathrm{ML}} = 41$ mA, and (d) $I_{\mathrm{ML}} = 51$ mA. At $I_{\mathrm{ML}} = 10$ mA, the master DFB2 is near or below threshold, so injection locking does not occur and a comb with clearly resolved lines is not formed. Once the master reaches lasing, an OFC appears (Fig. 5.20(b)) with characteristics similar to those in Fig. 5.19. As I_{ML} increases further, the detuning between DFB1 and DFB2 grows, leading to the spectrum in Fig. 5.20(c) ($\Delta f_{10\mathrm{dB}} = 107.5$ GHz, $CNR = 17$ dB, flatness = 0.86), where no comb lines are visible between the injection components and the slave-generated comb. A zoom around the injection region (Fig. 5.20(e)) resolves tones separated by 500 MHz. Comparing the cases, the comb in Fig. 5.20(b) ($\Delta f_{10\mathrm{dB}} = 89$ GHz, $CNR = 16$ dB, flatness = 0.75) exhibits a smaller span and lower flatness, whereas Fig. 5.20(c) shows a slightly broader and flatter spectrum. However, the comb tones display increased noise (not shown) due to the weaker OI locking at large detuning (∼100 GHz in this case).

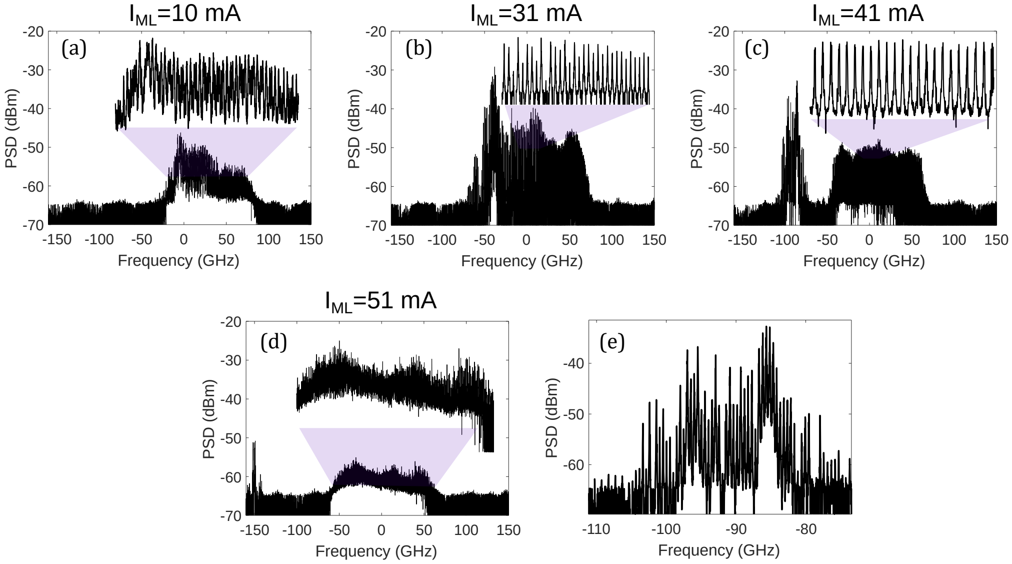

Figure 5.20: Optical frequency comb generation as a function of ML bias current. (a–d) Optical spectra recorded with the HR-OSA for increasing I_{ML} from 10 to 51 mA while keeping $V_{\mathrm{RF}} = 1.8$ $\mathrm{V_p}$, $I_{\mathrm{SL}} = 6$ mA, and $I_{\mathrm{H}} = 0$ mA constant. The inset in (d) shows that for large detuning between the ML and the SL, injection locking is lost. (e) Zoom around the injection region showing residual 500 MHz-spaced lines, indicating strong mutual coupling in the absence of optical isolation, which perturbs the master emission.

In Fig. 5.20(d), the detuning between the ML and SL is sufficiently large that injection locking no longer occurs, as evident in the inset. This operating point also coincides with one of the resonances identified in Fig. 5.15, resulting in very low power around the injection frequency. For higher ML currents, the OFC ceases to form because locking is lost; however, residual lines remain visible near the injection frequency with a spacing of 500 MHz (see, e.g., Fig. 5.20(e)). This behaviour indicates strong mutual coupling between the ML and SL in the absence of optical isolation, leading to instabilities and perturbations in the ML emission similar to those observed in off-chip master-slave configurations.

Recent studies developed after these experiments have shown that exploiting the mutual coupling between two lasers can improve the quality of the generated OFCs in integrated GS systems [223]. The latter and other works [174] have demonstrated that mutual (symmetric) coupling, where both lasers are biased at comparable currents, can actually enhance comb characteristics compared with asymmetric coupling, in which the ML operates at a much higher bias than the SL. Under symmetric coupling, locking in CW operation is optimised, improving the OFC performance once GS is applied. Although this configuration requires biasing the SL above threshold (otherwise the ML cannot provide effective OI locking), the modulation of the SL drives it below threshold during the negative cycles. This approach has so far been explored only at high repetition rates (around 6.8 GHz), while its application to low repetition rates remains unreported. In these experiments, the master-slave configuration operates in the asymmetric regime. However, the CW locking analysis in Fig. 5.17 provides a solid foundation for future exploration of symmetric injection under GS conditions in the same platform.

The other two parameters (the heater current and the SL bias) did not exhibit clear dependencies. The heater current provides fine detuning control and can be adjusted to obtain a local optimum comb. However, once the other parameters are fixed, it does not lead to significant improvement. The current was swept from 0 to 50 mA, with increased detuning resulting in a gradual degradation of comb quality. Regarding I_{SL}, it must remain sufficiently low to ensure that the laser switches off between pulses. Within the range of 6-10 mA, no consistent trend was observed in the figures of merit, although for each I_{SL} the same behaviour described above was reproduced when varying V_{RF} and I_{ML}.

OFC generation was also investigated at other repetition rates between 500 MHz and 5 GHz, including pulsed operation from 500 MHz to 1 GHz, observing similar behaviours. Pulsed excitation was provided by a low-frequency RF generator and a SRD, indicating that the system could be developed for inexpensive OFC generators, following what has been done in [169][191]. Overall, the results indicate a reconfigurable, optically injected GS OFC source on PIC that can deliver good spectral coverage and good CNR and acceptable flatness across repetition rates compatible with high spectral resolution. We demonstrate that the repetition rate of GS combs on a PIC can be reduced to 500 MHz in a fully integrated master–slave configuration. In terms of stability, heterodyne beating between comb lines shows sub-kHz relative coherence.

The perturbation of the ML emission in the absence of on-chip optical isolators gives rise to complex dynamics within the monolithically integrated system, where compound-cavity and mutual coupling effects occur. Although these effects do not prevent comb generation, they limit the use of this configuration for dual-comb operation, as the instability introduced by the ML perturbation degrades performance. The next section proposes a solution to mitigate these effects.

Finally, this comb source was considered as a single dual-comb generator for spectroscopy using the Parallel Heterodyne Interferometry via Repetition-rate (PHIRE) technique [245] applied to GS OFCs, referred to here as gated [246]. However, the limited coherence length of the ML and the low power of the optical lines prevented on-chip implementation.

The same method was therefore successfully demonstrated using discrete components in [179]. In that work, dual-comb spectroscopy was achieved with a single optically injected gain-switched laser diode whose repetition rate was rapidly toggled so that one source produced two mutually coherent OFCs with slightly different repetition rates. The GS OFCs were generated in a discrete mode laser (DML) operating at a repetition rate of approximately 250

MHz and injected by a narrow-linewidth ECL. The repetition rate of the OFC was alternated at a frequency $f_m \ll f_r$, and the signal was split into two paths: one delayed by 1 km of fiber synchronised with the f_m toggle, and the other shifted by 80 MHz using an AOM. Both signals were then combined on a balanced PD, producing a down-converted RF comb with a line spacing of $2f_m$. This dual-comb source successfully retrieved the absorption line of HCN with high precision, closely matching the HITRAN database values. Building on the insights gained from this discrete implementation and the understanding of the limitations of the integrated system, the gated approach could be revisited in future work for application to the present monolithic platform.

5.3 Optically injected gain-switched integrated semiconductor ring lasers

In integrated optically injected GS OFC systems, unwanted feedback or coupling from the SL can perturb the ML, posing a major challenge to the realisation of such sources on generic PIC platforms. As an alternative to on-chip optical isolators, this section introduces an architecture that minimises ML perturbation by using semiconductor ring lasers (SRLs) to realise a highly unidirectional coupling from ML to SL [247]. The concept exploits SRL operating regimes arising from the coexistence of two counter-propagating fields, clockwise (C-W) and counter-clockwise (CC-W), in the ring cavity [248]. Under OI, the symmetry between these modes is broken so that only the modes in the direction of the OI lase, while the counter-propagating modes are suppressed. In practice, this prevents the SL from perturbing the ML emission [249].

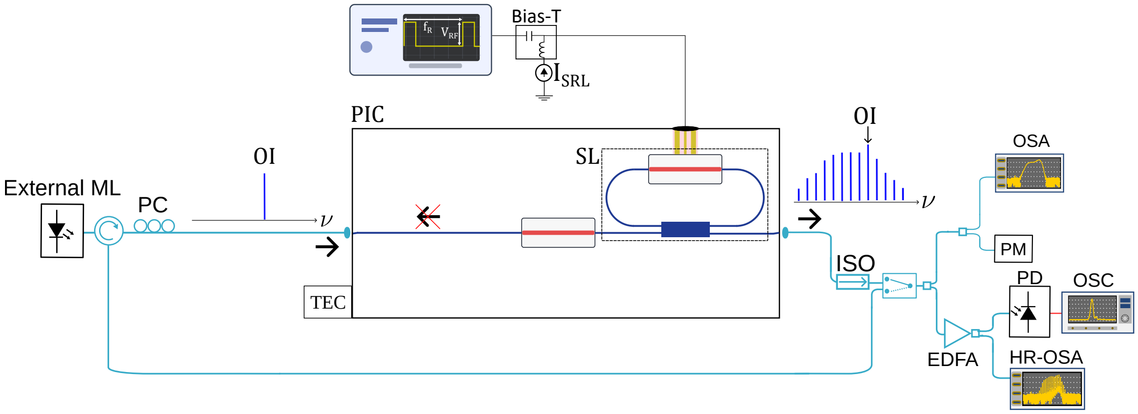

Figure 5.21: Schematic of the proposed unidirectional optically injected SRL scheme. The configuration consists of a master–slave setup in which a ML injects light into a GS SRL acting as the SL. A SOA placed before the SRL controls the injection power from the ML to the SL. OI into the SRL breaks the C-W/CC-W symmetry, favouring OFC emission in the CC-W direction.

The proposed scheme is illustrated in Fig. 5.21. It is based on a master-slave configuration in which a ML (which is represented as external but can be integrated) injects light into a gain-switched SRL acting as the SL. An SOA placed before the SRL provides control over the injected power from the ML to the SL. OI into the SRL breaks the C-W/CC-W symmetry and favours the emission of the OFC in the CC-W direction, which is collected at the east facet. At the west facet, the C-W propagating field can be monitored, where only the injection component is observed.

This architecture forms the basis of the dual-comb generator described in Section 6.1. The design described there was implemented on a PIC fabricated through a SMART Photonics MPW using standard PDK library elements. While the SRL itself is not a standard BB, it was realised by combining a SOA (serving as the active medium) with a 2 × 2 MMI that provides both the optical feedback and the output coupling. The SRL features a custom GSG line designed for high-speed modulation of the SOA. Further details of the SRL characteristics and the PIC design and fabrication are given in Section 6.1. Here, we describe the OFC generation from a single SRL, and the scheme in Fig. 5.21 is therefore simplified.

The PIC described in Section 6.1 following this concept was characterised in the proe station stabilised to 25°C. The outputs from the east and west facets were acquired quasi-simultaneously using an optical switch alternating between the two paths (Section 6.1). Fig. 5.22(a) shows spectra recorded in the HR-OSA from the east (black) and west (red) facets, and Fig. 5.22(b) zooms in on a representative region when the SRL is gain-switched at 1 GHz but no OI is performed. The SOA preceding the SRL is biased at $I_{\mathrm{SOA}} = 50$ mA. At the east facet (i.e., the CC-W propagation direction) the spectrum exhibits the longitudinal modes of the SRL cavity under direct modulation. As the pulses originate from the broadband spontaneous emission of the SOA, no OFC is formed in the absence of stimulated emission for the pulses to build up from. Locking any one of these longitudinal modes would enforce coherence and produce a comb. By contrast, at the west facet (C-W direction) no resolvable SRL modes are observed. This indicates strong unidirectional emission of the SRL, which is forced by the spontaneous emission injected in the CC-W by the SOA.

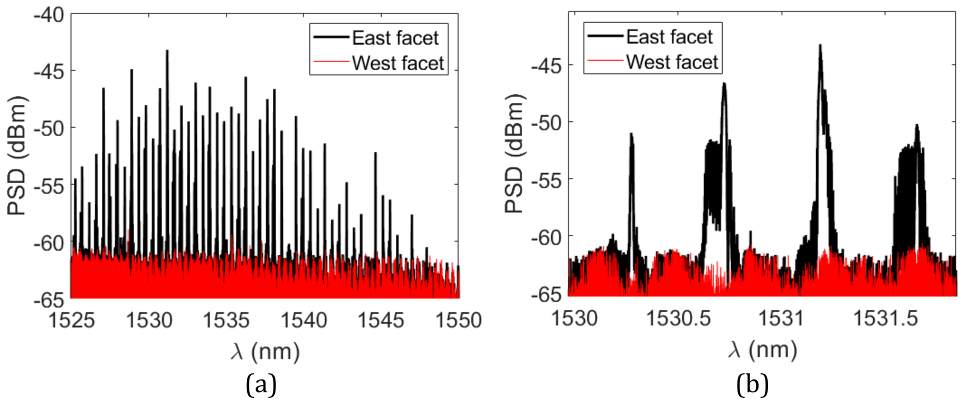

Figure 5.22: Spectral characterisation of the unidirectional SRL configuration. (a) Optical spectra recorded with the HR-OSA from the east (black) and west (red) facets, and (b) zoom into a representative spectral region when the SRL is gain-switched at 1 GHz without OI.

To perform OI, the narrow-linewidth tunable laser operating in the C-band was used to target the longitudinal modes observed in Fig. 5.22(a) and to generate the OFCs. Light was injected into the PIC through an optical circulator, which enabled simultaneous monitoring of the C-W propagating field while coupling the external laser into the chip via a lensed fiber. The injected light, polarised in the TE mode, was amplified on-chip by the SOA located at the fibre input. The injected power was approximately 0 dBm at 1549.64 nm, corresponding to one of the SRL longitudinal modes. Previous studies have shown that OI locking in gain-switched lasers can occur even for suppressed or low-power longitudinal modes, provided that the injection wavelength lies sufficiently close to the mode emission [250]. This principle can be extended to SRLs to selectively excite individual longitudinal modes and generate OFCs at different wavelengths, an approach that has recently proven effective for multi-gas sensing using optically injected GS sources [168].

Fig. 5.23(a) and (b) show the spectra recorded with the HR-OSA from the west and east facets, respectively, when the SRL is gain-switched at a repetition rate of 500 MHz under OI. The spectra are normalised to the injection peak (-18 dBm). The driving currents are $I_{\mathrm{SL}} = 20$ mA and $I_{\mathrm{SOA}} = 10$ mA, and the peak-to-peak amplitude of the modulation signal is $V_{\mathrm{RF}} = 2$ V. At the east facet, an OFC with 500 MHz spacing is observed, exhibiting $\Delta f_{10\mathrm{dB}} = 40$ GHz, CNR = 26 dB, and flatness = 0.81. The injection peak at 1549.64 nm is particularly prominent, confirming effective OI locking, as the SL emission is pulled towards the ML wavelength, enabling stable OFC formation.

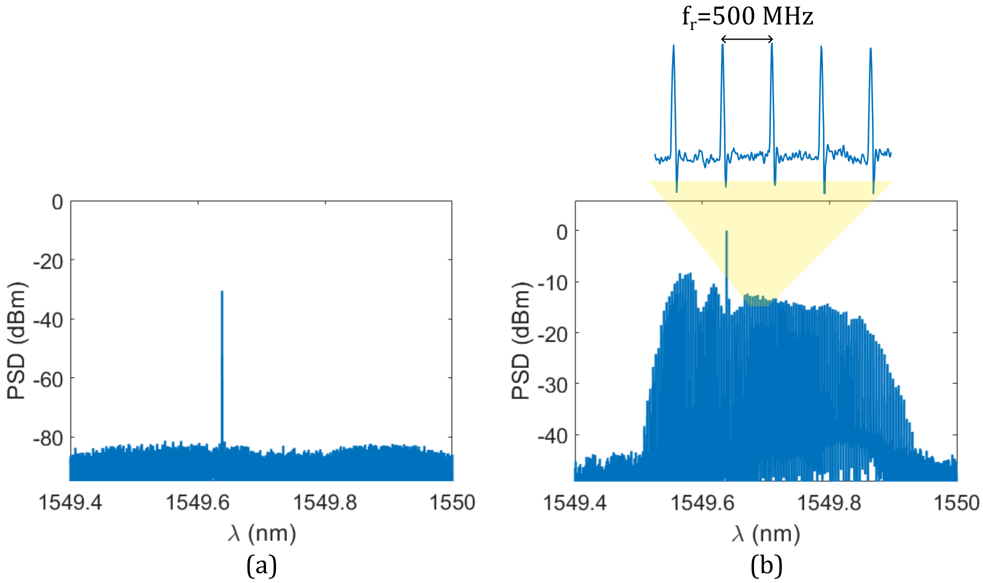

Figure 5.23: OFC generation in the optically injected SRL. (a) and (b) Optical spectra recorded with the HR-OSA from the west and east facets, respectively, when the SRL is gain-switched at 500 MHz under external OI.

At the west facet Fig. 5.23(b), the spectrum shows only the injection peak, suppressed by more than 20 dB. This residual signal originates from reflections at the PIC facet and from on-chip reflections of the injected light that are reinjected into the circulator. The measured isolation between the circulator ports (40 dB) was taken into account when estimating the reflected power. Increasing I_{SOA} enhances the intensity of this peak, as the reinjected reflections are further amplified, yet no OFC emission is observed in the C-W direction. This confirms that the comb emission is highly unidirectional and does not perturb the ML.

5.4 Conclusions

This chapter has studied the generation of OFCs on PICs through both Q-switching and GS mechanisms, combining theoretical modelling, simulations, and experimental implementation.

In the first section (Section 5.1), a rate-equation model was developed to study the dynamics of QS in an optically injected single-mode semiconductor laser. The laser was based on a four-section DBR with an intracavity EAM to perform QS. This design is compatible with standardised BBs in generic integration platforms, and the simulation parameters were chosen accordingly, tied to realistic parameters. A balance was found in the EAM design between the maximum achievable ER, the insertion losses, its length, and the threshold at the low loss state. The laser design was then optimised to give the maximum dynamic range between the losses in the on and off state. The simulations showed that actively modulating the cavity losses produces intense, short optical pulses with a large dynamic chirp. This chirp is linked to the strong carrier excursion that occurs when the cavity switches from the high-loss to the low-loss state and results in a pronounced broadening of the optical spectrum. The model therefore predicts that QS could offer OFCs with significantly larger bandwidths than those typically achieved with conventional GS operation while maintaining low repetition rates.

A first attempt at implementing this QS concept in an InP PIC fabricated through a SMART Photonics MPW run was also carried out. The device incorporated an EAM within the laser cavity following the simulated design, with several EAM lengths included to assess their influence on performance. However, CW characterisation revealed high insertion losses in the EAM section, which prevented the laser from reaching threshold at the available drive currents. Consequently, QS operation could not be experimentally demonstrated. This limitation is attributed to excess absorption in the EAM and insufficient cavity gain, but it provides valuable feedback for future iterations. These issues could be mitigated by increasing the SOA length or optimising the EAM design, which would also contribute to reducing the total cavity losses. Despite these experimental challenges, the implementation demonstrates the feasibility of monolithically integrated QS sources and establishes a clear path for future development, as QS-based OFCs have not yet been reported on InP PIC platforms.

The second part of the chapter (Section 5.2) focused on the generation of GS OFCs in a monolithically integrated master–slave configuration. Two DFB lasers were integrated on the same PIC using standard BBs from the Fraunhofer HHI InP platform. The ML optically injected the SL, which was gain-switched by electrical modulation. The use of a SRD enabled the generation of short electrical pulses. Through systematic characterisation, OFCs were successfully generated over a wide range of repetition rates (from 5 GHz down to 500 MHz) demonstrating low repetition rate GS OFCs on a full monolithic PIC implementation. The resulting combs exhibited broad spectral spans, good CNR, and acceptable flatness, validating the potential of this configuration for reconfigurable on-chip comb generation.

The experiments provided valuable insight into the behaviour of monolithically integrated master-slave systems, while also revealing several practical constraints. The absence of on-chip optical isolators resulted in strong mutual coupling between the ML and SL when operating under asymmetric optical injection (with the ML biased at a much higher current than the SL). In addition, compound-cavity effects and unwanted spectral modulations were observed, which hindered systematic optimisation of the operating parameters. The system also showed high sensitivity to small detuning variations, and the finite linewidth of the integrated DFBs limited the achievable coherence of the generated combs.

Finally, Section 5.3 presented an approach based on optically injected SRLs as GS OFC sources, designed to overcome the lack of on-chip optical isolators by enforcing unidirectional emission. The experiments demonstrated stable OFC generation in a single direction, with the ML remaining unaffected by the SRL emission. This strategy proved effective for controlled on-chip GS OFC generation and provides a solid basis for the next chapter, where these OFCs are used to realise and demonstrate a dual-comb generator in a monolithic PIC.

Chapter 6

Integrated dual-comb interferometry

This chapter presents the design, implementation, and experimental demonstration of a monolithically integrated dual-comb generator and a FS subsystem architecture developed on a generic InP platform. The dual-comb system is conceived as a flexible and reconfigurable source capable of generating mutually coherent OFCs without requiring optical isolators, instead exploiting the inherent unidirectional emission of optically injected SRLs.

Section 6.1 describes the operational principle and experimental validation of the dual-comb generator, including its ability to produce OFCs with tunable repetition rates from 500 MHz to 4 GHz, and large compression factors of up to 50,000, demonstrating its suitability for high-resolution spectroscopy with low-bandwidth detection. This section builds upon results reported in López-Querol *et al.*, *Optics and Laser Technology*, 181, 113317 (2025), extending the discussion with additional experimental data.

Section 6.2 introduces a monolithically integrated FS based on an IQ modulator, designed to overcome the limitations of baseband dual-comb detection, where the overlap between positive and negative frequency components hampers accurate spectral reconstruction of the interrogated sample. The proposed device demonstrates effective single-sideband, carrier-suppressed (SSB-CS) modulation. The results described in this section were originally published in López-Querol *et al.*, *Optics and Laser Technology*, 179, 111274 (2024).

Together, these two subsystems represent a significant step towards the realisation of a fully monolithically integrated dual-comb spectrometer. This chapter employs a combination of theoretical modelling, layout- and system-level simulations, and experimental validation to pave the way for future iterations of monolithically integrated dual-comb interferometers.

6.1 Dual-comb generator based on semiconductor ring lasers

A dual-comb generator based on a PIC is realised by exploiting the unidirectional operation of optically injected SRLs. Fig. 6.1 shows a schematic layout of the proposed design and a photograph of the fabricated PIC. The device comprises two parallel SRLs (SRL1 and SRL2) that act as the OFC sources. When gain-switched at slightly different repetition rates, they generate a dual-comb. To ensure mutual coherence, OI is performed in a master-slave configuration using either an internal or an external ML. The internal OI is provided by a SG-DBR laser [78] to provide tunability. SOA1 and SOA2 control the injected power into SRL1 and SRL2, respectively. Two additional semiconductor optical amplifiers, SOA-IN and SOA-OUT, boost the signals at the on-chip I/O ports, EXTERNAL LASER INPUT on the west facet (for external-laser OI) and SYSTEM OUTPUT on the east facet (comb output), respectively. The SG-DBR can be characterised independently via the LASER OUTPUT port located on the east facet.

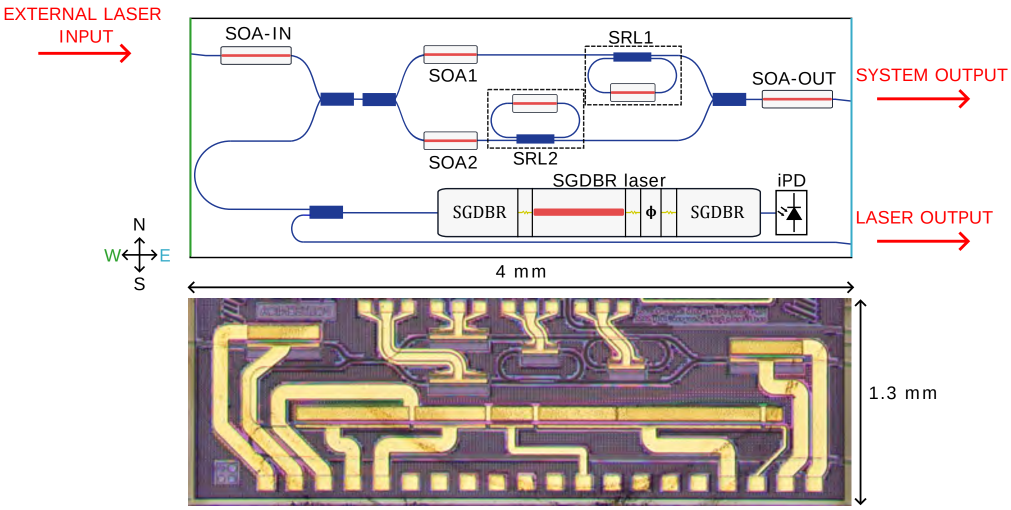

Figure 6.1: Scheme and photograph of the integrated dual-comb generator system. SOA: semiconductor optical amplifier; SG-DBR: sampled-grating distributed Bragg reflector; SRL: semiconductor ring laser; MMI: multimode interference coupler; PD: photodetector.

The design was carried out using the standard BBs provided by SMART Photonics in its PDK library. Fabrication was performed through a MPW run. The system footprint is 4 mm×1.3 mm. SOA-IN and SOA-OUT are 500 μm long, while SOA1 and SOA2 are 400 μm long. The optical facets of the PIC (west and east) are AR-coated and the on-chip I/O waveguides are tilted by 7° with respect to the PIC facets. All optical routing employs deep-etched, single-mode waveguides of 1.5 μm width (losses $\sim$ 3 dB/cm), except the I/O where wider shallow-etched waveguides are employed to improve the PIC to fiber coupling. Shallow-to-deep transitions are omitted in the schematic for simplicity. The bend radius of the waveguide bends is 100 μm. Both the SRLs and the SG-DBR are CBBs based on the basic BBs of the foundry, since they are not offered as standardised BBs.

The SRLs follow the design described in Section 5.3. Each ring incorporates a 250 μm-long SOA, and the cavity is formed by the standard deep-etched waveguides with a bend radius of 100 μm. The total physical cavity length is 1.42 mm, which gives an FSR of approximately 0.46 nm, assuming a group index $n_g \approx 3.65$. The electrical terminations provided by the PDK SOAs are not intended for high-speed modulation. Therefore, to enable GS, a custom GSG metal interconnect was designed to provide RF access to the SRLs and to SOA1 and SOA2.

The internal SG-DBR ML comprises two SG-DBR mirrors separated by a gain section and an intra-cavity phase shifter. The gain is provided by a 500 μm SOA (not labelled in Fig. 6.1), followed by a 300 μm phase section for fine wavelength tuning. Each SG-DBR mirror consists of a periodic configuration of gratings interspersed with phase shifter sections, as described in [100], where a tunability of 34 nm was achieved.

The periodicity of the SG-DBRs gives rise to periodic maxima in their reflection spectrum, which can be tuned by driving their current [251], thus enabling the tuning of the laser emission wavelength to perform OI in different spectral regions. The front SG-DBR comprises fourteen periods, each formed by a 10 μm grating segment and a 50 μm phase section. The rear SG-DBR contains twenty-five periods with the same grating length and 54 μm phase sections. The grating pitch is 0.237 μm, which places the Bragg maxima near 1550 nm. The laser includes an integrated photodiode (iPD) at the rear facet for power monitoring. Six DC contacts provide access to the SOA, the front and rear SG-DBR mirrors, the fine-tuning phase section, iPD, and a common ground. The physical cavity length is 3227 μm, and assuming a coupling constant κ of 50 cm^{-1} and group index $n_g \approx 3.65$, the total effective cavity length is around 2622 μm and the FSR is 0.13 nm.

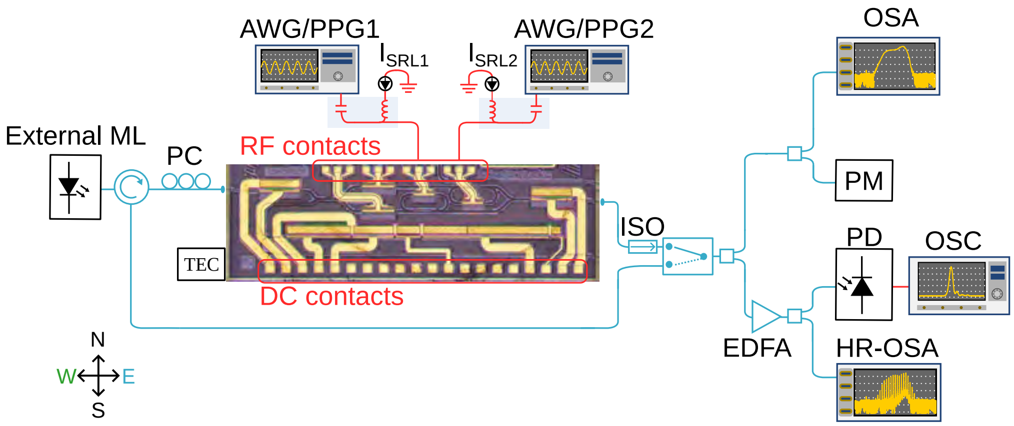

Figure 6.2: Schematic of the experimental setup used for the characterization of the integrated dual-comb generator system. PPG: pulse pattern generator; AWG: arbitrary waveform generator; PC: polarization controller; ISO: optical isolator; EDFA: erbium doped fiber amplifier; OSA: optical spectrum analyzer; HR-OSA: High-Resolution Optical Spectrum Analyzer; OSC: oscilloscope; PD: photodetector; PM: power meter.

To characterise the PIC, the setup described in Fig. 6.2 is employed. The OSA and PM are used for fiber alignment and characterisation in CW. On the other branch, the EDFA is used to boost the signal, which is then analysed by the HR-OSA and a real-time oscilloscope. Two lensed fibers, positioned at the west and east facets of the PIC, are used to inject and collect light. The optical switch alternates between these facets and directs the collected light to two branches of the instrument, as illustrated in Fig. 6.2. The measured light at the west facet consists of the light reflected at the facet, the CC-W emission from SRL1, and the C-W emission from SRL2. The external laser used for injection is the tunable, narrow linewidth laser covering the C-band.

The PIC is mounted on the probe station of Section 4.1 and its temperature is stabilised to 25°. Two probe arrays provide electrical access to the PIC. DC probes are used for the input and output amplification SOAs (SOA-IN and SOA-OUT), as well as for the SG-DBR. RF probes, on the other hand, are used for the SOAs of the SRLs and the OI amplification SOAs (SOA1 and SOA2). All SOAs (except the SRL SOAs) and the integrated ML are driven by DC current sources. The bias currents of the SRLs are set by a DC current source and combined with the RF GS signals in bias-tees. The RF signal is provided by either the PPG or the AWG.

Continuous-wave characterisation of the master and slave lasers

Before investigating the GS operation and OI locking behaviour of the SRLs, it is useful to first characterise the integrated SRLs by measuring their PI curves and optical spectra at different driving currents. This provides a deeper understanding of the operational characteristics of the device. The PI curve is obtained using the PM, while the optical spectra are recorded with the OSA.

For completeness, the characterisation of a stand-alone SRL, isolated from the rest of the system, is also reported, as the dual-comb configuration introduces additional complexity to SRL operation due to the presence of other integrated components. The isolated SRL, fabricated on the same PIC, is schematically shown in Fig. 6.3(a). Its physical dimensions and structure are identical to those of SRL1 and SRL2, except that one of its optical outputs includes a slow integrated PD acting as a laser monitor, and the electrical contacts are DC pads. As shown, the laser features an optical output for measuring the CC-W emission spectrum and optical power, while the monitor enables measurement of the C-W optical power.

Fig. 6.3(b) shows the CC-W and C-W PI curves of the single SRL for currents ranging from 0 to 120 mA in 1 mA steps, with a threshold current of around 15 mA. The vertical axis represents the photocurrent proportional to the optical power measured at the external PD and at the monitor, respectively. The data have been normalised to the maximum value of each measurement, corresponding to photocurrents of 7 mA and 0.5 mA measured at the monitor and PM, respectively.

Slightly above the threshold and up to a driving current of 30 mA, bidirectional emission from the two counter-propagating optical fields can be seen. From 30 mA onward, the power emitted by each direction is anti-correlated and this is maintained for all current values, operating the laser in a bidirectional regime with no complete unidirectional emission observed.

Regarding the optical spectra, Fig. 6.3(c) presents a current–wavelength map of the C–W emission measured with the OSA over the same bias range as the PI curve in panel (b). Just above the threshold and up to approximately 50 mA, the device operates in single mode with occasional longitudinal mode hops. Above 50 mA, the SRL emission becomes predominantly multimode. The longitudinal mode spacing is about 0.5 nm, which is in good agreement with the expected FSR (0.463 nm). Both the PI characteristics and the spectra are consistent with previous reports [252], where irregularities in the PI curve are attributed to changes in the modal composition of the spectrum. It is also worth noting that the presence of the monitoring PD measuring the light emitted in the C-W direction may affect the propagation and modal dynamics within the cavity, although this effect has not been investigated in this work.

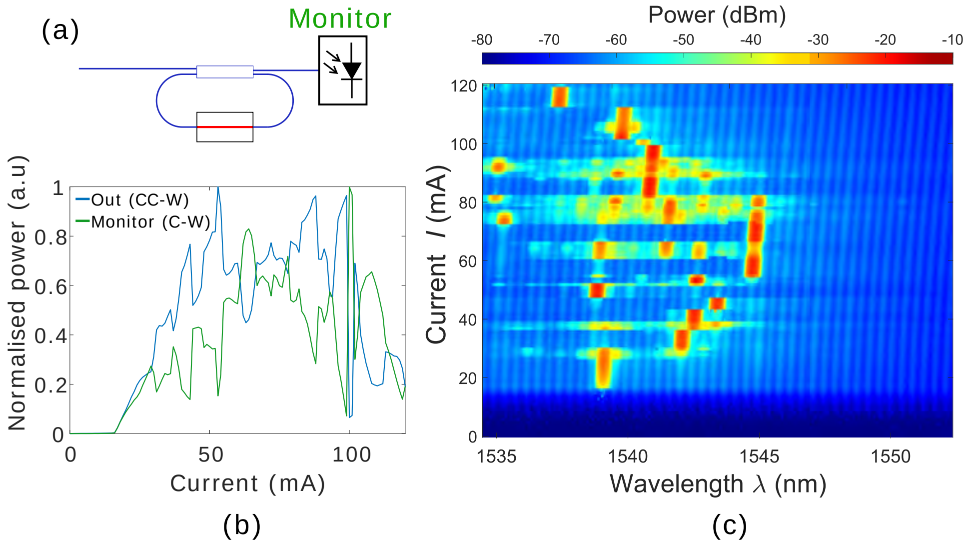

Figure 6.3: (a) Schematic of the stand-alone SRL integrated in the same PIC as the dual-comb system. (b) Normalized PI curve of the SRL in both propagation directions, and (c) Map of the spectra as a function of the driving current of the SRL.

The same characterisation for SRL1 within the dual-comb system is shown in Fig. 6.4, where this time the current ranges from 0 to 50 mA in steps of 1 mA. It plots the photocurrent measured at the east and west facets of the PIC as a function of the DC drive current of SRL1 (I_{SRL1}), with SRL2 unbiased and both SOA-IN and SOA-OUT held at 100 mA. These SOA biases are maintained for all subsequent measurements.

The photocurrent in panel (a) (east facet) corresponds to optical power from SRL1 propagating C-W, whereas panel (b) (west facet) corresponds to CC-W propagation. In both panels, data are shown for several fixed values of the SOA1 bias current (I_{SOA1}). The threshold current of SRL1 is approximately 20 mA, and it decreases with increasing I_{SOA1}. This reduction is attributed to optical seeding from SOA1 amplified spontaneous emission (ASE) that generates a certain level of carriers in the SRL1 active region. Furthermore, SRL1 emission is enhanced in both directions for increasing SOA1 currents.

As it can be observed in Fig. 6.4, the power obtained at the east facet (C-W emission) is four to five times greater than that obtained at the west facet (CC-W). This is related to the

ASE injected by the different SOAs in the system in one of the propagation directions. When all SOAs are driven with a current above their transparency, the ASE coming from SOA-IN and SOA1 reaches the SRL1 injecting in the C-W direction. The amount of ASE injected in this direction is higher than that injected in the CC-W direction by SOA-OUT. Thus, this enhances emission in the C-W direction, an outcome observed in Section 5.3 indicating high unidirectionality in the SRL emission.

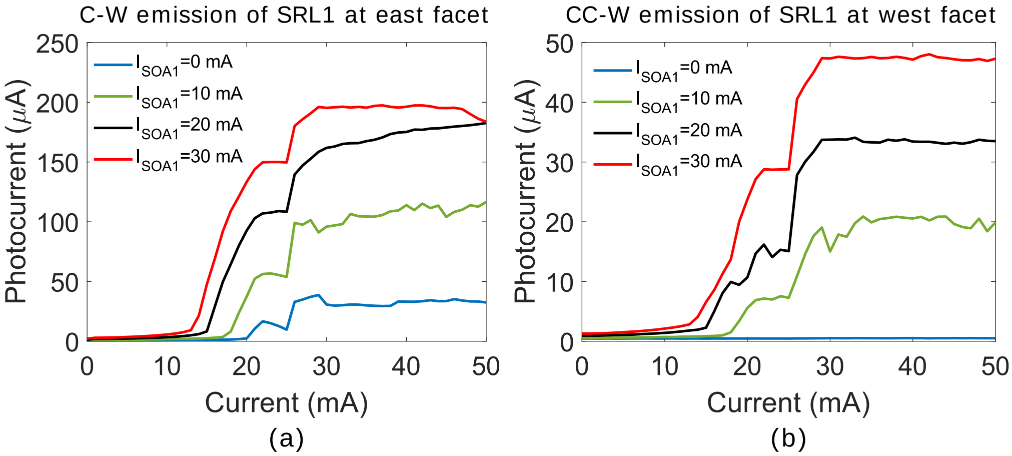

Figure 6.4: PI characteristics of the SRL1 laser. (a) C-W PI curve measured on the east facet of the PIC for different SOA1 injection currents (I_{SOA1}). (b) CC-W PI curve measured on the west facet of the PIC under identical conditions as in panel (a).

In addition, the PI characteristic exhibits a pronounced plateau for drive currents above ~ 30 mA. The plateau persists across different I_{SOA1} values, indicating that its origin is unlikely to be gain saturation in the SOAs. In light of these results, and the absence of such behaviour in the isolated SRL (Fig. 6.3), we attribute the effect to the influence of the on-chip SOAs. Notably, around this current the stand-alone SRL began to show anti-correlated C-W/CC-W emission and successive mode hops without a stable unidirectional state, similar to that reported in [252], which reported bidirectional emission with comparable powers close to threshold and, at higher pump currents, regions of unbalanced anti-correlated C-W/CCW power, but no plateau in the PI characteristic.

The presence of SOA1 in the dual-comb configuration may alter the power anti-correlation between the counterpropagating modes of the SRL, either disrupting it or partially rebalancing the emitted power in each direction. This effect can lead to an apparent clamping of the total photocurrent, manifested as the plateau observed in the PI curve. Similar behaviour is observed for SRL2. To the best of our knowledge, this plateau effect in integrated SRLs has not been previously reported and warrants further investigation, although it does not affect the results presented in the following.

Figure 6.5 shows the spectra recorded at SYSTEM OUTPUT for SRL1 and SRL2 operated individually (a) and simultaneously (b) at a bias current of 40 mA. The SOA currents are set to 0 mA in both cases. At this bias and across most of the bias range in Fig. 6.4 both SRLs lase on a single longitudinal mode, although at some regions there are mode hops and simultaneous emission from two or three modes, as observed in the isolated SRL characterisation Fig. 6.3. The FSR is approximately 0.5 nm, in accordance with the designed value. When both lasers operate simultaneously, the measured spectrum is essentially the superposition of the individual spectra, indicating negligible mutual coupling under these conditions.

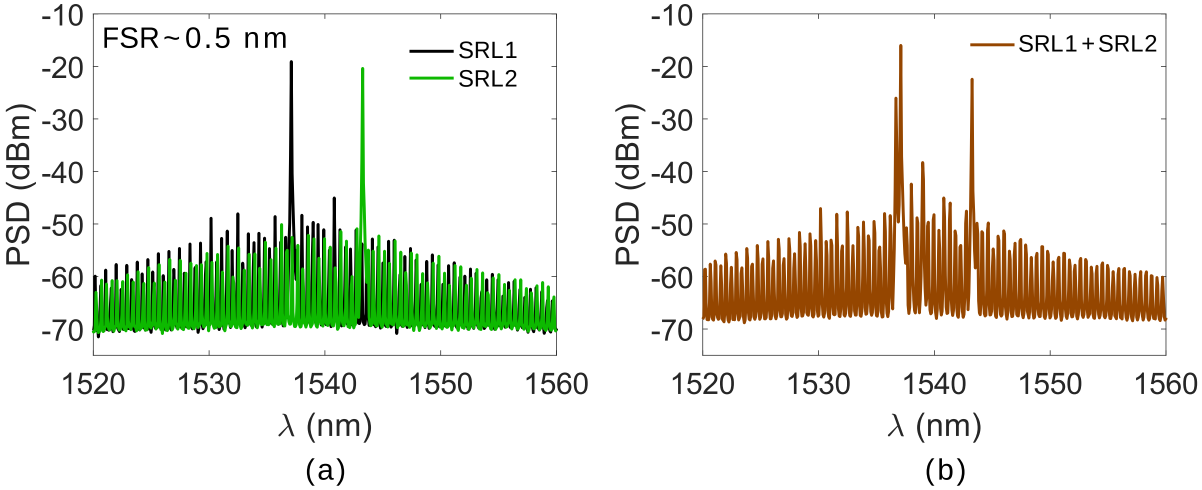

Figure 6.5: Optical spectra of the two SRLs. (a) Individual optical spectra of SRL1 (blue) and SRL2 (red), each operating at 40 mA. (b) Resulting optical spectrum when both SRL1 and SRL2 are simultaneously operating at 40 mA. More details on the operating conditions can be found in the text.

Finally, the integrated SG-DBR laser PI curve and the spectrum recorded at LASER OUTPUT are shown in Fig. 6.6. Panel (a) plots the photocurrent measured at the external PD and iPD in 1 mA current steps. The traces are normalised to their respective maxima, which are 6 mA at the external PD and 0.5 mA at iPD. The threshold current is approximately 20 mA. Two kinks at 23 mA and 80 mA, attributed to longitudinal mode hops, are evident in the PI curve measured by the iPD. The same features are present in the PI measured at the PIC output, but they are not distinguishable in the figure due to the lower detected power.

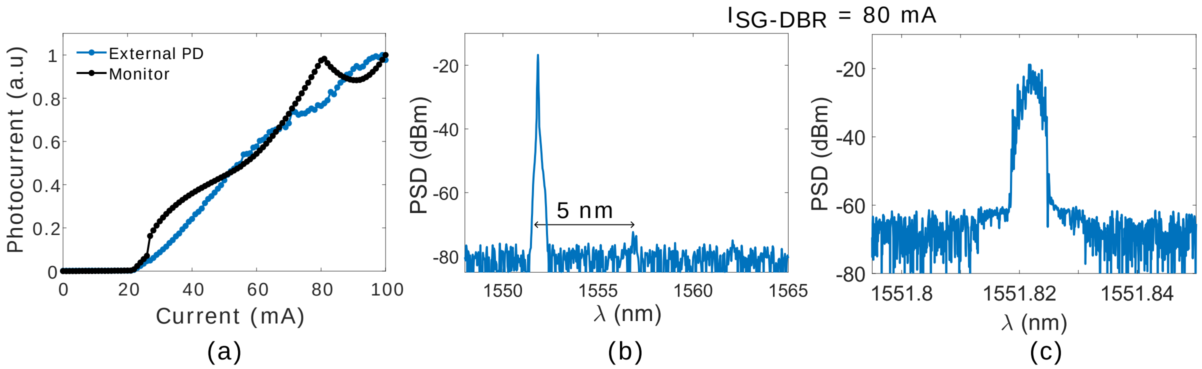

Figure 6.6: (a) PI curve of the integrated SG-DBR laser measured at the LASER OUTPUT of the PIC and at its internal monitor, respectively. Spectra of the integrated SG-DBR laser at a current of 80 mA measured with (b) the OSA and (c) the HR-OSA.

Panels (b) and (c) show spectra at $I_{\mathrm{SGDBR}} = 80$ mA, recorded simultaneously with the OSA and the HR-OSA, respectively. The lasing wavelength is 1551.82 nm. The HR-OSA trace indicates an optical linewidth of ~ 540 MHz measured at -20 dB, which indicates that the Lorentzian or intrinsic linewidth is substantially larger than the narrow linewidths reported before for integrated SG-DBR, e.g. 70 kHz in [253]. However, linewidths exceeding 100 MHz have been observed in SG-DBRs under certain conditions [254] attributed to the lack of optimisation of the operating conditions of the laser, mainly the mirror tuning.

Therefore, we attribute the observed broad linewidth to a misalignment of the SG-DBR mirrors, which could not be properly tuned. This misalignment lowers the effective mirror reflectivity and increases cavity losses at the operating wavelength, thereby broadening the emission spectrum [104], [254]. Although tuning the SG-DBR mirrors should improve the linewidth, no wavelength tunability was observed when the injection current in the SG-DBR mirror sections was varied. This lack of tunability is likely due to ineffective current injection into the SG-DBR mirror sections.

Optical frequency comb generation

This section presents OFC generation results obtained from the SRLs, complementing Section 5.3. First, OFC generation was investigated using the internal SG-DBR laser as the ML to optically inject the gain-switched SRL1. For this purpose, the setup shown in Fig. 6.2 was employed without the external ML. A sinusoidal signal from the AWG, subsequently amplified, provided the GS drive. The SRL operating conditions and OI parameters for comb generation were empirically adjusted in each case to obtain OFCs with optimal characteristics, as their systematic optimisation lies beyond the scope of this study.

Fig. 6.7 shows the measured spectra at the west (a) and east facet (b) when a 1 GHz repetition rate OFC is generated by SRL1 at driving currents of $I_{\mathrm{SRL1}} = 20$ mA, $I_{\mathrm{SOA1}} = 10$ mA and $I_{\mathrm{SG-DBR}} = 83$ mA. The peak-to-peak amplitude of the sinusoidal modulating signal is set to $V_{\mathrm{RF}} = 3.5$ V, and spectra are recorded in the HR-OSA. In the same way as observed in Section 5.3, OI forces a highly unidirectional emission, where in this case the signal propagating in the CC-W direction only consists of the OI peak and is suppressed by more than 50 dB.

The comb features 30 optical lines above the noise floor, with the injection peak around 1551.85 nm being particularly prominent. In the inset of Fig. 6.7(b), it can be seen how the SL inherits the linewidth of the ML through the OI locking mechanism [153]. The observed tone linewidth is as wide as the single-mode linewidth of the integrated SG-DBR laser, shown in Fig. 6.6. This demonstrates that OI locking is effectively achieved as the SL emission is pulled towards the ML emission. Furthermore, no other longitudinal mode of the SRL1 is observed, indicating that they are suppressed due to the OI.

However, the limited tunability of the integrated ML makes it unsuitable for DCI. Dual-comb operation relies on setting an appropriate detuning between the ML and each SRL, and this detuning must be adjusted with fine wavelength control to optimise both combs. Since the SG-DBR wavelength cannot be tuned, the system is constrained to a fixed detuning that is generally not optimal. In practice, this prevents proper optimisation of the OFC emission and restricts access to specific spectral regions. For these reasons, a tunable external ML is used, as it allows the detuning to be set with the precision required for the simultaneous locking and optimisation of both SRLs.

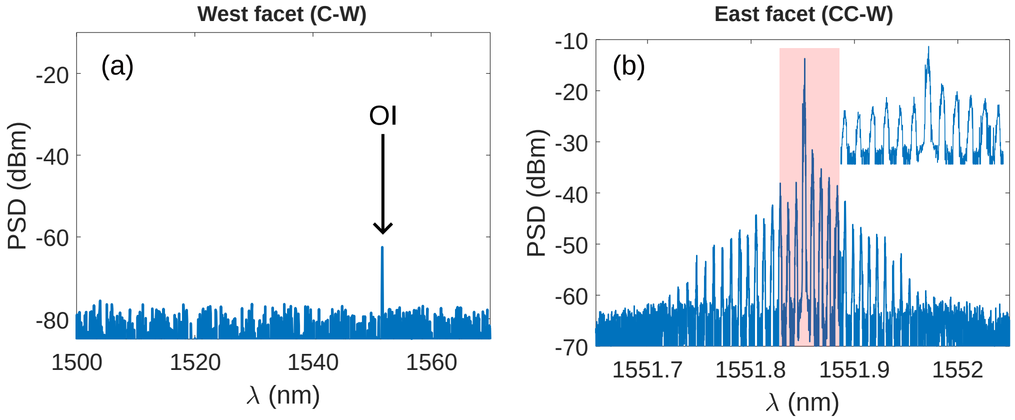

Figure 6.7: Measured optical spectra with the HR-OSA at the west (a) and east (b) facets when SRL1 is gain-switched at a 1 GHz repetition rate and optically injected by the integrated SG-DBR laser. The spectra show that under OI the SRL emission is forced to follow the injection direction.

For this reason, the tunable, narrow-linewidth external ML was employed to demonstrate dual-comb generation and to achieve OI locking in both OFCs simultaneously. The setup of Fig. 6.2 was used, performing OI with the external ML. Note that the external light is injected into the C-W (CC-W) propagation direction of SRL1 (SRL2). Fig. 6.8 shows how OI locking affects the emission of SRL1 in CW. Spectra were measured at SYSTEM OUTPUT. The blue trace corresponds to the free-running laser, while the black and red traces correspond to external OI at 1545.6 nm and 1549.74 nm, respectively, showing enhancement of the injected mode and suppression of the others. The injected power at SYSTEM INPUT is 0 dBm. SOA1 is biased at 50 mA, and SRL1 at 40 mA.

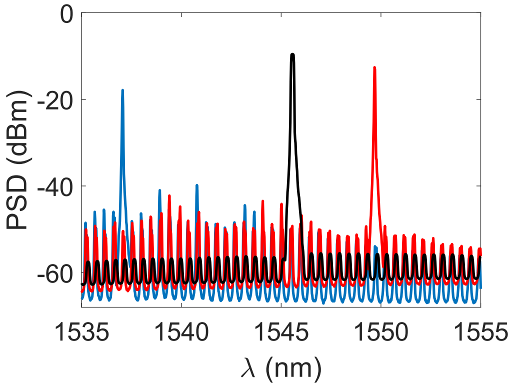

Figure 6.8: Optical spectra of SRL1 measured at SYSTEM OUTPUT under free-running operation (blue) and under OI locking at 1545.6 nm (black) and 1549.74 nm (red) by an external narrow-linewidth tunable laser.

The SRL1 is gain-switched with a 500 MHz pulsed signal generated by the PPG with an 8 V peak-to-peak amplitude and a bias current of $I_{SRL1} = 15$ mA. Fig. 6.8 shows the optical spectra of the OFCs generated with SRL1 when $I_{\mathrm{SOA1}} = 0$ mA and $I_{\mathrm{SOA1}} = 10$ mA. The OI is performed at a wavelength of 1549.79 nm. The driving currents of SOA2 and SRL2 are kept at 0 mA.

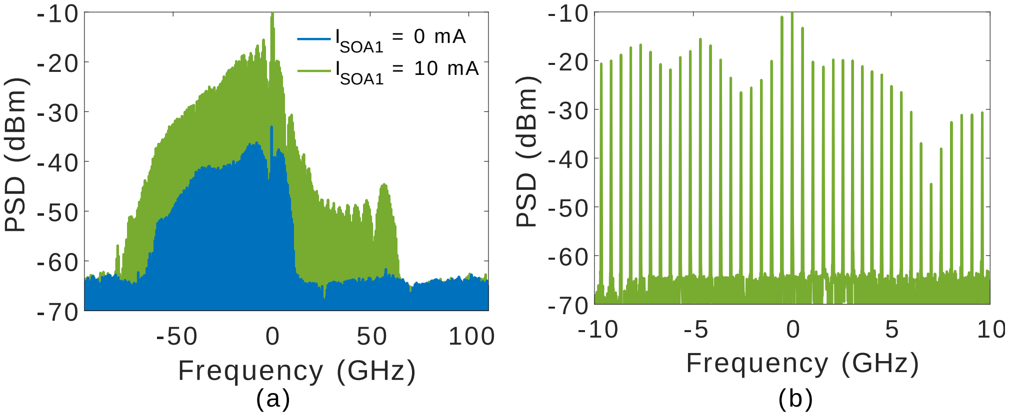

(a)

(b)

Figure 6.9: Spectra of the OFCs generated by SRL1 at a repetition rate of 500 MHz under OI from the external laser. (a) OFCs for $I_{\mathrm{SOA1}} = 0$ mA and $I_{\mathrm{SOA1}} = 10$ mA measured in the HR-OSA. The injection wavelength (1549.79 nm) is located at the origin of the frequency axis. (b) Detailed view of the OFC for $I_{\mathrm{SOA1}} = 10$ mA.

Fig. 6.9(b) shows a zoomed-in spectrum for $I_{\mathrm{SOA1}} = 10$ mA, where comb lines are resolved with a spacing of 500 MHz. The injection wavelength (1549.79 nm) defines the 0 GHz line. The -20 dB optical bandwidth of both combs is approximately 40 GHz. As I_{SOA1} increases from 0 mA to 10 mA, the comb power increases consistent with the enhancement of the peak power of the pulses over time. No further increase is observed when I_{SOA1} is raised from 10 mA to 50 mA. Notably, even at $I_{SOA1} = 0$ mA, despite substantial absorption of the injected light, the injected power is sufficient to achieve OI locking and generate an OFC because the injection is aligned to a longitudinal mode of the SRL [250].

The driving current of SOA2 does not significantly impact the OFC generation in SRL1. This evidences that, aside from the thermal effects that may manifest when both SRLs and SOAs are operating, the two SRL branches would work primarily in an optically independent manner, which is important for flexible operation, and the use of SRLs is a significant benefit for the integrated dual-comb generator system.

Dual-comb generation

Building on this basis, we investigate dual-comb generation. Both SRLs are gain-switched at slightly different repetition frequencies, while mutual coherence between the two combs is provided by the tunable laser injected into the PIC. For each operating point, the drive currents, GS drive, injection conditions, and PIC temperature are adjusted to optimise flatness and optical bandwidth. The HR-OSA is used to measure the generated OFCs, allowing to resolve the individual comb lines. Finally, the interferograms resulting from the interference of the two OFCs on the high-speed PD are monitored with the real-time oscilloscope (Fig. 6.2).

Fig. 6.10(a), shows the spectra of the two OFCs generated non-simultaneously in SRL1 and SRL2, with repetition frequencies of 2 GHz and 2.1 GHz (δf_r = 100 MHz), respectively. Therefore, the compression factor (see Section 3.3) is CF = 20. Fig. 6.10(b) shows the spectra when both OFCs are generated simultaneously. For both SRLs the bias current is 20 mA, and the GS signal from the AWG has a peak-to-peak amplitude of 3.5 V. To ensure OI locking in both SRLs, the injection is set at 1549.62 nm with 0 dBm power, which defines the 0 GHz reference in the spectra.

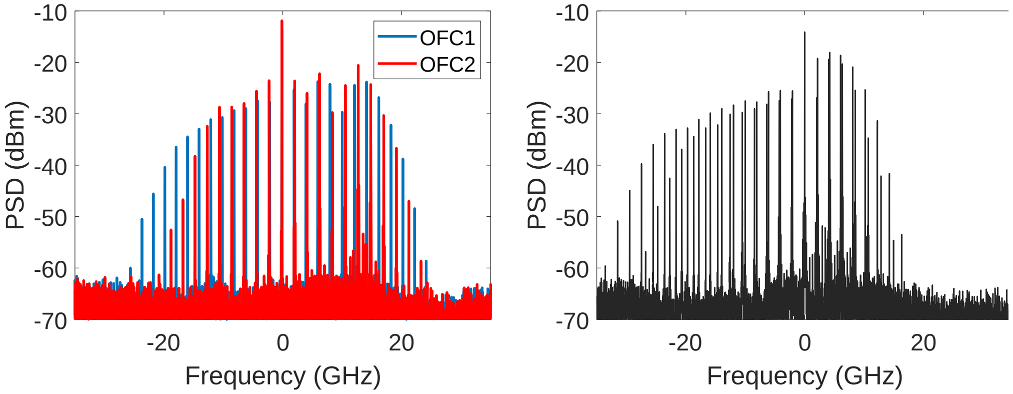

Figure 6.10: OFCs generated (a) separately and (b) simultaneously by SRL1 and SRL2, with repetition rates of 2 GHz and 2.1 GHz, respectively, for the same driving conditions.

Each OFC contains around 15 tones within the −20 dB envelope (≈ 30 GHz optical bandwidth). The spectrum obtained when both combs are generated simultaneously mostly matches the superposition of the spectra measured non-simultaneously. The observed differences arise from device heating when all elements operate concurrently, producing a shift towards more negative optical frequencies (i.e., longer, red-shifted wavelengths).

The beating of the two combs produces the interferogram in Fig. 6.11(a). Successive bursts repeat every 10 ns, consistent with $1/\delta f_r$ for $\delta f_r = 100$ MHz. The squared-magnitude Fourier transform of these interferograms gives the RF dual-comb in Fig. 6.11(b), with line spacing of 100 MHz, confirming successful dual-comb generation. The DC (0 Hz) component corresponds to the beating of the OI lines, which coincide in both combs, as seen in Fig. 6.10.

Thus, the optical bandwidth is compressed by the factor CF = 20 to 30 GHz/20 = 1.5 GHz. The replicas in the higher order Nyquist zones arising from non-adjacent optical line beatings are centred near 2 GHz and its multiples. Three such zones are shown. In this operating point, CF is smaller than the number of visible comb lines, so adjacent Nyquist zones overlap, hindering a one-to-one, alias-free mapping of the optical spectrum (see Eq. (3.17)).

To avoid this overlap, we explored dual-comb generation at lower repetition frequency and increasing the compression factors. Fig. 6.12(a) shows the interferogram obtained for $f_{r1} = 500$ MHz and $f_{r2} = 500.01$ MHz (i.e. $\delta f_r = 10$ kHz, CF $= 50,000$), together with the corresponding RF comb. The combs are generated using pulsed GS signals from the PPG. The OFC characteristics are similar to those in Fig. 6.9. As can be seen, the Nyquist zones are now well separated (every 500 MHz). For clarity, only the strongest lines within the lower half of the first Nyquist zone are shown. These results demonstrate that our dual-comb generator is flexible in the choice of repetition frequency, either obtained by pulsed or sinusoidal excitation, as well as in the achievable CF.

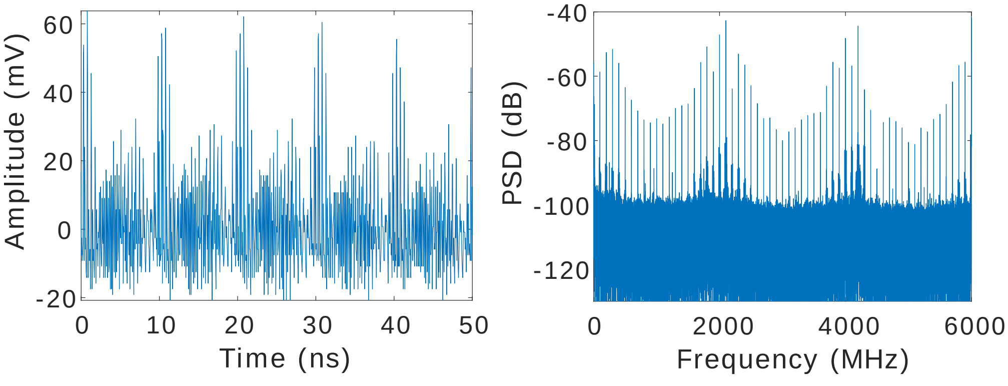

(a)   (b)

Figure 6.11: Dual-comb generation with the previously shown OFCs featuring $f_r = 2$ GHz and $\delta f_r = 100$ MHz (CF = 20). (a) Interferograms in time measured with the real-time oscilloscope. (b) Down-converted spectrum obtained from the FFT of the interferograms showing three Nyquist zones.

Simultaneous optimisation of both combs was challenging because the two SRLs exhibited slightly different emission envelopes, requiring careful adjustment of the parameters involved in OFC generation. The operating point that maximises the CNR for one comb therefore does not necessarily coincide with that of the other. Since each RF tone originates from the beating of corresponding optical lines, any imbalance in optical power or CNR between the two combs results in uneven RF tone amplitudes and local variations in SNR across the RF spectrum. In particular, strong optical lines from one comb may beat with weaker lines from the other, producing lower-amplitude RF tones and locally reducing the SNR. Despite these differences, the measured average SNR of approximately 20 dB is sufficient to resolve molecular absorption features in typical gases. For instance, the absorption lines of CO_2 and HCN in the C and L bands correspond to optical losses of a few decibels for cm-scale path lengths, while CO and NH_4 exhibit weaker but still detectable features under similar conditions [168].

The plotted electrical spectrum arises from the expected overlap between the negative and positive components within the first Nyquist zone. Under baseband detection, beat notes from comb lines to the right of the OI line superpose with the mirror contributions from lines to the left, folded about DC. This folding masks spectral features and complicates the retrieval of a sample's amplitude response. In bulk dual-comb systems, introducing a frequency shift, typically via an AOM, prevents this overlap by moving the first Nyquist zone away from DC. As AOMs are impractical in monolithic implementations, and to preserve a fully integrated InP approach, the next section introduces a frequency shifter built from standard BBs in the same generic InP foundry, enabling future co-integration with the dual-comb generator and displacement of the RF mapping from baseband without resorting to bulk, external AOMs.

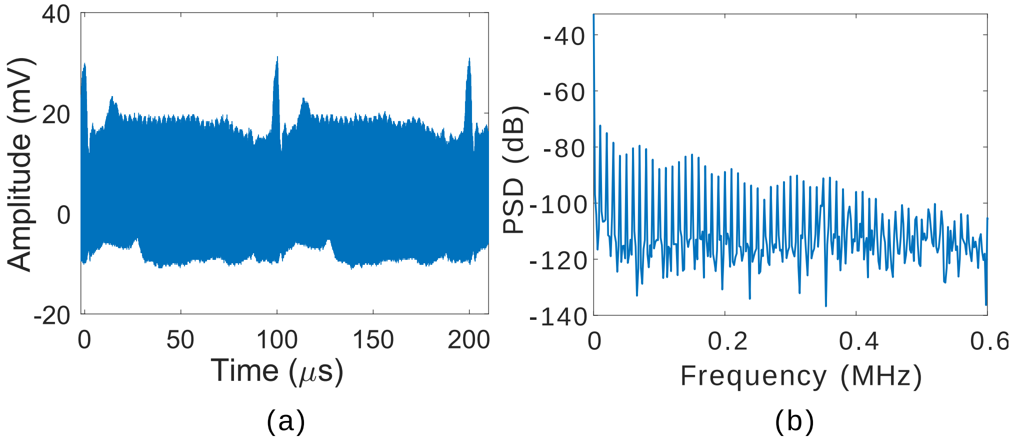

Figure 6.12: Dual-comb generation with OFCs of $f_\mathrm{R} = 500$ MHz and $\Delta f_\mathrm{R} = 10$ kHz (CF = 50,000). (a) Interferogram measured with the real-time oscilloscope. (b) Down-converted spectrum obtained from the FFT of the interferogram.

6.2 Optical frequency shifter for dual-comb interferometers

In this section, a fully monolithic optical frequency shifter implemented with an IQ modulator is realised on the SMART Photonics platform using standard BBs, as schematically shown in Fig. 6.13. IQ-based single-sideband, carrier-suppressed (SSB-CS) modulation has emerged as a practical alternative to AOMs [255], [256]. On silicon-based PICs, such shifters have demonstrated frequency offsets up to 10 GHz, with carrier and spurious-sideband suppression ratios in the 16-23 dB range [257]. The performance of these devices is typically assessed in terms of the carrier suppression ratio (CSR), which quantifies the rejection of the optical carrier, and the sideband suppression ratio (SBSR), which measures the suppression of the unwanted sideband relative to the desired one.

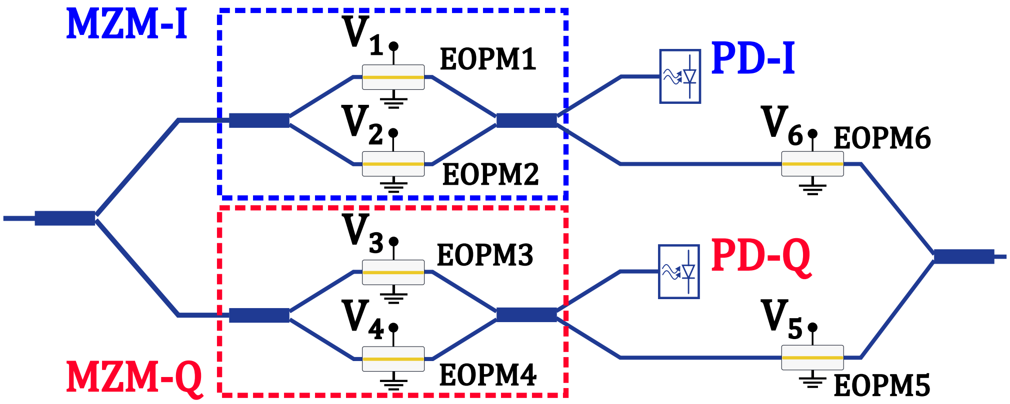

Figure 6.13: Schematic of the integrated frequency shifter based on a IQ modulator.

A conventional IQ modulator comprises two nominally identical MZMs in parallel, the in-phase (I) and quadrature (Q) arms, together with a phase shifter that imposes a $\pi/2$ offset between the two arms. To realise the frequency shift, both MZMs are driven in push-pull ($V_A(t) = -V_B(t)$), so their EOPMs induce equal and opposite phase shifts ($\varphi_A(t) = -\varphi_B(t)$). With each MZM biased at minimum transmission and driven by quadrature RF waveforms (cosine on the I arm, sine on the Q arm) and a constant $\pi/2$ phase offset between I and Q, the output field, $E_{out}(t)$ becomes an attenuated, frequency-shifted replica of the input $E_{in}(t) = E_0 e^{j\omega_c t}$ at the RF drive ω_s. For a small drive $R = A/V_\pi$ relative to the half-wave voltage V_π, the Jacobi-Anger series can be truncated to first order, and the output field is given by

$$E_{out} = \frac{1}{\sqrt{2}}\left(E_{out}^{I} + E_{out}^{Q}\right) = E_0 J_1(\pi R) e^{j(\omega_c \pm \omega_s)t} \tag{6.1}$$

where E_{out}^{I} and E_{out}^{Q} are the optical field outputs of the I- and Q-branch MZMs, respectively, and $J_1(\pi R)$ is the value at πR of the first order Bessel function of the first kind. The sign of the frequency shift in Eq. (6.1) depends on the relative sign of the modulating RF signals.

The operating principle outlined above is implemented in a monolithic InP IQ modulator. However, two practical aspects must be addressed regarding the implementation into this platform. First, the InP EOPMs available in this platform differ from conventional LN devices because they are based on InP/InGaAsP PIN junctions that are driven under reverse bias [258]. In this regime, the combined action of field-induced (predominantly Pockels) and carrier-induced (plasma dispersion and band-filling) effects produces an effective phase shift that is approximately linear with the applied voltage. This bias point also offers good device characteristics such as high electrical bandwidth. Under the usual sign convention, the induced phase shift is negative [259], which necessitates minor adjustments to the differential RF drive and biasing of the MZMs relative to the textbook case.

Secondly, the modulator half-wave voltage V_π scales inversely with the EOPM length. Extending the phase shifter therefore reduces the required drive voltage and improves compatibility with standard laboratory voltage sources, but at the cost of a larger footprint and higher optical insertion losses. The choice of length is thus a design trade-off between V_π, loss, and footprint.

Beyond these platform-level considerations, fabrication tolerances introduce uncontrolled differences in each EOPM. This can translate to differences in the V_π value and additional voltage-independent phase shifts (φ_0) due to the differences in the optical path. As a result, a first calibration of the IQ modulator must be done that requires access to the optical power at several points in the circuit.

To enable the on-chip calibration process, the design in Fig. 6.13 integrates two on-chip photodiodes (PD-I and PD-Q) employing a 2 × 2 MMI coupler at the output of the MZMs. These allow monitoring of the optical output power of each MZM, providing direct measurements of the V_π and other parameters as it will be detailed in the following. To better understand the operation of the device, the expression of the optical field reaching PD-I and PD-Q and at the output of the MZMs can be written as

$$E_{PD}^{I}(t) = \frac{E_{in}(t)}{2\sqrt{2}}\left(e^{j(\varphi_1(t)+\frac{\pi}{2})} + e^{j\varphi_2(t)}\right), \tag{6.2}$$

$$E^{I}_{out}(t) = \frac{E_{in}(t)}{2\sqrt{2}}\left(e^{j\varphi_1(t)} + e^{j(\varphi_2(t)+\frac{\pi}{2})}\right), \tag{6.3}$$

for the I branch, and

$$E^{Q}_{PD}(t) = \frac{E_{in}(t)}{2\sqrt{2}}\left(e^{j(\varphi_3(t)+\frac{\pi}{2})} + e^{j\varphi_4(t)}\right), \tag{6.4}$$

$$E^{Q}_{out}(t) = \frac{E_{in}(t)}{2\sqrt{2}}\left(e^{j\varphi_3(t)} + e^{j(\varphi_4(t)+\frac{\pi}{2})}\right), \tag{6.5}$$

for the Q branch. In these expressions $\varphi_i(t) = \varphi_{0i} + \Delta\varphi_i(t)$ is the total phase shift induced by each EOPM, including the voltage independent term φ_{0i} arising from the fabrication tolerances and the voltage dependent term $\Delta\varphi_i(t) = \pi V_i(t)/V_{\pi i}$ from the i^{th} EOPM. It is convenient to rewrite Eq. (6.3) and Eq. (6.5) as

$$E^{I}_{out}(t) = \frac{E_{in}(t)}{2\sqrt{2}}e^{j\alpha_I}\left(e^{j\left[\Delta\varphi_1-\left(\varphi^I_0+\frac{\pi}{2}\right)\right]} + e^{j\Delta\varphi_2}\right), \tag{6.6}$$

$$E^{Q}_{out}(t) = \frac{E_{in}(t)}{2\sqrt{2}}e^{j\alpha_Q}\left(e^{j\left[\Delta\varphi_3-\left(\varphi^Q_0+\frac{\pi}{2}\right)\right]} + e^{j\Delta\varphi_4}\right), \tag{6.7}$$

respectively, where $\alpha_I = \varphi_{02} + \pi/2$, $\alpha_Q = \varphi_{04} + \pi/2$, $\varphi^I_0 = \varphi_{02} - \varphi_{01}$ and $\varphi^Q_0 = \varphi_{04} - \varphi_{03}$.

Since the measurable magnitude in the integrated PDs is the generated photocurrent proportional to the optical power, given by $P = |E|^2$, it is convenient to write the expressions

$$P^{I}_{PD} = \frac{P_{in}}{2}\cos^2\left(\frac{\Delta\varphi_1 - \Delta\varphi_2 - \varphi^I_0 + \frac{\pi}{2}}{2}\right), \tag{6.8}$$

for the PD at the I branch and

$$P^{Q}_{PD} = \frac{P_{in}}{2}\cos^2\left(\frac{\Delta\varphi_3 - \Delta\varphi_4 - \varphi^Q_0 + \frac{\pi}{2}}{2}\right), \tag{6.9}$$

for the PD at the Q branch where P_{in} is the input power. By recording the powers measured at the integrated PDs for a range of static drive voltages of each EOPM and using Eqs. (6.8) and (6.9), we can extract not only the individual V_π values but also the voltage-independent phase offsets φ^I_0 and φ^Q_0.

Because the InP EOPMs operate under reverse bias, the condition for obtaining an optical field at the output of each MZM of the form

$$E^{I,Q}_{out} = \frac{E_{in}}{\sqrt{2}}e^{j\alpha_{I,Q}}\cos\Delta\varphi_{2,4}, \tag{6.10}$$

cannot be satisfied by applying equal and opposite voltages to each EOPM. When these experiments were conducted, the foundry did not yet offer push–pull EOPMs on this PIC platform, so each modulator was driven independently through its own electrode, with the operating point set by on-chip monitoring and calibration. Recent process updates have since introduced push–pull devices [102], enabling symmetric drive in future implementations. Although the platform has since evolved, the results presented here accurately represent the behaviour of the devices and remain relevant for future implementations.

In the absence of push-pull operation, the phase condition to obtain Eq. (6.10) can be equivalently written as

$$\Delta\varphi_{1,3} - \varphi_0^{I,Q} - \frac{\pi}{2} = 2\pi n - \Delta\varphi_{2,4} \tag{6.11}$$

expressed in terms of $\varphi_0^{I,Q}$. In addition, the requirement for the modulators to operate under negative (reverse) drive voltages at all times imposes a constraint on the values of n, which define the minimum reverse-bias level applied to each EOPM.

Choosing $V_{2b} = -V_{\pi 2}/2$ as the minimum-transmission bias voltage at the I branch ensures that the modulation voltage $V_2(t) = V_{2b} + RV_{\pi 2}\sin(\omega_s t)$ remains negative for relatively large values of the modulation depth $R \leq 0.5$. The condition defined in Eq. (6.11) imposes $V_1(t) = V_{1b} - RV_{\pi 1}\sin(\omega_s t)$, with $V_{1b} = V_{\pi 1}\left(2n + 1 + \varphi_0^I/\pi\right)$ and therefore, the minimum reverse bias voltage $|V_{1b}|$ ensuring $V_1(t) < 0$ depends on the phase difference φ_0^I, resulting

$$V_{1b} = \begin{cases} -V_{\pi 1}\left(1 - \frac{\varphi_0^I}{\pi}\right) & \text{for} \quad -1 \leq \frac{\varphi_0^I}{\pi} \leq 1 - R \\ \\ -V_{\pi 1}\left(3 - \frac{\varphi_0^I}{\pi}\right) & \text{for} \quad 1 - R \leq \frac{\varphi_0^I}{\pi} \leq 1 \end{cases} \tag{6.12}$$

for $n = -1$ and $n = -2$, respectively, where φ_0^I has been chosen to range between $-\pi$ and π.

The same reasoning applies for the Q branch, where for $V_4(t) = V_{4b} \pm RV_{\pi 4}\cos(\omega_s t)$, $V_3(t) = V_{3b} \mp RV_{\pi 3}\cos(\omega_s t)$ with

$$V_{1b} = \begin{cases} -V_{\pi 3}\left(1 - \frac{\varphi_0^Q}{\pi}\right) & \text{for} \quad -1 \leq \frac{\varphi_0^Q}{\pi} \leq 1 - R \\ \\ -V_{\pi 3}\left(3 - \frac{\varphi_0^Q}{\pi}\right) & \text{for} \quad 1 - R \leq \frac{\varphi_0^Q}{\pi} \leq 1 \end{cases} \tag{6.13}$$

for $n = -1$ and $n = -2$, respectively.

In summary, the RF driving voltages of each phase modulator should be

$$V_1 = V_{1b} - RV_{\pi 1}\sin(\omega_s t) \tag{6.14a}$$
$$V_2 = V_{2b} - RV_{\pi 2}\sin(\omega_s t) \tag{6.14b}$$
$$V_3 = V_{3b} \mp RV_{\pi 3}\cos(\omega_s t) \tag{6.14c}$$
$$V_4 = V_{4b} \mp RV_{\pi 4}\cos(\omega_s t) \tag{6.14d}$$

where the corresponding DC bias voltages for $i = 1, 3$ are given by Eqs. (6.12) and (6.13) and for $i = 2, 4$ by

$$V_{2b} = -\frac{V_{\pi 2}}{2} \tag{6.15a}$$

$$V_{4b} = -\frac{V_{\pi 4}}{2} \tag{6.15b}$$

Finally, the required $\pi/2$ phase offset between the branch signals can be set by biasing one of the phase shifters (devices 5 or 6). Assuming only EOPM 6 is biased, the static phases contributed by the two paths are φ_{05} and $\varphi_{06} + \Delta\varphi_6(V_6)$, where φ_{05} and φ_{06} are the voltage independent phase shifts and $\Delta\varphi_6(V_6) = \pi V_6/V_{\pi 6}$ is the voltage dependent phase shift induced by EOPM 6. Therefore, the signal at the output of the device can be expressed as follows

$$E_{out}(t) = \frac{E_{in}(t)}{2}[e^{j(\alpha_I+\varphi_{06}+\Delta\varphi_6)}\cos\Delta\varphi_2 + e^{j\left(\alpha_Q+\varphi_{05}\right)}\cos\Delta\varphi_4]. \tag{6.16}$$

It is convenient to write these expressions in terms of the uncontrolled phases $\beta_I = \alpha_I + \varphi_{06}$ and $\beta_Q = \alpha_Q + \varphi_{05}$, and the voltage controlled $\Delta\varphi_6$, thus

$$E_{out}(t) = \frac{E_{in}(t)}{2}[e^{j(\beta_I+\Delta\varphi_6)}\cos\Delta\varphi_2 + e^{j\beta_Q}\cos\Delta\varphi_4],$$

that, in turn, can be written in terms of $\beta = \beta_I - \beta_Q$ which can be experimentally determined. Then, the optical field at the output is

$$E_{out}(t) = \frac{E_{in}(t)}{2}e^{j\beta_Q}[e^{j(\beta+\Delta\varphi_6)}\cos\Delta\varphi_2 + \cos\Delta\varphi_4], \tag{6.17}$$

and the voltage V_6 should ensure the following phase condition

$$\frac{V_6\pi}{V_{\pi 6}} + \beta = \frac{\pi}{2} + 2\pi n. \tag{6.18}$$

Therefore, the minimum negative bias voltage V_6 is given by

$$V_6 = \begin{cases} V_{\pi 6}\left(\frac{1}{2} - \frac{\beta}{\pi}\right) & for \quad \frac{1}{2} \leq \frac{\beta}{\pi} \leq 1 \\ V_{\pi 6}\left(-\frac{3}{2} - \frac{\beta}{\pi}\right) & for \quad -1 \leq \frac{\beta}{\pi} \leq \frac{1}{2} \end{cases} \tag{6.19}$$

for $n = 0$ and $n = -1$, respectively.

By substituting Eq. (6.18) into Eq. (6.17) and substituting also $\Delta\varphi_2(t)$ and $\Delta\varphi_4(t)$ to the corresponding RF driving voltages given by Eq. (6.14), the output optical field reads as

$$E_{out}(t) = \frac{E_{in}(t)}{2}e^{j\beta_Q}[j\sin\left(R\pi\sin\omega_s t\right) \pm \sin\left(R\pi\cos\omega_s t\right)], \tag{6.20}$$

If we assume that R is small enough, Eq. (6.20) can be approximated by the leading term of its Jacobi-Anger expansion, resulting in

$$E_{out}(t) = E_{in}(t)J_1\left(\pi R\right)e^{j\beta_Q}\left[j\sin\omega_s t \pm \cos\omega_s t\right]$$

that can be written in the form

$$E_{out}(t) = \pm E_0 J_1\left(\pi R\right)e^{j\beta_Q}e^{j(\omega_c\pm\omega_s)t}. \tag{6.21}$$

It is apparent that this corresponds to the frequency-shifted response of the device to the input optical field, by an amount of $+\omega_s$ or $-\omega_s$ depending on the sign convention adopted in Eq. (6.14c) and Eq. (6.14d).

Finally, as noted before, both $V_{\pi 6}$ and β can be obtained experimentally by analysing how the device's output power varies with V_6, while selecting suitable DC biases V_1, V_2, V_3, and V_4. These biases should satisfy the phase conditions in Eq. (6.11) and enforce $\Delta\varphi_2 = \Delta\varphi_4 = \Delta\varphi$. Under these drives, choosing $\Delta\varphi = -\pi$ (to maximise the output power) reduces to

$$E_{out}(t) = -\frac{E_{in}(t)}{2} e^{j\beta_Q} [e^{j(\beta+\Delta\varphi_6)} + 1]$$

and the corresponding power is given by

$$P_{out} = P_{in} \cos^2 \left[\frac{1}{2} \left(\frac{V_6}{V_{\pi 6}} \pi + \beta \right) \right]. \tag{6.22}$$

Design and fabrication of the PIC

Fig. 6.14 shows a photograph of the fabricated PIC, implementing the scheme in Fig. 6.13 using standard BBs from the SMART Photonics PDK. The IQ branches and individual components are indicated in it. The chip provides two optical I/O with 7° tilt, and the facets are AR-coated. Light from an external source is coupled into the input waveguide via lensed fiber and employing a polarisation controller to inject into the TE mode. This signal is amplified by a 350 μm-long SOA (SOA-IN). A 1×2 MMI then splits the signal into the I and Q branches. Each branch implements a dual-drive MZM comprising two parallel 2mm-long EOPMs (MZM-I: EOPM1/2; MZM-Q: EOPM3/4). The length was chosen to target $V_\pi \approx 4.5$ V based on simulations and foundry data.

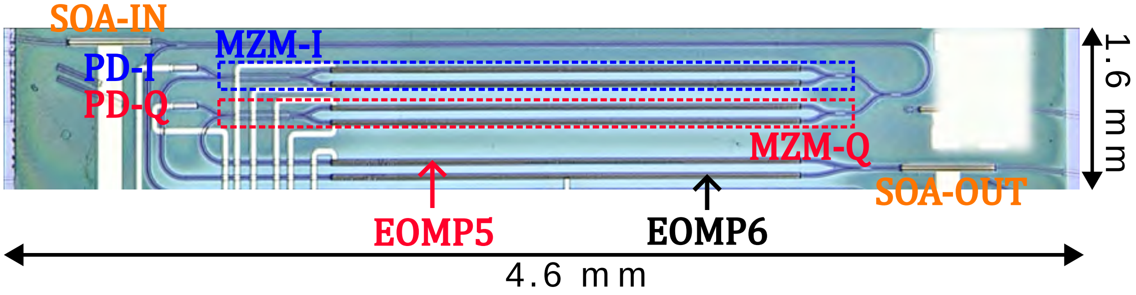

Figure 6.14: Photograph of the integrated IQ modulator, with the main on-chip components labelled.

The outputs of each MZM are combined and split by a 2×2 MMI for routing to PD-I and PD-Q. EOPM5/6 set the relative phase so that I and Q are in quadrature and are 2 mm-long. The optical path lengths of the I and Q branches are intentionally non-identical to achieve a more compact footprint. The resulting additional I-branch loss (0.1 dB) is expected to have a negligible impact on performance. Finally, a 2×1 MMI recombines the branches and a 400 μm-long SOA (SOA-OUT) provides output amplification.

Regarding the electrical connections, the PIC includes ten DC pads used to bias the functional elements and to read out the internal photodiodes, together with a common n-type substrate contact shared by all elements. At the time of fabrication, SMART Photonics employed n-type conductive substrates, which allowed a common contact but could lead to electrical crosstalk and limited modulation bandwidth. The foundry has since transitioned to semi-insulating substrates. All PICs from SMART Photonics presented earlier in this work were fabricated on these later semi-insulating substrates. Consequently, future iterations of the present design could benefit from simplified drive schemes and reduced parasitic coupling.

The EOPMs employ lumped electrodes rather than TWE, which limits the modulation bandwidth to a few hundred MHz but remains adequate for the operating range considered and relaxes the requirements on the RF drive source. This design choice is well suited to the target application, which involves low-frequency shifts of up to a few hundred MHz, as in the dual-comb experiments. In addition, the use of lumped electrodes reduces footprint and routing complexity.

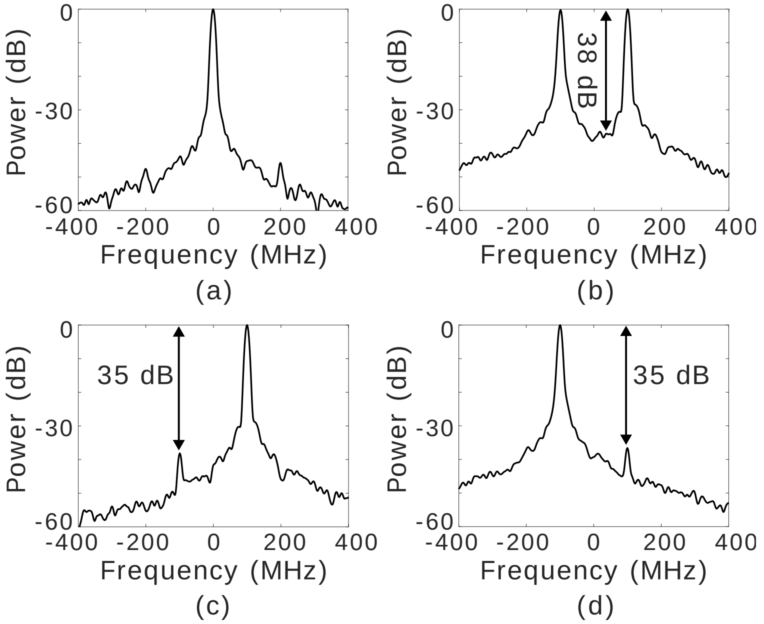

Figure 6.15: Simulated spectra of the optical field in frequency shifter operation for $f_s = \pm 100$ MHz at (a) the PD-I input; (b) the MZM-I output; and the output of the system for a (c) positive (d) and negative shift. The resolution of the OSA has been set to 10 MHz to adequate the results to the HR-OSA. All the spectra are normalized.

Layout-aware simulations of the PIC were then performed using VPI and the SMART Photonics PDK to validate the proposed design and the analytical model. Fig. 6.15 shows the simulated optical spectra when the EOPM drive signals follow Eqs. (6.12), (6.13), (6.14), (6.15a) and (6.15b), targeting a 100 MHz frequency shift with $R = 0.4$. Fig. 6.15(a) depicts the spectrum incident on PD-I, and Fig. 6.15(b) the spectrum at the output of MZM-I. With the MZM biased at minimum transmission, the carrier and odd harmonics are directed to the PD branch, while the even harmonics propagate to the output branch. The Q path behaves identically. In Fig. 6.15(b) the optical carrier is effectively suppressed (≈ 38 dB), and only the first-order sidebands remain appreciable, consistent with the expected single-sideband operation.

Fig. 6.15(c) and (d) show the simulated optical spectra at the device output for positive and negative frequency shifts, respectively. In both cases, the optical carrier remains suppressed. With the I and Q branches held in quadrature, the MZM outputs interfere destructively for one sideband, yielding its effective cancellation and thus SSB-CS modulation. Comparable behaviour is observed across different shift frequencies, providing qualitative validation of the theoretical model.

Experimental results

The fabricated PIC was characterised experimentally using the setup in Fig. 6.16(a). Each MZM was first characterised individually via the on-chip PDs, and the overall device performance was then assessed at the optical output, which was collected with a lensed fiber at the PIC output facet. The output was monitored simultaneously on the HR-OSA and on an external PM. The input light, provided by the same narrow-linewidth tunable laser used previously and centred at 1550 nm injecting 5 dBm, was coupled in with a lensed fiber. Alignment was performed by maximising the power measured on the internal PDs.

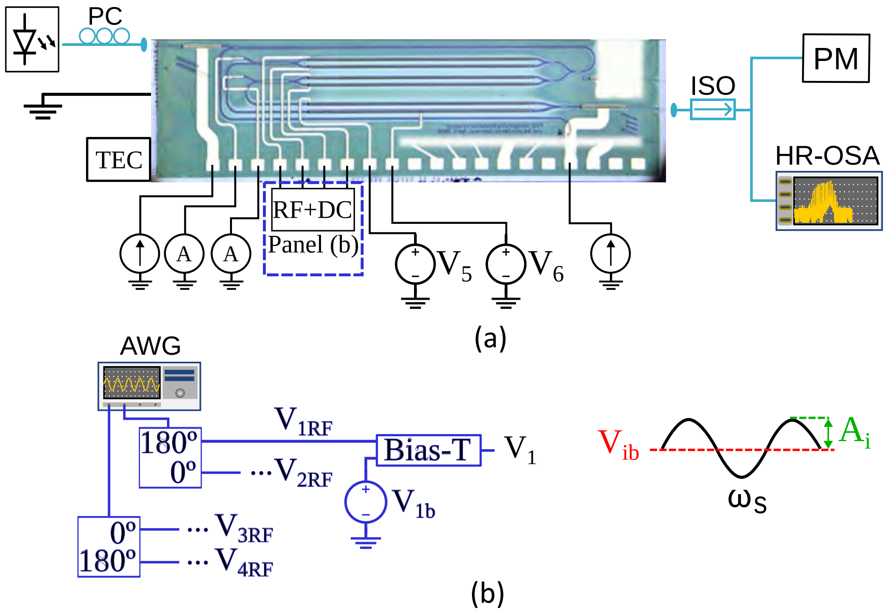

Figure 6.16: (a) Experimental setup for the characterization of the PIC and (b) driving scheme for the EOPMs. The RF signal is combined with a DC bias through a Bias-Tee. In this way, the modulating signal consist in a DC component (V_{ib}) plus a RF signal with frequency ω_s and amplitude A_i.

Several current and voltage sources were used to bias the chip. The input and output SOAs were driven at 80 mA to boost the input and output powers, respectively. Photocurrents from the internal and external PDs were read with digital multimeters. The EOPM drive scheme is shown in Fig. 6.16(b): two outputs of the AWG supply RF signals in quadrature (0° and

90°), which are combined with DC via bias-tees. The chip was mounted on the probe station and its temperature stabilised to 25°.

First, the individual MZMs are characterised to extract the key parameters described previously, which enable operation as a frequency shifter/SSB-CS modulator. Fig. 6.17(a-d) summarises the procedure: the drive voltage of one EOPM is swept while the other is held at a fixed bias V_f, thereby mapping the transfer function of each MZM as a function of the two EOPM biases. The half-wave voltage V_π is obtained as the voltage difference between constructive interference (maximum) and destructive interference (minimum).

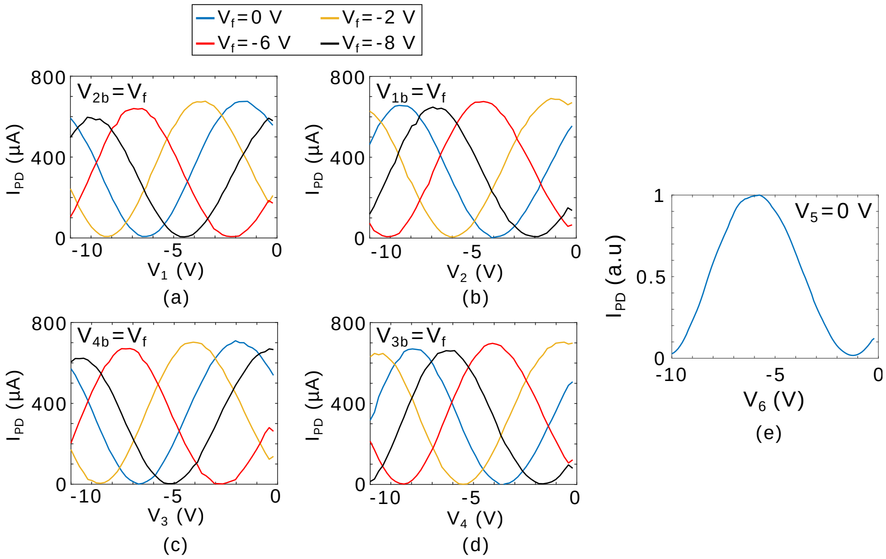

Figure 6.17: Response of the MZMs measured at the internal photodiodes for different DC bias voltages. (a) Bias voltage sweep of EOPM1 for different biases of EOPM2, (b) bias voltage sweep of EOPM2 for different biases of EOPM1, (c) bias voltage sweep of EOPM3 for different biases of EOPM4 and (d) bias voltage sweep of EOPM4 for different biases of EOPM3.

These measurements correspond to Eqs. (6.8) and (6.9), from which the static phase offsets φ_0^I and φ_0^Q are obtained. Unlike in typical LN MZMs, the response here is highly stable over time, which simplifies parameter extraction. A gradual reduction in the peak photocurrent (corresponding to 0.8 mA) with increasing reverse bias is observed in Fig. 6.17. This behaviour reflects bias-dependent propagation loss caused by electro-absorption through the Franz–Keldysh effect under higher electric fields.

Fig. 6.17(e) shows a sweep of the EOPM6 bias while EOPM5 is fixed at $V_5 = 0$ V for simplicity. Under these conditions, β is extracted by fitting the measured output power to Eq. (6.19). The V$_\pi$ of the modulator is obtained from the voltage difference between adjacent maxima and minima.

The characterisation of the device yielded the key system parameters listed in Table 6.1. Based on these values, the EOPM drive signals for frequency-shifter operation were set according to Eqs. (6.14) and (6.19). The bias voltages were $V_{1b} = -2.95$, $V_{2b} = -2.23$, $V_{3b} = -3.72$,

$V_{4b} = -2.41$, $V_5 = 0$ V, and $V_{6b} = -1.7$. Small modulation amplitudes A_i were initially selected to achieve a low modulation depth ($R = 0.05$) and ensure small-signal operation, with minor fine-tuning of the biases and amplitudes performed to optimise performance.

Table 6.1: Experimentally determined parameter values of the integrated frequency-shifter system.

Parameter	**Value**	**Units**
$V_{\pi 1}$	4.54	V
$V_{\pi 2}$	4.46	V
$V_{\pi 3}$	4.51	V
$V_{\pi 4}$	4.82	V
$V_{\pi 6}$	4.28	V
φ_0^I	1.1	rad
φ_0^Q	0.55	rad
β	0.29	rad

System performance is quantified by the carrier suppression ratio (CSR) and the sideband suppression ratio (SBSR), defined as the power ratio between the shifted component and the carrier, and between the shifted component and the undesired sideband, respectively. Fig. 6.18 shows the optical spectra measured at the PIC output with the HR-OSA for several frequency shifts. Each column corresponds to a given shift with opposite signs. The sign is easily controlled either by adjusting the relative phase of the RF drives to EOPM3/4 or by changing the bias of EOPM6. The frequency shifter achieves CSR > 15 dB for shifts below 250 MHz, degrading to ~ 10 dB at 300 MHz. SBSR remains above 15 dB across the measured range. These results are highly stable over time, and no drift was observed within 1 hour of operation.

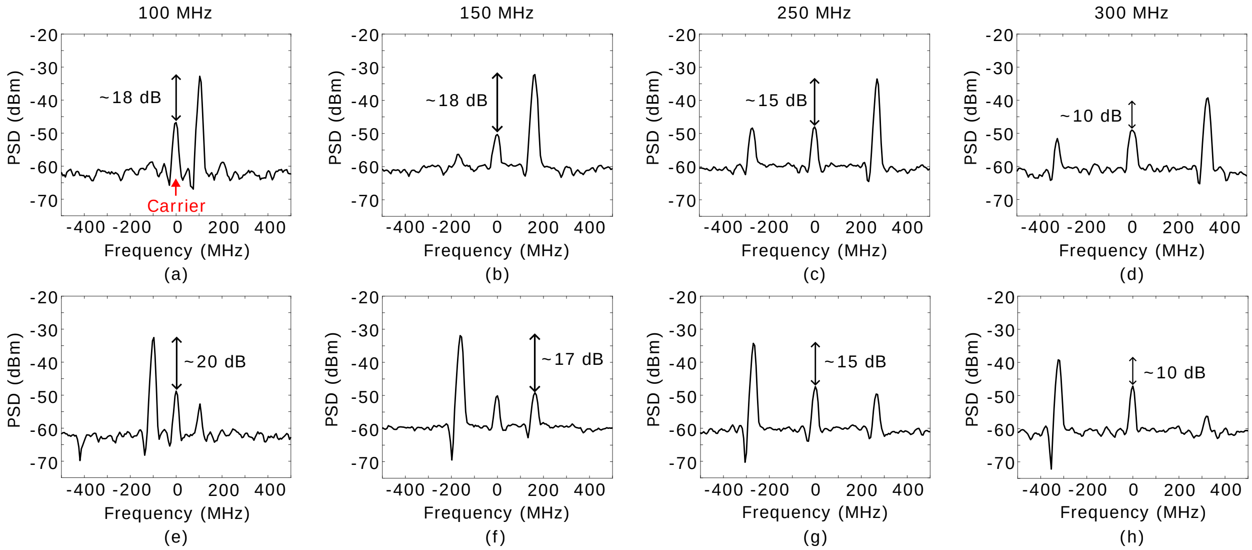

Figure 6.18: Measured frequency shifts for different modulation frequencies. Each column shows equal and opposite shifts relative to the reference frequency, which corresponds to a wavelength of 1550 nm.

Fig. 6.19 plots CSR and SBSR against the modulation frequency for negative (a) and positive (b) shifts from 50 to 300 MHz. The FS supports operation up to approximately 300 MHz, above which its performance degrades, and the device ceases to operate effectively as a FS. This limitation is primarily attributed to the bandwidth of the lumped electrodes in the EOPMs and other system non-idealities. The phase-shifting efficiency of the EOPMs also exhibits a weak dependence on the optical power and polarisation state, effects not examined in this study. Despite these factors, the experimental results are in qualitative agreement with simulations and confirm that the proposed device performs as intended within the measured range.

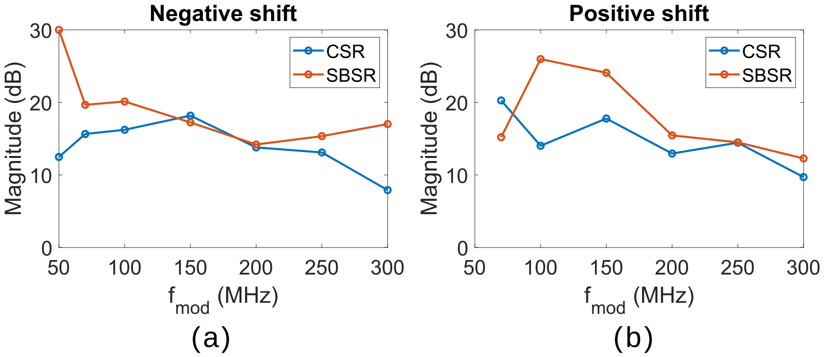

Figure 6.19: Evolution of CSR and SBSR with modulation frequency for (a) negative and (b) positive frequency shifts, over a modulation range from 50 MHz to 300 MHz.

In the context of dual-comb detection, the FS acts as an auxiliary subsystem that relocates the detected spectrum away from DC, enabling heterodyne detection without overlap between positive and negative frequency components in the baseband. Its performance is characterised by the CSR and the SBSR. The CSR represents the residual carrier power that contributes to beating at baseband when the carrier is not fully suppressed. This component gives rise to multiheterodyne terms around DC, which do not interfere with the shifted comb but divert part of the optical power that would otherwise contribute to the translated signal. The CF must therefore be sufficiently large to prevent spectral overlap between the baseband multiheterodyne region and the shifted comb. For CSR values above 10 dB, the power coupled to baseband remains low, and most of the comb power is preserved within the shifted detection band.

The SBSR quantifies the suppression of the undesired sideband relative to the desired one. The unwanted sideband generates an additional set of beat products between its optical lines and those of the shifted comb, as well as with the residual carrier components. However, the latter contribution is negligible due to the strong carrier and sideband suppression. The beat terms arising from the beating of the suppressed band and the shifted one produce a mirrored replica of the signal within the same Nyquist zone. When the SBSR exceeds 15 dB, the power of this mirrored contribution is sufficiently reduced to make this effect negligible, preserving the accuracy of the spectral reconstruction. Notably, for frequency shifts below 100 MHz, the present FS exhibits SBSR values above 15 dB, further minimising this effect.

Overall, the experimental results demonstrate that the integrated FS performs as a viable functional subsystem for dual-comb detection. It could effectively mitigate spectral overlap that arises in unshifted configurations and provide the signal translation required for accurate retrieval of spectral features in dual-comb interferometric systems.

6.3 Conclusions

A fully monolithic and reconfigurable dual-comb generator has been experimentally demonstrated. The system overcomes the absence of optical isolators in generic integration platforms by exploiting the inherent unidirectionality of the SRL emission under OI, achieving stable operation and mutual coherence between the combs. CFs of up to 50,000 have been obtained at repetition rates of 500 MHz, confirming the capability of the integrated source to generate dual-comb signals suitable for low-bandwidth detection and high-resolution interrogation. Moreover, the system has been proved to be reconfigurable as a dual-comb generator in terms of the repetition rate ranging from 2 GHz to 500 MHz and in terms of CF ranging between 20 and 50,000. The interference of the dual combs features a SNR of around 20 dB, which demonstrates that the system already provides sufficient signal quality for spectroscopic measurements, with sensitivity compatible with the detection of typical molecular absorption features in the C and L bands. The flexibility of the design and the GS implementation enables operation across a wide range of conditions and repetition frequencies.

The on-chip SG-DBR did not ultimately succeed as the ML for dual-comb operation due to its unexpectedly limited continuous tuning range and broad linewidth. This limitation made the optimisation of dual-comb generation with the integrated ML difficult. Nonetheless, the SG-DBR served as a valuable proof of concept. It enabled OI and comb generation at GHz repetition rates, and it remains a promising route for full integration.

Furthermore, baseband detection of the dual-comb signal complicates the retrieval of spectral information from interrogated samples due to the overlap between positive and negative frequency components. Although gas-absorption measurements were attempted, the resulting spectra could not be reliably extracted under these conditions. To overcome this limitation in future implementations, we proposed and demonstrated a monolithically integrated FS realised on the same generic InP platform as the dual-comb generator. An extensive analytical model of the device, based on measurable parameters obtained via on-chip PDs for calibration, was developed and validated through layout-level simulations using PDK models. Experimentally, the device achieves SSB-CS operation with CSR and SBSR values above 10–15 dB for frequency shifts up to 300 MHz, with improved performance below 100 MHz. This frequency-shift range is sufficient for dual-comb interferometric applications, and the measured results agree qualitatively with both the analytical model and the simulations, supporting the validity of the proposed approach.

Although both implementations are proofs of concept, they establish a clear path to co-integration on the same platform to realise a fully integrated dual-comb spectrometer. A revised design with improved characteristics has already been completed and is expected to enable gas-sensing measurements in subsequent runs. Particularly in the case of the FS, process updates towards semi-insulating substrates offering dual-drive modulators should enhance modulation bandwidth and device performance, enabling more efficient frequency shifting and broader operational flexibility.

Integrating the frequency shifter with the dual-comb generator would inevitably increase system complexity and electrical interconnection requirements. Nonetheless, the compact footprint achievable by merging both subsystems remains compatible with dense packaging strategies, which can be carried out in the laboratory with the electrical packaging system proposed in Section 4.2. Such integration would unlock the full potential of the system, offering a compact and fully integrated dual-comb platform for high-resolution optical spectroscopy and sensing.

Chapter 7

Conclusions and future lines

7.1 Conclusions

This thesis has focused on the development of integrated OFC sources based on semiconductor lasers for dual-comb generation, as well as on the design and characterisation of the subsystems required for a complete DCI implementation. The OFCs are generated by optically injected, directly modulated semiconductor lasers. Accordingly, this work has investigated their realisation on PICs fabricated through generic InP integration platforms using MPW runs.

With respect to **OFC generation in PICs**, mechanisms for generating OFCs in PICs through direct modulation of semiconductor lasers have been investigated, with a dedicated review addressing GS OFC generation within integrated photonic platforms. A rate-equation model describing the dynamics of an optically injected semiconductor laser under QS modulation was developed. The simulations predict that OFCs generated using the QS technique exhibit broader spectral coverage than GS OFCs for similar excitation conditions. This is primarily attributed to the larger dynamic chirp induced by modulation. Furthermore, QS operation benefits from repetition rates in the MHz range, determined by the modulating signal, which allows for wide combs with high spectral resolution and flexibility in the repetition frequency.

The proposed implementation can be realised in open-access foundries employing generic integration processes. It consists of a three-section DBR laser with an EAM embedded within the cavity to modulate the internal losses and achieve QS operation. Simulations based on the rate-equation model and using realistic parameters reported in the literature predict optical bandwidths of approximately 200 GHz for repetition frequencies around 100 MHz, corresponding to about 2,000 optical lines. Several lasers were fabricated through SMART Photonics following a design derived from these simulations, optimised to maximise the comb bandwidth. However, higher-than-expected cavity losses prevented experimental demonstration. Despite this, the rate-equation model employed has previously shown good agreement with experimental results for GS lasers, and future implementations are expected to confirm the QS technique experimentally. Implementing these lasers as sources for DCI would enable broader spectral coverage while maintaining high resolution.

Regarding GS OFC generation in PICs, although previous demonstrations exist, implementing master–slave configurations in generic foundry platforms remains challenging due to the absence of optical isolators, which can lead to mutual perturbation of the ML. In this work, a master–slave system for generating GS OFCs has been proposed and realised on a PIC fabricated through a Fraunhofer HHI MPW run. The scheme consists of two mutually coupled DFB lasers, exhibiting rich locking and mutual coupling dynamics. CW characterisation revealed stable locking regimes with improved emission characteristics of the coupled system. These insights provide foundations for OFC generation under asymmetric and symmetric coupling regimes. OFCs with repetition rates between several GHz and 500 MHz were successfully generated using excitation signals from a SRD. Although the mutual coupling perturbs the ML, the scheme is able to generate flat and relatively broad combs with an acceptable CNR. The CNR is mainly limited by the low off-chip optical power. A systematic study of the comb generation as a function of the driving parameters, such as the modulation signal amplitude, the OI power, and the bias current of the SL, has been conducted. The results demonstrate that generating GS OFCs with repetition rates below 1 GHz on PICs fabricated through generic integration platforms is feasible, offering characteristics comparable to those of discrete semiconductor lasers.

In systems where mutual coupling can degrade performance, such as in dual-comb generators, a mechanism is required to suppress perturbations from the SL to the ML. This thesis introduces an effective strategy to overcome the absence of on-chip optical isolators by exploiting the intrinsic emission dynamics of SRLs. By applying OI in one of the two possible propagation directions, unidirectional lasing is enforced, thereby preventing any disturbance of the ML.

This approach has been experimentally validated in a monolithic PIC fabricated through a MPW run. Under OI, the SRL exhibits strictly unidirectional emission, and when GS, the resulting OFC is emitted exclusively in the injection direction. OFC generation has been demonstrated for a wide range of repetition rates, from several GHz to 500 MHz, confirming stable low-repetition-rate operation without perturbing the OI. To the best of our knowledge, this constitutes the first demonstration of OFC generation from optically injected SRLs.

In relation to **integrated dual-comb interferometers,** the unidirectional emission observed in SRLs enables the implementation of a fully integrated monolithic dual-comb generator based on GS OFCs, in which a common ML injects two SRLs. In this work, BBs from SMART Photonics have been employed to realise a dual-comb system where both SRLs can be injected from either an integrated laser or provided externally. The integrated ML is a SG-DBR laser, which is not part of the standard PDK of the foundry but was custom designed for this work. In previous studies using the same foundry, this type of SG-DBR demonstrated a tuning range of up to 40 nm and a linewidth in the kHz range, both advantageous for coherence and noise performance. The availability of external injection provides additional robustness in case the SG-DBR does not exhibit the expected characteristics. In both internal and external injection configurations, unidirectional comb emission is preserved without perturbation of the master laser. SOAs have also been incorporated at the SRL inputs to control the injection power and to reinforce unidirectional operation through spontaneous emission in the injected direction.

CW characterisation showed that the SRLs predominantly emitted in one direction over the other, a behaviour attributed to the SOAs injecting spontaneous emission into the SLs mainly in the favoured direction. However, an unexpected plateau appeared in the PI curve beyond a certain current level. Analysis of an isolated laser with similar characteristics revealed that, above this same current, the ring emitted in both directions in an anticorrelated manner. When OI was applied to one of the SRL longitudinal modes, even at low power, that mode was favoured while the others were suppressed. The SG-DBR laser exhibited mirror detuning, and no tuning of the mirrors was achieved upon current injection, which hindered proper wavelength tunability and limited the ability to generate two OFCs in the SRLs simultaneously with optimised characteristics. As a result, it was not possible to adjust the OI conditions to obtain well-performing combs from both lasers at the same time. Moreover, the mirror misalignment resulted in a broader linewidth. Nevertheless, OFCs were successfully generated in one of the rings under internal injection, with repetition frequencies ranging from 1 GHz to 4 GHz, without any perturbation from the SL to the ML.

Using an external master laser, the system successfully demonstrated dual comb generation, with both the interferogram and the down converted RF comb clearly detected, representing the first time this has been achieved in an integrated implementation with GS OFCs. This configuration enables a flexible dual-comb generator with repetition frequencies between 500 MHz and 4 GHz and compression factors as high as 50,000, allowing high-resolution optical-domain measurements to be mapped into electrical bandwidths of only a few kHz. This greatly simplifies the detection scheme and reduces system costs while achieving performance comparable to bulk implementations. The two SRLs exhibit largely independent behaviour, with minimal mutual influence. The detected SNR, around 20 dB, would allow information retrieval from samples. However, spectral overlap at the baseband and in successive Nyquist zones led to partial masking of the absorption features, since the mirrored negative-frequency components overlapped with the positive-frequency spectrum. Although gas absorption measurements were attempted, no unambiguous detection could be achieved under these conditions. To overcome this limitation, the system can be integrated with a FS to displace the signal away from DC and avoid spectral overlapping.

A compatible FS has been proposed and implemented on an early version of the same platform, operating within the frequency-shift range typically required for DCI, with CSR values above 10 dB and SMSR consistently exceeding 15 dB. The system, based on an IQ modulator, provides frequency shifts of up to 250 MHz. An extensive theoretical model was developed, supported by measurable system parameters obtained through two integrated PDs at the outputs of the MZM. After appropriate system calibration, the MZM could be operated in a mode analogous to push–pull operation. Although the EOPM bandwidth was not fully optimised for high-frequency operation, the concept was successfully demonstrated.

The measured CSR and SMSR were found to be adequate for dual-comb operation. A CSR of around 10 dB results in a small residual carrier that produces partial beating of the unshifted comb with its frequency-shifted replica and with the other comb in DC. The former gives rise to a weak low-frequency component, while the latter introduces a small DC term in the detected signal. For large CF, both effects result in negligible power loss. The SMSR, always above 15 dB and improving under 100 MHz frequency shift, ensures that the unwanted sideband remains well suppressed, yielding a clean, single-sided RF comb with minimal mirror artefacts. This circuit was fabricated prior to the DCI system using an older PDK version with lower high-speed performance and fewer MZM features. Consequently, newer fabrication processes would enable higher bandwidths and improved overall performance. Joint integration of the FS and DCI would substantially enhance system capability and enable a fully functional and robust on-chip DCI.

Finally, with respect to **open-access foundries**, extensive work has been devoted to the design and characterisation of PICs fabricated through these platforms. They have demonstrated significant potential for implementing complex systems and enabling cost-effective prototyping of advanced photonic architectures. The work presented in this thesis contributes to this progress by demonstrating the feasibility of realising complete photonic subsystems within open-access foundries.

Several limitations related to the maturity of these technologies have been identified. The long fabrication times restrict the number of possible design iterations within the timeframe of a PhD thesis. The development of advanced systems typically requires multiple feedback cycles, where each characterisation informs the next design. Fabrication times in the employed foundries can reach up to one year, and full characterisation may take several months, thus extending the feedback loop. Additionally, device reproducibility between runs is not yet at the expected level, with variations observed from one MPW to another. Although this can be mitigated through design redundancy, it still complicates the iterative process.

These limitations particularly affected the QS laser implementation, as the long fabrication cycle prevented an additional MPW run to address the issues identified during its characterisation. The SG-DBR laser was also impacted, since its performance did not meet the expected specifications, and further iterations would be required to diagnose and resolve these deviations. Despite these challenges, this work demonstrates that complex photonic systems can be successfully realised in open-access foundries, achieving promising levels of performance. Additional results presented in the Appendix further highlight the potential of MPW runs for the prototyping of advanced integrated photonic systems.

In conclusion, this thesis has demonstrated the feasibility of generating and integrating dual-comb interferometers using semiconductor lasers and generic InP photonic platforms. It provides both theoretical and experimental validation of novel schemes for OFC generation and DCI integration, paving the way towards low-cost, compact, and fully integrated DCI systems.

7.2 Outlook

The work conducted during this doctoral thesis can be further extended to address remaining challenges and to explore new research directions of scientific and technological interest. Some of the lines of future investigation are outlined below.

With respect to OFC generation in PICs:

- **Experimental validation of the QS technique for OFC generation.** Future work should focus on the experimental realisation of the QS technique to validate the predictions obtained from the rate-equation simulations. This would enable direct comparison between simulated and measured comb spectra, particularly in terms of spectral bandwidth, flatness, and repetition-rate tunability. The fabrication of optimised devices with reduced cavity losses will be essential to demonstrate the full potential of QS operation for integrated broadband comb generation.

- **Master–slave DFB system.** Further research should address the enhancement of GS OFCs in the master–slave DFB configuration. In particular, exploring the symmetrical coupling regime and optimising the mutual injection dynamics could lead to broader comb bandwidths and improved power uniformity.

- **Extension to other wavelength bands.** The fabrication of future devices in alternative wavelength bands, such as the O band now offered by SMART Photonics, would extend the application range of these OFC sources.

With respect to integrated dual-comb interferometers:

- **Spectroscopic measurements of gases.** Although the integrated DCI has been successfully demonstrated, its validation as a GS dual-comb spectrometer for the detection of absorbing species remains a key next step. Future work should include the measurement of gas samples such as CO_2, HCN, CO or NH_4 to experimentally confirm the system's spectroscopic capability. Implementing an asymmetric configuration to extract absorption information from phase analysis could further enhance sensitivity under low-SNR conditions. Improvements in the detection scheme and the use of a fully functional SG-DBR would also enable multi-gas operation.

- **Full monolithic integration of the DCI.** A natural continuation of this work is the full integration of the DCI and FS on the same chip. This would eliminate residual DC components and enable complete on-chip generation and detection of frequency-shifted interferograms. The compactness of such a configuration could be complemented by dense packaging techniques developed in our laboratory, leading to a portable dual-comb system. Moreover, improving the ML design could remove the need for an external laser source.

- **Reduction of system cost.** The development of dedicated, low-cost, and portable electronics is essential for the viability of integrated dual-comb systems outside the lab. Future implementations should exploit compact and low-cost components such as SRDs for pulse generation, SDR platforms for simplifying the detection, and FPGA-based architectures for real-time digital processing. Such an approach would significantly reduce system complexity and cost while maintaining high performance.

- **Improvement of the FS performance.** Although the FS demonstrated in this work already exhibits characteristics sufficient for the intended applications, its performance could be further enhanced. The updated PDK versions available in the current platform provide faster modulators and improved high-speed components, which would allow higher frequency shifts and greater sideband suppression. These improvements would directly translate into cleaner RF spectra and increased SNR in dual-comb measurements.

- **On-chip comb filtering as an alternative to FS.** An alternative approach to mitigate the baseband overlap observed in the down-converted RF comb is to implement an on-chip optical filter that removes the frequency components to the left of the injection frequency (including the injection itself), thereby preventing the appearance of negative-frequency mirrored replicas in the detected spectrum. Realising such a filter within a PIC could simplify the overall system architecture by eliminating the need for an active FS. However, designing a filter with the required spectral selectivity and low insertion loss would be challenging and would require careful optimisation of the integrated photonic structure, as well as means to accurately tune the filter response.

- **Exploration of applications for the integrated DCI.** The integrated DCI concept could be extended to a variety of applications beyond spectroscopy, including optical ranging, coherent imaging, and precise distance measurement. Such implementations would benefit from the compactness, stability, and reconfigurability of the on-chip dual-comb architecture. In addition, the detection stage could be enhanced through the use of highly sensitive or single-photon detectors, which would compensate for the limited optical power typically available from PIC-based OFC sources.

Appendix A

Additional PIC designs and experiments

This annex presents additional PIC designs developed throughout this thesis. In Section A.1, the design and characterisation of a random modulated continuous wave (RMCW) light detection and ranging (LiDAR) system with coherent detection for distance measurement are described. This PIC was fabricated at SMART Photonics through an MPW run. It represents a complete system implementation aligned with the objective of developing complex photonic systems within open-access foundries.

In Section A.2, the results obtained during a three-month research stay at the Institute of Photonics (IoP) of the University of Strathclyde in Glasgow are presented. During this period, PICs were designed, fabricated, and characterised on a SiN platform in the IoP facilities. These chips contained ring and racetrack microresonators, and the goal was to enhance their nonlinearity through micro-transfer printing of a membrane made of a highly nonlinear material onto the resonators. This approach aims to enable efficient OFC generation in microresonators through a heterogeneous integration technique.

These works are currently under further development. Although they have not been included in the main body of this thesis due to their stage of progress or because they fall outside its primary scope, they form part of the research carried out during this doctoral work and outline potential directions for future investigation.

A.1 LiDAR systems

LiDAR is an active sensing technique that operates by detecting the laser light that is scattered back from a target after interacting with matter within a medium. The basic principle involves illuminating an object and analysing the reflected signal to retrieve information about the observed environment. Depending on the implementation, parameters such as time of flight (ToF), phase shift between emitted and received signals, or variations in absorption and scattering can be measured to determine the target's distance or position. Although LiDAR and radar share the same fundamental operating principle, LiDAR has intrinsic advantages because it uses optical frequencies rather than radio waves. The much shorter wavelength of light results in significantly reduced beam divergence, enabling higher spatial resolution and more accurate distance measurements. For this reason, LiDAR has become an important technology for high-precision applications such as autonomous navigation, topography, 3D imaging, and environmental sensing.

LiDAR technology enables distance measurements [260]. Moreover, Doppler LiDAR systems can determine the velocity of particles or objects by measuring the frequency shift of the backscattered light. Similarly, differential absorption lidar (DIAL) instruments can quantify the concentration of aerosols and trace gases in the atmosphere by comparing the absorption of two laser wavelengths tuned to different spectral lines.

It is because of these capabilities that LiDAR is now a widespread technology. Topographic mapping was the dominant application area for LiDAR in 2021. However, the leading sector is projected to shift towards advanced driver-assistance systems and autonomous vehicle technologies by 2027.

LiDAR can be qualitatively described by the LiDAR equation [261], given by the convolution of the transmitted signal with the response of the medium:

$$y(t) = \int_{-\infty}^{+\infty} x(t-t')h(t')dt' + b(t), \tag{A.1}$$

where $x(t)$ represents the transmitted signal, $h(t)$ represents the temporal impulse response of the medium, $b(t)$ represents background noise, and $y(t)$ represents the received signal. The response function is often expressed as [262]:

$$h(t) = kG(z)\beta(z)T(z), \tag{A.2}$$

Where K is a performance factor for the system, $G(z)$ describes range-dependent geometry, and $\beta(z)$ is a backscattering coefficient for aerosols and molecules as a function of distance. T(z) is the transmission through the medium, defined as the fraction of light reaching the detection system after being backscattered by the target. More details on these terms and how to extract them can be found in [262].

Of the various LiDAR techniques and architectures used to measure distances, ToF is one of the most notable. This method is based on estimating the time it takes for a signal to travel to a target, be reflected back to the system, and arrive. The delay in the signal provides an indication of the distance.

$$d = \frac{c \cdot t}{2} \tag{A.3}$$

Where d is the distance between the target and the transmitter, $c = c_0/n$ is the speed of light in the medium (where n is the refractive index), and t is the travel time. The factor of 2 arises from the fact that light travels the distance twice.

Since the backscattered optical signal is often strongly attenuated and the desired return signal can easily be masked by noise, improving the SNR has become one of the principal drivers in LiDAR implementations. The most significant factors contributing to this degradation of the SNR are the inverse square law and the albedo, or reflectivity, of the target, which determines the proportion of incident light reflected back towards the detector. Depending on how distance information is encoded, ToF LiDAR systems can be categorised as pulsed, frequency-modulated continuous-wave (FMCW), or RMCW. In pulsed LiDAR, distance is measured from the round-trip time of short optical pulses. In contrast, FMCW LiDAR employs a continuous-wave laser whose frequency is swept linearly over time, and the distance is extracted from the beat frequency between the transmitted and reflected waves.

The RMCW technique [261] involves periodically modulating the amplitude [263] or phase [264] of a continuous optical wave using a pseudo-random binary sequence (PRBS). A PRBS is a deterministic sequence of binary values (typically 0 and 1) that repeats after a defined period. Such signals can be generated using linear feedback shift registers (LFSRs), which can be implemented in field-programmable gate arrays (FPGAs). The main advantage of PRBS modulation is that its statistical properties closely approximate those of random signals, providing excellent autocorrelation characteristics. The length of a PRBS is given by $2^N - 1$, where N is the number of stages in the LFSR.

In RMCW LiDAR, the received backscattered signal is cross-correlated with a replica of the transmitted PRBS to retrieve the time delay corresponding to the target distance. The position of the cross-correlation peak provides distance information. This technique has the advantages of low optical power requirements (typically in the mW range) and high immunity to interference and crosstalk, thanks to the low cross-correlation between independent PRBS sequences [265]. The sequence length determines the maximum unambiguous measurement range, i.e., the range in which a measurement can be taken without ambiguity. This is given by

$$R_{\text{unamb}} = \frac{Tc}{2} = \frac{N\tau_c}{2} \tag{A.4}$$

where $T = N\tau_c$ is the period of the PRBS, and τ_c is the bit rate (or chip time). The spatial resolution is defined as the minimum distance at which two close targets can be distinguished. It can be derived from the Nyquist theorem to avoid aliasing when sampling.

$$\Delta z = \frac{\tau_s c}{2} \tag{A.5}$$

The RMCW technique can be implemented by directly modulating a laser or by modulating it externally. External modulation offers several advantages, such as avoiding frequency chirp and the associated distortions that arise from directly modulating the laser drive current.

Further improvement of the SNR can be achieved through coherent detection, in which the received optical field is mixed with a strong LO. This approach enables simultaneous recovery of the amplitude and phase of the backscattered signal, unlike direct detection, which measures only intensity. Two configurations are typically used: homodyne and heterodyne detection.

In homodyne detection, the LO frequency matches that of the received signal, leading to a baseband output that directly encodes phase and amplitude information with high sensitivity. In heterodyne detection, the LO is offset by a small frequency from the signal, generating an intermediate-frequency beat that shifts the detected signal away from DC. This facilitates selective detection around the intermediate-frequency and improves immunity to low-frequency noise. In both cases, coherent mixing enhances the detected signal proportionally to the LO amplitude and strongly suppresses background noise, resulting in a significantly higher SNR and improved sensitivity.

In coherent LiDAR systems, detection is typically implemented using an optical 90° hybrid followed by BPDs, enabling the extraction of both the I and Q components of the received optical field. The resulting complex signal, I+jQ, represents the demodulated baseband waveform. By performing a cross-correlation between this signal and the reference PRBS used for modulation, the time delay corresponding to the target distance can be determined.

PICs have enabled LiDAR systems to be miniaturised. Distance-measuring FMCW LiDAR systems have been demonstrated in SiP platform [266], [267]. A monolithically integrated DIAL based on a generic InP platform has been reported targeting a CO_2 absorption line [242].

Regarding coherent receivers on PICs, one alternative to 90° hybrids is 120° hybrid coherent receivers. They offer improved fabrication tolerance, broader optical bandwidth, and a simpler architecture based on 2×3 MMIs coupler and three PDs. Due to its reduced complexity, it is particularly well suited for monolithic photonic integration [268], [269], [270].

When a 120° hybrid is used, the complex signal I+jQ can be obtained directly by multiplying the photocurrents from the PDs by a constant-coefficient matrix, as expressed in [269]:

$$\begin{bmatrix} I \\ Q \end{bmatrix} = \begin{bmatrix} -\frac{1}{2} & 1 & -\frac{1}{2} \\ \frac{\sqrt{3}}{2} & 0 & -\frac{\sqrt{3}}{2} \end{bmatrix} \cdot \begin{bmatrix} I_1 \\ I_2 \\ I_3 \end{bmatrix} \tag{A.6}$$

where I_1, I_2, and I_3 are the generated photocurrents in the three PDs respectively. A calibration is required to correct for imbalances induced during fabrication. This calibration is typically done once at a central wavelength using a least-squares fit. Due to the broadband and tolerant behaviour of the 2×3 MMI, this calibration remains valid across a wide spectral range, enabling operation over the S, C, and L bands with minimal additional calibration [269].

Building upon these developments, this work presents a coherent RMCW LiDAR architecture for distance measurement, implemented on a PIC fabricated through a MPW run provided by SMART Photonics. It is worth mentioning that in the field of LiDARs in PICs, a DIAL design has also been developed within this thesis for CO_2 sensing applications through an HHI MPW run. However, the details of this implementation are not disclosed here due to confidentiality agreements.

Circuit design and fabrication

The proposed design is schematised in Fig. A.1, together with the characterisation setup. The system includes a LO implemented as an ECL following the design proposed in [104]. This laser consists of a DBR laser, comprising a SOA embedded between two DBR mirrors, coupled to an external cavity that includes an EOPM for fine cavity-length tuning and a third DBR at the end. By properly aligning the three DBR mirrors, the laser can operate at the point of minimum linewidth, where [104] reported a value below 10 kHz. The laser also provides an independent output for direct characterisation.

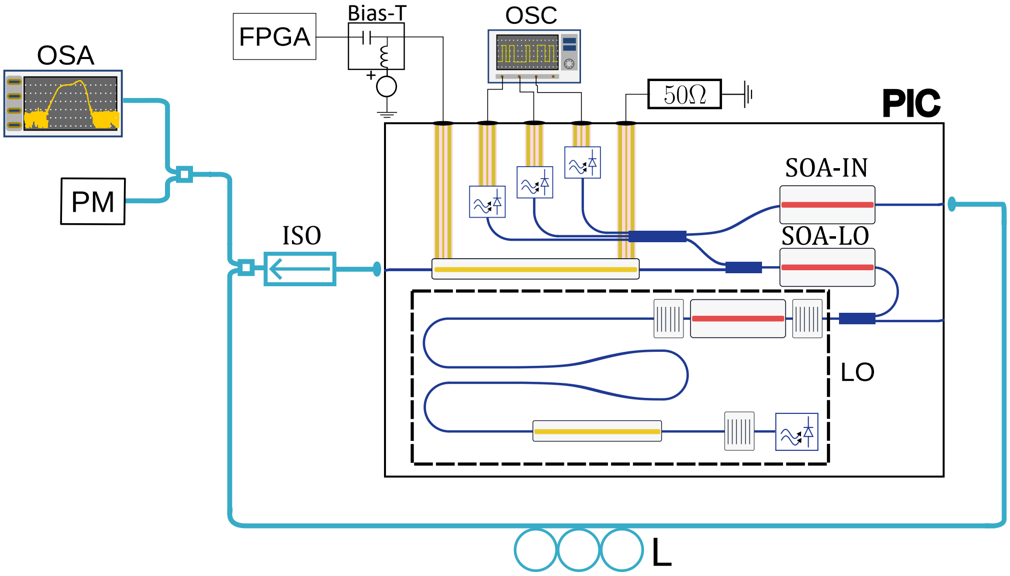

Figure A.1: Description and characterisation setup of the proposed integrated coherent LiDAR for distance measurements. The PIC integrates a LO based on an ECL that beats with the signal modulated by an EOPM driven by a PRBS sequence. After propagating through an in-fiber path of length L, the returned signal interferes with the LO, generating photocurrents in the three on-chip PDs, from which the complex signal $\mathrm{I} + \mathrm{jQ}$ can be reconstructed. Two SOAs, labelled SOA-LO and SOA-IN, control the optical power of the LO and the injected signal, respectively.

Achieving narrow linewidths is essential in coherent LiDAR systems, as the laser linewidth sets the minimum achievable modulation speed and thus limits the maximum unambiguity range. If the phase modulation rate is lower than the laser linewidth, the resulting phase noise will dominate, masking the modulation of the PRBS and thereby degrading the cross-correlation between the phase of the complex $\mathrm{I} + \mathrm{jQ}$ signal and the PRBS.

The EOPM employed is a high-speed TWE modulator, used to modulate the phase of the LO according to the PRBS generated by an FPGA. The modulator is operated under reverse bias and terminated in 50Ω to ensure proper impedance matching. The FPGA used is a Digilent Eclypse Z7. For an M-sequence of length 255, the system achieves range resolutions of 15 m, 6 m, and 3 m at chip rates of 10 MHz, 25 MHz, and 50 MHz, respectively. These correspond to maximum unambiguous ranges of approximately 3.8 km, 1.5 km, and 0.76 km, respectively.

The LO is mixed with the modulated signal after the latter has propagated through the medium. Both signals can be independently amplified by SOA (SOA–LO and SOA–IN, respectively). The modulated signal is divided into two branches: one is directed to the alignment stage, which includes the OSA and the PM, while the other propagates through an optical fiber of known length L. This fiber represents the distance to be measured, and the signal emerging from it is re-injected into the PIC, where it is mixed with the LO.

The receiver consists of a 2 × 3 MMI coupler followed by three PDs. The photocurrents generated by the PDs are recorded using an oscilloscope and subsequently processed using the coefficients from Eq. (A.6), after calibration. The optical paths from the MMI outputs to the three PDs have been designed to be identical in length, ensuring path balance and preventing differential delays that could introduce phase errors or amplitude imbalances in the detected signals.

The 2 × 3 MMI coupler was not available as a standard BB in the SMART Photonics library. Although the foundry provided access to FDTD simulation tools for passive component design, our group did not yet have practical experience with their use at that time. Consequently, the design of this coupler was carried out in collaboration with AG Photonics, a company with extensive experience in the design and optimisation of integrated photonic components. This collaboration enabled the development of a 2 × 3 MMI coupler that was included in the present PIC design.

In subsequent fabrication runs, the design capabilities for integrated components were incorporated into our group, and 1 × 3 and 2 × 3 couplers were designed using Tidy3D. The design process followed the standard self-imaging theory for MMIs, using 3D FDTD simulations to fine-tune the device dimensions and optimise power balance among the output ports. The input and output tapers were adjusted to minimise transition losses and ensure efficient coupling between the access waveguides and the multimode region. The resulting devices exhibit well-defined interference patterns and uniform power distribution across the output ports, confirming the correct operation of the designed structures. These results validate the use of Tidy3D as an accurate and flexible tool for the design of passive components compatible with the SMART Photonics platform.

In subsequent fabrication runs, the design capabilities for integrated components were incorporated into our group, and new 1 × 3 and 2 × 3 devices were designed using Tidy3D.

Figs. A.2 and A.3 present representative simulation results for these MMIs, which employ the deep-etched waveguide structure of the SMART Photonics platform. Fig. A.2(a) shows the optical field magnitude of the injected fundamental TE mode along the waveguide structure, featuring a width of 1.5 μm. Fig. A.2(b) displays a top view of the simulated structure. The simulation process included the design of adiabatic tapers for the inputs, the definition of the MMI region, the positioning of the input and output ports, and the optimisation of the device length. The resulting lengths were 232 μm for the 1×3 MMI coupler and 320 μm for the 2×3 MMI coupler, both with a multimode section width of 18 μm.

The simulated optical field distribution, obtained in the frequency domain at a wavelength of 1.55 μm, is shown in Fig. A.2(c). The results clearly illustrate the splitting of the injected optical power into three well-defined output branches, confirming the expected multimode interference behaviour and validating the design approach.

Fig. A.3(a) shows the simulated results for the 1×3 MMI. The figure presents the optical power flux at output ports 1 and 2, as well as the optical field magnitude at the three output ports. The flux values have been normalised so that 0 dB corresponds to the reference wavelength of 1.55 μm, where the insertion loss is approximately 6 dB. At this wavelength, the power imbalance between the output ports is below 0.2 dB. Owing to the structural symmetry with respect to the propagation axis, ports 1 and 3 exhibit identical behaviour, so only ports 1 and 2 are shown for clarity.

Fig. A.3(b) shows the simulated optical power flux at output ports 1 and 2 and the back-reflected signal for the 2×3 MMI. At 1.55 μm, the power imbalance between the output ports is below 0.1 dB, confirming highly uniform splitting. The flux has been normalised to 0 dB at this wavelength, corresponding to an insertion loss of approximately 7 dB. The reflected signal is attenuated by about 24 dB with respect to the transmitted power, demonstrating good return loss performance.

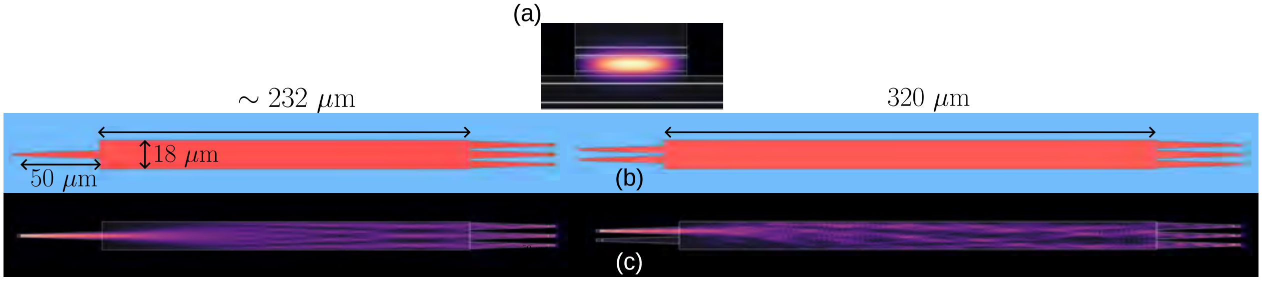

Figure A.2: Simulation results of the 1×3 and 2×3 MMI couplers designed using Tidy3D. (a) Optical field magnitude of the injected fundamental TE mode along the MMI structure (1.5 μm waveguide width). (b) Top view of the simulated layout. (c) Simulated optical field distribution at 1.55 μm showing power splitting into three output branches.

Both devices have been included in a new layout that has been submitted for fabrication through the SMART Photonics platform in a MPW run. Their integration will allow for on-chip experimental validation of the simulated performance and further optimisation of the devices.

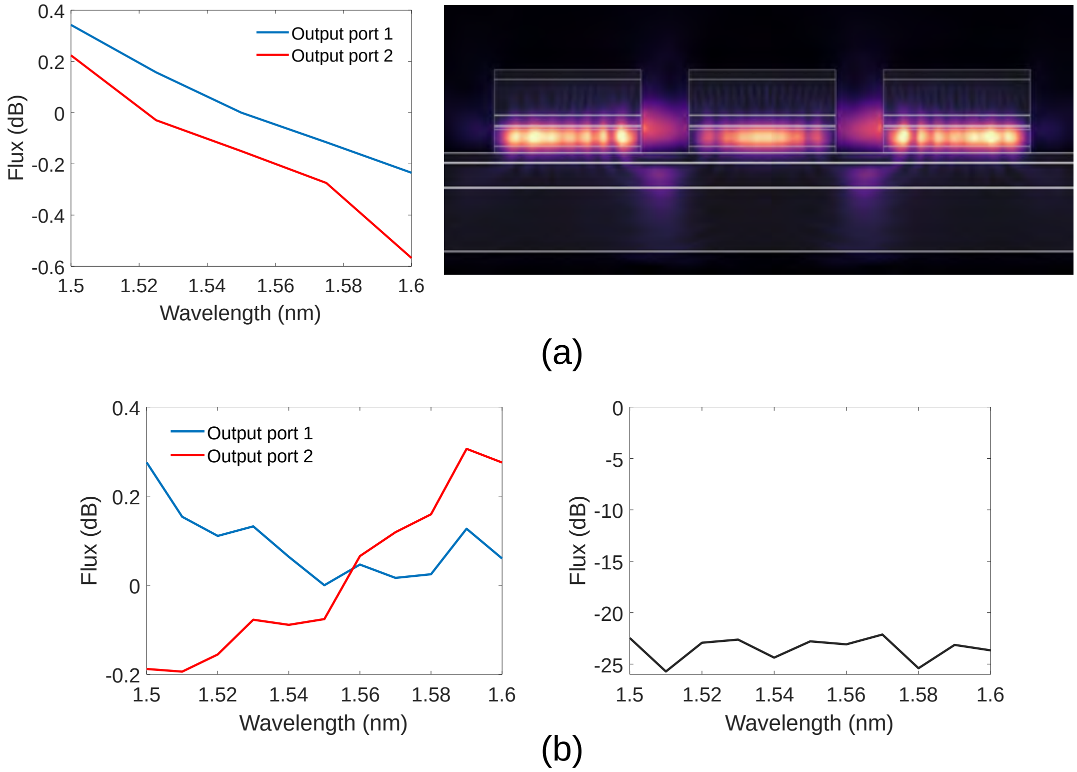

Figure A.3: (a) Simulated optical power flux and field magnitude at the output ports of the 1×3 MMI. (b) Simulated power flux and back-reflected signal for the 2×3 MMI.

Experimental results

The LiDAR PIC was encapsulated using the setup described in Section 4.2 for characterisation. Fig. A.4 summarises the results obtained for the LO narrow-linewidth laser. The PI curve, shown in Fig. A.4(a), was measured by sweeping the SOA current from 0 to 100 mA in 1 mA steps while keeping all other sections unbiased. The optical power, recorded through the integrated monitor PD and normalised to its maximum value, reveals a threshold current of approximately 18 mA. Above this value, the output power increases steadily, and beyond 78 mA the slope efficiency rises noticeably, reaching a maximum detected photocurrent of about 0.8 mA.

The spectral properties of the LO were analysed under the same bias conditions. The optical spectrum, displayed in Fig. A.4(c), confirms single-mode emission centred at 1565 nm. To quantify the linewidth, the self-delayed heterodyne technique [244] was employed, as shown in Fig. A.4(b). The laser output was delayed by 25 km of fibre and recombined with itself, producing an uncoherent self-beat signal that was fitted to a Voigt profile. The full width at half maximum (FWHM) of this fit yields an estimated linewidth of approximately 1 MHz, measured with the SOA biased at 40 mA and the remaining sections left unbiased. Linewidths below 1 MHz were obtained under certain conditions of the bias of the mirror and phase sections (not shown here).

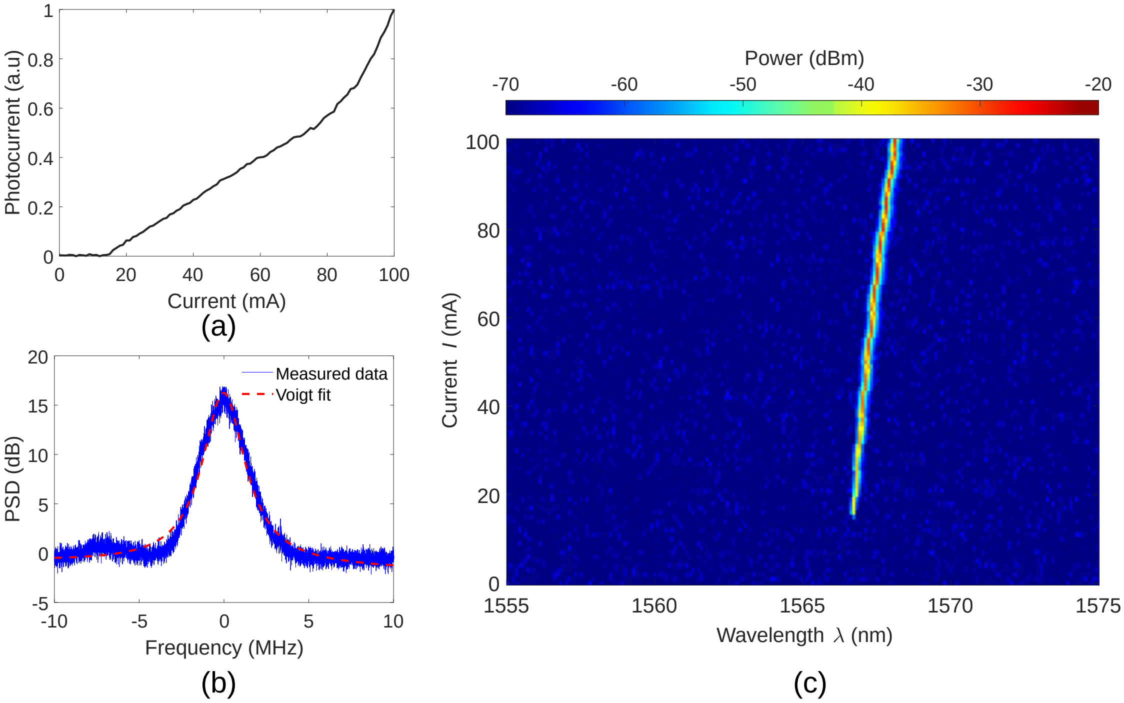

Figure A.4: Characterisation of the LO laser. (a) PI curve measured by sweeping the SOA current while keeping all other sections unbiased. (b) Linewidth measurement using the self-delayed heterodyne technique with a 25 km fibre delay. The Voigt-profile fit yields a linewidth of approximately 1 MHz for $I_{\text{SOA}} = 40$ mA. (c) Optical spectrum under the same bias conditions, showing single-mode emission centred at 1565 nm.

The LO laser was successfully employed to perform distance measurements. The EOPM was driven with a PRBS at a rate of 50 MHz and with an amplitude close to the modulator's V_π. Fig. A.5(a) shows the photocurrents detected by the three on-chip PDs (phase 1, 2, and 3) when the modulated light was reinjected into the PIC after propagating through a fiber of length $L = 500$ m and subsequently beating with the on-chip LO. Although the detected signals exhibit a low SNR, coherent detection allows accurate distance retrieval. This is shown in Fig. A.5(c), where the normalised cross-correlation between the amplitude of the reconstructed complex signal $I + jQ$, obtained from Eq. (A.6), and the original PRBS sequence produces a clear correlation peak at a delay corresponding to 500 m. The upper panel displays the result without averaging, while the lower panel shows the same measurement averaged over 100 acquisitions, yielding an SNR improvement of 12.6 dB.

A second measurement was performed using a 1 km fiber link under identical operating conditions. As expected, the detected photocurrents showed reduced amplitude due to the increased propagation loss. The cross-correlation analysis again produced a distinct peak at the corresponding delay, confirming correct distance retrieval. However, the higher attenuation led to a lower SNR of approximately 6.5 dB, demonstrating the sensitivity of the system performance to optical path loss.

These results demonstrate that the integrated system can accurately measure distances using a PRBS-modulated signal generated by an FPGA and coherently detected on-chip. Current work focuses on further characterising the system and indicates a promising route for a monolithically integrated coherent LiDAR.

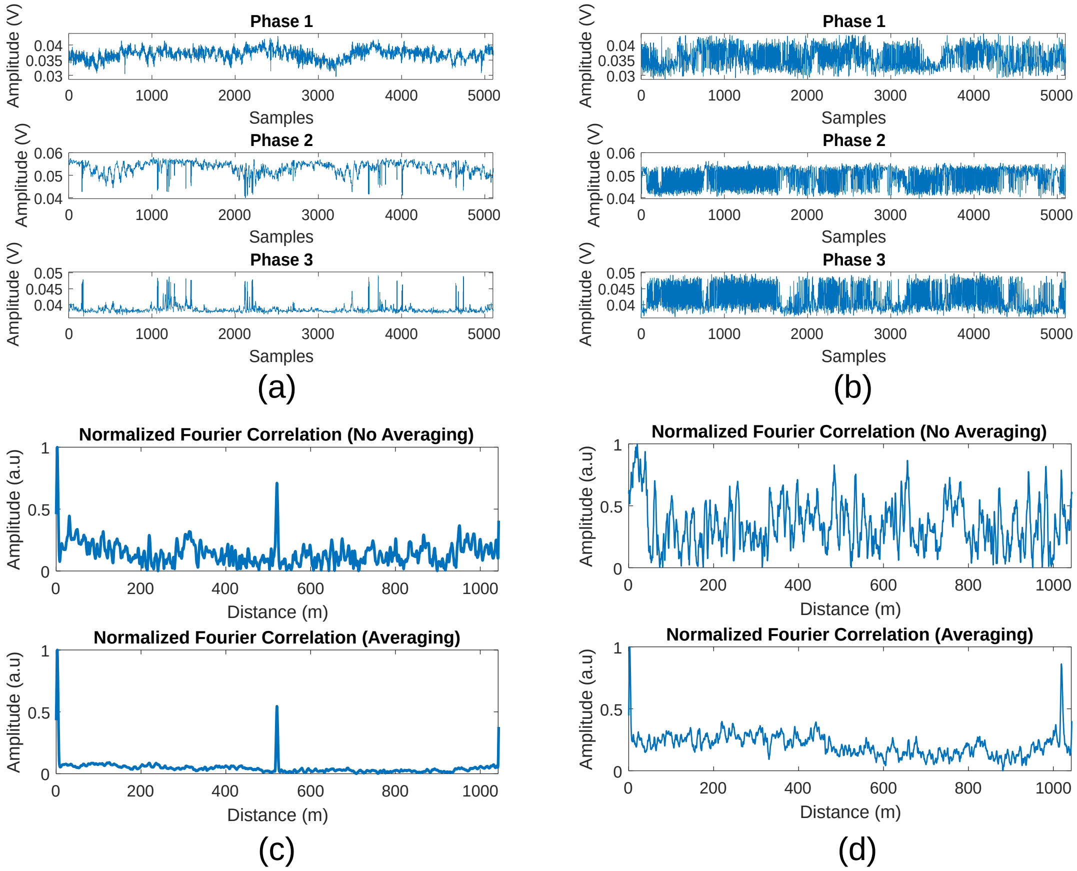

(a)

(b)

(c)

(d)

Figure A.5: Experimental results of distance measurements using the integrated coherent LiDAR. (a, b) Photocurrents detected by the three on-chip PDs when a PRBS-modulated signal propagated through a 500 m fiber and 1 km respectively, and beat with the on-chip LO. (c, d) Normalised amplitude cross-correlatoon between the reconstructed complex signal $\mathrm{I} + j\mathrm{Q}$ and the original PRBS sequence, showing a clear correlation peak at the expected distances of 500 m and 1 km respectively.

A.2 Nonlinear enhancement of SiN microring resonators

In Chapter 3, microring resonators were introduced as OFC sources. The generation of comb frequencies in these devices relies on nonlinear effects that occur within the ring resonator, resulting in the creation of new frequency lines spaced by the resonator's FSR. These nonlinear effects are typically FWM in materials exhibiting Kerr nonlinearity and are only triggered when the optical power circulating inside the resonator exceeds the parametric oscillation threshold.

This threshold corresponds to the condition where the nonlinear gain compensates for the total cavity losses (both intrinsic and coupling-related). The high Q-factor of the resonator enables significant field enhancement, whereby the optical power builds up within the cavity and the effective intensity seen by the nonlinear medium increases. Once the intracavity power reaches the threshold, modulation instability occurs, and sidebands begin to appear symmetrically around the pump frequency. These sidebands then trigger a cascade of FWM interactions, resulting in a broadband, coherent optical frequency comb.

The parametric oscillation threshold power P_{th} can be approximated by [197]

$$P_{th} \approx 1.54 \frac{\pi}{2} \frac{1}{\eta} \frac{n}{n2} \frac{\omega}{D_1} \frac{A_{eff}}{Q_T^2} \tag{A.7}$$

where $\eta = \kappa_e/\kappa$ is the coupling factor (ratio of external to total decay rate between 0 and 1); n and n_2 are the linear and Kerr nonlinear refractive indices, respectively; ω_0 is the pump angular frequency; D_1 is the first-order dispersion parameter $D_1 = 2\pi \cdot FSR$ near ω_0; A_{eff} is the effective mode area; Q_T is the loaded or total Q-factor of the cavity.

From this expression, it follows that high-Q resonators, materials with large Kerr nonlinearity (n_2), and tight modal confinement (small A_{eff}) are key to minimising pump power and achieving efficient comb formation. Recently, AlGaAsOI platform has enabled efficient microcomb generation due to its high Kerr nonlinear coefficient ($n_2 = 2.6 \cdot 10^{-13}\,\mathrm{cm^2W^{-1}}$), around two orders of magnitude higher than that of SiN ($n_2 = 2.5 \cdot 10^{-15}\,\mathrm{cm^2W^{-1}}$). Due to this, microrings in AlGaAsOI have demonstrated superior comb-generation efficiency, even with loaded quality factors lower than those typically obtained in SiN. (engineered). The key resonator parameters reported in representative studies are summarised in Table A.1.

Table A.1: Key performance aspects regarding AlGaAsOI microrresonatros in the literature.

Reference	Q_T	A_{eff} (μm^2)	P_{th} (mW)	FSR (GHz)
[271]	$1.5 \cdot 10^5/2 \cdot 10^5$	0.32 × 0.62	3/6	995/98
[197]	$1.5 \cdot 10^6$	0.4 × 0.7	0.036	1000
[272]	$3.52 \cdot 10^6$	0.4 × 0.7	0.02/0.12	1000/90
[273]	$\sim 10^4$	0.29 × 0.465	0.9	690
[274]	$7 \cdot 10^6$	0.32 × 0.47	-	710

During this thesis, we explored a heterogeneous SiN/AlGaAs approach to microcomb generation, taking advantage of the increased Kerr nonlinearity of AlGaAs. This research was conducted during a three-month research stay at the Institute of Photonics (IoP) at the University of Strathclyde in Glasgow, where the SiN/AlGaAs heterostructures were fabricated and their preliminary characterisation was performed. The approach is based on micro-transfer printing a thin AlGaAs membrane onto a SiN racetrack resonator, thereby creating a high n_2 interaction region within the cavity. The resulting structure exhibits strong optical mode overlap with the AlGaAs layer, which predominantly guides the mode thanks to its higher refractive index. Meanwhile, the underlying SiN racetrack defines the resonant geometry.

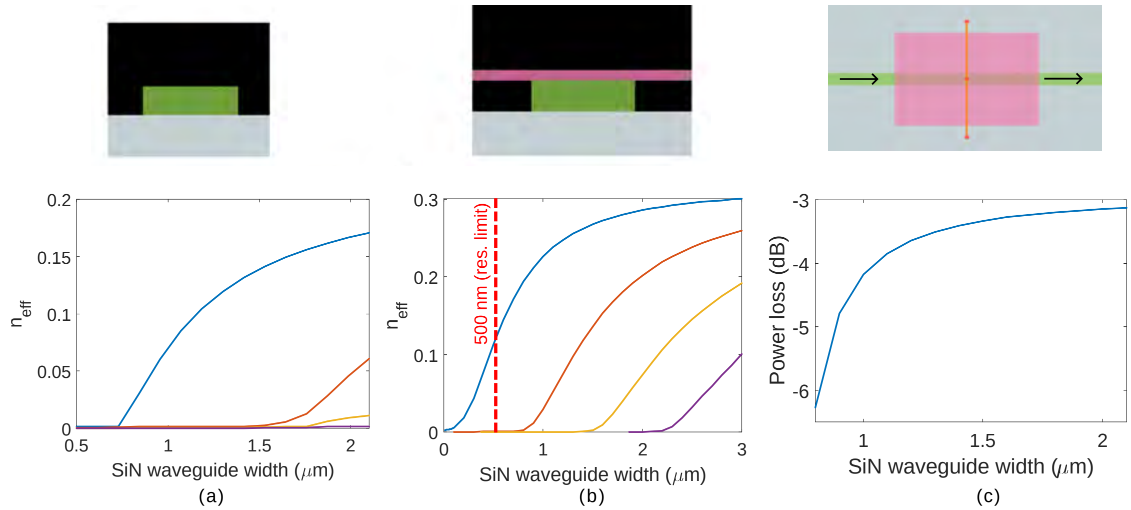

(a)

(b)

(c)

Figure A.6: (a, b) Effective refractive indices of the first four guided modes as a function of the waveguide width for SiN and AlGaAs/SiN structures, respectively. The SiN core height is 300 nm, and the indices are referenced to the substrate index (set to zero) to identify the guided modes. (c) Simulated coupling losses due to the AlGaAs membrane.

As a starting point, the optical modes supported by the different waveguide geometries were simulated using ANSYS Lumerical, a commercial finite-difference eigenmode (FDE) and finite-difference time-domain (FDTD) solver widely employed for modelling photonic components. The simulations were used to study both the SiN waveguide and the hybrid configuration where a 100 nm-thick AlGaAs membrane is placed on top. The refractive-index data for SiN were taken from the manufacturer, while the AlGaAs indices were obtained from a material model corresponding to an aluminium composition of 0.7. Figure Fig. A.6(a, b) shows the effective refractive indices of the first four guided modes as a function of the waveguide width, for both structures. The SiN core height was kept constant at 300 nm. The effective indices are shown with respect to the substrate index (set to zero) to verify which modes fulfil the guiding condition. As expected, wider waveguides support multiple transverse modes, whereas the narrower geometries remain single-mode. The vertical line in Fig. A.6(b) indicates the narrower feasible width that can be fabricated in the cleanroom.

A second set of simulations evaluated the coupling losses introduced by the AlGaAs membrane. In this case, the fundamental mode of the SiN waveguide was injected into a structure where the AlGaAs layer covered only a section of the propagation path. The transmitted field was monitored at the output, and the overlap with the injected mode was used to extract the total power loss. The results, summarised in Fig. A.6(c), show that losses decrease as the waveguide width is reduced.

The design of the SiN resonators starts with the design of the coupling section based on directional couplers. A directional coupler consists of two parallel waveguides brought within evanescent-coupling distance over a coupling length L_c. In this region, the individual waveguide modes decompose into even and odd supermodes. The refractive indices n_1 and n_2 determine the power exchange between the guides. If all the optical power is injected into waveguide 1 at z = 0, the power coupling ratio is given by

$$K = \frac{P_2}{P_1} = \sin^2\left(\frac{\pi L_c \Delta n}{\lambda_0}\right) \tag{A.8}$$

where P_1 and P_2 are the input power and the power coupled to the second waveguide, $\Delta n = n_1 - n_2$ and λ_0 are the free space wavelengths.

Fig. A.7 shows simulated $K = |\kappa|^2$, where κ is the field transmission coefficient, as a function of the beating length between two identical 2.1 μm-wide SiN waveguides, for three different gap sizes and $\lambda_0 = 1.55\,\mu$m. As can be observed, increasing the separation between the two waveguides weakens the overlap of their evanescent fields, thereby reducing the coupling coefficient K. Consequently, a smaller K caused by a larger gap requires a proportionally longer beating length to achieve the same coupling ratio. The length that gives complete transfer $L_c = \lambda_0/2\Delta n$.

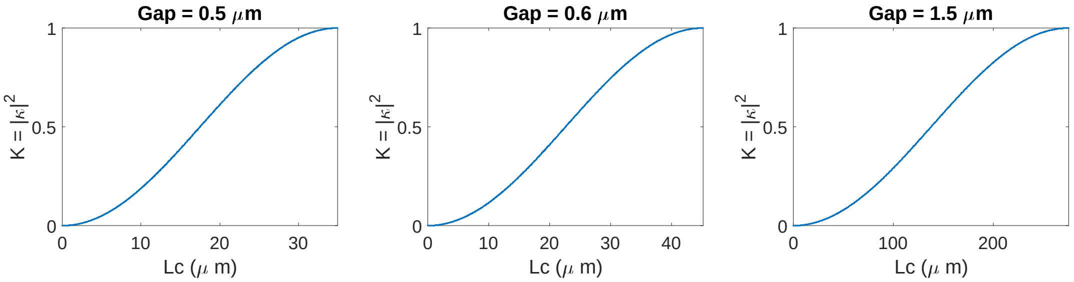

Figure A.7: Simulated optical power coupling between two parallel SiN waveguides as a function of the propagation (beating) length for different separation gaps of 0.5 μm, 0.6 μm, and 1.5 μm.

Circuit design and fabrication

The transmission function of a ring or racetrack resonator can be derived by considering the interference between the optical fields circulating in the resonator and those propagating directly through the bus waveguide. Let us first assume a notch racetrack where E_{i1} is the input field, E_{t1} is the field coupled into the ring resonator, E_{i2} is the field after travelling inside the resonator, and E_{t2} is the optical field coupled back to the bus waveguide after propagating through the resonator. These fields are described by the complex field amplitude, which is normalised so that $|E|^2 = P$, with P being the optical power.**??** illustrates the fields and transmission coefficients of the basic notch ring resonator.

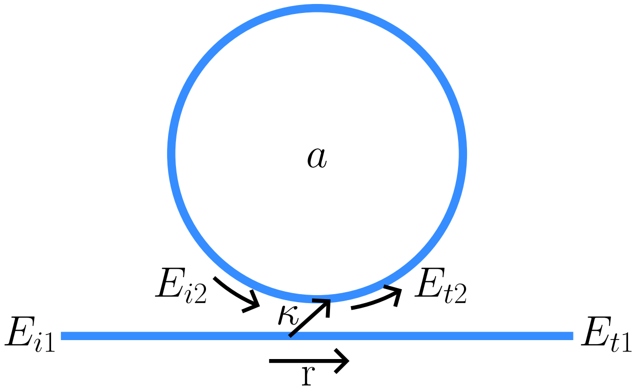

Figure A.8: Basic schematic of a notch ring resonator showing the relevant fields and transmission coefficients.

The analysis assumes a steady-state condition in which, after many round trips, the intracavity field becomes the superposition of all the successively coupled fields from the bus waveguide, each attenuated by propagation losses and phase-shifted by the round-trip phase $\phi = \beta L$, where L is the length of the resonator.

The resonator is characterised by its round-trip amplitude factor $a = e^{-\alpha L}$, its coupling coefficient from the bus to the ring κ, and the transmission coefficient between bus and bus r. Since we are considering a reciprocal network, $|r|^2 + |\kappa|^2 = 1$, which implies that the optical power is conserved in the coupling region. Therefore, the term a must include the losses in the coupling region to ensure that this condition holds and to accurately model the resonances and transfer function of the resonator.

The factor a is defined as the single-pass attenuation coefficient, i.e. the amount by which the field is attenuated after one round trip in the resonator. It includes the distributed losses of the resonator, such as sidewall scattering, material absorption, losses in the coupling section, and bending losses. The FWHM of the resonances decreases (and the Q-factor increases) as losses are reduced; therefore, correctly determining a is essential to model the transfer function of the resonator. Since it is an experimental parameter, several test structures are usually included in the same PIC, consisting of long waveguides to obtain a statistical estimation of the losses.

Employing the transfer function of the bus waveguide, the fields can be computed as

$$\begin{bmatrix} E_{t1} \\ E_{t2} \end{bmatrix} = \begin{bmatrix} r & \kappa \\ -\kappa^* & r \end{bmatrix} \begin{bmatrix} E_{i1} \\ E_{i2} \end{bmatrix} \tag{A.9}$$

where * indicates the complex conjugate. More details about the expressions that will be shown in the following and their derivation can be found in [275], [276]. Here, a basic description is provided.

Developing Eq. (A.9) leads to the power transmission function and power coupling to the ring function being

$$T_n = \left|\frac{E_{t1}}{E_{i1}}\right|^2 = \frac{a^2 + |r|^2 - 2a|r|\cos(\phi + \varphi_t)}{1 + a^2|r|^2 - 2a|r|\cos(\phi + \varphi_t)} \tag{A.10}$$

and

$$K_n = \left|\frac{E_{t2}}{E_{i1}}\right|^2 = \frac{|\kappa|^2}{1 + a^2|r|^2 - 2a|r|\cos(\phi + \varphi_t)} \tag{A.11}$$

where $\phi = \beta L = kn_{eff}L$ is the round-trip phase and φ_t is the phase for the coupling section.

At resonance, when the round-trip phase satisfies $\phi + \varphi_t = 2m\pi$ (m is an integer), the above expressions remain:

$$T_n = \frac{a - |r|^2}{1 - a|r|^2} \tag{A.12}$$

and

$$K_n = \frac{|\kappa|^2}{1 - a|r|^2}. \tag{A.13}$$

At resonance, constructive interference inside the cavity maximises the circulating power, and destructive interference at the bus can lead to zero transmission if the critical coupling condition $r = \sqrt{1 - \kappa^2} = a$ is met. In this regime, the power coupled into the ring exactly balances the internal round-trip losses, and all the input light is dissipated or stored within the resonator, resulting in a deep notch in the through-port spectrum.

For the add–drop configuration, where the resonator is coupled to two bus waveguides (the input or through bus and the drop bus), the same approach can be extended by applying the field continuity conditions at both couplers. Denoting the amplitude transmission and coupling coefficients of the input coupler as r_1 and κ_1, and those of the drop coupler as r_2 and κ_2, the resulting power transmissions at the pass and drop ports are given by

$$T_p = \frac{|r_2|^2 a^2 - 2|r_1||r_2|\cos(\phi) + |r_1|^2}{1 - 2|r_1||r_2|\cos(\phi) + (|r_1||r_2|a)^2} \tag{A.14}$$

and

$$T_d = \frac{(1 - |r_1|^2)\,(1 - |r_2|^2)\,a}{1 - 2|r_1||r_2|\cos(\phi) + (|r_1||r_2|a)^2} \tag{A.15}$$

At resonance ($\phi = 2\pi m$), the optical field in the ring constructively interferes with itself, leading to maximum energy build-up and efficient transfer to the drop port.

For symmetric couplers ($r_1 = r_2 = r$), maximum power is extracted at the drop port when

$$r = a^{1/4}, \tag{A.16}$$

corresponding to a power coupling

$$K = 1 - \sqrt{\alpha}. \tag{A.17}$$

This is the critical coupling condition for an add–drop resonator.

Additionally, two distinct coupling regimes can be identified depending on the relative magnitude of the coupling coefficient and the round-trip loss in the ring. When the self-coupling amplitude of the coupler is larger than the round-trip transmission amplitude ($r > a$), the resonator is said to operate in the undercoupled regime. In this case, only a small fraction of the input power is coupled into the ring, resulting in a shallow notch in the through-port transmission spectrum and limited energy build-up within the cavity.

When $r < a$, the system enters the overcoupled regime, where the coupling to the ring exceeds the internal losses. Although the resonance depth in the through-port spectrum decreases again, the linewidth broadens because the loaded quality factor is dominated by the external coupling rather than by intrinsic propagation losses.

The first fabrication run included both notch and add-drop racetrack resonators with varying coupling lengths and gaps, covering a wide range of regimes from undercoupling to overcoupling. In addition, directional couplers were incorporated with coupling lengths corresponding to the overcoupled rings and to 50:50 in order to validate the simulation results. Figure A.9 shows the layout of the fabricated PIC, together with microscope photographs of the fabricated resonators.

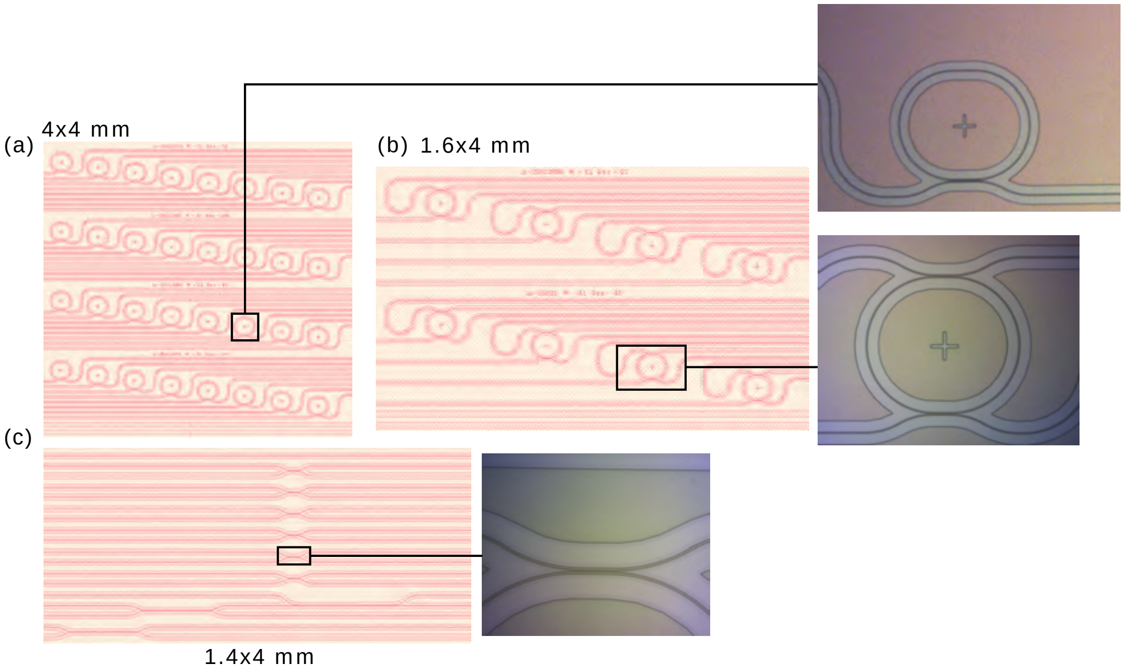

Figure A.9: PIC layout designed for the first fabrication run. (a) Notch racetrack resonators with varying coupling gaps and lengths, alongside a microscope image of one fabricated device. (b) Add-drop racetrack resonators with different coupling configurations and a corresponding photograph. (c) Directional couplers with various coupling ratios, shown together with a fabricated example.

The layout was produced using GDSHelpers instead of NAZCA for practical reasons related to availability. GDSHelpers is a Python-based environment that allows automated GDSII generation and efficient parameterisation of photonic components, similarly to NAZCA.

Alignment slabs were also added across the PIC to aid optical alignment during measurements.

For the resonator design, a round-trip amplitude factor of $a = 0.95$ was assumed, based on previous experience within the group. However, an additional PIC containing several passive test structures was also fabricated to accurately quantify propagation losses; its design is not shown here. According to FDTD simulations, the critical coupling length varies between 5 and 20 μm depending on the coupling gap.

Regarding the fabrication of the devices presented here, the process consisted of four main stages: (i) surface preparation and resist coating, (ii) UV maskless lithography using a Heidelberg writer followed by resist development, (iii) dry etching of the SiN layer to transfer the pattern, and (iv) resist removal and wafer cleaving. All fabrication steps, as well as the subsequent micro-transfer printing of the AlGaAs membranes, were carried out in the IoP cleanroom facilities under the supervision of the researchers Jack Smith and Elise Burns.

Characterisation of the fabricated devices

The fabricated resonators were extensively characterised. A CW tunable external laser was coupled into the PIC, and the output was monitored using both an IR camera and a PD connected to an oscilloscope. By sweeping the emission wavelength of the external laser, the resonance characteristics of the resonators were obtained.

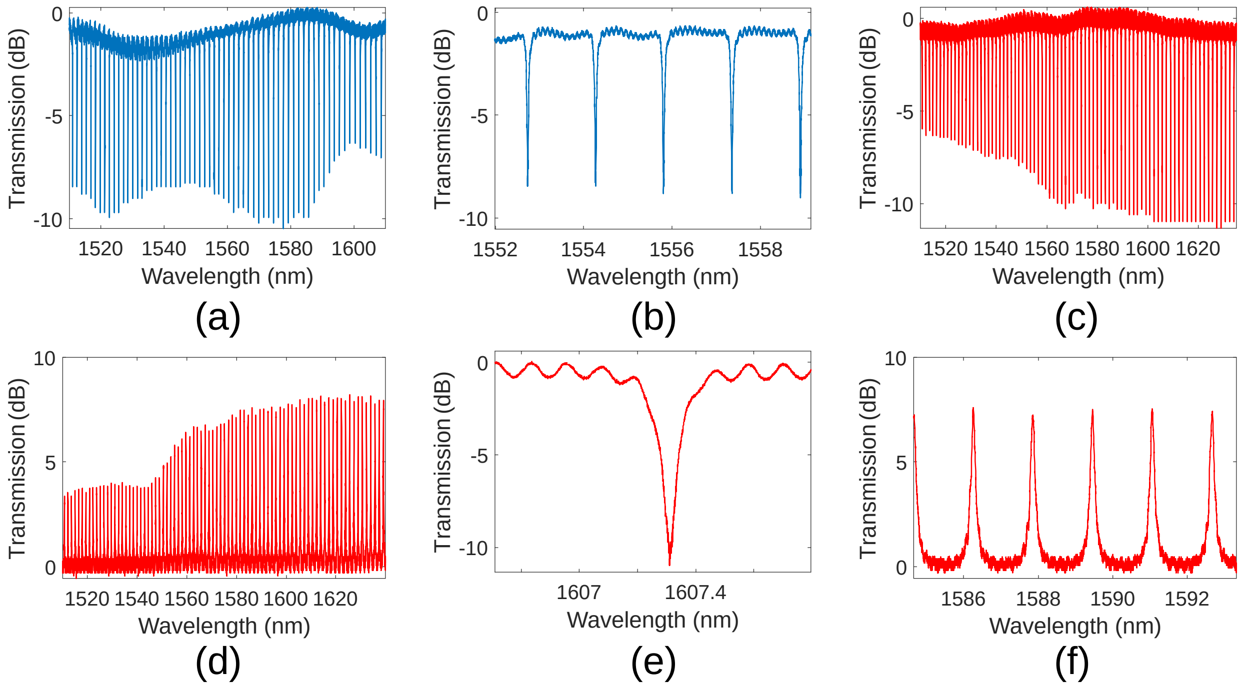

Figure A.10: (a) Measured transmission spectrum of an overcoupled notch racetrack resonator showing periodic resonances, and (b) a zoomed-in view of one resonance. (c) Measured transmission spectrum of an overcoupled add-drop racetrack at the through port and (d) at the drop port, with zoomed-in views shown in (e) and (f), respectively.

Fig. A.10(a) shows the measured transmission spectrum of a representative notch racetrack resonator, with a zoomed-in view in Fig. A.10(b). The measured free spectral range (FSR) is 1.61 nm, corresponding to an optical path length of approximately 0.78 mm, in excellent agreement with the designed resonator radius of 120 μm.

Fitting the measured resonances with Eq. (A.10) yields Q-factors on the order of 10^4, confirming that the device operates in the overcoupled regime.

Fig. A.10(c, d) show the measured transmission spectra of a representative add-drop racetrack resonator at the through and drop ports, respectively, together with a zoomed-in view of the resonances in Fig. A.10(e,f). The measured FSR is again approximately 1.6 nm, consistent with the results obtained for the notch configuration. Fitting the resonances yields Q-factors on the order of 10^4, indicating that this device also operates in the overcoupled regime.

The ring resonator selected for the transfer-printing experiment was specifically chosen to operate in the overcoupled regime. The introduction of the AlGaAs membrane modifies the coupling conditions by increasing the effective refractive index and introducing additional optical losses in the coupling region, thereby reducing the overall coupling strength and modifying the coupling obtained in Fig. A.7. This membrane was fabricated in the IoP facilities by Elise Burns, a PhD student. By selecting an initially overcoupled resonator, the goal was to compensate for this expected reduction and prevent the device from entering the undercoupled regime after the membrane transfer.

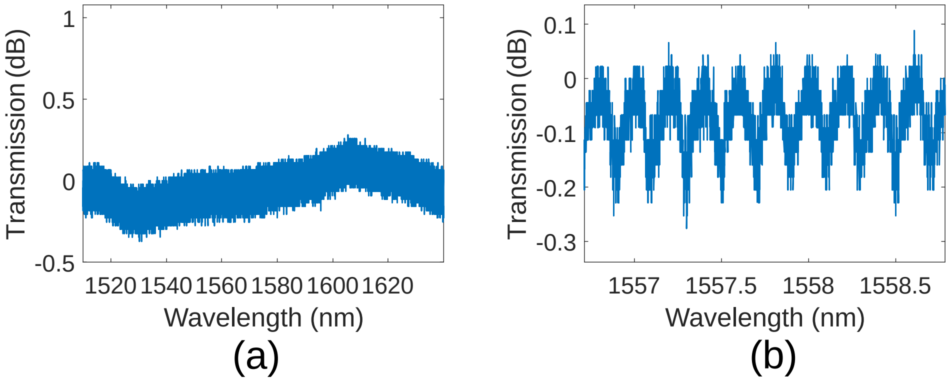

Figure A.11: Measured transmission spectrum of an add-drop racetrack resonator after micro-transfer printing of the AlGaAs membrane. (a) Full transmission spectrum and (b) Zoomed-in view.

One of the factors contributing to these results is the significant optical power loss observed after the membrane transfer. For the employed SiN waveguide width of 2.1 μm, the addition of the AlGaAs membrane alters the modal confinement, causing part of the optical power to couple into higher-order modes. These modes experience substantially higher propagation losses, which result in the reduced resonance depth observed in Fig. A.11. In addition to this, the abrupt appearance of the high-index AlGaAs layer introduces a strong local scattering point. In the absence of an adiabatic taper, this discontinuity further increases insertion loss and contributes to the degradation of the resonance.

To further improve coupling efficiency, the design shown in Fig. A.12(a) was proposed. The concept consists of narrowing the waveguides in the coupling section and in the ring itself to a width of 800 μm, while maintaining a wider access waveguide outside the membrane region to facilitate alignment with external fibers. The AlGaAs membrane is overlaid on the region where coupling losses are minimised, thereby improving the optical overlap between the SiN waveguide and the high-index AlGaAs film. To match the different waveguide widths, an adiabatic taper with a length of 75 μm was designed to maximise transmitted optical power. The taper simulations were carried out using Lumerical FDTD.

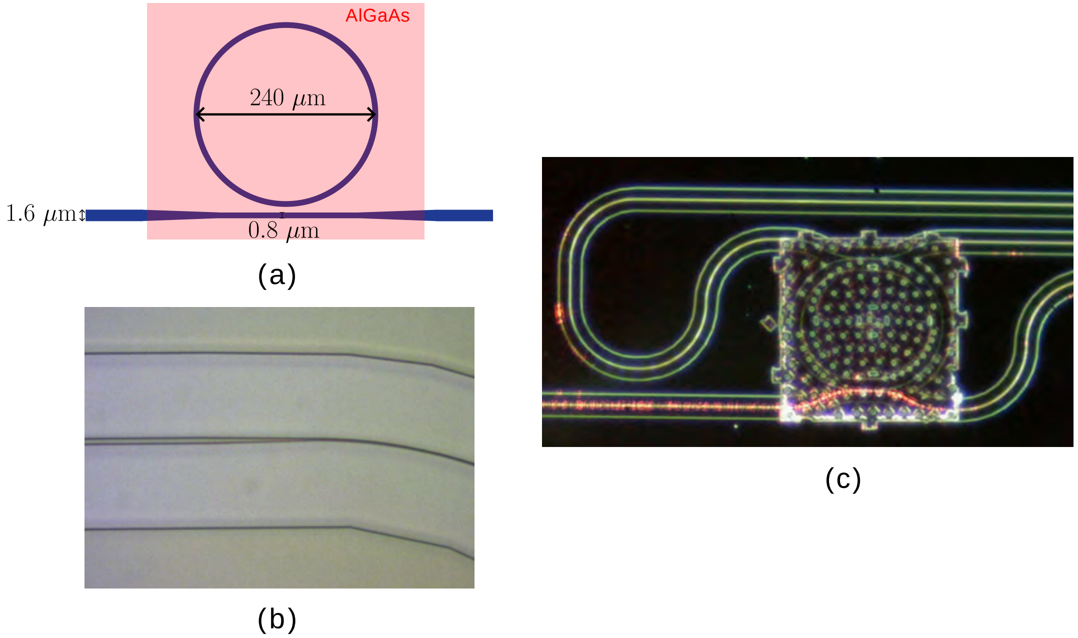

(a)

(b)

(c)

Figure A.12: (a) Schematic of the proposed racetrack resonator design with a tapered coupling section for improved alignment with the AlGaAs membrane. (b) Microscope image of the fabricated taper section. (c) Top-view photograph of the racetrack resonator with the transferred AlGaAs membrane under red laser illumination, showing significant propagation losses.

Figure A.12(b) shows a microscope image of the fabricated taper section. At this stage, however, the full functionality of the fabricated waveguides could not be guaranteed, since the resolution of the lithography tool was insufficient to reproducibly define the narrow waveguide widths and small coupling gaps required. Several fabrication runs were therefore attempted, but the coupling gap remained inconsistent between devices.

During the same period, the equipment required to process the AlGaAs stamps used for micro-transfer printing suffered a malfunction. As a result, pre-existing AlGaAs membranes were used, which were not optimised for the newly designed SiN rings. Figure A.12(c) shows a top-view image of one of the fabricated rings after transfer printing, with red laser light injected for diagnostic purposes. The low transmitted power clearly indicates suboptimal coupling and significant losses, attributed mainly to deviations in the fabricated waveguide dimensions and coupling gaps from the intended design.

When the stay concluded, there was insufficient time to carry out additional fabrication runs that could have addressed these limitations. It should be noted that such processes are inherently complex and require iterative optimisation to achieve reproducible performance.

Despite these challenges, the work carried out during this period advanced the understanding of heterogeneous integration of AlGaAs membranes on SiN microrings via transfer printing, aimed at enhancing the nonlinear response of integrated resonators for OFC generation. The tasks performed included analytical modelling of ring resonator behaviour, numerical simulations of waveguide and coupling structures, design and layout generation, fabrication of SiN photonic integrated circuits, and experimental characterisation.

The first fabrication run resulted in devices with good performance, and add-drop racetrack resonators were successfully demonstrated on the in-house SiN platform. Although the main objective could not be fully achieved within the available time, the results provided valuable insight into the reproducibility of the lithography process and the alignment requirements for transfer-printed membranes. These findings contribute to the development of integrated nonlinear resonators and lay the groundwork for future fabrication runs with improved lithographic resolution and membrane compatibility. Despite the limited duration of the three-month stay, this work established a promising direction for future research and significantly strengthened my expertise in the simulation, modelling, and fabrication of integrated photonic devices, complementing the characterisation techniques developed in the Applied Photonics group at UPM.

List of publications

Journal articles

P. López-Querol, C. Quevedo-Galán, A. Pérez-Serrano, J. M. G. Tijero, and I. Esquivias, "Generation of optical frequency combs by Q-switching integrated multi-section semiconductor lasers," *Optics Express*, vol. 31, no. 20, pp. 33475–33485, 2023. DOI: 10.1364/OE.498426.

P. López-Querol, A. Soria-Gómez, A. Quirce, J. M. G. Tijero, I. Esquivias and A. Pérez-Serrano, “InP-based integrated optical frequency shifter for heterodyne detection applications,” *Optics and Laser Technology*, vol. 179, p. 111274, Dec. 2024. DOI: 10.1016/j.optlastec.2024.111274.

P. López-Querol, C. Quevedo-Galán, P. Castera, J. M. G. Tijero, I. Esquivias and A. Pérez-Serrano, “Monolithically integrated dual-comb generator based on gain-switched semiconductor ring lasers,” *Optics and Laser Technology*, vol. 181, p. 113317, Jan. 2025. [Online]. DOI: 10.1016/j.optlastec.2024.113317.

L. Monroy, A. Rosado, C. Quevedo-Galán, P. López-Querol, A. Pérez-Serrano, J. M. G. Tijero and I. Esquivias, “Dual-comb spectroscopy from an optically injected single gain-switched semiconductor laser source,” *Journal of Lightwave Technology*, vol. 43, no. 12, pp. 5797-5803, Jun. 2025. doi: 10.1109/JLT.2025.3556554.

International conferences[1]

P. López-Querol, C. Quevedo-Galán, A. Pérez-Serrano, J. M. G. Tijero◇, and I. Esquivias, "Low repetition rate optical frequency combs generated by pulsed gain-switching of semiconductor lasers," in *27th International Semiconductor Laser Conference (ISLC)*, Potsdam (Germany), October 2021 [Poster]. DOI: 10.1109/ISLC51662.2021.9615720.

C. Quevedo-Galán◇, P. López-Querol, A. Pérez-Serrano, J. M. G. Tijero, and I. Esquivias, "Gain-switched optical frequency combs with comb spacing down to 5 MHz," in *European Semiconductor Laser Workshop*, Paris (France), September 2021 [Oral].

P. López-Querol◇, A. Soria-Gómez, A. Quirce, I. Esquivias, J. M. G. Tijero, and A. Pérez-Serrano, "Integrated Frequency Shifter based on an Indium Phosphide Generic Platform for Heterodyne Detection Systems," in *Frontiers in Optics/Laser Science*, Rochester, New York (USA), October 2022, Paper JW5B.38 [Poster]. DOI: 10.1364/FIO.2022.JW5B.38.

C. Quevedo-Galán◇, P. López-Querol, E. Sentre-Arribas, A. Pérez-Serrano, J. M. G. Tijero,

---

[1] The author who presented the contribution is indicated with ◇.

and I. Esquivias, "Dual-Comb Ranging Using Low-Repetition-Rate Gain-Switched Semiconductor Lasers," in *Frontiers in Optics/Laser Science*, Rochester, New York (USA), October 2022, Paper JW5B.18 [Poster]. DOI: 10.1364/FIO.2022.JW5B.18.

P. López-Querol$^{\diamond}$, C. Quevedo-Galán, A. Pérez-Serrano, J. M. G. Tijero, and I. Esquivias, "Q-switched semiconductor lasers as sources for optical frequency comb generation," in *CLEO/Europe-EQEC*, Munich (Germany), June 2023, Paper cbp15 [Poster]

C. Quevedo-Galán$^{\diamond}$, A. Rosado, P. López-Querol, A. Pérez-Serrano, J. M. G. Tijero, and I. Esquivias, "Dual-comb interferometer based on densified gain-switched laser diodes for high-resolution sensing applications," in *CLEO/Europe-EQEC*, Munich (Germany), June 2023, Paper cb74 [Oral]. DOI: 10.1109/CLEO/Europe-EQEC57999.2023.10231545.

P. López-Querol$^{\diamond}$, C. Quevedo-Galán, J. M. G. Tijero, I. Esquivias and A. Pérez-Serrano, "Monolithically Integrated Dual-Comb Generator Based on a Generic Platform Photonic Integrated Circuit," in *CLEO/Europe-EQEC*, Munich (Germany), June 2025, [Oral]. DOI: 10.1109/CLEO/Europe-EQEC65582.2025.11110209.

L. Monroy, A. Rosado$^{\diamond}$, C. Quevedo-Galán, P. López-Querol, A. Pérez-Serrano, J. M. G. Tijero, and I. Esquivias, "Dual-optical frequency comb generation for gas spectroscopy using a single gain-switched externally-injected semiconductor laser, in *CLEO/Europe-EQEC*, Munich (Germany), June 2025, [Oral].

P. Grześ$^{\diamond}$, P. López-Querol, C. Quevedo-Galán, J. G. Tijero, I. Esquivias, and A. Pérez-Serrano, "Differential absorption lidar for carbon dioxide remote sensing based on a photonic integrated circuit", Proc. SPIE 13668, Remote Sensing of Clouds and the Atmosphere XXX, 136680A (29 October 2025). DOI: 10.1117/12.3069908.

National conferences

P. López-Querol$^{\diamond}$, C. Quevedo-Galán, A. Pérez-Serrano, J. M. G. Tijero, and I. Esquivias, "Experimental analysis of low repetition rate optical frequency combs generated by pulsed gain-switching of optically injected laser diodes," in *OPTOEL'21*, Virtual, July 2021 [Poster].

P. López-Querol$^{\diamond}$, C. Quevedo-Galán, A. Soria-Gómez, I. Pintor, J. M. G. Tijero, I. Esquivias, and A. Pérez-Serrano, "Photonic Integrated Circuits at CEMDATIC-UPM," in *OPTOEL'23*, Sevilla (Spain), June 2023 [Poster].

S. del Río-Martín$^{\diamond}$, C. Quevedo-Galán, P. López-Querol, and I. Esquivias, "Photonic Microwave Phase Shifter based on an I/Q modulator," in *OPTOEL'23*, Sevilla (Spain), June 2023 [Poster].

D. Domínguez-Castillejo$^{\diamond}$, C. Quevedo-Galán, P. López-Querol, and A. Pérez-Serrano, "Pseudo Random Phase Modulation Coherent LIDAR," in *OPTOEL'23*, Sevilla (Spain), June 2023 [Poster].

C. Quevedo-Galán$^{\diamond}$, A. Rosado, L. Monroy, P. López-Querol, A. Pérez-Serrano, J. M. G. Tijero, and I. Esquivias, "Ultra-high resolution dual comb spectroscopy based on gain-switching optical frequency combs," in *OPTOEL'23*, Sevilla (Spain), June 2023 [Poster].

Bibliography

[1] R. N. Hall, G. E. Fenner, J. D. Kingsley, T. J. Soltys, and R. O. Carlson, “Coherent Light Emission From GaAs Junctions”, en, *Physical Review Letters*, vol. 9, no. 9, pp. 366–368, 1962. DOI: `10.1103/PhysRevLett.9.366`.

[2] S. E. Miller, “Integrated optics: An introduction”, *The Bell System Technical Journal*, vol. 48, no. 7, pp. 2059–2069, 1969. DOI: `10.1002/j.1538-7305.1969.tb01165.x`.

[3] Y. Shi, Y. Zhang, Y. Wan, Y. Yu, Y. Zhang, X. Hu, X. Xiao, H. Xu, L. Zhang, and B. Pan, “Silicon photonics for high-capacity data communications”, EN, *Photonics Research*, vol. 10, no. 9, A106–A134, 2022. DOI: `10.1364/PRJ.456772`.

[4] S. Daudlin, A. Rizzo, S. Lee, D. Khilwani, C. Ou, S. Wang, A. Novick, V. Gopal, M. Cullen, R. Parsons, K. Jang, A. Molnar, and K. Bergman, “Three-dimensional photonic integration for ultra-low-energy, high-bandwidth interchip data links”, en, *Nature Photonics*, vol. 19, no. 5, pp. 502–509, 2025. DOI: `10.1038/s41566-025-01633-0`.

[5] Y. Guo, L. Zhou, L. Guo, W. Jiang, J. Du, X. Chen, H. Wang, X. Bao, Y. Du, J. Qu, Y. Zhong, R. Zhou, Y. Wu, Y. Guo, and W. Chen, “Integrated photonics for space communication and sensing”, en, *Journal of Physics: Photonics*, vol. 7, no. 4, p. 042 001, 2025. DOI: `10.1088/2515-7647/ade64b`.

[6] A. Hänsel and M. J. R. Heck, “Opportunities for photonic integrated circuits in optical gas sensors”, en, *Journal of Physics: Photonics*, vol. 2, no. 1, p. 012 002, 2020. DOI: `10.1088/2515-7647/ab6742`.

[7] E. Pelucchi, G. Fagas, I. Aharonovich, D. Englund, E. Figueroa, Q. Gong, H. Hannes, J. Liu, C.-Y. Lu, N. Matsuda, J.-W. Pan, F. Schreck, F. Sciarrino, C. Silberhorn, J. Wang, and K. D. Jöns, “The potential and global outlook of integrated photonics for quantum technologies”, en, *Nature Reviews Physics*, vol. 4, no. 3, pp. 194–208, 2022. DOI: `10.1038/s42254-021-00398-z`.

[8] K. E. Zinoviev, A. B. Gonzalez-Guerrero, C. Dominguez, and L. M. Lechuga, “Integrated Bimodal Waveguide Interferometric Biosensor for Label-Free Analysis”, *Journal of Lightwave Technology*, vol. 29, no. 13, pp. 1926–1930, 2011. DOI: `10.1109/JLT.2011.2150734`.

[9] R. Singh, J. García Rupérez, and L. M. Lechuga, "Design of subwavelength grating-based bimodal waveguide interferometric sensor in visible range for enhancing diagnostics sensitivity", en, *Journal of Physics: Photonics*, vol. 7, no. 4, p. 045 009, 2025. DOI: `10.1088/2515-7647/adfda1`.

[10] J. N. Eckstein, A. I. Ferguson, and T. W. Hänsch, "High-Resolution Two-Photon Spectroscopy with Picosecond Light Pulses", *Physical Review Letters*, vol. 40, no. 13, pp. 847–850, 1978. DOI: `10.1103/PhysRevLett.40.847`.

[11] T. Udem, J. Reichert, R. Holzwarth, and T. W. Hänsch, "Absolute Optical Frequency Measurement of the Cesium ${\mathit{D}}_{1}$ Line with a Mode-Locked Laser", *Physical Review Letters*, vol. 82, no. 18, pp. 3568–3571, 1999. DOI: `10.1103/PhysRevLett.82.3568`.

[12] M. Smit, K. Williams, and J. van der Tol, "Past, present, and future of InP-based photonic integration", *APL Photonics*, vol. 4, no. 5, p. 050 901, 2019. DOI: `10.1063/1.5087862`.

[13] R. V. Schmidt and I. P. Kaminow, "Metal-diffused optical waveguides in LiNbO3", *Applied Physics Letters*, vol. 25, no. 8, pp. 458–460, 1974. DOI: `10.1063/1.1655547`.

[14] I. Kaminow, V. Ramaswamy, R. Schmidt, and E. Turner, "Lithium niobate ridge waveguide modulator", *IEEE Journal of Quantum Electronics*, vol. 10, no. 9, pp. 731–731, 1974. DOI: `10.1109/JQE.1974.1068254`.

[15] R. A. Logan and F. K. Reinhart, "Optical waveguides in GaAs–AlGaAs epitaxial layers", *Journal of Applied Physics*, vol. 44, no. 9, pp. 4172–4176, 1973. DOI: `10.1063/1.1662912`.

[16] S. Somekh, E. Garmire, A. Yariv, H.L. Garvin, and R.G. Hunsperger, "Channel optical waveguide directional couplers", *Applied Physics Letters*, vol. 22, pp. 46–47, 1973. DOI: `10.1063/1.1654468`.

[17] S. Valette, G. Labrunie, J.-C. Deutsch, and J. Lizet, "Planar optical waveguides in ion-implanted ZnTe", *IEEE Journal of Quantum Electronics*, vol. 11, no. 9, pp. 861–862, 1975. DOI: `10.1109/JQE.1975.1068814`.

[18] M. K. Barnoski, R. G. Hunsperger, R. G. Wilson, and G. Tangonan, "Proton-implanted GaP optical waveguide", *Journal of Applied Physics*, vol. 44, no. 4, pp. 1925–1926, 1973. DOI: `10.1063/1.1662486`.

[19] F. K. Reinhart and R. A. Logan, "GaAs-AlGaAs double heterostructure lasers with taper-coupled passive waveguides", *Applied Physics Letters*, vol. 26, no. 9, pp. 516–518, 1975. DOI: `10.1063/1.88239`.

[20] D. W. Bellavance and J. C. Campbell, “Room-temperature mesa lasers grown by selective liquid phase epitaxy”, *Applied Physics Letters*, vol. 29, no. 3, pp. 162–164, 1976. DOI: `10.1063/1.89008`.

[21] J. Campbell and D. Bellavance, “Monolithic laser/waveguide coupling by evanescent fields”, *IEEE Journal of Quantum Electronics*, vol. 13, no. 4, pp. 253–255, 1977. DOI: `10.1109/JQE.1977.1069306`.

[22] P. K. Tien, “Integrated optics and new wave phenomena in optical waveguides”, *Reviews of Modern Physics*, vol. 49, no. 2, pp. 361–420, 1977. DOI: `10.1103/RevModPhys.49.361`.

[23] K. Aiki, M. Nakamura, and J. Umeda, “Frequency multiplexing light source with monolithically integrated distributed-feedback diode lasers”, *Applied Physics Letters*, vol. 29, no. 8, pp. 506–508, 1976. DOI: `10.1063/1.89140`.

[24] R. Soref and J. Lorenzo, “Single-crystal silicon: A new material for 1.3 and 1.6 m integrated-optical components”, *Electronics Letters*, vol. 21, no. 21, pp. 953–954, 1985. DOI: `10.1049/el:19850673`.

[25] J. Schmidtchen, A. Splett, B. Schüppert, K. Petermann, and G. Burbach, “Low loss singlemode optical waveguides with large cross-section in silicon-on-insulator”, *Electronics Letters*, vol. 27, no. 16, pp. 1486–1488, 1991. DOI: `10.1049/el:19910930`.

[26] M. Smit, “New focusing and dispersive planar component based on an optical phased array”, *Electronics Letters*, vol. 24, no. 7, pp. 385–386, 1988. DOI: `10.1049/el:19880260`.

[27] H. Takahashi, S. Suzuki, K. Kato, and I. Nishi, “Arrayed-waveguide grating for wavelength division multi/demultiplexer with nanometre resolution”, *Electronics Letters*, vol. 26, no. 2, pp. 87–88, 1990. DOI: `10.1049/el:19900058`.

[28] C. Dragone, “An N*N optical multiplexer using a planar arrangement of two star couplers”, *IEEE Photonics Technology Letters*, vol. 3, no. 9, pp. 812–815, 1991. DOI: `10.1109/68.84502`.

[29] M. Zirngibl and C. Joyner, “High performance, 12 frequency optical multichannel controller”, *Electronics Letters*, vol. 30, no. 9, pp. 700–701, 1994. DOI: `10.1049/el:19940501`.

[30] M. Smit, J. van der Tol, and M. Hill, “Moore’s law in photonics”, en, *Laser & Photonics Reviews*, vol. 6, no. 1, pp. 1–13, 2012. DOI: `10.1002/lpor.201100001`.

[31] S. Shekhar, W. Bogaerts, L. Chrostowski, J. E. Bowers, M. Hochberg, R. Soref, and B. J. Shastri, “Roadmapping the next generation of silicon photonics”, en, *Nature Communications*, vol. 15, no. 1, p. 751, 2024. DOI: `10.1038/s41467-024-44750-0`.

[32] J. A. Smith, D. Jevtics, B. Guilhabert, M. D. Dawson, and M. J. Strain, "Hybrid integration of chipscale photonic devices using accurate transfer printing methods", *Applied Physics Reviews*, vol. 9, no. 4, p. 041 317, 2022. DOI: `10.1063/5.0121567`.

[33] T. Komljenovic, M. Davenport, J. Hulme, A. Y. Liu, C. T. Santis, A. Spott, S. Srinivasan, E. J. Stanton, C. Zhang, and J. E. Bowers, "Heterogeneous Silicon Photonic Integrated Circuits", *Journal of Lightwave Technology*, vol. 34, no. 1, pp. 20–35, 2016. DOI: `10.1109/JLT.2015.2465382`.

[34] N. Margalit, C. Xiang, S. M. Bowers, A. Bjorlin, R. Blum, and J. E. Bowers, "Perspective on the future of silicon photonics and electronics", *Applied Physics Letters*, vol. 118, no. 22, p. 220 501, 2021. DOI: `10.1063/5.0050117`.

[35] EUROPRACTICE. "Photonics packaging". en, Accessed: Dec. 2, 2025. [Online]. Available: `https://europractice-ic.com/services/packaging/photonics-packaging/`.

[36] W. Xu, Q. Yuan, Y. Yang, L. Lu, J. Chen, and L. Zhou, "Progress and prospects for LiDAR-oriented optical phased arrays based on photonic integrated circuits", en, *npj Nanophotonics*, vol. 2, no. 1, p. 14, 2025. DOI: `10.1038/s44310-025-00059-4`.

[37] R. Halir, A. Ortega-Moñux, D. Benedikovic, G. Z. Mashanovich, J. G. Wangüemert-Pérez, J. H. Schmid, Í. Molina-Fernández, and P. Cheben, "Subwavelength-Grating Metamaterial Structures for Silicon Photonic Devices", *Proceedings of the IEEE*, vol. 106, no. 12, pp. 2144–2157, 2018. DOI: `10.1109/JPROC.2018.2851614`.

[38] R. Halir, P. J. Bock, P. Cheben, A. Ortega-Moñux, C. Alonso-Ramos, J. H. Schmid, J. Lapointe, D.-X. Xu, J. G. Wangüemert-Pérez, Í. Molina-Fernández, and S. Janz, "Waveguide sub-wavelength structures: A review of principles and applications", *Laser & Photonics Reviews*, vol. 9, no. 1, pp. 25–49, 2015. DOI: `10.1002/lpor.201400083`.

[39] J. H. Schmid et al., "Recent advances in integrated photonics with subwavelength and resonant metamaterials", in *Integrated Optics: Devices, Materials, and Technologies XXVIII*, vol. PC12889, SPIE, 2024, PC128890M. DOI: `10.1117/12.3000757`.

[40] D. Marpaung, C. Roeloffzen, R. Heideman, A. Leinse, S. Sales, and J. Capmany, "Integrated microwave photonics", *Laser & Photonics Reviews*, vol. 7, no. 4, pp. 506–538, 2013. DOI: `10.1002/lpor.201200032`.

[41] S. Jia, M.-C. Lo, L. Zhang, O. Ozolins, A. Udalcovs, D. Kong, X. Pang, R. Guzman, X. Yu, S. Xiao, S. Popov, J. Chen, G. Carpintero, T. Morioka, H. Hu, and L. K. Oxenløwe, "Integrated dual-laser photonic chip for high-purity carrier generation enabling ultrafast terahertz wireless communications", en, *Nature Communications*, vol. 13, no. 1, p. 1388, 2022. DOI: `10.1038/s41467-022-29049-2`.

[42] G. Carpintero, K. Balakier, Z. Yang, R. C. Guzmán, A. Corradi, A. Jimenez, G. Kervella, M. J. Fice, M. Lamponi, M. Chitoui, F. van Dijk, C. C. Renaud, A. Wonfor,

E. A. J. M. Bente, R. V. Penty, I. H. White, and A. J. Seeds, “Microwave Photonic Integrated Circuits for Millimeter-Wave Wireless Communications”, *Journal of Lightwave Technology*, vol. 32, no. 20, pp. 3495–3501, 2014. DOI: `10.1109/JLT.2014.2321573`.

[43] F. van Dijk, G. Kervella, M. Lamponi, M. Chtioui, F. Lelarge, E. Vinet, Y. Robert, M. J. Fice, C. C. Renaud, A. Jimenez, and G. Carpintero, “Integrated InP Heterodyne Millimeter Wave Transmitter”, *IEEE Photonics Technology Letters*, vol. 26, no. 10, pp. 965–968, 2014. DOI: `10.1109/LPT.2014.2309353`.

[44] A. Dutt, C. Joshi, X. Ji, J. Cardenas, Y. Okawachi, K. Luke, A. L. Gaeta, and M. Lipson, “On-chip dual-comb source for spectroscopy”, *Science Advances*, vol. 4, no. 3, e1701858, 2018. DOI: `10.1126/sciadv.1701858`.

[45] L. Chang, S. Liu, and J. E. Bowers, “Integrated optical frequency comb technologies”, en, *Nature Photonics*, vol. 16, no. 2, pp. 95–108, 2022. DOI: `10.1038/s41566-021-00945-1`.

[46] A. Hermans, K. Van Gasse, and B. Kuyken, “On-chip optical comb sources”, *APL Photonics*, vol. 7, no. 10, p. 100 901, 2022. DOI: `10.1063/5.0105164`.

[47] W. Bogaerts, D. Pérez, J. Capmany, D. A. B. Miller, J. Poon, D. Englund, F. Morichetti, and A. Melloni, “Programmable photonic circuits”, en, *Nature*, vol. 586, no. 7828, pp. 207–216, 2020. DOI: `10.1038/s41586-020-2764-0`.

[48] P. Del’Haye, A. Schliesser, O. Arcizet, T. Wilken, R. Holzwarth, and T. J. Kippenberg, “Optical frequency comb generation from a monolithic microresonator”, en, *Nature*, vol. 450, no. 7173, pp. 1214–1217, 2007. DOI: `10.1038/nature06401`.

[49] G. T. Reed and A. P. Knights, *Silicon Photonics: An Introduction*, en, 1st ed. Wiley, 2004. DOI: `10.1002/0470014180`.

[50] T. Kim and J. Lee, “Fabrication and characterization of silicon-on-insulator wafers”, en, *Micro and Nano Systems Letters*, vol. 11, no. 1, p. 15, 2023. DOI: `10.1186/s40486-023-00181-y`.

[51] M. A. Al-Qadasi, L. Chrostowski, B. J. Shastri, and S. Shekhar, “Scaling up silicon photonic-based accelerators: Challenges and opportunities”, *APL Photonics*, vol. 7, no. 2, p. 020 902, 2022. DOI: `10.1063/5.0070992`.

[52] Z. Lu, K. Murray, H. Jayatilleka, and L. Chrostowski, “Michelson interferometer thermo-optic switch on SOI with a 50-W power consumption”, in *2016 IEEE Photonics Conference (IPC)*, 2016, pp. 107–110. DOI: `10.1109/IPCon.2016.7831002`.

[53] B. Murray, C. Antony, G. Talli, and P. D. Townsend, “Predistortion for High-Speed Lumped Silicon Photonic Mach-Zehnder Modulators”, *IEEE Photonics Journal*, vol. 14, no. 2, pp. 1–11, 2022. DOI: `10.1109/JPHOT.2022.3158255`.

[54] X. Wu, B. Dama, P. Gothoskar, P. Metz, K. Shastri, S. Sunder, J. Van der Spiegel, Y. Wang, M. Webster, and W. Wilson, “A 20Gb/s NRZ/PAM-4 1V transmitter in 40nm CMOS driving a Si-photonic modulator in 0.13μm CMOS”, in *2013 IEEE International Solid-State Circuits Conference Digest of Technical Papers*, 2013, pp. 128–129. DOI: `10.1109/ISSCC.2013.6487667`.

[55] A. H. Talkhooncheh, W. Zhang, M. Wang, D. J. Thomson, M. Ebert, L. Ke, G. T. Reed, and A. Emami, “A 2.4pJ/b 100Gb/s 3D-integrated PAM-4 Optical Transmitter with Segmented SiP MOSCAP Modulators and a 2-Channel 28nm CMOS Driver”, in *2022 IEEE International Solid-State Circuits Conference (ISSCC)*, vol. 65, 2022, pp. 284–286. DOI: `10.1109/ISSCC42614.2022.9731563`.

[56] M. S. Nezami, T. F. de Lima, M. Mitchell, S. Yu, J. Wang, S. Bilodeau, W. Zhang, M. Al-Qadasi, I. Taghavi, A. Tofini, S. Lin, B. J. Shastri, P. R. Prucnal, L. Chrostowski, and S. Shekhar, “Packaging and Interconnect Considerations in Neuromorphic Photonic Accelerators”, *IEEE Journal of Selected Topics in Quantum Electronics*, vol. 29, no. 2: Optical Computing, pp. 1–11, 2023. DOI: `10.1109/JSTQE.2022.3200604`.

[57] S. A. Srinivasan, C. Porret, S. Balakrishnan, Y. Ban, R. Loo, P. Verheyen, J. Van Campenhout, and M. Pantouvaki, “60Gb/s waveguide-coupled O-band GeSi quantum-confined Stark effect electro-absorption modulator”, in *2021 Optical Fiber Communications Conference and Exhibition (OFC)*, 2021, pp. 1–3.

[58] J. A. Smith, H. Francis, G. Navickaite, and M. J. Strain, “SiN foundry platform for high performance visible light integrated photonics”, EN, *Optical Materials Express*, vol. 13, no. 2, pp. 458–468, 2023. DOI: `10.1364/OME.479871`.

[59] D. J. Blumenthal, R. Heideman, D. Geuzebroek, A. Leinse, and C. Roeloffzen, “Silicon Nitride in Silicon Photonics”, *Proceedings of the IEEE*, vol. 106, no. 12, pp. 2209–2231, 2018. DOI: `10.1109/JPROC.2018.2861576`.

[60] C. Xiang, W. Jin, and J. E. Bowers, “Silicon nitride passive and active photonic integrated circuits: Trends and prospects”, EN, *Photonics Research*, vol. 10, no. 6, A82–A96, 2022. DOI: `10.1364/PRJ.452936`.

[61] Y. Okawachi, K. Saha, J. S. Levy, Y. H. Wen, M. Lipson, and A. L. Gaeta, “Octave-spanning frequency comb generation in a silicon nitride chip”, EN, *Optics Letters*, vol. 36, no. 17, pp. 3398–3400, 2011. DOI: `10.1364/OL.36.003398`.

[62] C. Xiang, W. Jin, D. Huang, M. A. Tran, J. Guo, Y. Wan, W. Xie, G. Kurczveil, A. M. Netherton, D. Liang, H. Rong, and J. E. Bowers, “High-Performance Silicon Photonics Using Heterogeneous Integration”, *IEEE Journal of Selected Topics in Quantum Electronics*, vol. 28, no. 3: Hybrid Integration for Silicon Photonics, pp. 1–15, 2022. DOI: `10.1109/JSTQE.2021.3126124`.

[63] C. Xiang, J. Guo, W. Jin, L. Wu, J. Peters, W. Xie, L. Chang, B. Shen, H. Wang, Q.-F. Yang, D. Kinghorn, M. Paniccia, K. J. Vahala, P. A. Morton, and J. E. Bowers, "High-performance lasers for fully integrated silicon nitride photonics", en, *Nature Communications*, vol. 12, no. 1, p. 6650, 2021. DOI: `10.1038/s41467-021-26804-9`.

[64] M. Churaev, R. N. Wang, A. Riedhauser, V. Snigirev, T. Blésin, C. Möhl, M. H. Anderson, A. Siddharth, Y. Popoff, U. Drechsler, D. Caimi, S. Hönl, J. Riemensberger, J. Liu, P. Seidler, and T. J. Kippenberg, "A heterogeneously integrated lithium niobate-on-silicon nitride photonic platform", en, *Nature Communications*, vol. 14, no. 1, p. 3499, 2023. DOI: `10.1038/s41467-023-39047-7`.

[65] C. G. H. Roeloffzen et al., "Low-Loss Si3N4 TriPleX Optical Waveguides: Technology and Applications Overview", *IEEE Journal of Selected Topics in Quantum Electronics*, vol. 24, no. 4, pp. 1–21, 2018. DOI: `10.1109/JSTQE.2018.2793945`.

[66] D. Zhu, L. Shao, M. Yu, R. Cheng, B. Desiatov, C. J. Xin, Y. Hu, J. Holzgrafe, S. Ghosh, A. Shams-Ansari, E. Puma, N. Sinclair, C. Reimer, M. Zhang, and M. Lončar, "Integrated photonics on thin-film lithium niobate", EN, *Advances in Optics and Photonics*, vol. 13, no. 2, pp. 242–352, 2021. DOI: `10.1364/AOP.411024`.

[67] Y. Qi and Y. Li, "Integrated lithium niobate photonics", en, *Nanophotonics*, vol. 9, no. 6, pp. 1287–1320, 2020. DOI: `10.1515/nanoph-2020-0013`.

[68] M. Xu, M. He, H. Zhang, J. Jian, Y. Pan, X. Liu, L. Chen, X. Meng, H. Chen, Z. Li, X. Xiao, S. Yu, S. Yu, and X. Cai, "High-performance coherent optical modulators based on thin-film lithium niobate platform", en, *Nature Communications*, vol. 11, no. 1, p. 3911, 2020. DOI: `10.1038/s41467-020-17806-0`.

[69] J. Lin, F. Bo, Y. Cheng, and J. Xu, "Advances in on-chip photonic devices based on lithium niobate on insulator", EN, *Photonics Research*, vol. 8, no. 12, pp. 1910–1936, 2020. DOI: `10.1364/PRJ.395305`.

[70] R. Wu, M. Wang, J. Xu, J. Qi, W. Chu, Z. Fang, J. Zhang, J. Zhou, L. Qiao, Z. Chai, J. Lin, and Y. Cheng, "Long Low-Loss-Litium Niobate on Insulator Waveguides with Sub-Nanometer Surface Roughness", en, *Nanomaterials*, vol. 8, no. 11, p. 910, 2018. DOI: `10.3390/nano8110910`.

[71] M. Zhang, C. Wang, R. Cheng, A. Shams-Ansari, and M. Lončar, "Monolithic ultra-high-Q lithium niobate microring resonator", EN, *Optica*, vol. 4, no. 12, pp. 1536–1537, 2017. DOI: `10.1364/OPTICA.4.001536`.

[72] L. Shao, M. Yu, S. Maity, N. Sinclair, L. Zheng, C. Chia, A. Shams-Ansari, C. Wang, M. Zhang, K. Lai, and M. Lončar, "Microwave-to-optical conversion using lithium niobate thin-film acoustic resonators", EN, *Optica*, vol. 6, no. 12, pp. 1498–1505, 2019. DOI: `10.1364/OPTICA.6.001498`.

[73] S. H. Badri, M. V. Kotlyar, R. Das, Y. Arafat, O. Moynihan, B. Corbett, L. O'Faolain, and S. Ghosh, "Compact modulators on silicon nitride waveguide platform via micro-transfer printing of thin-film lithium niobate", en, *Scientific Reports*, vol. 15, no. 1, p. 11 681, 2025. DOI: `10.1038/s41598-025-95397-w`.

[74] X. Zhang, X. Liu, L. Liu, Y. Han, H. Tan, L. Liu, Z. Lin, S. Yu, R. Wang, and X. Cai, "Heterogeneous integration of III–V semiconductor lasers on thin-film lithium niobite platform by wafer bonding", *Applied Physics Letters*, vol. 122, no. 8, p. 081 103, 2023. DOI: `10.1063/5.0142077`.

[75] M. Wang, Z. Fang, H. Zhang, J. Lin, J. Zhou, T. Huang, Y. Zhu, C. Li, S. Yu, B. Fu, L. Qiao, and Y. Cheng, "Recent Progresses on Hybrid Lithium Niobate External Cavity Semiconductor Lasers", en, *Materials*, vol. 17, no. 18, p. 4453, 2024. DOI: `10.3390/ma17184453`.

[76] H. Sattari, I. Prieto, H. Zarebidaki, J. Leo, G. Choong, M. Orvietani, F. Arefi, A. D. Torre, Y. Petremand, M. Palmieri, O. Dubochet, and M. Despont, "Standardized TFLN Photonic Integrated Circuits Platform", en, in *The 25th European Conference on Integrated Optics*, J. Witzens, J. Poon, L. Zimmermann, and W. Freude, Eds., Springer Nature Switzerland, 2024, pp. 85–89. DOI: `10.1007/978-3-031-63378-2_15`.

[77] H. Sattari, I. Prieto, H. Zarebidaki, J. Leo, G. Choong, F. Arefi, M. Orvietani, A. D. Torre, A. Mettraux, F. Dubois, D. Herle, Y. Petremand, M. Palmieri, O. Dubochet, and M. Despont, "Thin-film lithium niobate PICs: Advancements and potential applications in telecom and beyond", in *Integrated Photonics Platforms III*, vol. 13012, SPIE, 2024, pp. 86–89. DOI: `10.1117/12.3026042`.

[78] V. Jayaraman, Z.-M. Chuang, and L. Coldren, "Theory, design, and performance of extended tuning range semiconductor lasers with sampled gratings", *IEEE Journal of Quantum Electronics*, vol. 29, no. 6, pp. 1824–1834, 1993. DOI: `10.1109/3.234440`.

[79] L. A. Coldren, S. C. Nicholes, L. Johansson, S. Ristic, R. S. Guzzon, E. J. Norberg, and U. Krishnamachari, "High Performance InP-Based Photonic ICs—A Tutorial", *Journal of Lightwave Technology*, vol. 29, no. 4, pp. 554–570, 2011. DOI: `10.1109/JLT.2010.2100807`.

[80] R. R. Kumar, A. Hänsel, M. F. Brusatori, L. Nielsen, L. M. Augustin, N. Volet, and M. J. R. Heck, "A 10-kHz intrinsic linewidth coupled extended-cavity DBR laser monolithically integrated on an InP platform", EN, *Optics Letters*, vol. 47, no. 9, pp. 2346–2349, 2022. DOI: `10.1364/OL.454478`.

[81] J. Halldorsson, N. B. Arnfinnsdottir, A. B. Jonsdottir, B. Agnarsson, and K. Leosson, "High index contrast polymer waveguide platform for integrated biophotonics", EN, *Optics Express*, vol. 18, no. 15, pp. 16 217–16 226, 2010. DOI: `10.1364/OE.18.016217`.

[82] R. Dangel, J. Hofrichter, F. Horst, D. Jubin, A. L. Porta, N. Meier, I. M. Soganci, J. Weiss, and B. J. Offrein, "Polymer waveguides for electro-optical integration in data centers and high-performance computers", EN, *Optics Express*, vol. 23, no. 4, pp. 4736–4750, 2015. DOI: `10.1364/OE.23.004736`.

[83] X.-Y. Han, Z.-L. Wu, S.-C. Yang, F.-F. Shen, Y.-X. Liang, L.-H. Wang, J.-Y. Wang, J. Ren, L.-Y. Jia, H. Zhang, S.-H. Bo, G. Morthier, and M.-S. Zhao, "Recent Progress of Imprinted Polymer Photonic Waveguide Devices and Applications", en, *Polymers*, vol. 10, no. 6, p. 603, 2018. DOI: `10.3390/polym10060603`.

[84] H. Zuo, S. Yu, T. Gu, and J. Hu, "Low loss, flexible single-mode polymer photonics", EN, *Optics Express*, vol. 27, no. 8, pp. 11 152–11 159, 2019. DOI: `10.1364/OE.27.011152`.

[85] I. Taghavi, M. Moridsadat, A. Tofini, S. Raza, N. A. F. Jaeger, L. Chrostowski, B. J. Shastri, and S. Shekhar, "Polymer modulators in silicon photonics: Review and projections", en, *Nanophotonics*, vol. 11, no. 17, pp. 3855–3871, 2022. DOI: `10.1515/nanoph-2022-0141`.

[86] W. a. P. M. Hendriks, M. Dijkstra, S. Mardani, I. Hegeman, and S. M. Garcia-Blanco, "Low-loss photonic integrated circuits for UV applications", in *Integrated Optics: Devices, Materials, and Technologies XXVII*, vol. 12424, SPIE, 2023, p. 1 242 402. DOI: `10.1117/12.2657143`.

[87] W. A. P. M. Hendriks, L. Chang, C. I. van Emmerik, J. Mu, M. de Goede, M. Dijkstra, and S. M. Garcia-Blanco, "Rare-earth ion doped Al2O3 for active integrated photonics", *Advances in Physics: X*, vol. 6, no. 1, p. 1 833 753, 2021. DOI: `10.1080/23746149.2020.1833753`.

[88] A. Raju, D. Hungund, D. Krueger, Z. Dong, Z. Sakotic, A. B. Posadas, A. A. Demkov, and D. Wasserman, "High-Q Monolithic Ring Resonators in Low-Loss Barium Titanate on Silicon", en, *Laser & Photonics Reviews*, vol. 19, no. 16, p. 2 402 086, 2025. DOI: `10.1002/lpor.202402086`.

[89] D. M. Lukin, C. Dory, M. A. Guidry, K. Y. Yang, S. D. Mishra, R. Trivedi, M. Radulaski, S. Sun, D. Vercruysse, G. H. Ahn, and J. Vučković, "4H-silicon-carbide-on-insulator for integrated quantum and nonlinear photonics", en, *Nature Photonics*, vol. 14, no. 5, pp. 330–334, 2020. DOI: `10.1038/s41566-019-0556-6`.

[90] B. Docter, J. Pozo, d. Vries T., E. Geluk, J. Bolk, E. Smalbrugge, F. Karouta, Y. Oei, H. Ambrosius, and M. Smit, "The 243 steps of making photonic integrated circuits in InP", *Proceedings of the 15th Annual Symposium of the IEEE Photonics Benelux Chapter, 18-19 November 2010, Delft, The Netherlands*, J. Pozo, M. Mortensen, P. Urbach, X. Leijtens, and M. Yousefi, Eds., pp. 89–92, 2010.

[91] S. Tahvili, S. Latkowski, B. Smalbrugge, X. J. M. Leijtens, P. J. Williams, M. J. Wale, J. Parra-Cetina, R. Maldonado-Basilio, P. Landais, M. K. Smit, and E. A. J. M. Bente,

“InP-Based Integrated Optical Pulse Shaper: Demonstration of Chirp Compensation”, *IEEE Photonics Technology Letters*, vol. 25, no. 5, pp. 450–453, 2013. DOI: `10.1109/LPT.2013.2240383`.

[92] F. Bontempi, S. Pinna, N. Andriolli, A. Bogoni, X. J. M. Leijtens, J. Bolk, and G. Contestabile, “Multifunctional Current-Controlled InP Photonic Integrated Delay Interferometer”, *IEEE Journal of Quantum Electronics*, vol. 48, no. 11, pp. 1453–1461, 2012. DOI: `10.1109/JQE.2012.2219038`.

[93] JePPIX Consortium. “Jeppix roadmap — latest edition”, Accessed: Oct. 31, 2025. [Online]. Available: `https://www.jeppix.eu/about-us/roadmap-latest-edition/`.

[94] J. V. Erps, A. Senes, L. Augustin, M. Rensing, M. Heuken, A. Thorsten, A. Kapoor, and V. Dolores-Calzadilla, “The open innovation photonics pilot line for northwest Europe (OIP4NWE) and its service offering”, in *Integrated Photonics Platforms III*, vol. 13012, SPIE, 2024, pp. 36–39. DOI: `10.1117/12.3017995`.

[95] S. Latkowski, D. Pustakhod, M. Chatzimichailidis, W. Yao, and X. J. M. Leijtens, “Open Standards for Automation of Testing of Photonic Integrated Circuits”, *IEEE Journal of Selected Topics in Quantum Electronics*, vol. 25, no. 5, pp. 1–8, 2019. DOI: `10.1109/JSTQE.2019.2921401`.

[96] SMART Photonics. “Smart photonics — home”, Accessed: Oct. 31, 2025. [Online]. Available: `https://smartphotonics.nl/`.

[97] Fraunhofer Heinrich Hertz Institute. “Fraunhofer hhi”, JePPIX, Accessed: Oct. 31, 2025. [Online]. Available: `https://www.jeppix.eu/project/fraunhofer-hhi/`.

[98] M. Smit et al., “An introduction to InP-based generic integration technology”, en, *Semiconductor Science and Technology*, vol. 29, no. 8, p. 083 001, 2014. DOI: `10.1088/0268-1242/29/8/083001`.

[99] N. Grote, M. Baier, and F. Soares, “Photonic Integrated Circuits on InP”, en, in *Fibre Optic Communication: Key Devices*, H. Venghaus and N. Grote, Eds., Springer International Publishing, 2017, pp. 799–840. DOI: `10.1007/978-3-319-42367-8_16`.

[100] P. An and M. J. R. Heck, “Sampled-Grating Distributed Bragg Reflector Laser based on a Generic Photonic Integration Platform”, EN, in *OSA Advanced Photonics Congress (AP) 2020 (IPR, NP, NOMA, Networks, PVLED, PSC, SPPCom, SOF) (2020), paper JTh2A.6*, Optica Publishing Group, 2020, JTh2A.6. DOI: `10.1364/IPRSN.2020.JTh2A.6`.

[101] M. Trajkovic, “High speed electro-absorption modulators in indium phosphide generic integration technologies”, Phd Thesis 1 (Research TU/e / Graduation TU/e), Technische Universiteit Eindhoven, 2019.

[102] J. A. Hillier, Q. Hu, H. Chen, A. Meighan, L. Augustin, M. Wale, K. Williams, and W. Yao, "A Co-planar Stripline Mach-Zehnder Modulator Enabling 160 GBd PAM-4 on an Indium Phosphide Platform", in *2024 Optical Fiber Communications Conference and Exhibition (OFC)*, 2024, pp. 1–3.

[103] N. T. Hung, S. Stainton, S. T. Le, P. A. Haigh, H. P. Tien, N. D. N. Vien, and N. V. Tuan, "High-speed PAM4 transmission using directly modulated laser and artificial neural network nonlinear equaliser", *Optics & Laser Technology*, vol. 157, p. 108 642, 2023. DOI: `10.1016/j.optlastec.2022.108642`.

[104] R. R. Kumar, A. Hänsel, M. F. Brusatori, L. Nielsen, N. H. Arent, N. Volet, and M. J. R. Heck, "Sub-10 kHz Intrinsic Linewidth Extended Cavity DBR laser on InP Generic Foundry Platform", in *2022 Optical Fiber Communications Conference and Exhibition (OFC)*, 2022, pp. 01–03.

[105] T. Udem, R. Holzwarth, and T. W. Hänsch, "Optical frequency metrology", en, *Nature*, vol. 416, no. 6877, pp. 233–237, 2002. DOI: `10.1038/416233a`.

[106] A. Rosado, A. Pérez-Serrano, J. M. G. Tijero, Á. Valle, L. Pesquera, and I. Esquivias, "Experimental study of optical frequency comb generation in gain-switched semiconductor lasers", *Optics & Laser Technology*, vol. 108, pp. 542–550, 2018. DOI: `10.1016/j.optlastec.2018.07.038`.

[107] J. Johnston, "Transform coding of audio signals using perceptual noise criteria", *IEEE Journal on Selected Areas in Communications*, vol. 6, no. 2, pp. 314–323, 1988. DOI: `10.1109/49.608`.

[108] N. Dimarcq et al., "Roadmap towards the redefinition of the second", en, *Metrologia*, vol. 61, no. 1, p. 012 001, 2024. DOI: `10.1088/1681-7575/ad17d2`.

[109] The Nobel Foundation. "Nobel lecture: Defining and measuring optical frequencies", Reviews of Modern Physics, Accessed: Sep. 27, 2025. [Online]. Available: `https://journals.aps.org/rmp/abstract/10.1103/RevModPhys.78.1279`.

[110] J. K. Ranka, R. S. Windeler, and A. J. Stentz, "Visible continuum generation in air–silica microstructure optical fibers with anomalous dispersion at 800 nm", EN, *Optics Letters*, vol. 25, no. 1, pp. 25–27, 2000. DOI: `10.1364/OL.25.000025`.

[111] D. J. Jones, S. A. Diddams, J. K. Ranka, A. Stentz, R. S. Windeler, J. L. Hall, and S. T. Cundiff, "Carrier-Envelope Phase Control of Femtosecond Mode-Locked Lasers and Direct Optical Frequency Synthesis", *Science*, vol. 288, no. 5466, pp. 635–639, 2000. DOI: `10.1126/science.288.5466.635`.

[112] S. A. Diddams, D. J. Jones, J. Ye, S. T. Cundiff, J. L. Hall, J. K. Ranka, R. S. Windeler, R. Holzwarth, T. Udem, and T. W. Hänsch, "Direct link between microwave and optical frequencies with a 300 thz femtosecond laser comb", *Physical Review Letters*, vol. 84, no. 22, pp. 5102–5105, 2000. DOI: `10.1103/PhysRevLett.84.5102`.

[113] T. Fortier and E. Baumann, "20 years of developments in optical frequency comb technology and applications", en, *Communications Physics*, vol. 2, no. 1, p. 153, 2019. DOI: `10.1038/s42005-019-0249-y`.

[114] T. Udem, J. Reichert, R. Holzwarth, and T. W. Hänsch, "Accurate measurement of large optical frequency differences with a mode-locked laser", EN, *Optics Letters*, vol. 24, no. 13, pp. 881–883, 1999. DOI: `10.1364/OL.24.000881`.

[115] Larry A. Coldren, Scott W. Corzine, and Milan L. Masanovic, "Diode Lasers and Photonic Integrated Circuits", en, *ResearchGate*, 2012. DOI: `10.1117/1.601191`.

[116] U. Keller, K. Weingarten, F. Kartner, D. Kopf, B. Braun, I. Jung, R. Fluck, C. Honninger, N. Matuschek, and J. Aus der Au, "Semiconductor saturable absorber mirrors (SESAM's) for femtosecond to nanosecond pulse generation in solid-state lasers", *IEEE Journal of Selected Topics in Quantum Electronics*, vol. 2, no. 3, pp. 435–453, 1996. DOI: `10.1109/2944.571743`.

[117] U. Keller, "Recent developments in compact ultrafast lasers", en, *Nature*, vol. 424, no. 6950, pp. 831–838, 2003. DOI: `10.1038/nature01938`.

[118] N. R. Newbury, "Searching for applications with a fine-tooth comb", en, *Nature Photonics*, vol. 5, no. 4, pp. 186–188, 2011. DOI: `10.1038/nphoton.2011.38`.

[119] V. Vujicic, C. Calò, R. Watts, F. Lelarge, C. Browning, K. Merghem, A. Martinez, A. Ramdane, and L. P. Barry, "Quantum Dash Mode-Locked Lasers for Data Centre Applications", *IEEE Journal of Selected Topics in Quantum Electronics*, vol. 21, no. 6, pp. 53–60, 2015. DOI: `10.1109/JSTQE.2015.2487884`.

[120] P. Marin-Palomo, J. N. Kemal, P. Trocha, S. Wolf, K. Merghem, F. Lelarge, A. Ramdane, W. Freude, S. Randel, and C. Koos, "Comb-based WDM transmission at 10 Tbit/s using a DC-driven quantum-dash mode-locked laser diode", EN, *Optics Express*, vol. 27, no. 22, pp. 31 110–31 129, 2019. DOI: `10.1364/OE.27.031110`.

[121] A. Parriaux, K. Hammani, and G. Millot, "Electro-optic frequency combs", EN, *Advances in Optics and Photonics*, vol. 12, no. 1, pp. 223–287, 2020. DOI: `10.1364/AOP.382052`.

[122] T. Sakamoto, T. Kawanishi, and M. Izutsu, "Asymptotic formalism for ultraflat optical frequency comb generation using a Mach-Zehnder modulator", EN, *Optics Letters*, vol. 32, no. 11, pp. 1515–1517, 2007. DOI: `10.1364/OL.32.001515`.

[123] Y. Dou, H. Zhang, and M. Yao, "Generation of Flat Optical-Frequency Comb Using Cascaded Intensity and Phase Modulators", *IEEE Photonics Technology Letters*, vol. 24, no. 9, pp. 727–729, 2012. DOI: `10.1109/LPT.2012.2187330`.

[124] R. Wu, V. R. Supradeepa, C. M. Long, D. E. Leaird, and A. M. Weiner, "Generation of very flat optical frequency combs from continuous-wave lasers using cascaded intensity

and phase modulators driven by tailored radio frequency waveforms", EN, *Optics Letters*, vol. 35, no. 19, pp. 3234–3236, 2010. DOI: `10.1364/OL.35.003234`.

[125] V. Torres-Company, J. Lancis, and P. Andrés, "Lossless equalization of frequency combs", EN, *Optics Letters*, vol. 33, no. 16, pp. 1822–1824, 2008. DOI: `10.1364/OL.33.001822`.

[126] T. Yang, J. Dong, S. Liao, D. Huang, and X. Zhang, "Comparison analysis of optical frequency comb generation with nonlinear effects in highly nonlinear fibers", EN, *Optics Express*, vol. 21, no. 7, pp. 8508–8520, 2013. DOI: `10.1364/OE.21.008508`.

[127] V. Durán and V. Torres-Company, "Ultrafast electrooptic dual-comb interferometry over 40-nm bandwidth", in *2016 Conference on Lasers and Electro-Optics (CLEO)*, 2016, pp. 1–2.

[128] M. Soriano-Amat, H. F. Martins, V. Durán, L. Costa, S. Martin-Lopez, M. Gonzalez-Herraez, and M. R. Fernández-Ruiz, "Time-expanded phase-sensitive optical time-domain reflectometry", en, *Light: Science & Applications*, vol. 10, no. 1, p. 51, 2021. DOI: `10.1038/s41377-021-00490-0`.

[129] B. Xue, Z. Wang, H. Zhang, K. Zhang, Y. Chen, M. He, B. Lin, and H. Wu, "Absolute Distance Measurement by Self-Heterodyne EO Comb Interferometry", *IEEE Photonics Technology Letters*, vol. 30, no. 9, pp. 861–864, 2018. DOI: `10.1109/LPT.2018.2820710`.

[130] V. Torres-Company and A. M. Weiner, "Optical frequency comb technology for ultra-broadband radio-frequency photonics", *Laser & Photonics Reviews*, vol. 8, no. 3, pp. 368–393, 2014. DOI: `10.1002/lpor.201300126`.

[131] A. Pasquazi, M. Peccianti, L. Razzari, D. J. Moss, S. Coen, M. Erkintalo, Y. K. Chembo, T. Hansson, S. Wabnitz, P. Del'Haye, X. Xue, A. M. Weiner, and R. Morandotti, "Micro-combs: A novel generation of optical sources", *Physics Reports*, Micro-combs: A novel generation of optical sources, vol. 729, pp. 1–81, 2018. DOI: `10.1016/j.physrep.2017.08.004`.

[132] T. J. Kippenberg, R. Holzwarth, and S. A. Diddams, "Microresonator-Based Optical Frequency Combs", *Science*, vol. 332, no. 6029, pp. 555–559, 2011. DOI: `10.1126/science.1193968`.

[133] T. J. Kippenberg, A. L. Gaeta, M. Lipson, and M. L. Gorodetsky, "Dissipative Kerr solitons in optical microresonators", *Science*, vol. 361, no. 6402, eaan8083, 2018. DOI: `10.1126/science.aan8083`.

[134] B. Meng, M. Singleton, J. Hillbrand, M. Franckié, M. Beck, and J. Faist, "Dissipative Kerr solitons in semiconductor ring lasers", en, *Nature Photonics*, vol. 16, no. 2, pp. 142–147, 2022. DOI: `10.1038/s41566-021-00927-3`.

[135] L. A. Lugiato and R. Lefever, "Spatial Dissipative Structures in Passive Optical Systems", *Physical Review Letters*, vol. 58, no. 21, pp. 2209–2211, 1987. DOI: `10.1103/PhysRevLett.58.2209`.

[136] T. Herr, V. Brasch, J. D. Jost, C. Y. Wang, N. M. Kondratiev, M. L. Gorodetsky, and T. J. Kippenberg, "Temporal solitons in optical microresonators", en, *Nature Photonics*, vol. 8, no. 2, pp. 145–152, 2014. DOI: `10.1038/nphoton.2013.343`.

[137] X. Xue, Y. Xuan, Y. Liu, P.-H. Wang, S. Chen, J. Wang, D. E. Leaird, M. Qi, and A. M. Weiner, "Mode-locked dark pulse Kerr combs in normal-dispersion microresonators", en, *Nature Photonics*, vol. 9, no. 9, pp. 594–600, 2015. DOI: `10.1038/nphoton.2015.137`.

[138] C. Wang, M. Zhang, M. Yu, R. Zhu, H. Hu, and M. Loncar, "Monolithic lithium niobate photonic circuits for Kerr frequency comb generation and modulation", en, *Nature Communications*, vol. 10, no. 1, p. 978, 2019. DOI: `10.1038/s41467-019-08969-6`.

[139] Y. He, Q.-F. Yang, J. Ling, R. Luo, H. Liang, M. Li, B. Shen, H. Wang, K. Vahala, and Q. Lin, "Self-starting bi-chromatic $LiNbO_3$ soliton microcomb", EN, *Optica*, vol. 6, no. 9, pp. 1138–1144, 2019. DOI: `10.1364/OPTICA.6.001138`.

[140] C. Xiang, J. Liu, J. Guo, L. Chang, R. N. Wang, W. Weng, J. Peters, W. Xie, Z. Zhang, J. Riemensberger, J. Selvidge, T. J. Kippenberg, and J. E. Bowers, "Laser soliton microcombs heterogeneously integrated on silicon", *Science*, vol. 373, no. 6550, pp. 99–103, 2021. DOI: `10.1126/science.abh2076`.

[141] B. Stern, X. Ji, Y. Okawachi, A. L. Gaeta, and M. Lipson, "Battery-operated integrated frequency comb generator", en, *Nature*, vol. 562, no. 7727, pp. 401–405, 2018. DOI: `10.1038/s41586-018-0598-9`.

[142] P. Marin-Palomo, J. N. Kemal, M. Karpov, A. Kordts, J. Pfeifle, M. H. P. Pfeiffer, P. Trocha, S. Wolf, V. Brasch, M. H. Anderson, R. Rosenberger, K. Vijayan, W. Freude, T. J. Kippenberg, and C. Koos, "Microresonator-based solitons for massively parallel coherent optical communications", en, *Nature*, vol. 546, no. 7657, pp. 274–279, 2017. DOI: `10.1038/nature22387`.

[143] B. Corcoran, A. Mitchell, R. Morandotti, L. K. Oxenløwe, and D. J. Moss, "Optical microcombs for ultrahigh-bandwidth communications", en, *Nature Photonics*, vol. 19, no. 5, pp. 451–462, 2025. DOI: `10.1038/s41566-025-01662-9`.

[144] E. Lucas, P. Brochard, R. Bouchand, S. Schilt, T. Südmeyer, and T. J. Kippenberg, "Ultralow-noise photonic microwave synthesis using a soliton microcomb-based transfer oscillator", en, *Nature Communications*, vol. 11, no. 1, p. 374, 2020. DOI: `10.1038/s41467-019-14059-4`.

[145] D. T. Spencer et al., "An optical-frequency synthesizer using integrated photonics", en, *Nature*, vol. 557, no. 7703, pp. 81–85, 2018. DOI: `10.1038/s41586-018-0065-7`.

[146] M.-G. Suh, Q.-F. Yang, K. Y. Yang, X. Yi, and K. J. Vahala, “Microresonator soliton dual-comb spectroscopy”, *Science*, vol. 354, no. 6312, pp. 600–603, 2016. DOI: `10.1126/science.aah6516`.

[147] J. Feldmann, N. Youngblood, M. Karpov, H. Gehring, X. Li, M. Stappers, M. Le Gallo, X. Fu, A. Lukashchuk, A. S. Raja, J. Liu, C. D. Wright, A. Sebastian, T. J. Kippenberg, W. H. P. Pernice, and H. Bhaskaran, “Parallel convolutional processing using an integrated photonic tensor core”, en, *Nature*, vol. 589, no. 7840, pp. 52–58, 2021. DOI: `10.1038/s41586-020-03070-1`.

[148] J. Riemensberger, A. Lukashchuk, M. Karpov, W. Weng, E. Lucas, J. Liu, and T. J. Kippenberg, “Massively parallel coherent laser ranging using a soliton microcomb”, en, *Nature*, vol. 581, no. 7807, pp. 164–170, 2020. DOI: `10.1038/s41586-020-2239-3`.

[149] J. Liu, E. Lucas, A. S. Raja, J. He, J. Riemensberger, R. N. Wang, M. Karpov, H. Guo, R. Bouchand, and T. J. Kippenberg, “Photonic microwave generation in the X- and K-band using integrated soliton microcombs”, en, *Nature Photonics*, vol. 14, no. 8, pp. 486–491, 2020. DOI: `10.1038/s41566-020-0617-x`.

[150] H. Ito, H. Yokoyama, S. Murata, and H. Inaba, “Picosecond optical pulse generation from an r.f. modulated AlGaAs d.h. diode laser”, *Electronics Letters*, vol. 15, no. 23, pp. 738–740, 1979. DOI: `10.1049/el:19790528`.

[151] K. Y. Lau, “Gain switching of semiconductor injection lasers”, *Applied Physics Letters*, vol. 52, no. 4, pp. 257–259, 1988. DOI: `10.1063/1.99486`.

[152] P. M. Anandarajah, K. Shi, J. O’Carroll, A. Kaszubowska, R. Phelan, L. P. Barry, A. D. Ellis, P. Perry, D. Reid, B. Kelly, and J. O’Gorman, “Phase shift keyed systems based on a gain switched laser transmitter”, EN, *Optics Express*, vol. 17, no. 15, pp. 12 668–12 677, 2009. DOI: `10.1364/OE.17.012668`.

[153] P. M. Anandarajah, R. Maher, Y. Q. Xu, S. Latkowski, J. O’Carroll, S. G. Murdoch, R. Phelan, J. O’Gorman, and L. P. Barry, “Generation of Coherent Multicarrier Signals by Gain Switching of Discrete Mode Lasers”, *IEEE Photonics Journal*, vol. 3, no. 1, pp. 112–122, 2011. DOI: `10.1109/JPHOT.2011.2105861`.

[154] P. M. Anandarajah, S. P. Ó Dúill, R. Zhou, and L. P. Barry, “Enhanced Optical Comb Generation by Gain-Switching a Single-Mode Semiconductor Laser Close to Its Relaxation Oscillation Frequency”, *IEEE Journal of Selected Topics in Quantum Electronics*, vol. 21, no. 6, pp. 592–600, 2015. DOI: `10.1109/JSTQE.2015.2456751`.

[155] P. P. Vasil’ev, I. H. White, and J. Gowar, “Fast phenomena in semiconductor lasers”, en, *Reports on Progress in Physics*, vol. 63, no. 12, p. 1997, 2000. DOI: `10.1088/0034-4885/63/12/203`.

[156] A. Rosado, A. Pérez-Serrano, J. M. G. Tijero, A. V. Gutierrez, L. Pesquera, and I. Esquivias, “Numerical and Experimental Analysis of Optical Frequency Comb

Generation in Gain-Switched Semiconductor Lasers", *IEEE Journal of Quantum Electronics*, vol. 55, no. 6, pp. 1–12, 2019. DOI: `10.1109/JQE.2019.2943482`.

[157] A. Quirce, C. de Dios, A. Valle, and P. Acedo, "VCSEL-Based Optical Frequency Combs Expansion Induced by Polarized Optical Injection", *IEEE Journal of Selected Topics in Quantum Electronics*, vol. 25, no. 6, pp. 1–9, 2019. DOI: `10.1109/JSTQE.2018.2888560`.

[158] M. Srivastava, S. T. Ahmad, A. Sharma, P. D. Lakshmijayasimha, M. D. G. Pascual, F. Smyth, P. M. Anandarajah, and A. Kaszubowska-Anandarajah, "Monolithically Integrated Optical Frequency Comb Generator Based on Mutually Injection Locked Gain Switched Lasers", *IEEE Journal of Selected Topics in Quantum Electronics*, vol. 29, no. 5: Terahertz Photonics, pp. 1–8, 2023. DOI: `10.1109/JSTQE.2023.3305829`.

[159] R. Zhou, S. Latkowski, J. O'Carroll, R. Phelan, L. P. Barry, and P. Anandarajah, "40nm wavelength tunable gain-switched optical comb source", EN, *Optics Express*, vol. 19, no. 26, B415–B420, 2011. DOI: `10.1364/OE.19.00B415`.

[160] A. Rosado, M. R. Fernandez-Ruiz, P. Corredera, J. M. G. Tijero, and I. Esquivias, "High-density electro-optical densification of optical frequency combs generated by pulsed gain-switching of externally injected semiconductor lasers", EN, in *Frontiers in Optics + Laser Science 2022 (FIO, LS) (2022), paper JTu4B.11*, Optica Publishing Group, 2022, JTu4B.11. DOI: `10.1364/FIO.2022.JTu4B.11`.

[161] S. P. Ó Dúill, R. Zhou, P. M. Anandarajah, and L. P. Barry, "Analytical Approach to Assess the Impact of Pulse-to-Pulse Phase Coherence of Optical Frequency Combs", *IEEE Journal of Quantum Electronics*, vol. 51, no. 11, pp. 1–8, 2015. DOI: `10.1109/JQE.2015.2485228`.

[162] C. Quevedo-Galán, V. Durán, A. Rosado, A. Pérez-Serrano, J. M. G. Tijero, and I. Esquivias, "Gain-switched semiconductor lasers with pulsed excitation and optical injection for dual-comb spectroscopy", EN, *Optics Express*, vol. 28, no. 22, pp. 33 307–33 317, 2020. DOI: `10.1364/OE.404398`.

[163] P. López-Querol, C. Quevedo-Galán, A. Pérez-Serrano, J. M. G. Tijero, and I. Esquivias, "Low repetition rate optical frequency combs generated by pulsed gain-switching of semiconductor lasers", in *2021 27th International Semiconductor Laser Conference (ISLC)*, 2021, pp. 1–2. DOI: `10.1109/ISLC51662.2021.9615720`.

[164] Seo, Kim, and Liu, "Timing jitter reduction of gain-switched DFB laser by external injection-seeding", *Electronics Letters*, vol. 32, no. 1, pp. 44–45, 1996. DOI: `10.1049/el:19960019`.

[165] P. Gunning, J. Lucek, D. Moodie, K. Smith, R. Davey, S. Chernikov, M. Guy, J. Taylor, and A. Siddiqui, "Gain switched DFB laser diode pulse source using continuous wave light injection for jitter suppression and an electroabsorption modulator for

pedestal suppression”, *Electronics Letters*, vol. 32, no. 11, pp. 1010–1011, 1996. DOI: `10.1049/el:19960649`.

[166] C. Guignard, P. M. Anandarajah, A. Clarke, L. P. Barry, O. Vaudel, and P. Besnard, “Experimental investigation of the impact of optical injection on vital parameters of a gain-switched pulse source”, *Optics Communications*, vol. 277, no. 1, pp. 150–155, 2007. DOI: `10.1016/j.optcom.2007.04.058`.

[167] R. Zhou, T. N. Huynh, V. Vujicic, P. M. Anandarajah, and L. P. Barry, “Phase noise analysis of injected gain switched comb source for coherent communications”, EN, *Optics Express*, vol. 22, no. 7, pp. 8120–8125, 2014. DOI: `10.1364/OE.22.008120`.

[168] L. Monroy, A. Pérez-Serrano, J. M. G. Tijero, and I. Esquivias, “Multi-gas dual-comb spectroscopy with tunable gain-switched laser diodes”, en, *Scientific Reports*, vol. 15, no. 1, p. 7610, 2025. DOI: `10.1038/s41598-025-90108-x`.

[169] C. Quevedo-Galán, A. Pérez-Serrano, I. E. López-Delgado, J. M. G. Tijero, and I. Esquivias, “Dual-Comb Spectrometer Based on Gain-Switched Semiconductor Lasers and a Low-Cost Software-Defined Radio”, *IEEE Access*, vol. 9, pp. 92 367–92 373, 2021. DOI: `10.1109/ACCESS.2021.3091872`.

[170] C. Quevedo-Galán, A. Pérez-Serrano, J. M. G. Tijero, and I. Esquivias, “Dual-comb ranging with extended non-ambiguity range using densified gain-switched optical frequency combs”, *Optics & Laser Technology*, vol. 192, p. 113 480, 2025. DOI: `10.1016/j.optlastec.2025.113480`.

[171] H. Shams, T. Shao, M. J. Fice, P. M. Anandarajah, C. C. Renaud, F. Van Dijk, L. P. Barry, and A. J. Seeds, “100 Gb/s Multicarrier THz Wireless Transmission System With High Frequency Stability Based on A Gain-Switched Laser Comb Source”, *IEEE Photonics Journal*, vol. 7, no. 3, pp. 1–11, 2015. DOI: `10.1109/JPHOT.2015.2438437`.

[172] J. Pfeifle, V. Vujicic, R. T. Watts, P. C. Schindler, C. Weimann, R. Zhou, W. Freude, L. P. Barry, and C. Koos, “Flexible terabit/s Nyquist-WDM super-channels using a gain-switched comb source”, EN, *Optics Express*, vol. 23, no. 2, pp. 724–738, 2015. DOI: `10.1364/OE.23.000724`.

[173] Á. R. Criado, C. de Dios, E. Prior, G. H. Döhler, S. Preu, S. Malzer, H. Lu, A. C. Gossard, and P. Acedo, “Continuous-Wave Sub-THz Photonic Generation With Ultra-Narrow Linewidth, Ultra-High Resolution, Full Frequency Range Coverage and High Long-Term Frequency Stability”, *IEEE Transactions on Terahertz Science and Technology*, vol. 3, no. 4, pp. 461–471, 2013. DOI: `10.1109/TTHZ.2013.2260374`.

[174] J. McCarthy, Z. Jia, B. Kelleher, and F. H. Peters, “Gain Switched Frequency Comb Enhancement Using Monolithically Integrated Mutually Coupled Lasers”, *IEEE Photonics Technology Letters*, vol. 35, no. 22, pp. 1195–1198, 2023. DOI: `10.1109/LPT.2023.3307725`.

[175] P. López-Querol, C. Quevedo-Galán, P. Castera, J. M. G. Tijero, I. Esquivias, and A. Pérez-Serrano, "Monolithically integrated dual-comb generator based on gain switched semiconductor ring lasers", *Optics & Laser Technology*, vol. 191, p. 113 317, 2025. DOI: `10.1016/j.optlastec.2025.113317`.

[176] I. Coddington, N. Newbury, and W. Swann, "Dual-comb spectroscopy", EN, *Optica*, vol. 3, no. 4, pp. 414–426, 2016. DOI: `10.1364/OPTICA.3.000414`.

[177] S.-J. Lee, B. Widiyatmoko, M. Kourogi, and M. Ohtsu, "Ultrahigh Scanning Speed Optical Coherence Tomography Using Optical Frequency Comb Generators", en, *Japanese Journal of Applied Physics*, vol. 40, no. 8B, p. L878, 2001. DOI: `10.1143/JJAP.40.L878`.

[178] S. Schiller, "Spectrometry with frequency combs", EN, *Optics Letters*, vol. 27, no. 9, pp. 766–768, 2002. DOI: `10.1364/OL.27.000766`.

[179] L. Monroy, A. Rosado, C. Quevedo-Galán, P. López-Querol, A. Pérez-Serrano, J. M. G. Tijero, and I. Esquivias, "Dual-Comb Spectroscopy From an Optically Injected Single Gain-Switched Semiconductor Laser Source", en, *Journal of Lightwave Technology*, vol. 43, no. 12, pp. 5797–5803, 2025. DOI: `10.1109/jlt.2025.3556554`.

[180] M. A. Nagar, M. Wei, C. McArdle, A. Kaszubowska-Anandarajah, P. M. Anandarajah, and D. Janner, "High-Resolution FBG Strain Sensing With Dual-Comb Interrogation and Optimized Signal Processing", *Journal of Lightwave Technology*, vol. 43, no. 15, pp. 7455–7466, 2025. DOI: `10.1109/JLT.2025.3567158`.

[181] C. Bao, M.-G. Suh, and K. Vahala, "Microresonator soliton dual-comb imaging", EN, *Optica*, vol. 6, no. 9, pp. 1110–1116, 2019. DOI: `10.1364/OPTICA.6.001110`.

[182] F. U. Khan, G. Guarnizo, and P. Martín-Mateos, "Direct hyperspectral dual-comb gas imaging in the mid-infrared", EN, *Optics Letters*, vol. 45, no. 19, pp. 5335–5338, 2020. DOI: `10.1364/OL.402875`.

[183] I. Coddington, W. C. Swann, L. Nenadovic, and N. R. Newbury, "Rapid and precise absolute distance measurements at long range", en, *Nature Photonics*, vol. 3, no. 6, pp. 351–356, 2009. DOI: `10.1038/nphoton.2009.94`.

[184] C. Weimann, M. Lauermann, F. Hoeller, W. Freude, and C. Koos, "Silicon photonic integrated circuit for fast and precise dual-comb distance metrology", EN, *Optics Express*, vol. 25, no. 24, pp. 30 091–30 104, 2017. DOI: `10.1364/OE.25.030091`.

[185] N. Picqué and T. W. Hänsch, "Frequency comb spectroscopy", en, *Nature Photonics*, vol. 13, no. 3, pp. 146–157, 2019. DOI: `10.1038/s41566-018-0347-5`.

[186] I. Coddington, W. C. Swann, and N. R. Newbury, "Coherent Multiheterodyne Spectroscopy Using Stabilized Optical Frequency Combs", *Physical Review Letters*, vol. 100, no. 1, p. 013 902, 2008. DOI: `10.1103/PhysRevLett.100.013902`.

[187] B. Jerez, P. Martín-Mateos, E. Prior, C. d. Dios, and P. Acedo, “Dual optical frequency comb architecture with capabilities from visible to mid-infrared”, EN, *Optics Express*, vol. 24, no. 13, pp. 14 986–14 994, 2016. DOI: `10.1364/OE.24.014986`.

[188] B. Jerez, P. Martín-Mateos, E. Prior, C. d. Dios, and P. Acedo, “Gain-switching injection-locked dual optical frequency combs: Characterization and optimization”, EN, *Optics Letters*, vol. 41, no. 18, pp. 4293–4296, 2016. DOI: `10.1364/OL.41.004293`.

[189] E. P. Martin, S. Chandran, A. Rosado, E. P. Soderholm, J. K. Alexander, F. H. Peters, A. A. Ruth, and P. M. Anandarajah, “Mutually Injection Locked Gain Switched Optical Frequency Combs for Dual Comb Spectroscopy of H2S”, in *2020 Conference on Lasers and Electro-Optics (CLEO)*, 2020, pp. 1–2.

[190] E. P. Martin, S. T. Ahmad, S. Chandran, A. Rosado, A. A. Ruth, and P. M. Anandarajah, “Stability Characterisation and Application of Mutually Injection Locked Gain Switched Optical Frequency Combs for Dual Comb Spectroscopy”, *Journal of Lightwave Technology*, vol. 41, no. 13, pp. 4516–4521, 2023. DOI: `10.1109/JLT.2023.3255550`.

[191] L. Monroy, C. Quevedo-Galán, A. Pérez-Serrano, J. M. G. Tijero, and I. Esquivias, “Low-cost dual-comb spectrometer for CO2 monitoring based on gain-switched semiconductor lasers”, *Results in Physics*, vol. 58, p. 107 516, 2024. DOI: `10.1016/j.rinp.2024.107516`.

[192] A. L. Gaeta, M. Lipson, and T. J. Kippenberg, “Photonic-chip-based frequency combs”, en, *Nature Photonics*, vol. 13, no. 3, pp. 158–169, 2019. DOI: `10.1038/s41566-019-0358-x`.

[193] S. Cuyvers, B. Haq, C. O. de Beeck, S. Poelman, A. Hermans, Z. Wang, G. Roelkens, K. Van Gasse, and B. Kuyken, “Ultra-Dense III-V-on-Silicon Nitride Frequency Comb Laser”, in *2020 European Conference on Optical Communications (ECOC)*, 2020, pp. 1–3. DOI: `10.1109/ECOC48923.2020.9333402`.

[194] X. Guo, A. H. Quarterman, A. Wonfor, R. V. Penty, and I. H. White, “Monolithically integrated tunable mode-locked laser diode source with individual pulse selection and post-amplification”, EN, *Optics Letters*, vol. 41, no. 20, pp. 4835–4838, 2016. DOI: `10.1364/OL.41.004835`.

[195] Z. Wang, K. Van Gasse, V. Moskalenko, S. Latkowski, E. Bente, B. Kuyken, and G. Roelkens, “A III-V-on-Si ultra-dense comb laser”, en, *Light: Science & Applications*, vol. 6, no. 5, e16260–e16260, 2017. DOI: `10.1038/lsa.2016.260`.

[196] X. Yi, Q.-F. Yang, K. Y. Yang, and K. Vahala, “Active capture and stabilization of temporal solitons in microresonators”, EN, *Optics Letters*, vol. 41, no. 9, pp. 2037–2040, 2016. DOI: `10.1364/OL.41.002037`.

[197] L. Chang, W. Xie, H. Shu, Q.-F. Yang, B. Shen, A. Boes, J. D. Peters, W. Jin, C. Xiang, S. Liu, G. Moille, S.-P. Yu, X. Wang, K. Srinivasan, S. B. Papp, K. Vahala,

and J. E. Bowers, “Ultra-efficient frequency comb generation in AlGaAs-on-insulator microresonators”, en, *Nature Communications*, vol. 11, no. 1, p. 1331, 2020. DOI: `10.1038/s41467-020-15005-5`.

[198] T. Zhang, K. Yin, C. Zhang, R. Miao, and T. Jiang, “Integrated Electro-Optic Frequency Combs: Theory and Current Progress”, en, *Laser & Photonics Reviews*, vol. 18, no. 6, p. 2 301 363, 2024. DOI: `10.1002/lpor.202301363`.

[199] N. Andriolli, T. Cassese, M. Chiesa, C. de Dios, and G. Contestabile, “Photonic Integrated Fully Tunable Comb Generator Cascading Optical Modulators”, *Journal of Lightwave Technology*, vol. 36, no. 23, pp. 5685–5689, 2018. DOI: `10.1109/JLT.2018.2877020`.

[200] F. Bontempi, N. Andriolli, F. Scotti, M. Chiesa, and G. Contestabile, “Comb Line Multiplication in an InP Integrated Photonic Circuit Based on Cascaded Modulators”, *IEEE Journal of Selected Topics in Quantum Electronics*, vol. 25, no. 6, pp. 1–7, 2019. DOI: `10.1109/JSTQE.2019.2911459`.

[201] M. Zhang, B. Buscaino, C. Wang, A. Shams-Ansari, C. Reimer, R. Zhu, J. M. Kahn, and M. Lončar, “Broadband electro-optic frequency comb generation in a lithium niobate microring resonator”, en, *Nature*, vol. 568, no. 7752, pp. 373–377, 2019. DOI: `10.1038/s41586-019-1008-7`.

[202] H. Othman, G. Jain, M. Deseada Gutierrez Pascual, X. Ouyang, C. Antony, F. Smyth, and P. D. Townsend, “Integrated Comb Laser With Active De-Multiplexer for Spectrally Sliced Coherent Receiver”, *IEEE Photonics Technology Letters*, vol. 36, no. 12, pp. 787–790, 2024. DOI: `10.1109/LPT.2024.3398499`.

[203] D. Kazakov, M. Piccardo, Y. Wang, P. Chevalier, T. S. Mansuripur, F. Xie, C.-e. Zah, K. Lascola, A. Belyanin, and F. Capasso, “Self-starting harmonic frequency comb generation in a quantum cascade laser”, en, *Nature Photonics*, vol. 11, no. 12, pp. 789–792, 2017. DOI: `10.1038/s41566-017-0026-y`.

[204] P. Jouy, J. M. Wolf, Y. Bidaux, P. Allmendinger, M. Mangold, M. Beck, and J. Faist, “Dual comb operation of 8.2 m quantum cascade laser frequency comb with 1 W optical power”, *Applied Physics Letters*, vol. 111, no. 14, p. 141 102, 2017. DOI: `10.1063/1.4985102`.

[205] Q. Lu, F. Wang, D. Wu, S. Slivken, and M. Razeghi, “Room temperature terahertz semiconductor frequency comb”, en, *Nature Communications*, vol. 10, no. 1, p. 2403, 2019. DOI: `10.1038/s41467-019-10395-7`.

[206] H. Nguyen-Van, A. N. Baranov, Z. Loghmari, L. Cerutti, J.-B. Rodriguez, J. Tournet, G. Narcy, G. Boissier, G. Patriarche, M. Bahriz, E. Tournié, and R. Teissier, “Quantum cascade lasers grown on silicon”, en, *Scientific Reports*, vol. 8, no. 1, p. 7206, 2018. DOI: `10.1038/s41598-018-24723-2`.

[207] S. A. Diddams, L.-S. Ma, J. Ye, and J. L. Hall, “Broadband optical frequency comb generation with a phase-modulated parametric oscillator”, EN, *Optics Letters*, vol. 24, no. 23, pp. 1747–1749, 1999. DOI: `10.1364/OL.24.001747`.

[208] A. W. Bruch, X. Liu, Z. Gong, J. B. Surya, M. Li, C.-L. Zou, and H. X. Tang, “Pockels soliton microcomb”, en, *Nature Photonics*, vol. 15, no. 1, pp. 21–27, 2021. DOI: `10.1038/s41566-020-00704-8`.

[209] M. Jankowski, C. Langrock, B. Desiatov, A. Marandi, C. Wang, M. Zhang, C. R. Phillips, M. Loncar, and M. M. Fejer, “Ultrabroadband Nonlinear Optics in Nanophotonic Lithium Niobate Waveguides”, EN, in *OSA Advanced Photonics Congress (AP) 2020 (IPR, NP, NOMA, Networks, PVLED, PSC, SPPCom, SOF) (2020), paper NpM4D.3*, Optica Publishing Group, 2020, NpM4D.3. DOI: `10.1364/NP.2020.NpM4D.3`.

[210] Y. He, R. Lopez-Rios, Q. Yang, J. Ling, M. Li, K. Vahala, and Q. Lin, “Octave-spanning lithium niobate soliton microcombs”, in *2021 Conference on Lasers and Electro-Optics (CLEO)*, 2021, pp. 1–2.

[211] T. C. Briles, S.-P. Yu, L. Chang, C. Xiang, J. Guo, D. Kinghorn, G. Moille, K. Srinivasan, J. E. Bowers, and S. B. Papp, “Hybrid InP and SiN integration of an octave-spanning frequency comb”, *APL Photonics*, vol. 6, no. 2, p. 026 102, 2021. DOI: `10.1063/5.0035452`.

[212] S. Cuyvers, B. Haq, C. Op de Beeck, S. Poelman, A. Hermans, Z. Wang, A. Gocalinska, E. Pelucchi, B. Corbett, G. Roelkens, K. Van Gasse, and B. Kuyken, “Low Noise Heterogeneous III-V-on-Silicon-Nitride Mode-Locked Comb Laser”, en, *Laser & Photonics Reviews*, vol. 15, no. 8, p. 2 000 485, 2021. DOI: `10.1002/lpor.202000485`.

[213] H.-F. Liu, S. Arahira, T. Kunii, and Y. Ogawa, “Tuning characteristics of monolithic passively mode-locked distributed Bragg reflector semiconductor lasers”, *IEEE Journal of Quantum Electronics*, vol. 32, no. 11, pp. 1965–1975, 1996. DOI: `10.1109/3.541683`.

[214] M. Karpov, M. H. P. Pfeiffer, H. Guo, W. Weng, J. Liu, and T. J. Kippenberg, “Dynamics of soliton crystals in optical microresonators”, en, *Nature Physics*, vol. 15, no. 10, pp. 1071–1077, 2019. DOI: `10.1038/s41567-019-0635-0`.

[215] G. D. Domenico, S. Schilt, and P. Thomann, “Simple approach to the relation between laser frequency noise and laser line shape”, EN, *Applied Optics*, vol. 49, no. 25, pp. 4801–4807, 2010. DOI: `10.1364/AO.49.004801`.

[216] J. H. Marsh and L. Hou, “Mode-Locked Laser Diodes and Their Monolithic Integration”, *IEEE Journal of Selected Topics in Quantum Electronics*, vol. 23, no. 6, pp. 1–11, 2017. DOI: `10.1109/JSTQE.2017.2693020`.

[217] J. K. Alexander, P. E. Morrissey, H. Yang, M. Yang, P. J. Marraccini, B. Corbett, and F. H. Peters, “Monolithically integrated low linewidth comb source using gain

switched slotted Fabry-Perot lasers", EN, *Optics Express*, vol. 24, no. 8, pp. 7960–7965, 2016. DOI: `10.1364/OE.24.007960`.

[218] M. D. G. Pascual, V. Vujicic, J. Braddell, F. Smyth, P. M. Anandarajah, and L. P. Barry, "InP photonic integrated externally injected gain switched optical frequency comb", EN, *Optics Letters*, vol. 42, no. 3, pp. 555–558, 2017. DOI: `10.1364/OL.42.000555`.

[219] Y. Song, Y. Hu, X. Zhu, K. Yang, and M. Lončar, "Octave-spanning Kerr soliton frequency combs in dispersion- and dissipation-engineered lithium niobate microresonators", en, *Light: Science & Applications*, vol. 13, no. 1, p. 225, 2024. DOI: `10.1038/s41377-024-01546-7`.

[220] T. Ren, M. Zhang, C. Wang, L. Shao, C. Reimer, Y. Zhang, O. King, R. Esman, T. Cullen, and M. Lončar, "An Integrated Low-Voltage Broadband Lithium Niobate Phase Modulator", *IEEE Photonics Technology Letters*, vol. 31, no. 11, pp. 889–892, 2019. DOI: `10.1109/LPT.2019.2911876`.

[221] M. D. G. Pascual, V. Vujicic, J. Braddell, F. Smyth, P. Anandarajah, and L. Barry, "Photonic Integrated Gain Switched Optical Frequency Comb for Spectrally Efficient Optical Transmission Systems", *IEEE Photonics Journal*, vol. 9, no. 3, pp. 1–8, 2017. DOI: `10.1109/JPHOT.2017.2678478`.

[222] P. D. Lakshmijayasimha, A. Kaszubowska-Anandarajah, E. P. Martin, M. Srivastava, S. T. Ahmad, and P. M. Anandarajah, "Coherent Expansion of a Gain-Switched Optical Frequency Comb Employing a Dual-Stage Active Demultiplexer", EN, in *European Conference on Optical Communication (ECOC) 2022 (2022), paper We2E.5*, Optica Publishing Group, 2022, We2E.5.

[223] D. O. Sullivan, J. McCarthy, E. Russell, Z. Jia, B. Kelleher, and F. Peters, *Optical Frequency Comb Bandwidth Enhancement of a Monolithically Integrated Gain Switched Device*, en, 2025. DOI: `10.1364/opticaopen.29459153.v1`.

[224] F. Smyth, "Integrated Comb Lasers for Coherent Transceiver Scaling", EN, in *Advanced Photonics Congress 2024 (2024), paper SpTh1H.5*, Optica Publishing Group, 2024, SpTh1H.5. DOI: `10.1364/SPPCOM.2024.SpTh1H.5`.

[225] G. King. "Scaling coherent transceivers using integrated comb lasers", Pilot Photonics, Accessed: Sep. 18, 2025. [Online]. Available: `https://www.pilotphotonics.com/2023/07/13/comb-lasers-for-coherent-transceiver-scaling/`.

[226] S. Shao, J. Li, H. Chen, S. Yang, and M. Chen, "Gain-Switched Optical Frequency Comb Source Using a Hybrid Integrated Self-Injection Locking DFB Laser", *IEEE Photonics Journal*, vol. 14, no. 1, pp. 1–6, 2022. DOI: `10.1109/JPHOT.2022.3141424`.

[227] P. Trocha, M. Karpov, D. Ganin, M. H. P. Pfeiffer, A. Kordts, S. Wolf, J. Krockenberger, P. Marin-Palomo, C. Weimann, S. Randel, W. Freude, T. J. Kippenberg, and C. Koos,

"Ultrafast optical ranging using microresonator soliton frequency combs", *Science*, vol. 359, no. 6378, pp. 887–891, 2018. DOI: `10.1126/science.aao3924`.

[228] K. Hei, G. Shi, A. Hänsel, Z. Deng, S. Latkowski, S. A. Van den Berg, E. Bente, and N. Bhattacharya, "Distance Metrology With Integrated Mode-Locked Ring Laser", *IEEE Photonics Journal*, vol. 11, no. 6, pp. 1–10, 2019. DOI: `10.1109/JPHOT.2019.2940068`.

[229] I. Rebolledo-Salgado, C. Quevedo-Galán, Ó. B. Helgason, A. Lööf, Z. Ye, F. Lei, J. Schröder, M. Zelan, and V. Torres-Company, "Platicon dynamics in photonic molecules", en, *Communications Physics*, vol. 6, no. 1, p. 303, 2023. DOI: `10.1038/s42005-023-01424-5`.

[230] A. Shams-Ansari, M. Yu, Z. Chen, C. Reimer, M. Zhang, N. Picqué, and M. Lončar, "Thin-film lithium-niobate electro-optic platform for spectrally tailored dual-comb spectroscopy", en, *Communications Physics*, vol. 5, no. 1, p. 88, 2022. DOI: `10.1038/s42005-022-00865-8`.

[231] Z. Chen, K. Van Gasse, E. Vicentini, J. Huh, S. Poelman, Z. Wang, G. Roelkens, T. W. Hänsch, B. Kuyken, and N. Picqué, "High-Resolution Dual-Comb Gas-Phase Spectroscopy with a Mode-Locked Laser on a Photonic Chip", in *2020 Conference on Lasers and Electro-Optics (CLEO)*, 2020, pp. 1–2.

[232] K. Van Gasse, Z. Chen, E. Vincentini, J. Huh, S. Poelman, Z. Wang, G. Roelkens, T. W. Hänsch, B. Kuyken, and N. Picqué, "Dual-Comb Spectroscopy with Two On-Chip III-V-on-Silicon 1-GHz Mode-Locked Lasers", in *2021 Conference on Lasers and Electro-Optics (CLEO)*, 2021, pp. 1–2.

[233] J. K. Alexander, L. Caro, M. Dernaika, S. P. Duggan, H. Yang, S. Chandran, E. P. Martin, A. A. Ruth, P. M. Anandarajah, and F. H. Peters, "Integrated dual optical frequency comb source", EN, *Optics Express*, vol. 28, no. 11, pp. 16 900–16 906, 2020. DOI: `10.1364/OE.384706`.

[234] M. Trajkovic, F. Blache, H. Debregeas, K. A. Williams, and X. J. M. Leijtens, "Increasing the Speed of an InP-Based Integration Platform by Introducing High Speed Electroabsorption Modulators", *IEEE Journal of Selected Topics in Quantum Electronics*, vol. 25, no. 5, pp. 1–8, 2019. DOI: `10.1109/JSTQE.2019.2913727`.

[235] T. Tsukada and C. Tang, "Q-switching of semiconductor lasers", *IEEE Journal of Quantum Electronics*, vol. 13, no. 2, pp. 37–43, 1977. DOI: `10.1109/JQE.1977.1069280`.

[236] A. Rosado, A. Pérez-Serrano, J. M. G. Tijero, Á. Valle, L. Pesquera, and I. Esquivias, "Enhanced optical frequency comb generation by pulsed gain-switching of optically injected semiconductor lasers", EN, *Optics Express*, vol. 27, no. 6, pp. 9155–9163, 2019. DOI: `10.1364/OE.27.009155`.

[237] A. Consoli, I. Esquivias, F. J. Lopez Hernandez, J. Mulet, and S. Balle, “Characterization of Gain-Switched Pulses From 1.55-m VCSEL”, *IEEE Photonics Technology Letters*, vol. 22, no. 11, pp. 772–774, 2010. DOI: `10.1109/LPT.2010.2045648`.

[238] P. López-Querol, C. Quevedo-Galán, A. Pérez-Serrano, J. M. G. Tijero, and I. Esquivias, “Generation of optical frequency combs by Q-switching integrated multi-section semiconductor lasers”, EN, *Optics Express*, vol. 31, no. 20, pp. 33 475–33 485, 2023. DOI: `10.1364/OE.498426`.

[239] T. L. Koch and J. E. Bowers, “Nature of wavelength chirping in directly modulated semiconductor lasers”, EN, *Electronics Letters*, 1984. DOI: `10.1049/el:19840709`.

[240] J. Fridlander, V. Rosborough, F. Sang, M. Nickerson, J. Chen, K. Numata, P. Verrinder, F. Gambini, S. Pinna, S. Kawa, M. Stephen, L. Coldren, and J. Klamkin, “Photonic Integrated Circuits for Precision Spectroscopy”, in *2020 Conference on Lasers and Electro-Optics (CLEO)*, 2020, pp. 1–2.

[241] B. J. Isaac, B. Song, S. Pinna, L. A. Coldren, and J. Klamkin, “Indium Phosphide Photonic Integrated Circuit Transceiver for FMCW LiDAR”, *IEEE Journal of Selected Topics in Quantum Electronics*, vol. 25, no. 6, pp. 1–7, 2019. DOI: `10.1109/JSTQE.2019.2911420`.

[242] A. Pérez-Serrano, C. Quevedo-Galán, V. R. Aguilera-Sánchez, J. M. G. Tijero, and I. Esquivias, “Differential Absorption Lidar Transmitter Based on an Indium Phosphide Photonic Integrated Circuit for Carbon Dioxide Sensing”, *IEEE Journal of Selected Topics in Quantum Electronics*, vol. 28, no. 5: Lidars and Photonic Radars, pp. 1–8, 2022. DOI: `10.1109/JSTQE.2022.3156183`.

[243] J. Piprek, D. I. Babić, and J. E. Bowers, “Simulation and analysis of 1.55 m double-fused vertical-cavity lasers”, *Journal of Applied Physics*, vol. 81, no. 8, pp. 3382–3390, 1997. DOI: `10.1063/1.365033`.

[244] J. Dawson, N. Park, and K. Vahala, “An improved delayed self-heterodyne interferometer for linewidth measurements”, *IEEE Photonics Technology Letters*, vol. 4, no. 9, pp. 1063–1066, 1992. DOI: `10.1109/68.157150`.

[245] D. R. Carlson, D. D. Hickstein, D. C. Cole, S. A. Diddams, and S. B. Papp, “Dual-comb interferometry via repetition rate switching of a single frequency comb”, EN, *Optics Letters*, vol. 43, no. 15, pp. 3614–3617, 2018. DOI: `10.1364/OL.43.003614`.

[246] D. Baney and W. Sorin, “Measurement of a modulated DFB laser spectrum using gated delayed self-homodyne technique”, *Electronics Letters*, vol. 24, no. 11, pp. 669–670, 1988. DOI: `10.1049/el:19880453`.

[247] L. Chrostowski and W. Shi, “Monolithic Injection-Locked High-Speed Semiconductor Ring Lasers”, *Journal of Lightwave Technology*, vol. 26, no. 19, pp. 3355–3362, 2008. DOI: `10.1109/JLT.2008.928927`.

[248] M. Sorel, G. Giuliani, A. Scire, R. Miglierina, S. Donati, and P. Laybourn, “Operating regimes of GaAs-AlGaAs semiconductor ring lasers: Experiment and model”, *IEEE Journal of Quantum Electronics*, vol. 39, no. 10, pp. 1187–1195, 2003. DOI: `10.1109/JQE.2003.817585`.

[249] G. Yuan and S. Yu, “Bistability and Switching Properties of Semiconductor Ring Lasers With External Optical Injection”, *IEEE Journal of Quantum Electronics*, vol. 44, no. 1, pp. 41–48, 2008. DOI: `10.1109/JQE.2007.909523`.

[250] D. Plaza-Vas, M. Duque-Gijón, C. Masoller, J. Tiana-Alsina, Á. Valle, N. Vermeulen, and A. Quirce, “Experimental and theoretical study of optical frequency combs in gain-switched Discrete Mode Lasers under optical injection into suppressed longitudinal modes”, EN, *Optics Express*, vol. 33, no. 13, pp. 28 366–28 377, 2025. DOI: `10.1364/OE.565190`.

[251] L. A. Coldren, P. A. Verrinder, and J. Klamkin, “A Review of Photonic Systems-on-Chip Enabled by Widely Tunable Lasers”, *IEEE Journal of Quantum Electronics*, vol. 58, no. 4, pp. 1–10, 2022. DOI: `10.1109/JQE.2022.3168041`.

[252] I. V. Ermakov, S. Beri, M. Ashour, J. Danckaert, B. Docter, J. Bolk, X. J. M. Leijtens, and G. Verschaffelt, “Semiconductor Ring Laser With On-Chip Filtered Optical Feedback for Discrete Wavelength Tuning”, *IEEE Journal of Quantum Electronics*, vol. 48, no. 2, pp. 129–136, 2012. DOI: `10.1109/JQE.2011.2169945`.

[253] M. C. Larson, A. Bhardwaj, W. Xiong, Y. Feng, X. D. Huang, K. P. Petrov, M. Moewe, H. Y. Ji, A. Semakov, C. W. Lv, S. Kutty, A. Patwardhan, N. Liu, Z. M. Li, Y. J. Bao, Z. H. Shen, S. Bajwa, F. H. Zhou, and P. C. Koh, “Narrow linewidth sampled-grating distributed Bragg reflector laser with enhanced side-mode suppression”, EN, in *Optical Fiber Communication Conference (2015), paper M2D.1*, Optica Publishing Group, 2015, p. M2D.1. DOI: `10.1364/OFC.2015.M2D.1`.

[254] K. Shi, F. Smyth, P. M. Anandarajah, D. Reid, Y. Yu, and L. P. Barry, “Linewidth of SG-DBR laser and its effect on DPSK transmission”, *Optics Communications*, vol. 283, no. 24, pp. 5040–5045, 2010. DOI: `10.1016/j.optcom.2010.08.028`.

[255] M. Izutsu, S. Shikama, and T. Sueta, “Integrated optical SSB modulator/frequency shifter”, *IEEE Journal of Quantum Electronics*, vol. 17, no. 11, pp. 2225–2227, 1981. DOI: `10.1109/JQE.1981.1070678`.

[256] H. Yamazaki, T. Saida, T. Goh, S. Mino, M. Nagatani, H. Nosaka, and K. Murata, “Dual-Carrier Dual-Polarization IQ Modulator Using a Complementary Frequency Shifter”, *IEEE Journal of Selected Topics in Quantum Electronics*, vol. 19, no. 6, pp. 175–182, 2013. DOI: `10.1109/JSTQE.2013.2263120`.

[257] M. Lauermann, C. Weimann, A. Knopf, D. L. Elder, W. Heni, R. Palmer, D. Korn, P. C. Schindler, S. Koeber, L. Alloatti, H. Yu, W. Bogaerts, L. R. Dalton, C. Rembe,

J. Leuthold, W. Freude, and C. Koos, “Integrated Silicon-Organic Hybrid (SOH) Frequency Shifter”, EN, in *Optical Fiber Communication Conference (2014), paper Tu2A.1*, Optica Publishing Group, 2014, Tu2A.1. DOI: `10.1364/OFC.2014.Tu2A.1`.

[258] S. Andreou, K. A. Williams, and E. A. J. M. Bente, “Steady-State Analysis of the Effects of Residual Amplitude Modulation of InP-Based Integrated Phase Modulators in Pound–Drever–Hall Frequency Stabilization”, *IEEE Photonics Journal*, vol. 11, no. 3, pp. 1–14, 2019. DOI: `10.1109/JPHOT.2019.2915163`.

[259] S. Kumar and M. J. Deen, *Fiber Optic Communications: Fundamentals and Applications*, en. John Wiley & Sons, 2014.

[260] S. Royo and M. Ballesta-Garcia, “An Overview of Lidar Imaging Systems for Autonomous Vehicles”, en, *Applied Sciences*, vol. 9, no. 19, p. 4093, 2019. DOI: `10.3390/app9194093`.

[261] N. Takeuchi, N. Sugimoto, H. Baba, and K. Sakurai, “Random modulation cw lidar”, EN, *Applied Optics*, vol. 22, no. 9, pp. 1382–1386, 1983. DOI: `10.1364/AO.22.001382`.

[262] U. Wandinger, “Introduction to Lidar”, en, in *Lidar: Range-Resolved Optical Remote Sensing of the Atmosphere*, C. Weitkamp, Ed., Springer, 2005, pp. 1–18. DOI: `10.1007/0-387-25101-4_1`.

[263] J. Wang, G. Zhang, and Z. You, “High-resolution LiDAR using random modulated continuous wave with a low code rate”, *Measurement*, vol. 202, p. 111 719, 2022. DOI: `10.1016/j.measurement.2022.111719`.

[264] Z. Xu, F. Yu, Q. Bowen, Y. Zhang, X. Yu, and S. Pan, “Coherent Random-Modulated Continuous-Wave LiDAR Based on Phase-Coded Subcarrier Modulation”, English, *Photonics*, vol. 8, no. 11, 2021. DOI: `10.3390/photonics8110475`.

[265] C. Nagasawa, M. Abo, H. Yamamoto, and O. Uchino, “Random modulation cw lidar using new random sequence”, EN, *Applied Optics*, vol. 29, no. 10, pp. 1466–1470, 1990. DOI: `10.1364/AO.29.001466`.

[266] A. Martin, D. Dodane, L. Leviandier, D. Dolfi, A. Naughton, P. O’Brien, T. Spuessens, R. Baets, G. Lepage, P. Verheyen, P. De Heyn, P. Absil, P. Feneyrou, and J. Bourderionnet, “Photonic Integrated Circuit-Based FMCW Coherent LiDAR”, *Journal of Lightwave Technology*, vol. 36, no. 19, pp. 4640–4645, 2018. DOI: `10.1109/JLT.2018.2840223`.

[267] A. Lukashchuk, H. K. Yildirim, A. Bancora, G. Lihachev, Y. Liu, Z. Qiu, X. Ji, A. Voloshin, S. A. Bhave, E. Charbon, and T. J. Kippenberg, “Photonic-electronic integrated circuit-based coherent LiDAR engine”, en, *Nature Communications*, vol. 15, no. 1, p. 3134, 2024. DOI: `10.1038/s41467-024-47478-z`.

[268] P. J. Reyes-Iglesias, I. Molina-Fernández, A. Moscoso-Mártir, and A. Ortega-Moñux, “High-performance monolithically integrated 120° downconverter with relaxed hardware constraints”, EN, *Optics Express*, vol. 20, no. 5, pp. 5725–5741, 2012. DOI: `10.1364/OE.20.005725`.

[269] D. Izquierdo, J. Clemente, P. J. Reyes-Iglesias, A. Ortega-Moñux, J. A. Altabás, I. Molina-Fernández, J. G. Wangüemert-Pérez, J. de Oliva-Rubio, and I. Garcés, “Analysis of the Colorless Operation of a Calibrated 120° Coherent Receiver”, *Journal of Lightwave Technology*, vol. 39, no. 17, pp. 5405–5411, 2021. DOI: `10.1109/JLT.2021.3069393`.

[270] J. Clemente, D. Izquierdo, P. J. Reyes-Iglesias, A. Ortega-Moñux, J. A. Altabas, I. Molina-Fernández, G. Wangüemert-Pérez, J. de Oliva-Rubio, and I. Garcés, “Experimental Demonstration of Colorless Operation of an Integrated 120° Coherent Receiver”, in *2018 European Conference on Optical Communication (ECOC)*, 2018, pp. 1–3. DOI: `10.1109/ECOC.2018.8535586`.

[271] M. Pu, L. Ottaviano, E. Semenova, and K. Yvind, “Efficient frequency comb generation in AlGaAs-on-insulator”, EN, *Optica*, vol. 3, no. 8, pp. 823–826, 2016. DOI: `10.1364/OPTICA.3.000823`.

[272] W. Xie, L. Chang, H. Shu, J. C. Norman, J. D. Peters, X. Wang, and J. E. Bowers, “Ultrahigh-Q AlGaAs-on-insulator microresonators for integrated nonlinear photonics”, EN, *Optics Express*, vol. 28, no. 22, pp. 32 894–32 906, 2020. DOI: `10.1364/OE.405343`.

[273] E. Stassen, C. (Kim, D. (Kong, H. (Hu, M. Galili, L. K. Oxenløwe, K. Yvind, and M. (Pu, “Ultra-low power all-optical wavelength conversion of high-speed data signals in high-confinement AlGaAs-on-insulator microresonators”, *APL Photonics*, vol. 4, no. 10, p. 100 804, 2019. DOI: `10.1063/1.5115232`.

[274] C. Kim, C. Ye, Y. Zheng, E. Semenova, K. Yvind, and M. Pu, “Design and Fabrication of AlGaAs-on-Insulator Microring Resonators for Nonlinear Photonics”, *IEEE Journal of Selected Topics in Quantum Electronics*, vol. 29, no. 1: Nonlinear Integrated Photonics, pp. 1–14, 2023. DOI: `10.1109/JSTQE.2022.3212047`.

[275] D. G. Rabus and C. Sada, “Ring Resonators: Theory and Modeling”, en, in *Integrated Ring Resonators: A Compendium*, D. G. Rabus and C. Sada, Eds., Springer International Publishing, 2020, pp. 3–46. DOI: `10.1007/978-3-030-60131-7_2`.

[276] W. Bogaerts, P. De Heyn, T. Van Vaerenbergh, K. De Vos, S. Kumar Selvaraja, T. Claes, P. Dumon, P. Bienstman, D. Van Thourhout, and R. Baets, “Silicon microring resonators”, en, *Laser & Photonics Reviews*, vol. 6, no. 1, pp. 47–73, 2012. DOI: `10.1002/lpor.201100017`.